DICI
DIPARTIMENTO DI INGEGNERIA CIVILE E INDUSTRIALE

IN SUPREMÆ DIGNITATIS 1343

Parametric Identification of Backflow Vortex Instability: A Comparative Study

MASTER'S THESIS

Author: Álvaro Ruiz López

Supervisor: Luca d'Agostino

Counsellor: Stefano Guidolotti

Laurea Magistrale Aerospace Engineering
September, 5, 2022, Pisa

ACKNOWLEDGMENTS

"A ogni uccello, il suo nido è bello"
Italian proverb.

I would like to thank all the people who have crossed my life and have stayed with me even in the most difficult moments, helping me to be the person I am today.
Special mention to my parents, without their efforts I would never have reached this point. His sacrifice has allowed me to finish this stage of my life.
To Professor Luca d'Agostino, for allowing me to be part of this enriching project from which I have learned many things that I did not even know I did not know.
To Stefano Guidolotti, without his patience and help, the realization of this project would have been impossible. Thank you for every call explaining everything I should know and every message guiding me into finishing this document.
To Laia, I am sure that without her support, I would have left everything a long time ago. Thank you for always being there.

RESUMEN

En los motores líquidos de cohetes típicos, las turbobombas utilizadas para alimentar el propulsor son componentes cruciales: la presencia de inestabilidades de flujo es la limitación más estricta en el rendimiento de succión, la densidad de potencia y la vida operativa de estas máquinas. Este trabajo representa la extensión del método de estimación bayesiano aplicado para detectar y caracterizar eficazmente la inestabilidad del vórtice de reflujo, diseñado y probado con éxito por el Prof. Luca d'Agostino y sus colaboradores. El método se usó para la comparación cuantitativa de las inestabilidades de vórtice de reflujo detectadas en varios inductores de 3 y 4 palas que varían la carga, la holgura de la punta y diferentes regímenes de cavitación. Los resultados son consistentes con los datos de la literatura común que confirma que estos modelos pueden ser útiles para abordar de manera eficiente la optimización paramétrica preliminar del diseño del inductor del motor de cohete.

Palabras clave: Turbobombas, Inductores, Inestabilidades de Flujo, Cavitación de Vórtice de Reflujo, Estimación de Probabilidad Máxima.

ABSTRACT

In typical liquid rocket engines, turbopumps used to feed the propellant are crucial components: the presence of flow instabilities is the most stringent limitation in the suction performance, power density and operational life of these machines. This work represents the extension of the Bayesian estimation method applied to effectively detect and characterize backflow vortex instability successfully designed and tested by Prof. Luca d'Agostino and his collaborators. The method was used for the quantitative comparison of the backflow vortex instabilities detected in several 3- and 4-bladed inducers varying load, tip clearance and different cavitating regimes. The results are consistent with the reported data in common literature, that is particularly scant, confirming these models can be helpful in efficiently addressing the preliminary parametric optimization of rocket engine inducer design.

Keywords: Turbopumps, Inducers, Flow Instabilities, Backflow Vortex Cavitation, Maximum Likelihood Estimation.

RESUM

En els motors de coets líquids típics, les turbobombes que s'utilitzen per alimentar el propulsor són components crucials: la presència d'inestabilitats de flux és la limitació més estricta en el rendiment d'aspiració, la densitat de potència i la vida operativa d'aquestes màquines. Aquest treball representa l'extensió del mètode d'estimació bayesià aplicat per detectar i caracteritzar eficaçment la inestabilitat del vòrtex de retorn dissenyat i provat amb èxit pel Prof. Luca d'Agostino i els seus col·laboradors. El mètode es va utilitzar per a la comparació quantitativa de les inestabilitats del vòrtex de retrocés detectades en diversos inductors de 3 i 4 fulles que varien la càrrega, la separació de la punta i els diferents règims de cavitat. Els resultats són coherents amb les dades informades a la literatura comuna que confirma que aquests models poden ser útils per abordar de manera eficient l'optimització paramètrica preliminar del disseny de l'inductor del motor de coets.

Paraules clau: Turbobombes, Inductors, Inestabilitats de Flux, Cavitació de Vòrtex de Reflux, Estimació de Probabilitat Màxima.

Contents

List of Figures

List of Tables

NOMENCLATURE

Greek symbols

Γ	Circulation [m^2/s]
$\Delta\theta$	Angular separation [º]
Δt	Sampling interval [s]
ϕ	Flow coefficient [-]
Ψ	Head coefficient [-]
Ω	Rotational speed [s^{-1}]
α	Incidence angle [º]
β_{mb}	Blade taper meridional half angle [mm.]
Υ	Blade angle [º]
Υ_{xy}	Coherence function [-]
ε_{TOT}	Figure of merit [-]
υ	Kinematic viscosity [m^2/s]
ρ	Density [kg/m^3]
σ	Euler number [-]
σ	Solidity [-]
σ_g	Variance of the Gaussian [-]
φ	Phase of the cross-correlation [º]
ω	Angular speed [s^{-1}]
ω_γ	Angular velocity of the vortices [rad/s]

Roman symbols

A	Area [m^2]
C_a	Cavitation number [-]
C_p	Pressure coefficient [-]
D	Diffusion factor [-]
D	Referent to design [-]
H	Referent to hub [-]
J	Jacobian function [-]
N	Number of blades [-]
N	Number of vortices [-]
P	Pressure [Pa]
Q	Volumetric flow rate [m^3/s]
Re	Reynolds number [-]
S_{xx}	Power density function of the auto-spectrum [-]
S_{xy}	Power density function of the cross-spectrum [-]
U	Velocity [m/s]
a	Radial position of the vortices [m]
b_T	Meridional tip blade thickness [mm.]
c_a	Axial length (fully-developed blade) [mm.]
exp	Related to experimental [-]
f_c	Nyquist frequency [Hz]
l	Referent to liquid [-]
le	Referent to inlet [-]
$\dot{m}$	Mass flow [kg/s]
max	Referent to maximum [-]
min	Referent to minimum [-]
n_c	Number of rotating cells [-]
n_d	Number of data blocks [-]

$\hat{p}$	Pressure perturbation [Pa]
$\tilde{p}$	Pressure perturbation with frequency broadening [Pa]
r	Radius [m]
$r_{Sexp\ Sth}$	Cross-correlation coefficient [-]
t	Referent to tip [-]
te	Referent to outlet [-]
th	Related to theoretical [-]
v	Referent to vapor [-]

PART I: REPORT

1.Introduction

This Section presents an introduction of the Master's thesis developed. For this purpose, a statement of the problem can be found where the context in which the current work extends is detailed generically. Also, the basic concepts to understand flow instabilities due to cavitation in liquid rocket engine turbopump inducers are punctuated.

In addition, the objectives and motivation that have led to the realization of the project are shown.

Finally, the methodology used to carry out the project with the steps followed that have led to the achievement of this document is also explained.

1.1. Statement of the problem

When developing an inducer for a space rocket motor, many crucial aspects must be considered. Firstly, based on the desired pumping behaviour, a geometry must be chosen taking into account the internal flow evolution. However, this is insufficient as the pumping behaviour is degraded due to the cavitation phenomenon. Nowadays, the way to deal with this problem is through experimental research with the choice of appropriate scaling criteria. Therefore, the characterization of cavitation instabilities using an analytical model could represent a great advance. The use of this tool to identify the cavitation phenomenon and through a comparative study, the preliminary parametric optimization of the rocket motor inducer design is the basis of this project.

1.2. Basic concepts

1.2.1. CAVITATION

The phenomenon of cavitation is one of the most important limitations in the operation of liquid turbomachinery [6][19]. It is a significant source of deterioration of performance and efficiency and could influence fluid mechanic instabilities of the turbopump. Also, it is responsible for noise, vibration, and possible failure-inducing damage to the structure.

Cavitation is a term that could be related to boiling, but there is a significant difference between them. As in boiling, the change of phase occurs due to an increment of temperature, in the case of cavitation phenomena, it could be described as a process defined as the change of phase befalling in a liquid when the static pressure decreases below the vapor pressure leading to the formation of vapor bubbles as can be seen in Figure 1.1.

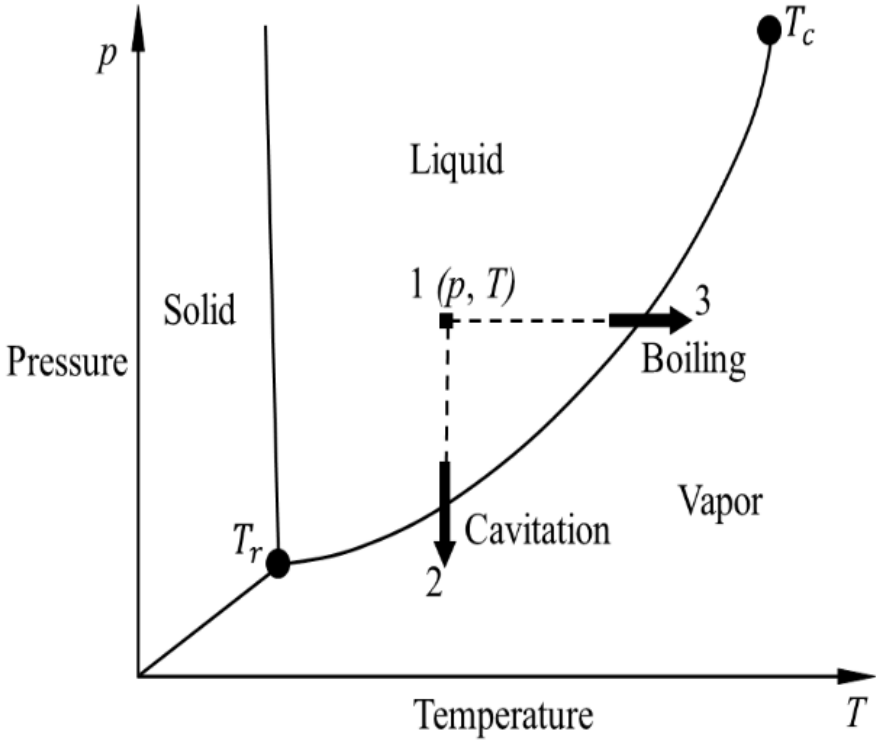

FIGURE 1.1: SCHEMATIC OF THE PHASE DIAGRAM OF FLUID [20]

It can be seen that the boiling process is the heating relatively at a constant pressure while the cavitation occurs from lowering the pressure relatively isothermally. Nevertheless, it is remotely feasible to change temperature uniformly in a large volume of liquid. For this reason, nucleation positions that are firstly activated are on the boundary because the temperature is higher there. Otherwise, in cavitation, the most susceptible nucleation sites are microbubbles.
The cavitation process can be divided into three phases well-differentiated:

1. **Cavitation inception**: Usually, the cavitation number (C_a) determines the proximity that exists between the pressure in the liquid flow and the vapor pressure. It is a dimensionless number expressing the potential of the flow to cavitate. It is another way of expressing the Euler number, as it is commented in detail in Subsection 1.2.3. However, this expression is used due to the fact that it makes it easier to explain the concept presented here.

$$\boldsymbol{C_a = \frac{2 \cdot (P_\infty - P_v)}{\rho_l \cdot U_\infty^2}} \qquad 1.1$$

   As this number is reduced, the cavitation number will arrive at a value C_{ai} called the incipient cavitation number. This value could be related to a value of pressure coefficient C_{pmin} but they are not equivalent due to several factors such as residence time in cavitation nuclei or fluctuations in pressure among others.

2. **Bubble growth**: The tendency of this phase is to be quite steady. All activated nuclei are inclined to grow to an equivalent maximum size because the time available for growth does not depend on the size of the original nucleus.

During the definition of cavitation and with respect to Figure 1.1, it has been said that it is practically an isothermal process. This is true in the case of fluids at low temperatures; in the case of high temperatures, there are differences in temperature between the bulk of fluid and vapor/liquid interface, and the growth rate is restrained.

3. **Bubble collapse**: Cavitation bubbles tend to collapse when confront with a region where static pressure is higher than the vapor pressure. The collapse is very violent, being able to damage structures critically. Also, the collapse forms many small bubbles that could regroup and collapse again.

Moreover, in order to understand the importance of the cavitation, some of the problems and disadvantages generated are listed below [6]:

- **Vibration and noise**: Cavitation generates a chaotic, unpatterned vibration at high frequencies with a wide bandwidth. The collapse of the bubbles generates vibration peaks at high frequencies. When cavitation bubbles collapse, they are emitting shock waves, an important source of noise and damage. Also, cavitation noise can even reach resonance amplitude with structural frequencies of vibration.

- **Surface damage**: The collapse of cavitation bubbles is an extremely abrupt process. Large-amplitude shock waves and microjets are generated in a very localized way. If the collapse occurs close to a solid surface, they are created strong surface stresses and damage the material when they are convected into regions of increased pressure. In the case that the material is soft, pits and erosion are present on the structure surface, damaging the performance and endangering the whole system. Some real examples of this problem are shown in Figures 1.2 and 1.3.

FIGURE 1.2: CAVITATION DAMAGE TO A FRANCIS TURBINE [6]

FIGURE 1.3: CAVITATION DAMAGE OF A PROPELLER [6]

- **Fatigue of the material**: If the material is hard, as is common in multiple applications, the collapses of cavitation bubbles create a cycle of loads affecting the material, reducing its useful life, and provoking detachments of pieces of material. However, cavitation peening could be used as improvement in the fatigue strength due to the introduction of compressive residual stress.

- **Reduction of performance**: The cavitation could cause a reduction in the mass flow capacity of the pump. If the volume occupied by vapor due to cavitation is high, there is a reduction of mass flow through the pump, and the level of performance falls.

- **Instabilities**: As it has been explained previously, cavitation produces instabilities with fluctuations in pressure and flow rate. For instance, the *rotating cavitation* generally can be seen when the cavitation number lowers until reaching a value at which the head is being affected by cavitation. It can be distinguished by a propagating velocity larger than the impeller speed. In this case, the cavitation is transmitted from a blade to adjacent blades.

Finally, it is appropriate to classify between different types of cavitation [6]. The uniqueness of the classification is far from being a reality and some forms of cavitation could occur far from the identified in the classification shown in Figure 1.4.

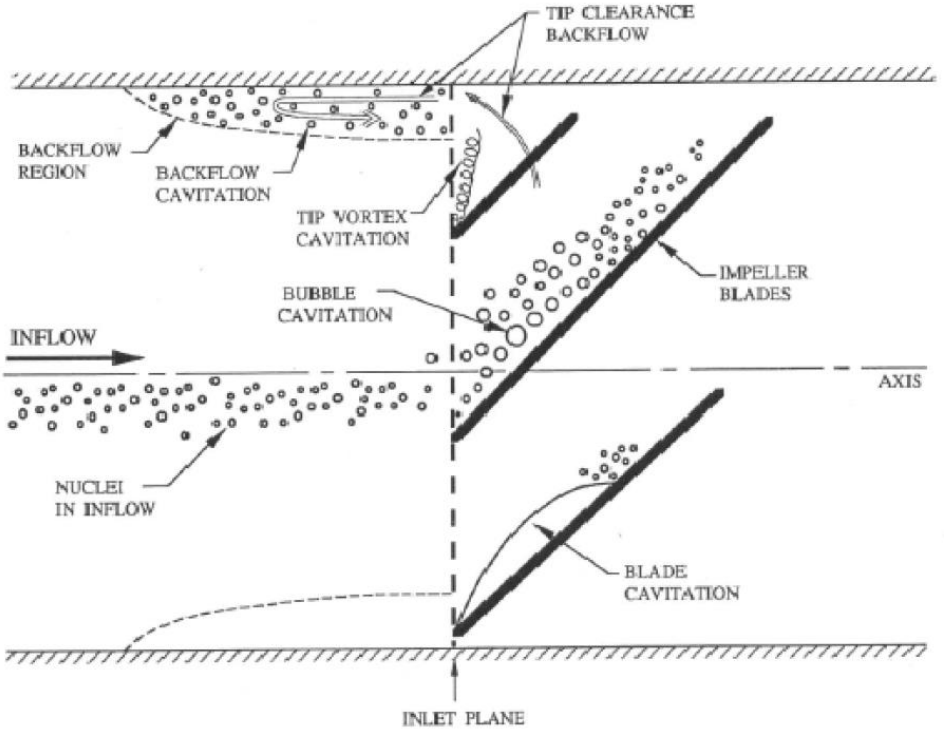

FIGURE 1.4: TYPES OF CAVITATION IN PUMPS [6]

With the reduction of the inlet pressure, the inception cavitation number C_{ai} is reached in the tip vortex generated by the corner where the tip and leading-edge meet causing **tip vortex cavitation**. If the value of the cavitation number keeps reducing its value, **bubble cavitation** is created. It is based on traveling bubble cavitation on the suction surfaces of the blades that collapse as they confront regions with higher pressure. As the cavitation number is reduced, it could be a combination of bubbles shaping large cavities attached to the suction surfaces of the blades producing the called **blade cavitation**. When blade cavitation is extended to the point on the suction surface opposite the leading-edge of the next blade, an increment in pressure in the blade passage collapses the cavity. **Partial cavitation** is formed when the blade cavitation is collapsed on the suction surface. In the present document, it is very important the concept of **backflow cavitation**.

In this case, it is adequate to define the dimensionless parameter *flow coefficient* used to describe the volume flow rate:

$$\phi = \frac{\dot{m} \cdot A}{\rho \cdot \Omega \cdot r_T} = \frac{Q}{\pi \cdot \Omega \cdot r_T^3} \qquad 1.2$$

It refers to cavitating bubbles and vortices located in the annular region of backflow upstream of the inlet plane when the pump is operating in a loaded condition below the design flow rate. The higher pressure across the pump under this conjuncture could entail the tip clearance flow penetrating upstream and generating a backflow extending many diameters upstream of the inlet plane. An example of backflow cavitation is shown in Figure 1.5.

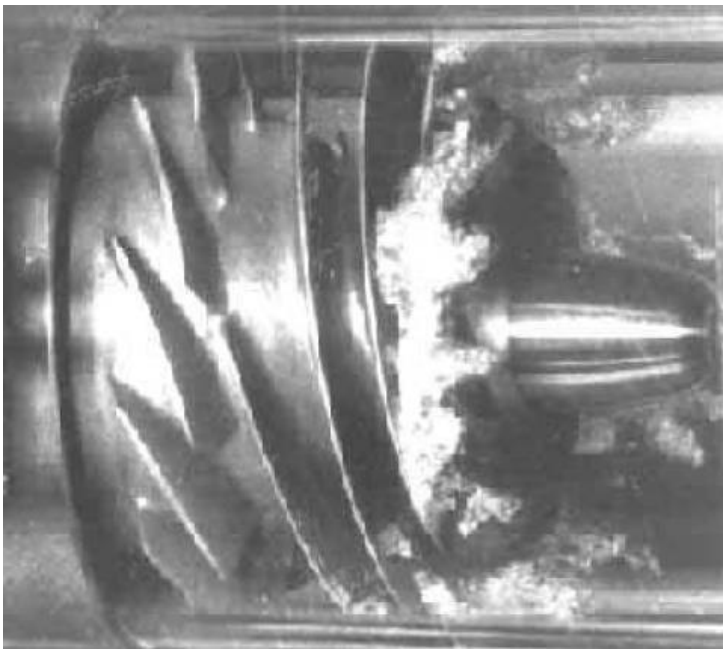

FIGURE 1.5: TYPICAL BACKFLOW CAVITATION [6]

The backflow is inflicted by the leakage flow between the tip of the blades of an impeller and the pump casing as it can be seen in Figure 1.6. After the tip fugue penetrates upstream a certain distance, it is produced the re-entrance of the fluid into the main inlet flow. As the flow coefficient is reduced, the penetration distance gets longer, even reaching many diameters upstream. In some pump development programs it has been tried to insert a "backflow deflector" improving pump performance by prevising the flow to penetrate a long distance upstream, reducing distortion of the inlet flow field, and recovering (as much as possible) the swirl energy in the backflow.

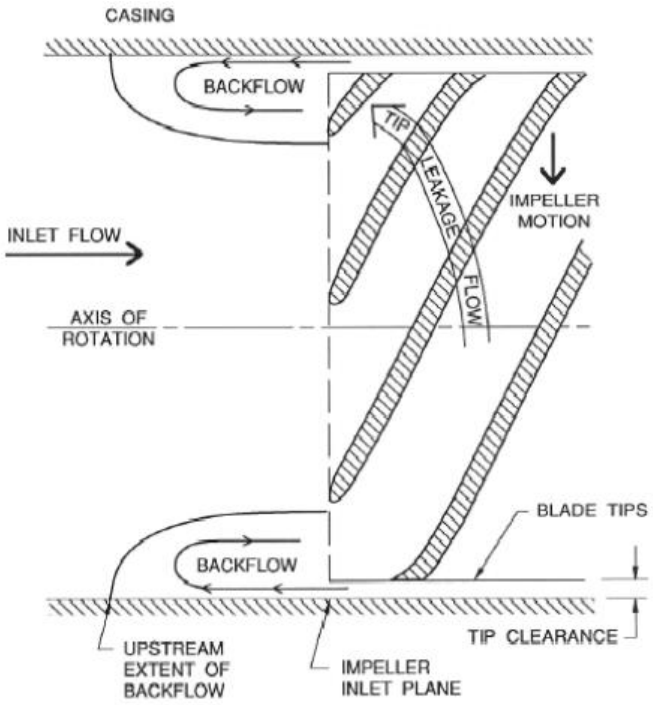

FIGURE 1.6: LATERAL VIEW OF IMPELLER INLET FLOW SHOWING TIP LEAKAGE FLOW LEADING TO BACKFLOW [6]

1.2.2. INDUCERS

The inducer is defined as the axial inlet portion of the turbopump rotor with the objective of incrementing the inlet pressure to a value sufficiently high in order to inhibit cavitation in the following stage that is the main pump [1]. This part of the geometry could be an integral part of the pump rotor, or it could be separated, upstream of the impeller.

Currently, inducers are used in rocket turbopumps upstream of the centrifugal stage. The aim of the inducer is to prevent problems related to cavitation, enhance the suction performance, and reduce pressure and weight from the propellant tank. The parameters of design are very important since the performance and efficiency of the inducer depends on different geometrical and design parameters.

Due to the aim of the inducer, it is common to find small angles of attack on long blades. Thus, there is enough time for the collapse of cavitation bubbles and the exchange of energy with the flow. That configuration is convenient in terms of cavitation performance, but the efficiency is very low due to viscous, turbulent, and dissipative flow inside the blade passage. Due to the advantages related to the design parameters of the angle of attack and length of the blades, it is obvious that a balance must be found between the cavitation performance and the efficiency expected of the inducer.

For the purpose of characterizing a classification of inducers, the dimensionless parameter *head coefficient* must be defined:

$$\Psi = \frac{p_2 - p_1}{\rho \cdot \Omega^2 \cdot r_T^2} \qquad 1.3$$

If the attention is paid to the head coefficient, inducers can be classified in function of head-rise capability. The division made is between low head and high head depending on the value of head coefficient, being the limit value 0.15. That means that if the head-rise capability is lower than 0.15 ($\Psi < 0.15$), it is called low head and in the case that the head coefficient is higher than 0.15 ($\Psi > 0.15$), it is called high head. The head-rise capability is function of the blade geometry and hub-tip contours. Basic inducer types are shown in Figure 1.7.

In the case of high head inducers, the pressure rise is due to hydrodynamic forces and centrifugal force. On the other hand, for low head inducers, the centrifugal force is negligible, and the pressure rise is a consequence of solely hydrodynamic forces.

Taking this classification into account, it can be said that the optimal configuration is a trade-off between good suction performance and maintaining integrity under all operating conditions defining the mission of the inducer. It must be an equilibrium between the mechanical problem (structural integrity enduring blade loading, instabilities, rotordynamic forces with an accurate choice of material) and the hydrodynamic problem (obtain the required suction performance without the undesired phenomenon of cavitation).

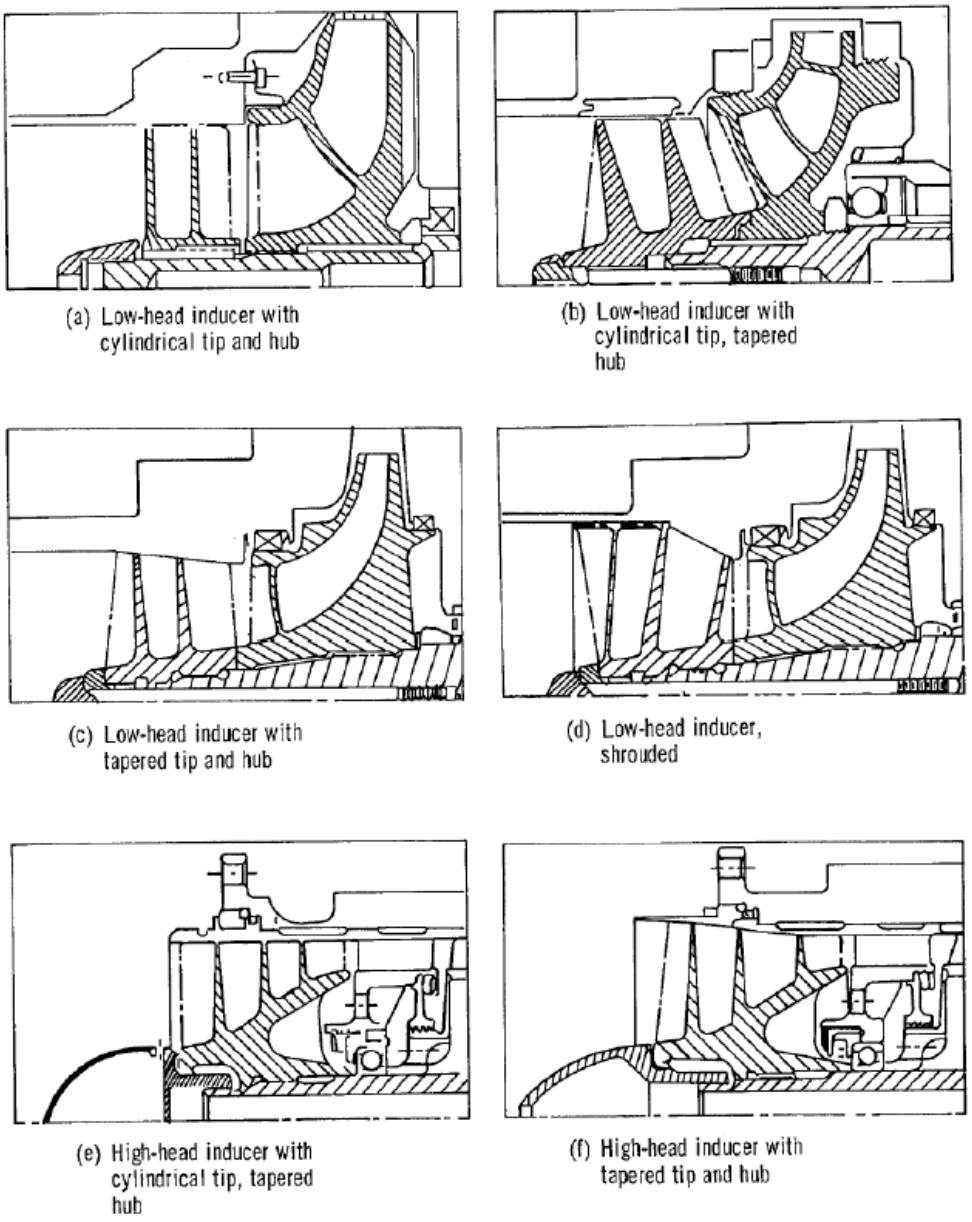

FIGURE 1.7: BASIC INDUCER TYPES [1]

1.2.3. PUMPING PERFORMANCE IN AXIAL INDUCERS

In the characterization of pumping performance, it is interesting to divide between non-cavitating and cavitating performance [1].
The non-cavitating performance is usually summarized by experimental evaluation of the characteristic curve at fully developed turbulent Reynolds number (Re > 10^6).

$$\Psi = \Psi(\phi) \qquad 1.4$$

with the nondimensional parameters:

$$\phi = \frac{\dot{m}/\rho \cdot A_1}{\Omega \cdot r_T} = \frac{Q}{\pi \cdot \Omega \cdot r_T^3}$$

$$\Psi = \frac{p_2 - p_1}{\rho \cdot \Omega^2 \cdot {r_T}^2} = \frac{\Delta p}{\rho \cdot \Omega^2 \cdot {r_T}^2} \qquad 1.5$$

$$Re = \frac{2 \cdot \Omega \cdot r_T^2}{\upsilon}$$

The pressure rise is measured by differential pressure transducers with the pressure taps located on the walls of the inlet/outlet lines. The volumetric flow rate is measured making use of two electromagnetic flowmeters mounted on the suction and discharge lines. The rotational speed remains constant by the main motor control device.

For the cavitating pumping performance, suction performance is obtained by the measurement of the head coefficient as a function of the inlet pressure (p_1) with constant values of flow coefficient and fully-developed turbulent Reynolds number ($Re > 10^6$).

$$\Psi = \Psi(\sigma) \qquad 1.6$$

In this case, the nondimensional parameter for the inlet pressure is the Euler number defined as:

$$\sigma = \frac{p_1 - p_v}{0.5 \cdot \rho \cdot \Omega^2 \cdot {r_T}^2} \qquad 1.7$$

The inlet pressure is obtained from an absolute pressure transducer installed upstream the inducer.

1.3. Objectives

The main objective of this document is the understanding and use of Bayesian estimation method to detect and characterize backflow vortex instability, one of the most important instabilities limiting liquid rocket engine turbopumps.

In order to achieve this objective, a tool of great importance is used: the utilization of *MATLAB* for the evaluation of the code based on the theoretical model developed by Prof. Luca d'Agostino and his collaborators and for carrying out different simulations for diverse inducers and parameters obtaining a quantitative comparation. Also, it is important to comment that all the identifications obtained agree with other 2 different theoretical models that are commented later in this document.
Thus, a secondary objective, it is intended that the author develops a certain familiarity and expertise with a program that has a great relevance in the aerospace and many other engineering fields.
Consequently, by the present Final Master Project it is intended to achieve:

- The understanding of Bayesian estimation method and cavitation-induced flow instabilities considering its importance in liquid rocket engines.
- Promote future academic projects with the line of research developed in this project and based on the same line of research from other documents considering the success in its implementation.
- Learning and managing the tools available in *MATLAB* allowing the gaining of experience in essential utilities for an engineer.

1.4. Motivation

One of the main motivations in the development of this work is the potential characterization of the backflow vortex instability by use of a MATLAB code.

The presences of flow instabilities in turbopumps that are used in typical liquid rocket engines to feed the propellant is considered crucial in the design process. Flow instabilities in this kind of components limits suction performance, power density and operational life. Besides, as it was commented in Subsection 1.2.1, cavitation induces different problems and disadvantages that must be considered in the design process of an inducer to obtain the real performance in operation. The characterization of backflow vortex instability represents a huge impact for turbopumps and the selection of design operating parameters.

Also, from an educational point of view, the understanding of the phenomena detailed in this Final Master's Project is an incentive due to the acquisition of knowledge in a field not so well known and not so detailed throughout the years of study.

1.5. Methodology

The methodology followed to prepare this Final Master Project can be broken down into different steps that are detailed below and explained in detail throughout the various Sections in which the document is divided:

1. Documentation period about cavitation phenomena and instabilities in turbopumps.
2. Analysis of the code that allows to detect and characterize backflow vortex instability.
3. Use of the code to perform many evaluations deriving a quantitative comparison for different inducers and several loads, tip clearances and different cavitating regimes.
4. Use of two theoretical models in order to validate the results obtained of the backflow vortex evaluation.
5. Extraction of the appropriate conclusions about utility and performance of the Bayesian estimation method on its use in detection of backflow vortex instability.

As a guidance for the final document, it has been divided in different Sections. Firstly, the experimental apparatus used for the development of the project is analysed. After that, the flow instabilities induced by cavitation are studied and the attention is fixed to the backflow vortex instability, the core of the project that has been carried out. The identification procedure is then presented and finally in the evaluation section, the results of the identifications made are presented with the theories used to validate the results and the conclusions referent to the method used are shown.

2. Experimental apparatus

In this Section, the experimental apparatus in which the experimental part of the project has been developed is presented.

The organization of this part consists in differentiating the different versions of the test facility between CPTF, CPRTF, CI2TF and CI2RTF highlighting the main components of the CPTF and the function of each of them. Later, the main differences between the different upgraded versions of the test facility are analysed.

Also, in this Section it is detailed the inducers that have been used to evaluate and identify backflow vortex instability in this project, dividing between DAPAMITO 3, DAPAMITO 4 and RAPDUD and showing the behaviour of each of them, together with the geometrical and operating parameters.

2.1. Cavitating Pump Test Facility (CPTF)

The Cavitating Pump Test Facility is basically a closed, water recirculating pump loop equipped with flow control and temperature systems as well as measurement devices [9]. A typical CPTF can be seen in Figure 2.1.

FIGURE 2.1: TYPICAL CAVITATING PUMP TEST FACILITY [1]

A schematic view of the main components defining the system can be found in Figure 2.2.

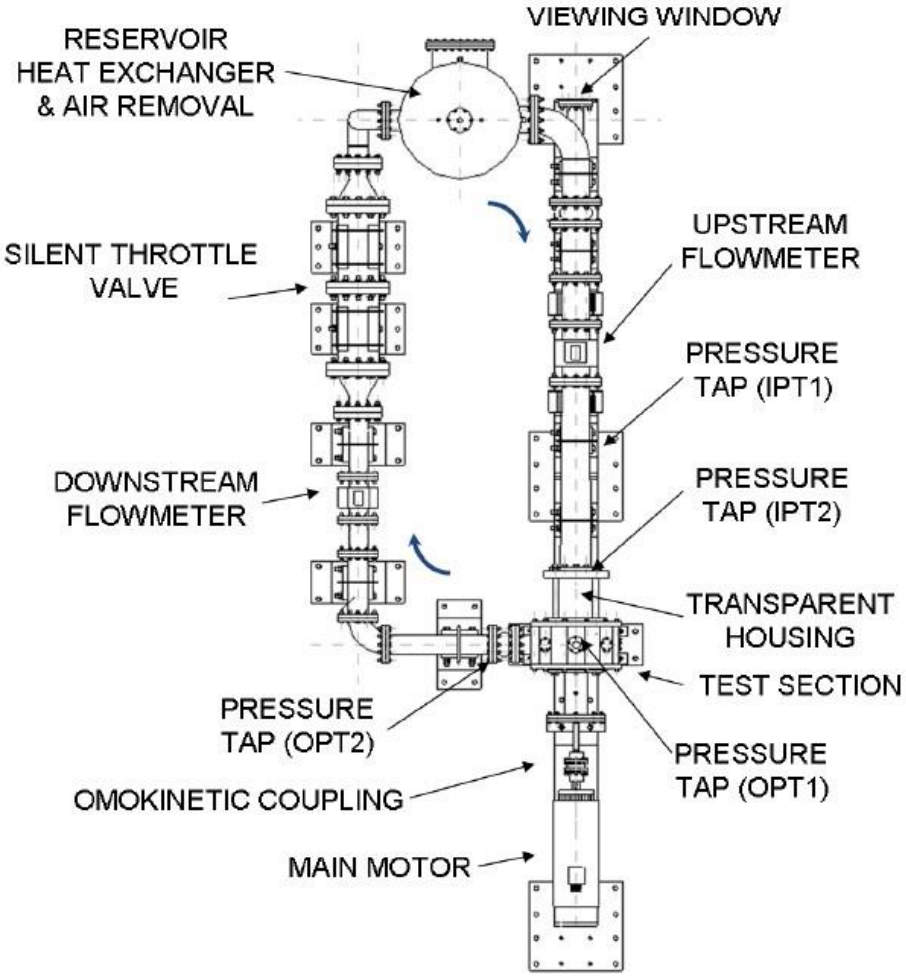

FIGURE 2.2: SCHEMATIC VIEW OF A CAVITATING PUMP TEST FACILITY [1]

The pump impeller is mounted within the loop and it is the primary source of recirculating flow in the loop.

In Figure 2.3, it is represented the inducer installation for flow visualization experiments, with several pressure taps that are located along the suction and discharge lines to evaluate the pumping performance of the test impellers. In Figure 2.2, it can be seen the low pressure tap (IPT1) that is located on the suction line at 6 inducer diameters upstream of the blade leading-edge and the high pressure tap (OPT2) that is located on the discharge line at 2.5 duct diameters downstream of the test chamber connection. In Figure 2.3, it is shown the situation of the low pressure tap (IPT2) and high pressure tap (OPT1), that are nearer to the test inducer.

Considering as the starting point the **reservoir heat exchanger and air removal** (Figure 2.4), it is capable of containing the different volume fluctuations related to the several operating conditions to test [9]. Also, it is possible to find a pressurization-depressurization circuit that allows the user by regulating the pressure inside it, control the pressure of the water in the tank and by that, at the end of the pump inlet.

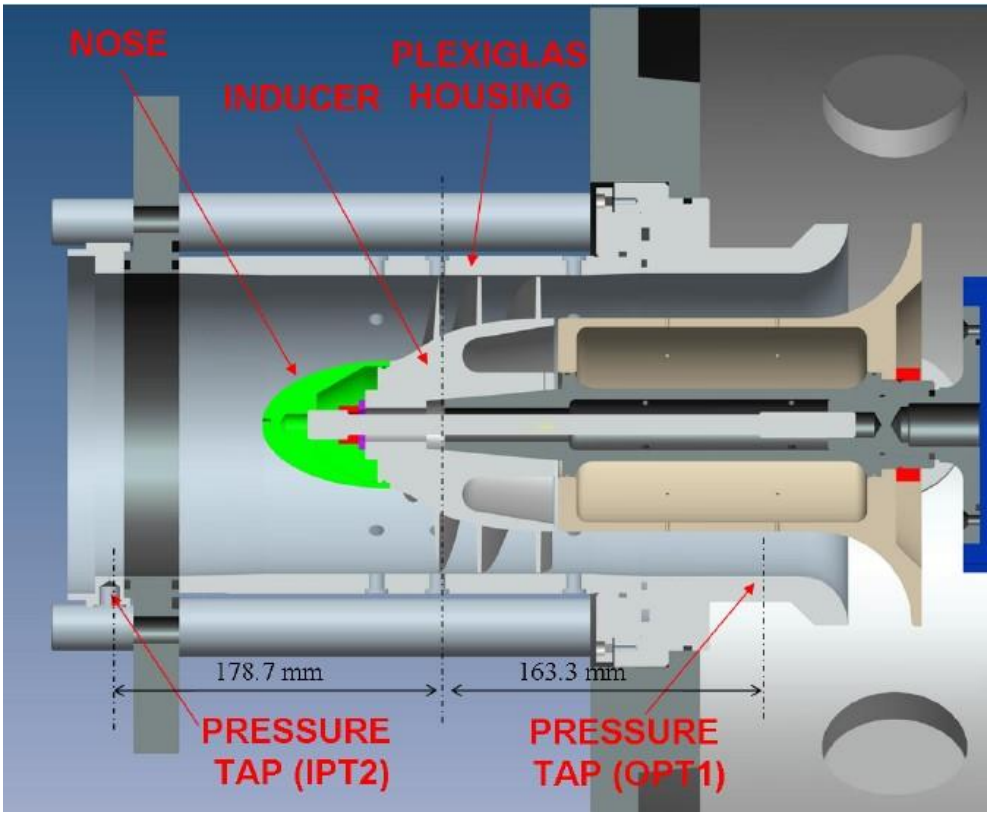

FIGURE 2.3: INDUCER INSTALLATION FOR FLOW VISUALIZATION EXPERIMENTS [1]

So, the main tasks can be enumerated as follows:

- Act as main tank for the water circulating in the circuit.
- Adjust the temperature of the working fluid.
- Absorb fluctuations in the volume of the working fluid due to self-oscillations of the system in cavitating regimes.
- Keep under control water pressure in the tank.
- Allow evacuation of a substantial fraction of bubbles contained in the water.

After leaving this tank, there is a **flow rectifier** (Figure 2.5) with the objective of breaking down large-scale turbulence that appears in the fluid when passing through the curve due to centrifugal term of the force. This objective is achieved by making the flow “comb” by a section of honeycomb with hexagonal mesh. After the flow rectifier, it can be found a **flowmeter**. It consists in a non-intrusive device that measures the flow passing through the circuit without any intervention in the flow itself.

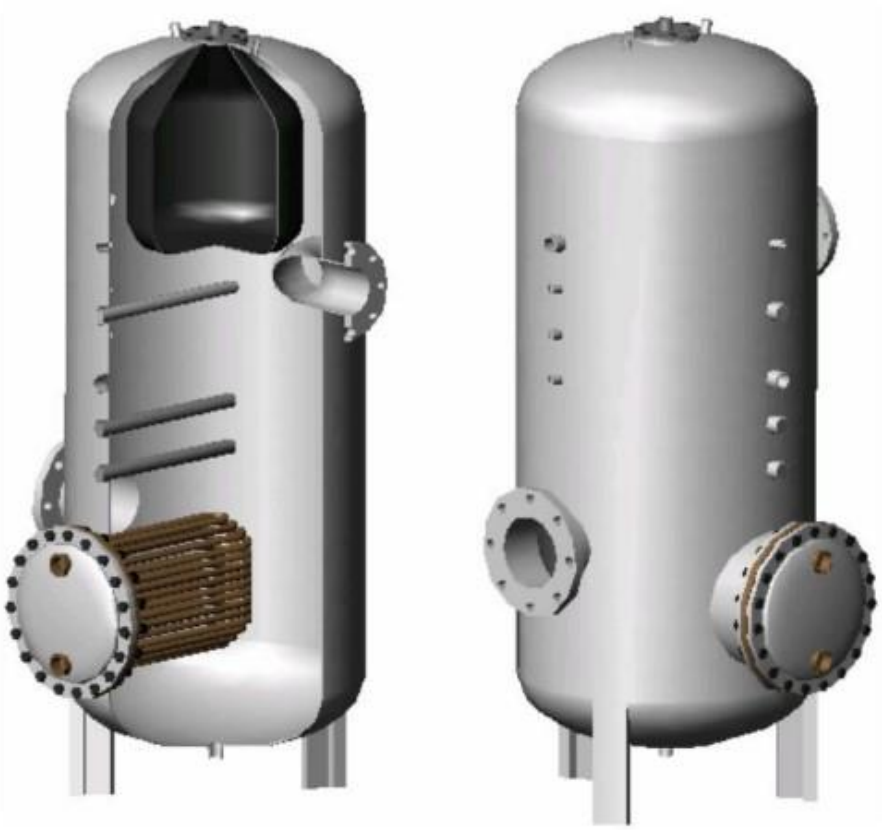

FIGURE 2.4: VIEW OF THE RESERVOIR HEAT EXCHANGER AND AIR REMOVAL [9]

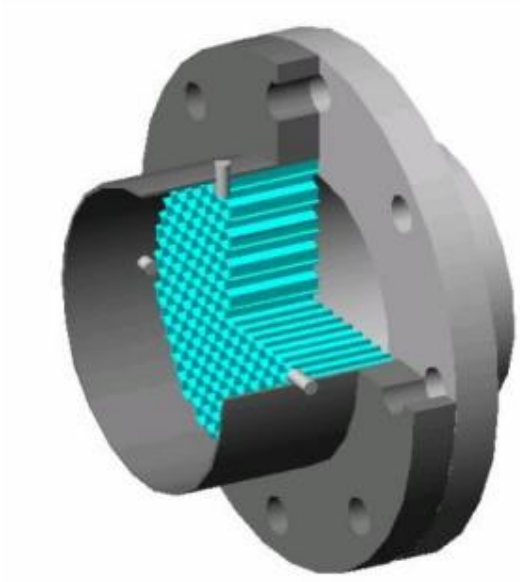

FIGURE 2.5: FLOW RECTIFIER DIAGRAM [9]

The following main component is the **test section** (Figure 2.6), the chamber inside which the pump to be tested is mounted. In the front part there is a transparent housing consisting in a transparent section allowing to display the flow at the pump inlet. Also, if is suitable for measuring fluid dynamic instabilities, it has the piezoelectric sensors.

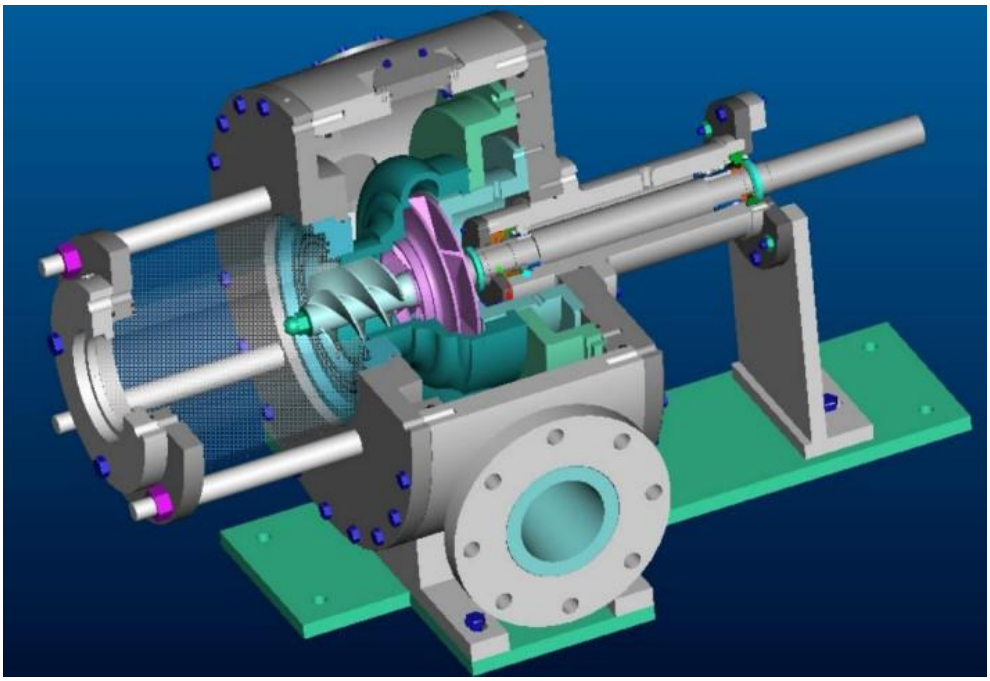

FIGURE 2.6: CROSS SECTION OF THE TEST CHAMBER [9]

It is possible that in the most severe operating conditions there is vibrations that could be propagated, so the test section must be isolated from the rest of the circuit. This is achieved by the use of elastic compensators.

The pump shaft is rotated by the **main motor** (Figure 2.7), provided with a control system that allows to maintain the rotational speed as a constant value. The connection between the pump shaft and the main motor is done by a constant velocity joint (**omokinetic joint**) that is torsionally rigid to avoid angular misalignments.

The main characteristics of the main motor are:

- Ability to keep rotation speed constant.
- Possibility of coupling with a secondary motor generating whirl motion.
- Possibility of knowing angular velocity.
- Ability to operate at low rotation speeds while still guaranteeing the torque required by the pump.

After the test section, it can be found another **flow rectifier and flowmeter**. The main objective is to monitor how it is the flow at the exhaust and allows a comparison with the inlet data obtained with the first flowmeter.

Before closing the loop, there is a **silent throttle valve** (Figure 2.8) with the task of causing a pressure drop in the working fluid. This component has the task of transforming the energy stored in the fluid in the form of pressure into internal energy of the fluid itself, making it perform a lamination transformation. This kind of valve causes the lamination to take place without appearing cavitation phenomena, so the problems of vibration and erosion in this kind of valve are reduced.

FIGURE 2.7: THE MAIN MOTOR [9]

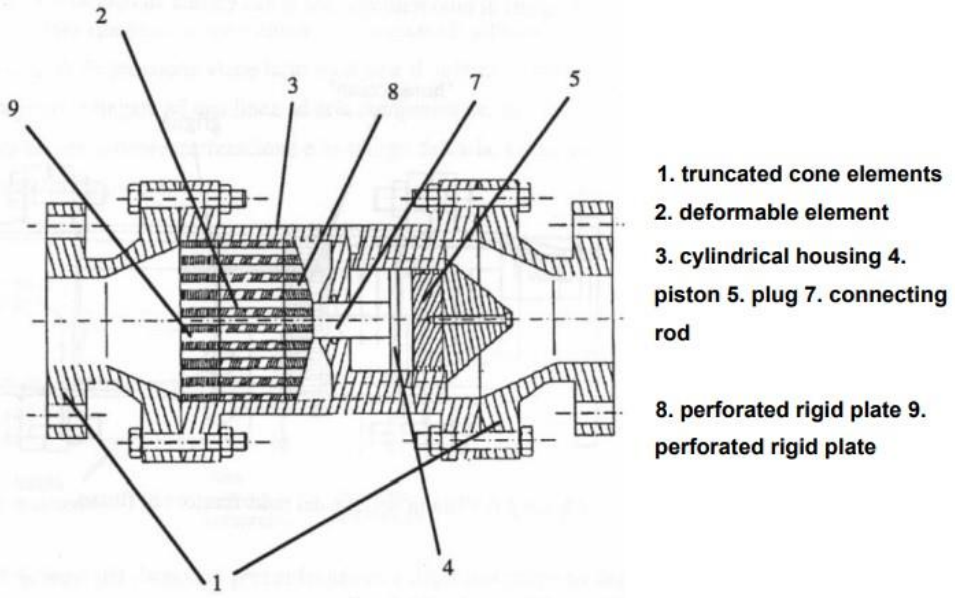

FIGURE 2.8: SECTION OF THE SILENT THROTTLE VALVE [9]

The overall circuit assembly is represented in Figure 2.9.

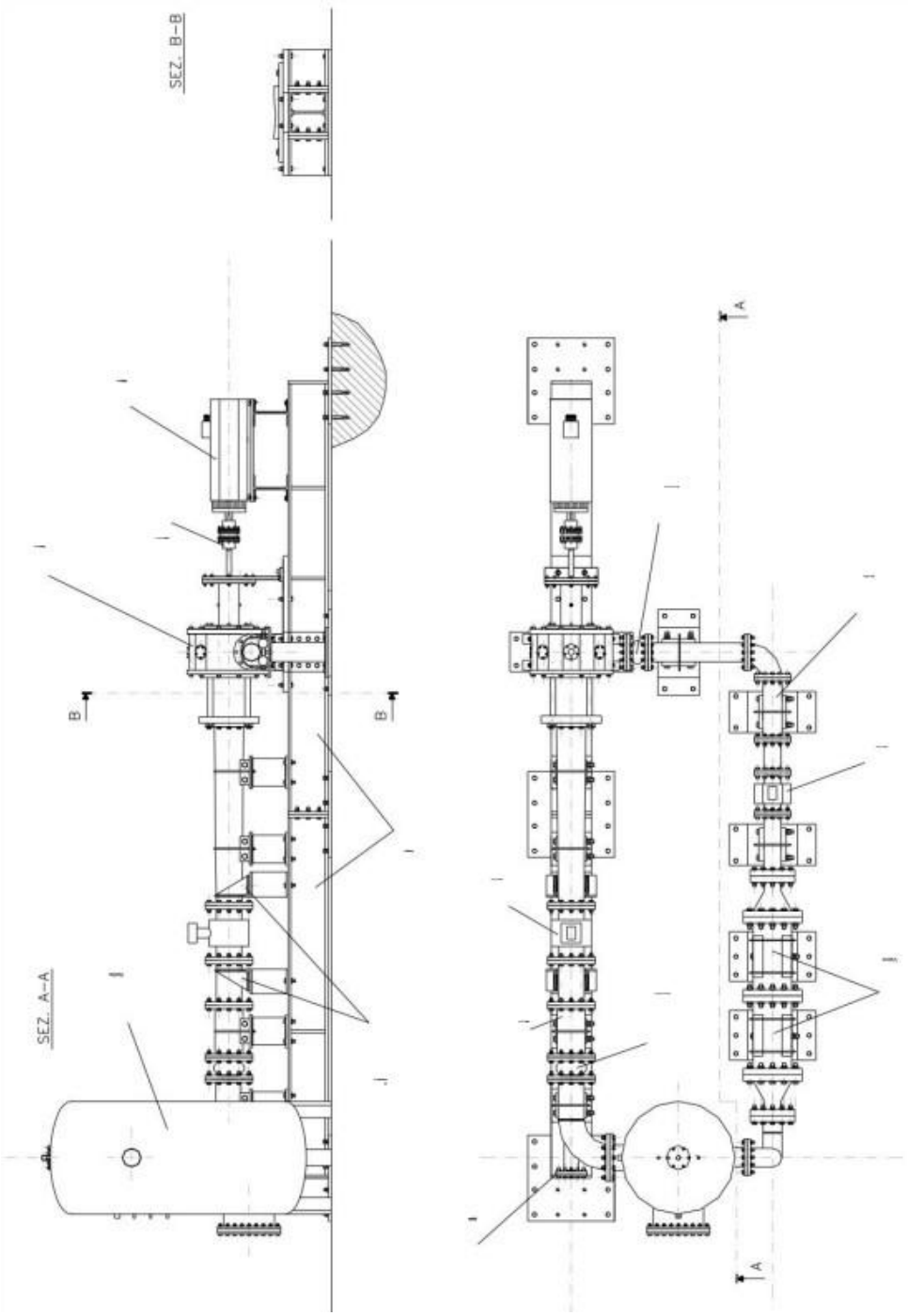

FIGURE 2.9: OVERALL CIRCUIT ASSEMBLY [9]

2.2. The CPRTF, CI^{2}TF and CI^{2}RTF

The used system has been designed to be extremely versatile, so there is possibility of different configurations of the system itself through the design and replacement of a few parts of the system.

The circuit is maintained identical to the CPTF but there are some localized changes in the test chamber and the interfaces, that are different depending on the machine to be tested. So, in this Subsection, it will be described the localized changes to obtain a Cavitating Pump Rotordynamic Test Facility (CPRTF), a Cavitation Induced Instabilities Test Facility (CI^{2}TF) and a Cavitation Induced Instabilities and Rotordynamic Test Facility (CI^{2}RTF).

2.2.1. CAVITATING PUMP ROTORDYNAMIC TEST FACILITY (CPRTF)

This kind of system is used for the study of rotordynamic forces on turbopumps in cavitating and non-cavitating conditions.

The Cavitating Pump Rotordynamic Test Facility configuration anticipates the presence of a secondary motor, rotating at angular speed ω, connected to the test chamber by an appropriate motion transmission system, generating a circular precession of the pump shaft, with an adjustable value of the radius of the orbit [9]. The secondary motor and the main one are connected by a control system allowing the ω/Ω ratio to be kept constant for the whole duration of the test. The ratio must be able to be fixed on values greater than 1, equal to 1 or less than 1 to generate a whirl supersynchronous, synchronous or subsynchronous respectively. Also, it must be able to be both positive and negative.

Studying this phenomenon is important because a precession motion typically occurs that is called whirl motion. The effect of rotordynamic forces (in particular lateral component) can be such as to make this motion unstable.

The study of the phenomena connected to whirl motion can follow the path of free oscillations or forced motion path. In the first one, there are safety and cost-effectiveness problems. In the second path, the forces are represented with a Fourier integral, that operationally is translated into reproducing whirl conditions controlled and defined in terms of eccentricity and whirl ratio Ω /ω measuring the forces in a reference system integral with the pump by means of a rotating dynamometer.

The Figure 2.10. represents the CPRTF cutaway.

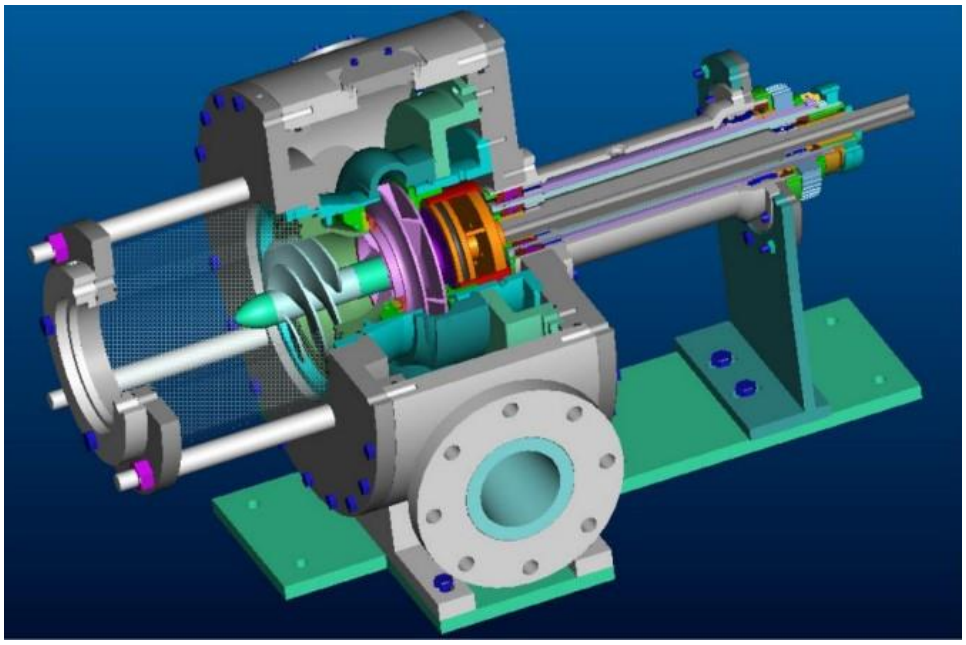

FIGURE 2.10: CAVITATING PUMP ROTORDYNAMIC TEST FACILITY CUTAWAY [1]

2.2.2. CAVITATION INDUCED INSTABILITIES TEST FACILITY (CI^2TF)

This system provides the possibility of studying the instabilities of the fluid dynamic field, in terms of pressure oscillations, on cavitating inducers [9]. This version allows to guarantee greater flexibility making use of the resources carefully. The use of the kinematic unit of the CPRTF is not logical when long operations are foreseen in conditions with not eccentricity. However, the kinematic unit of the CPTF is simpler and more reliable, reducing the degradation and wear of the kinematic unit.

The modification of the CI^2TF modifies the shaft of the CPTF inducing a conical attachment, and therefore, it is compatible with the interfaces of the CPRTF.

One of the main peculiarities of this system is the possibility of supporting dynamic pressure measurements on inducers. This peculiarity was made possible by bringing the position of the inducer completely out of the plane of the front cover, corresponding with a new optical access with a Plexiglas tube with several pressure transducers (and designing this element every time that a different inducer is tested).

The test section of the CI^2TF is represented in Figure 2.11. Also, it is possible to replace the Plexiglas tube equipped with the sensors with an intact tube in order to have optical access to the area where the instability develops, to highlight the phenomenon directly and to allow to see the phenomenon itself.

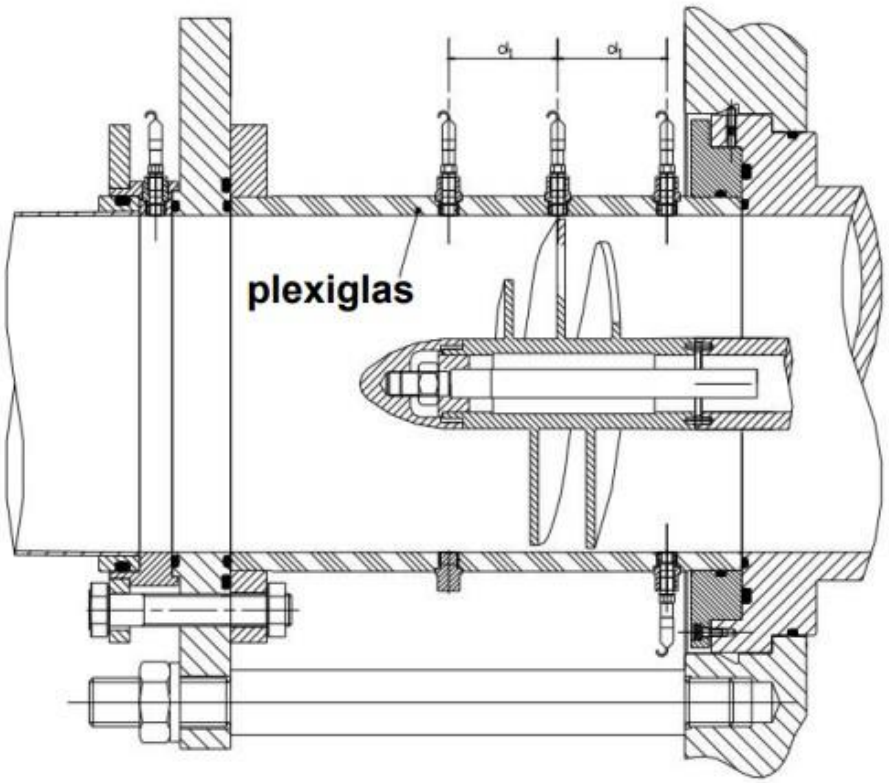

FIGURE 2.11: TEST SECTION OF THE CI²TF [1]

It is needed to have a fluid dynamic field that could be attributed only to the effects of the inducer. This fact, requires the elimination of the convergent section of the inlet duct and the strong perturbations introduced by the centrifugal pump. Therefore, it is used an inlet duct with a constant area section and the centrifugal pump is replaced with an impeller with the only objective of diverting the flow towards the volute, with a contour such as to produce a well-guided flow, without detachments. and recirculation zones (which can oscillate and introduce a disturbing component). This last detail must also be designed every time the dimensions of the inducer to be tested change.

2.2.3. CAVITATION INDUCED INSTABILITIES AND ROTORDYNAMIC TEST FACILITY (CI²RTF)

The system that allows to increase the capacity to investigate complex phenomena and relations between the various quantities involved is the CI²RTF. It is able to, simultaneously, carry out pressure and rotordynamic force measurements.

2.2.4. SIMILARITY CRITERIA

The operating characteristics of the diverse test facilities are very limited compared with the typical operating conditions needed in real operations. However, the results obtained experimentally by a conducted test are valid in different operating conditions than those adopted in the test only if there are conditions of geometric, fluid dynamics and thermal similarities between the model of the test and the real pump.

In the absence of cavitation, in order to have an excellent correspondence between the real data and those obtained from the experimental tests, it is sufficient that the conditions of geometric and fluid dynamics similarity are verified. Geometric similarity is ensured if the test model has the same dimensions as the real pump or if it is a perfectly scaled copy.

The geometric similarity can be written as:

$$\frac{x_{Real}}{x_{Model}} = Constant \qquad 2.1$$

Being x any geometrical dimension.

To ensure the fluid dynamics similarity, (to avoid dependence on the Reynolds number, both real pump and the test must be conducted at a fully developed Reynolds number) the model must work with same ϕ and Ψ than the real pump.

In the case of cavitating regime, as the phenomenon of cavitation is very complex, the similarity between turbopumps is not so simple, and it is influenced by numerous factors. For more information refer to [9].

2.2.5. INSTRUMENTATION AND DATA ACQUISITION SYSTEM

The instrumentation and data acquisition system used for the facility used in the project is listed below [1]:

- Two electromagnetic flowmeters (produced by Fisher-Rosemount, model 8705) that are mounted on the suction and discharge lines allowing to measure the flow rate (from 0 to 100 l/s) in the case of DAPAMITO inducers. For the RAPDUD inducer, the 2 electromagnetic inducers used are produced by Fisher-Rosemount, but the model is 8732E, with same range of measuring than the electromagnetic flowmeters of DAPAMITO inducers.

- An absolute pressure transducer (produced by Druck, model PMP 1400) with a measuring range from 0 to 1 bar, class 0.15% and compensated in temperatures between -20 and 80 ºC. It is placed on the sensor holder flange (in the CI^2TF version) with the aim of measuring the pressure at the inducer inlet, essential to trace the cavitation number in DAPAMITO inducers. In the case of RAPDUD inducer, there are 2 absolute pressure transducers placed one and six diameters upstream of the blade leading-edge with same productor and model.

- A differential pressure transducer (produced by Druck, model PMP 4170) with a measuring range between 0 and 1 bar and temperature compensated for DAPAMITO inducers. For RAPDUD, there are 2 differential pressure transducers that are produced by GE and model UNIK5000.
- Another differential pressure transducer (produced by Kulite, model BMD 1P 1500 100) with a measuring range between 0 and 7 bar, class 0.1% and temperature compensated between -29 and 82 ªC that allows to measure the increasement of pressure through

the pump for DAPAMITO inducers. In the case of RAPDUD inducer, it is a piezoresistive pressure transducer (produced by Kulite model XTM-190M).

- Eight piezoelectric transducers (PCB M112A22) used for measuring dynamic pressures such as those due to cavitation instabilities, placed in axial stations on the Plexiglas duct that houses the inducer in the case of DAPAMITO inducers. For the RAPDUD inducer used for the evaluation, the eight piezoelectric transducers used are PCB S112A22, flush-mounted on the Plexiglas casing at different axial and azimuthal positions.

- A thermometer and a thermostat located inside the tank that allows to measure and keep the water temperature under control.

- A medium speed acquisition system based on a signal conditioning module (produced by National Instruments, model SCXI 1520), and a 250 kS/s 16-channel acquisition card (produced by National Instruments, model PCI 6024). It is used to read the absolute and differential pressure, the flowmeter signal, the rotation speed of both motors (in the case of CPRTF) and the water temperature.

- A module with 8 channels (produced by National Instruments, model SCXI 1531) providing power supply and signal conditioning to the piezoelectric transducers, allowing samplings up to 125 kS/s.

- A PC with Labview software for channel management and digital data acquisition.

2.3. Used inducers

In this Subsection, they are listed the 3 types of inducers that have been used for the evaluation of the project.

2.3.1. DAPAMITO 3

It is an unshrouded inducer, designed by means of a reduced order model and procedure proposed by d'Agostino [8] [10] [19]. It consists in a high-head, mixed flow inducer with tapered-hub and variable-pitch. The geometry generated by the model is consistent with typical geometries and operational characteristics of modern space rocket inducers. Blade loading and high solidities values are moderate, with values chosen with the objective of reducing the leading-edge cavity and improving the suction performance.

The incidence-to-blade angle ratio $\alpha/\beta_b < 0.5$ has been selected for controlling the surge instabilities at design flow under cavitating conditions.
The DAPAMITO 3 inducer is shown in Figure 2.12.

FIGURE 2.12: FRONT VIEW (LEFT), SIDE VIEW (MIDDLE) AND INDUCER WITH THE NOSE (RIGHT) OF DAPAMITO 3 [1]

In the Table 2.1. is represented the main geometrical and operational parameters of the DAPAMITO 3 inducer:

Geometrical and operational parameters of DAPAMITO 3 inducer	
Design flow coefficient (ϕ_D) [-]	0.059
Number of blades (N) [-]	3
Tip radius (r_T) [mm.]	81.0
Inlet tip blade angle (Υ_{Tle}) [º]	83.10
Inlet hub radius with fully-developed blade (r_{Hle}) [mm.]	44.5
Outlet hub radius (r_{Hte}) [mm.]	58.5
Axial length with fully-developed blade (c_a) [mm.]	63.5
Rotational speed (Ω) [r.p.m.]	3000
Inlet hub radius (r_{Hle}) [mm.]	35.0
Axial length (L) [mm.]	90.0
Meridional tip blade thickness (b_T) [mm.]	2
Blade taper meridional half-angle (β_{mb}) [mm.]	1
Diffusion factor (D) [-]	0.039
Incidence and blade angles ratio (α/β_b) [-]	0.3
Tip solidity (σ_T) [-]	2.03
Hub solidity (σ_H) [-]	2.07
Incidence tip angle at design (α) [º]	2.07
Outlet tip blade angle (Υ_{Tte}) [º]	74.58

TABLE 2.1: GEOEMETRICAL AND OPERATIONAL PARAMETERS OF DAPAMITO 3 INDUCER

To characterize DAPAMITO 3 inducer, it is shown in Figure 2.13. the computer rendering of the bladings, where the variable blade pitch and the profiles of the tapered hub can be seen:

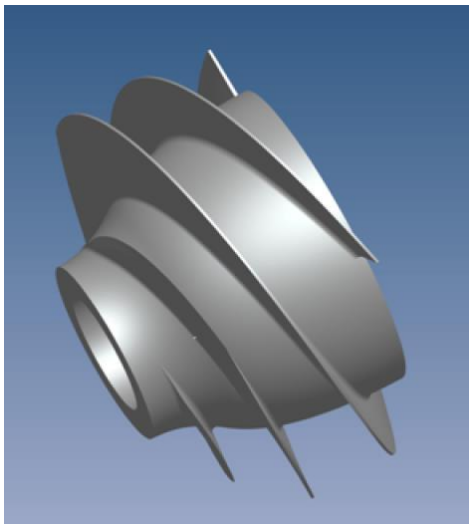

FIGURE 2.13: COMPUTER RENDERING OF THE BLADINGS OF DAPAMITO 3 [1]

In Figure 2.14 is represented the head coefficient based on the static and total pressure rise with and without losses.

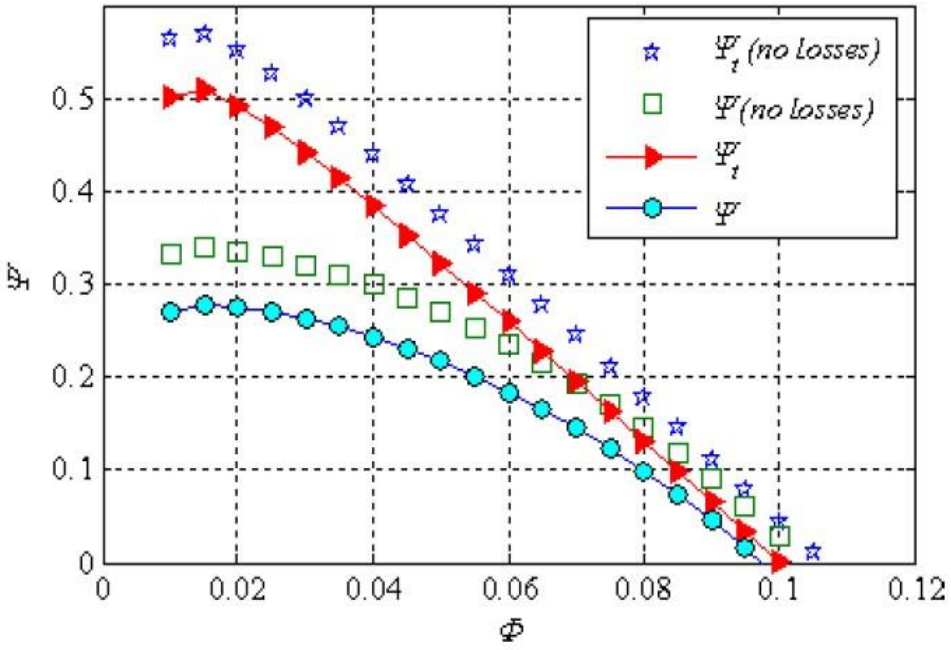

FIGURE 2.14: NON-CAVITATING PERFORMANCE OF DAPAMITO 3 [1]

The case of DAPAMITO 3 is the only one in which the radial clearance has been varied to study the effect of this parameter in the results of the performance. The 2 values used for radial clearance are 2 mm. and 0.8 mm. In the case of clearance 2 mm. there is a high value of the ratio between the clearance and mean blade height comparing with real applications. This has been done in order to get the same geometry than the one for rotordynamic tests.

For the **non-cavitating performance**, the values of the sample rate and of the number of samples that have been used in order to characterize a single experimental point of the performance curve are given in Table 2.2 [1].

Sampling for non-cavitating tests data acquisition	
Sample rate [sps]	200
Number of samples [-]	1000
Acquisition time [s]	5

TABLE 2.2: SAMPLING USED FOR NON-CAVITATING TESTS DATA ACQUISITION OF DAPAMITO 3

For the test carried out, the low and high pressure taps are IPT2 and OPT1 respectively. Also, the experimental data have been repeated with three different rotational speeds (Ω = 1500 rpm., Ω = 2000 rpm. and Ω = 2500 rpm.) for verifying the turbulent scaling. The theory states that the curves will be coincident since they must be independent of the Reynolds number because the flow is fully turbulent (Re > 10^6). In Figure 2.15. and Figure 2.16. it is represented the characteristic curve for non-cavitating pumping performance of DAPAMITO 3 for high clearance and low clearance respectively. Note that as in Figure 2.15. the curves are effectively superimposed, in Figure 2.16. it has been represented only Ω = 2500 rpm. since the independence has been already confirmed.

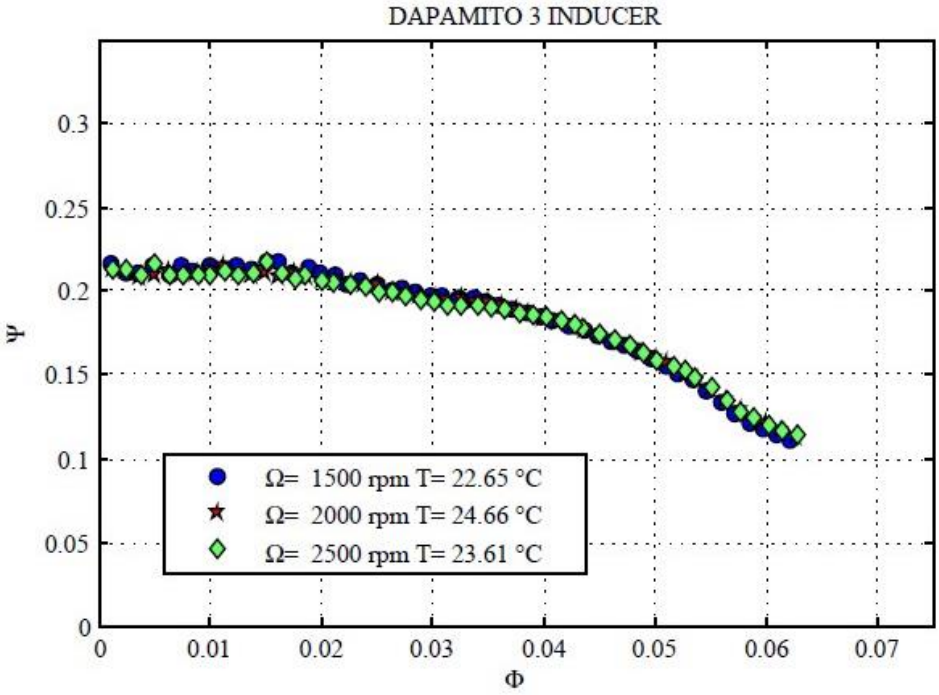

FIGURE 2.15: DAPAMITO 3 NON-CAVITATING PERFORMANCE WITH CLEARANCE = 2 MM. [1]

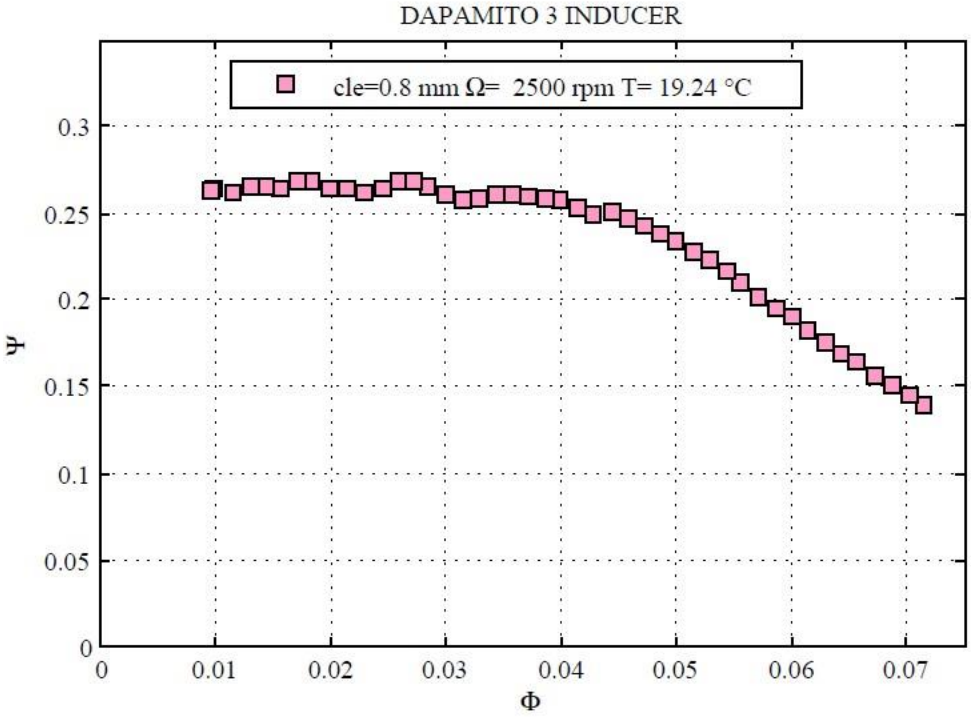

FIGURE 2.16: DAPAMITO 3 NON-CAVITATING PERFORMANCE WITH CLEARANCE = 0.8 MM. [1]

It can be seen that the case with low clearance is translated into an increasement of the pumping performance. The clearance strongly affects the pumping performance so it is an important parameter to consider.

Clearance changes affect the inducer head but also the flow coefficient, being both of them modified by the backflow. The relationship between variations of the head coefficient and variations of the flow coefficient are obtained with the hypothesis that the hydrodynamic nature

of the test rig losses is not influenced by changes of the inducer tip clearance and the operational conditions are kept the same.
Then, the relationship between head and flow coefficients with different clearances can be obtained as:

$$\phi_{low} = \phi_{high} \cdot \sqrt{\frac{\Psi_{low}}{\Psi_{high}}} \qquad 2.2$$

Being low and high references to the values of low clearance and high clearance.

For the **cavitating performance**, again it has been considered high and low clearances. The low pressure tap for the differential pressure transducer has been the IPT2 while for the high pressure tap, it has been the OPT1. The inlet pressure is measure by the IPT2 pressure tap.
In the case of the high clearance casing, several tests have been performed at ambient temperature characterizing the suction performance using two procedures: "steady-state" and "unsteady (continuous)". The tests were performed at Ω=3000 rpm. and for different flow coefficients representing the 105%, 100%, 95% and 90% of the design flow coefficient.

In Table 2.3, it can be seen the values of the sample rate and number of samples for a single experimental point of the suction curve using steady tests (each point obtained averaging the differential pressure and the inlet pressure signals).

Sampling for steady-state cavitating tests data acquisition	
Sample rate [sps]	1000
Number of samples [-]	5000
Acquisition time [s]	5

TABLE 2.3: SAMPLING USED FOR STEADY-STATE CAVITATING TESTS DATA ACQUISITION OF DAPAMITO 3

In Figure 2.17, it is represented the cavitating performance with "steady-state" tests and high clearance:

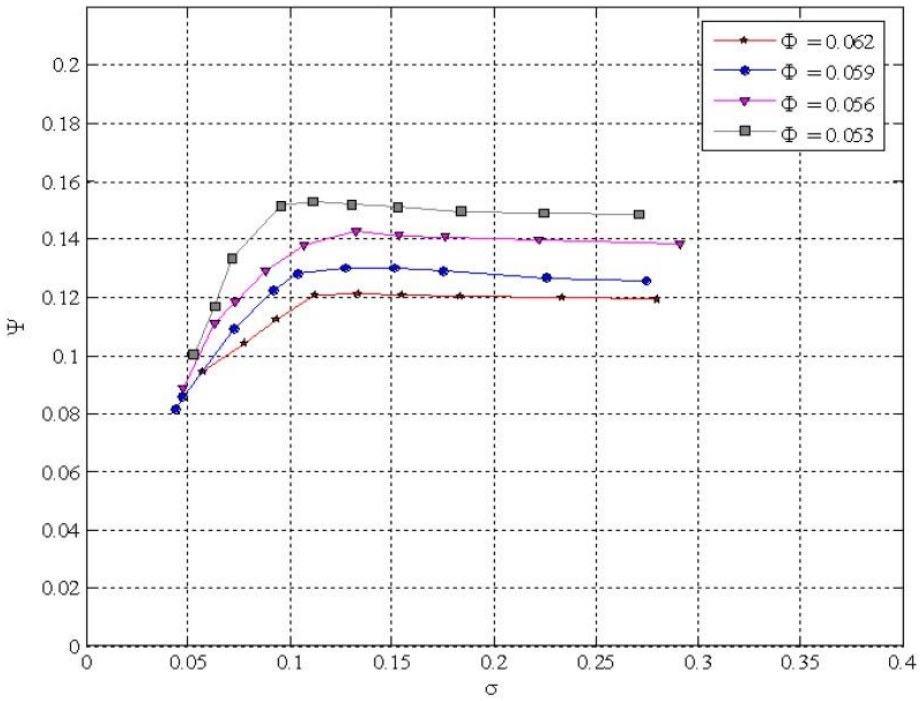

FIGURE 2.17: CAVITATING PERFORMANCE OF DAPAMITO 3 INDUCER WITH STEADY-STATE TEST AND HIGH CLEARANCE [1]

In the case of flow coefficient 105% or 100% of the design flow coefficient, there are difficulties in maintaining a constant value of flow rate at the lowest cavitation numbers. In breakdown condition with typical high levels of cavitation, tends to decrease the flow rate. To keep its value constant, it is necessary to open the flow regulating valve and, in some conditions, its full stroke could be reached, not allowing the passage of the correct amount of water.

Now, some Figures for each flow coefficient representing the appearance of cavitation with different cavitation numbers are shown with the mission of the better understanding of the cavitation level for the reader of the present document.

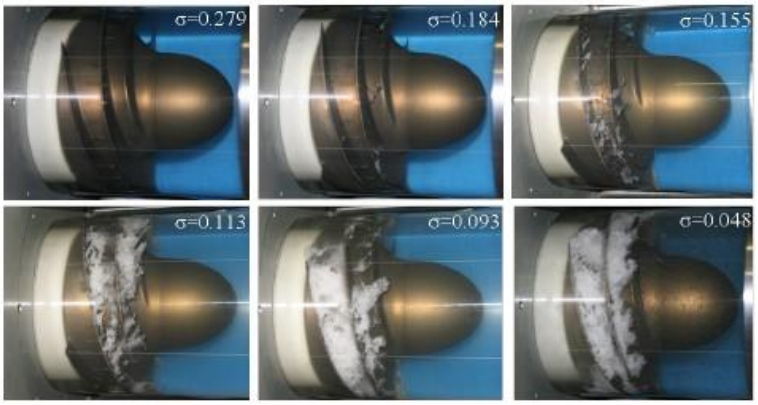

FIGURE 2.18: CAVITATION IN THE DAPAMITO 3 AT Ω=3000 RPM, T = 17.2 ºC, Φ = 0.062 AND CLEARANCE = 2 MM. [1]

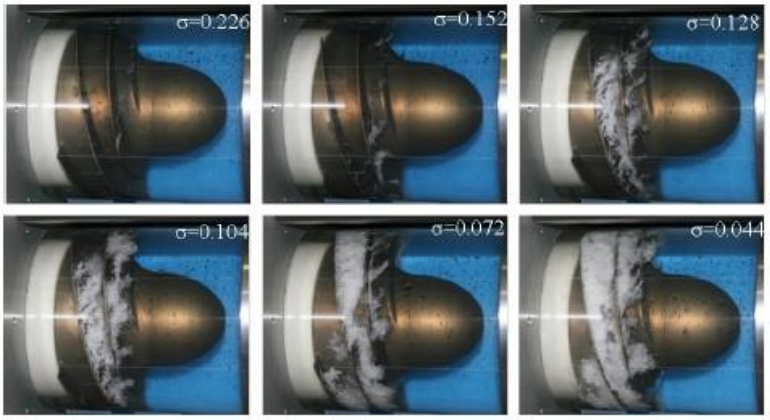

FIGURE 2.19: CAVITATION IN THE DAPAMITO 3 AT Ω=3000 RPM, T = 18.7 ºC, Φ = 0.059 AND CLEARANCE = 2 MM. [1]

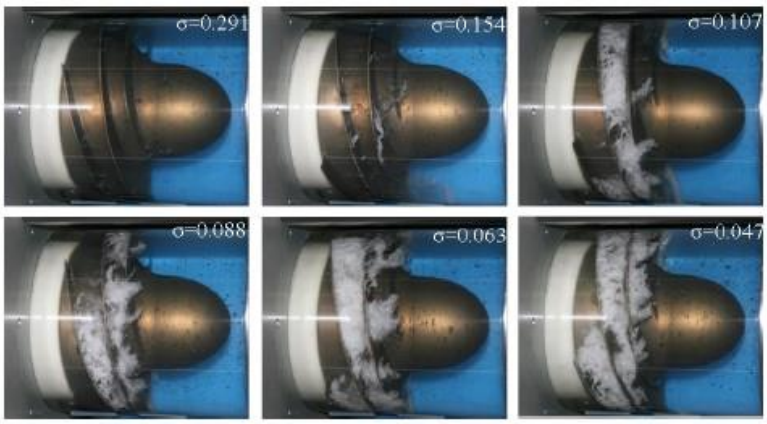

FIGURE 2.20: CAVITATION IN THE DAPAMITO 3 AT Ω=3000 RPM, T = 15.8 ºC, Φ = 0.056 AND CLEARANCE = 2 MM. [1]

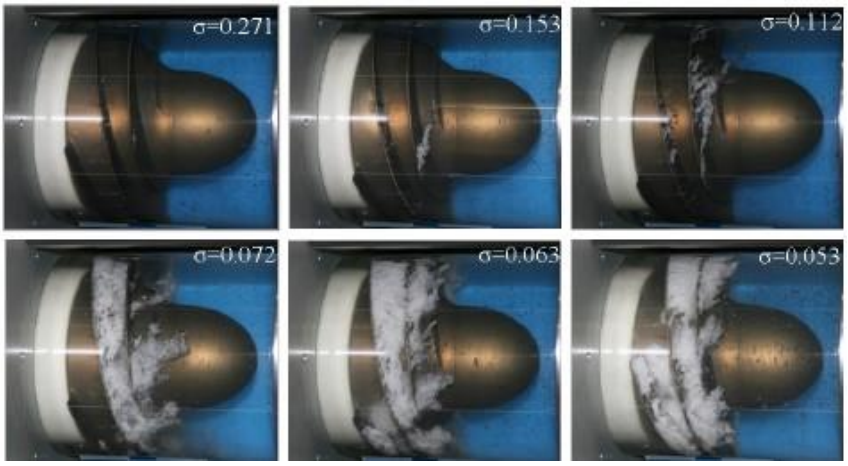

FIGURE 2.21: CAVITATION IN THE DAPAMITO 3 AT Ω=3000 RPM, T = 16.8 ºC, Φ = 0.053 AND CLEARANCE = 2 MM. [1]

For the continuous procedure, the main parameters of simulation including the sample rate, the number of samples, the duration of each run, the length of the time interval used in the data reduction for the representation of a single experimental point and the overlapping percentage between 2 adjacent intervals are represented in Table 2.4.

Sampling for continuous cavitating tests data acquisition	
Sample rate [sps]	1000
Number of samples [-]	300000-360000
Acquisition time [s]	300-360
Interval time [s]	4
Overlap % [s]	50

TABLE 2.4: SAMPLING USED FOR CONTINUOUS CAVITATING TESTS DATA ACQUISITION OF DAPAMITO 3 WITH HIGH CLEARANCE

Also, in Table 2.5, it can be seen the duration of the experiment, the mean water temperature, and the maximum gap between nominal flow coefficient and the actual one constant during the run:

Operational parameters for continuous cavitating tests			
Φ [-]	Mean temperature [ºC]	Test time [s]	$\varepsilon^{\Phi}_{\%}$
0.062	17.6	360	6.7
0.059	17.3	300	0.4
0.056	17.1	300	0.5
0.053	17.6	360	0.8

TABLE 2.5: OPERATIONAL PARAMETERS FOR CONTINUOUS CAVITATING TESTS OF DAPAMITO 3 WITH HIGH CLEARANCE

Following the conditions described previously to carry out the tests with continuous procedure, the results obtained are represented in Figure 2.22 together with the results obtained in steady-state procedure.

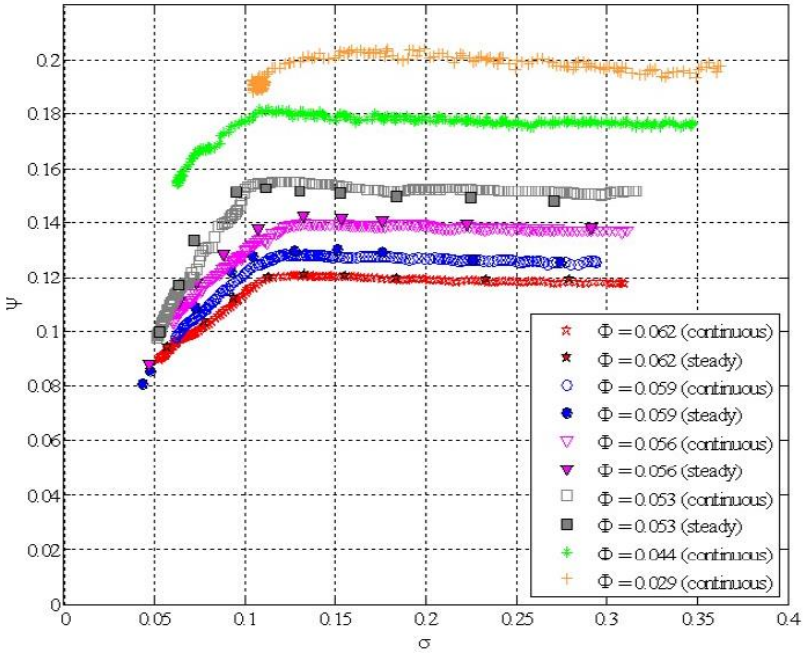

FIGURE 2.22: CAVITATING PERFORMANCE OF DAPAMITO 3 INDUCER WITH STEADY-STATE AND CONTINUOUS TESTS AND HIGH CLEARANCE [1]

In the case of continuous tests, the consideration with respect to the impossibility to keep a constant flow rate at highest flow coefficients under severe cavitating operation can be applied. Both tests show a head increase just before the decrease associated to breakdown conditions.

Now, the same procedure is followed for the low clearance case of 0.8 mm. For the steady-state tests, the rotational speed and the flow coefficients selected to perform the tests are the same than in the case of high clearance. Also, the sampling to carry out the tests is the same that the one that can be observed in Table 2.3.

The cavitating performance for low clearance in steady-state tests are shown in Figure 2.23.

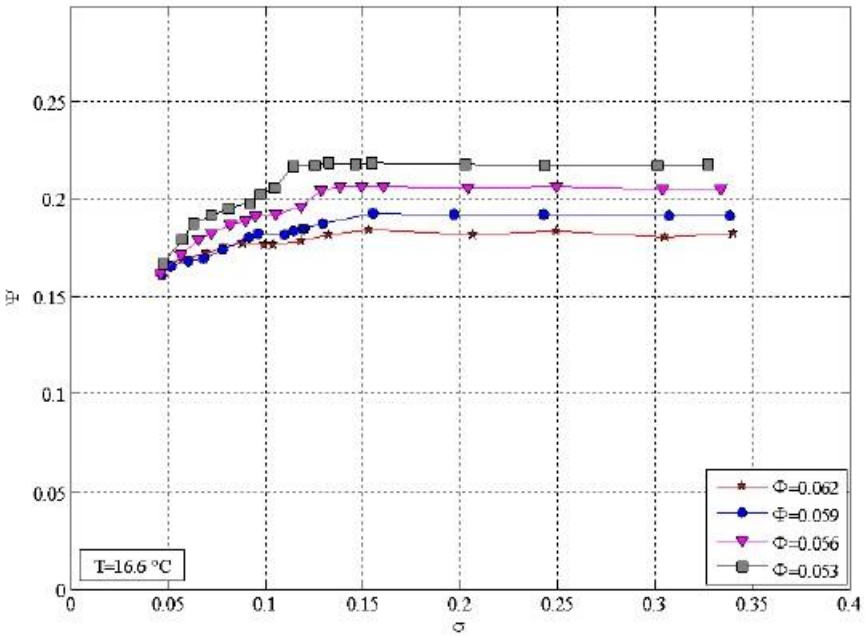

FIGURE 2.23: CAVITATING PERFORMANCE OF DAPAMITO 3 INDUCER WITH STEADY-STATE TEST AND LOW CLEARANCE [1]

Now, as in the case of high clearance, some Figures representing the development of cavitation with the reduction of the inlet pressure are shown. It is useful to know the appearance of the cavitation in order to identify the causes of degradation in a real problem, and that is the objective of the Figures.

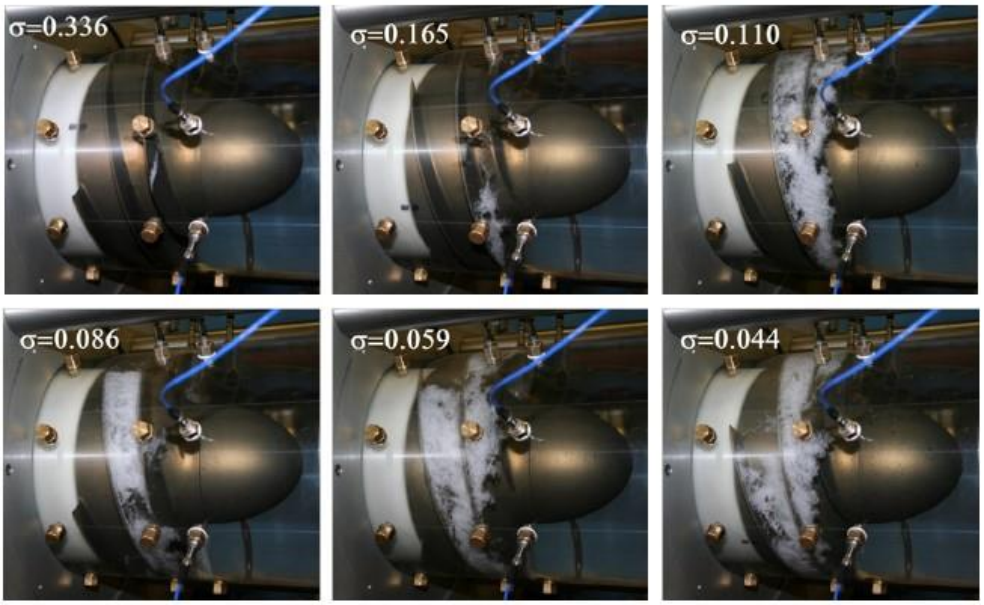

FIGURE 2.24: CAVITATION IN THE DAPAMITO 3 AT Ω=3000 RPM, T = 16.3 ºC, Φ = 0.062 AND CLEARANCE = 0.8 MM. [1]

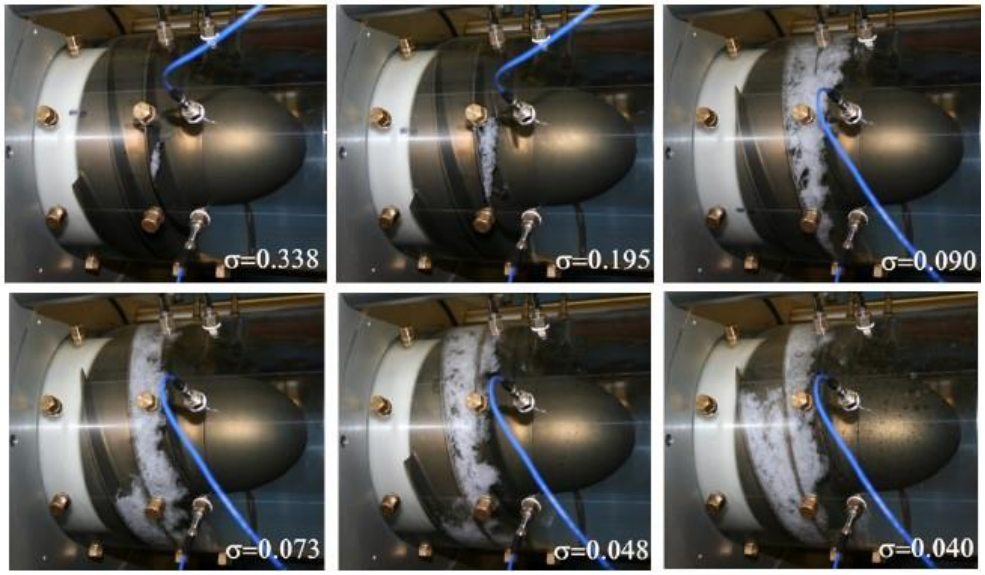

FIGURE 2.25: CAVITATION IN THE DAPAMITO 3 AT Ω=3000 RPM, T = 17.1 ºC, Φ = 0.059 AND CLEARANCE = 0.8 MM. [1]

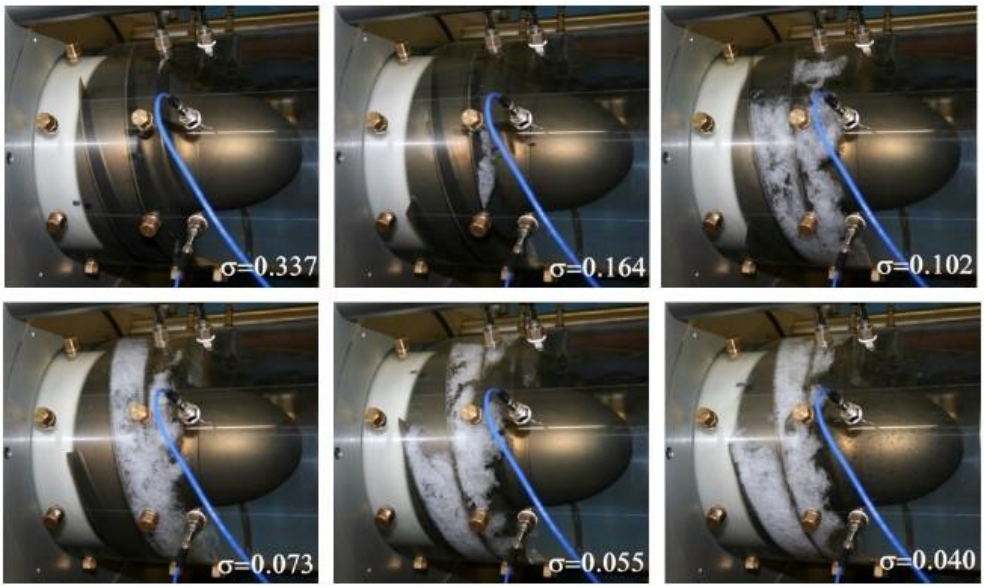

FIGURE 2.26: CAVITATION IN THE DAPAMITO 3 AT Ω=3000 RPM, T = 16.0 ºC, Φ = 0.056 AND CLEARANCE = 0.8 MM. [1]

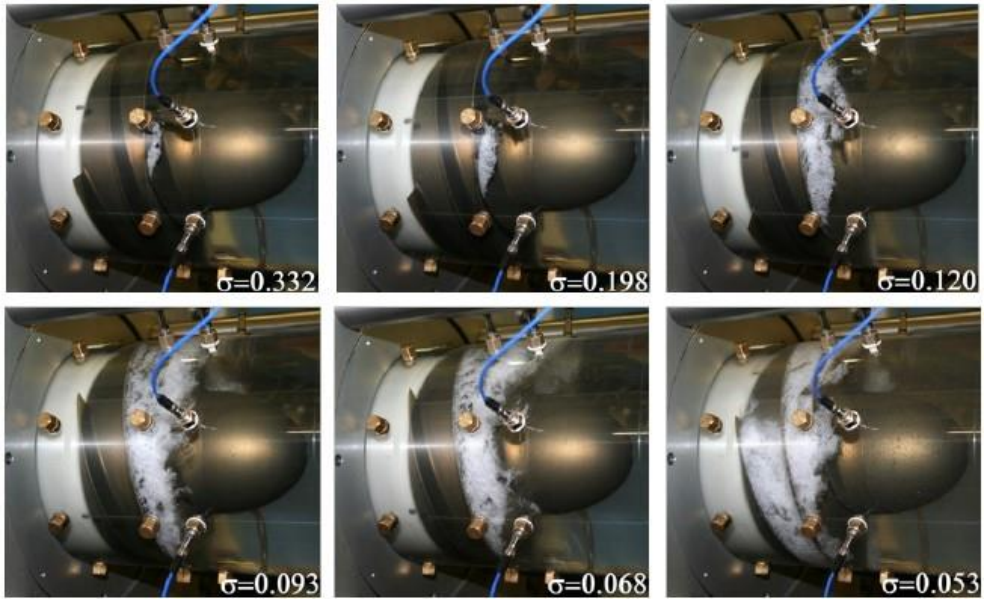

FIGURE 2.27: CAVITATION IN THE DAPAMITO 3 AT Ω=3000 RPM, T = 16.9 ºC, Φ = 0.053 AND CLEARANCE = 0.8 MM. [1]

For the continuous tests, the sampling and operational parameters used to carry out the experiments have changed, and the values are reported in Tables 2.6 and 2.7 respectively.

Sampling for continuous cavitating tests data acquisition	
Sample rate [sps]	1000
Number of samples [-]	240000
Acquisition time [s]	240
Interval time [s]	2.4
Overlap % [s]	50

TABLE 2.6: SAMPLING USED FOR CONTINUOUS CAVITATING TESTS DATA ACQUISITION OF DAPAMITO 3 WITH LOW CLEARANCE

Operational parameters for continuous cavitating tests			
Φ [-]	Mean temperature [ºC]	Test time [s]	$\varepsilon^{\Phi}_{\%}$
0.062	15.6	240	4.4
0.059	16.5	240	3.0
0.056	18.0	240	1.0
0.053	17.8	240	1.8
0.044	17.2	240	2.0

TABLE 2.7: OPERATIONAL PARAMETERS FOR CONTINUOUS CAVITATING TESTS OF DAPAMITO 3 WITH LOW CLEARANCE

Under these conditions, and making the same considerations as in the case of high clearance, the Figure 2.28 summarizes the DAPAMITO 3 cavitating performance obtained with different flow coefficients and with the results of the steady-state and continuous tests together for the low clearance case.

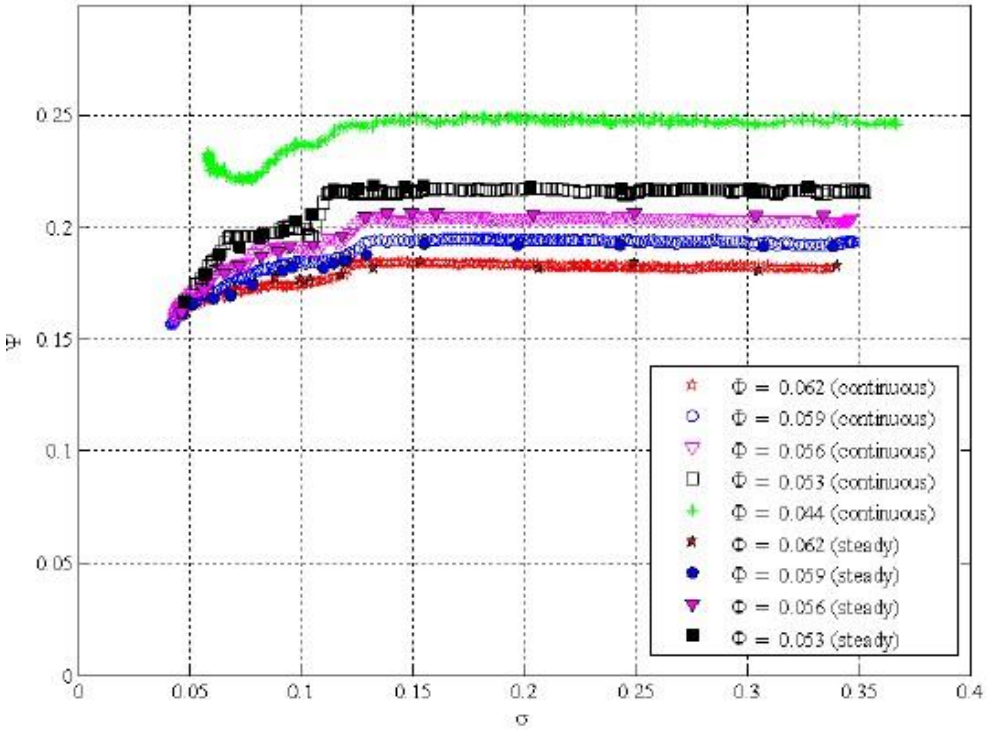

FIGURE 2.28: CAVITATING PERFORMANCE OF DAPAMITO 3 INDUCER WITH STEADY-STATE AND CONTINUOUS TESTS AND HIGH CLEARANCE [1]

Comparing the cavitating performances of the high clearance (2 mm.) and low clearance (0.8 mm.) cases, there are some observations that could be discussed. The head increase before the decrease associated to breakdown conditions is gradual, being the increase more significant for high tip blade clearance. Also, the cavitating behaviour is different. The curves with low clearance show a “one step” shape under breakdown conditions, consisting of an intermediate head drop during which there are some forms of instabilities that may occur. With higher clearance, inducer breakdown starts at lower cavitation number comparing with the lower clearance case, but complete breakdown conditions are achieved with lower cavitation numbers in the case of lower clearance.

To finish the comparation, it is represented in Figure 2.29 the appearance of cavitation on the inducer with the same flow coefficient and almost the same cavitation number. The conclusion obtained from the Figure is that with the higher clearance, the regions of cavitation are more irregular and directed upstream. In the case of lower value of the blade tip clearance, the

cavitation is not shown so directed upstream, as could be a consequence of the higher backflow intensity.

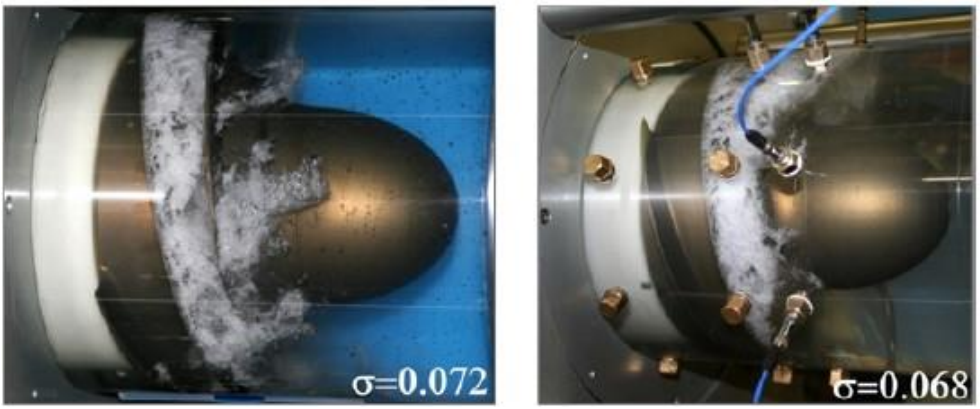

FIGURE 2.29: CAVITATION IN THE DAPAMITO 3 AT Φ = 0.053 AND SIMILAR CAVITATION NUMBER FOR HIGH CLEARANCE (LEFT) AND LOW CLEARANCE (RIGHT) [1]

2.3.2. DAPAMITO 4

The procedure to describe DAPAMITO 4 inducer is the same that the one developed in Subsubsection 2.3.1 for the DAPAMITO 3 inducer.

As in the case of DAPAMITO 3, the inducer DAPAMITO 4 is the same type of inducer with same characteristics. However, even for both of them having the same tip radius, exit hub radius, axial length and fully-developed blade axial length, there are some differences that must be taken into account. They differ in the number of blade (obviously, DAPAMITO 4 has 4 blades while DAPAMITO 3 has 3 blades), the inlet tip blade angle and the hub tapering.

The DAPAMITO 4 inducer is shown in Figure 2.30.

FIGURE 2.30: FRONT VIEW (LEFT), SIDE VIEW (MIDDLE) AND INDUCER WITH THE NOSE (RIGHT) OF DAPAMITO 4 [1]

The main geometrical and operating parameters of DAPAMITO 4 inducer are listed in Table 2.8 [1].

Geometrical and operational parameters of DAPAMITO 4 inducer	
Design flow coefficient (ϕ_D) [-]	0.070
Number of blades (N) [-]	4
Tip radius (r_T) [mm.]	81.0
Inlet tip blade angle (Υ_{Tle}) [º]	81.10
Inlet hub radius with fully-developed blade (r_{Hle}) [mm.]	48.0
Outlet hub radius (r_{Hte}) [mm.]	58.5
Axial length with fully-developed blade (c_a) [mm.]	63.5
Rotational speed (Ω) [r.p.m.]	3000
Inlet hub radius (r_{Hle}) [mm.]	35.0
Axial length (L) [mm.]	90.0
Meridional tip blade thickness (b_T) [mm.]	2
Blade taper meridional half-angle (β_{mb}) [mm.]	1
Diffusion factor (D) [-]	0.038
Incidence and blade angles ratio (α/β_b) [-]	0.3
Tip solidity (σ_T) [-]	2.25
Hub solidity (σ_H) [-]	2.27
Incidence tip angle at design (α) [º]	2.31
Outlet tip blade angle (Υ_{Tte}) [º]	72.46

TABLE 2.8: GEOEMETRICAL AND OPERATIONAL PARAMETERS OF DAPAMITO 4 INDUCER

As in the case of DAPAMITO 3, the Figure 2.31 represents the computer rendering of the blading of DAPAMITO 4 inducer:

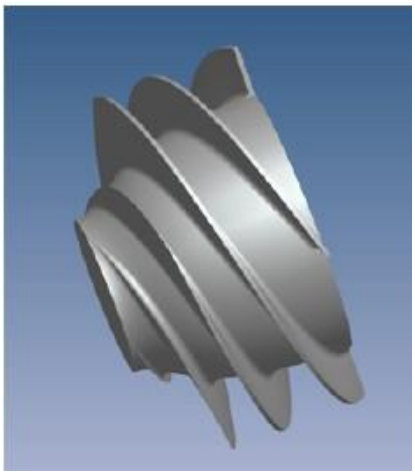

FIGURE 2.31: COMPUTER RENDERING OF THE BLADINGS OF DAPAMITO 4 [1]

The head coefficient for non-cavitating performance of DAPAMITO 4 is represented in Figure 2.32.

In the case of DAPAMITO 4, the radial clearance has been maintained in a value of 0.8 mm. because the influence of the clearance is studied in DAPAMITO 3 inducer so in this case only one value for the clearance is studied.

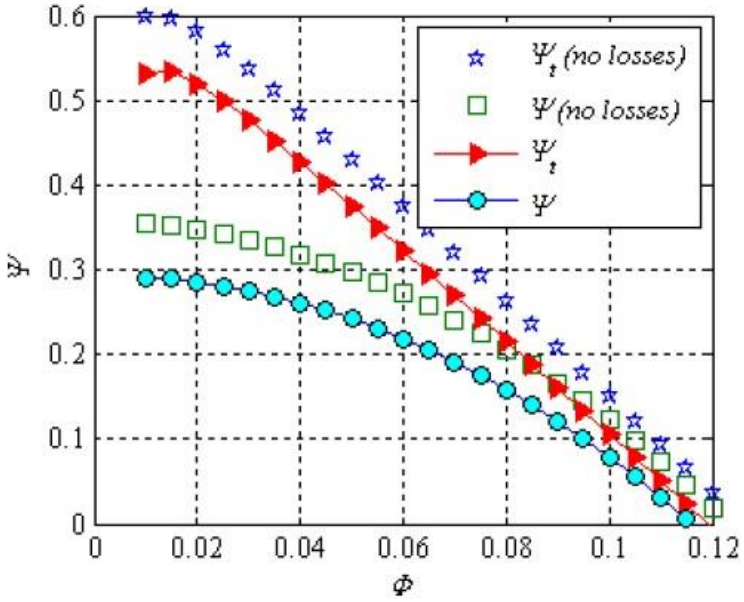

FIGURE 2.32: NON-CAVITATING PERFORMANCE OF DAPAMITO 4 [1]

For the **non-cavitating performance,** the values of the sampling used for data acquisition are the same that the sampling used for DAPAMITO 3 inducer, and the values are reported in Table 2.2.

The tests performed on the DAPAMITO 4 inducer have been carried out with a Plexiglas casing guaranteeing a tip blade clearance of 0.08 mm. In order to verify the turbulent scaling, as in the previous case, different rotational speeds have been used for the testing (Ω = 2000 rpm., Ω = 2500 rpm. and Ω = 3000 rpm.). The results are represented in Figure 2.33, being the characteristic curves independent of the Reynolds number as the flow is fully turbulent with a Reynolds number Re > 10^6.

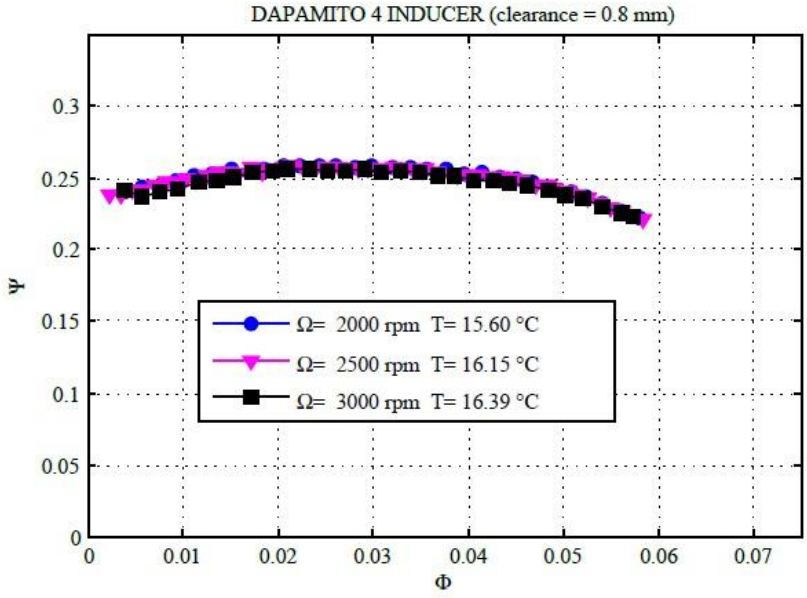

FIGURE 2.33: DAPAMITO 4 NON-CAVITATING PERFORMANCE WITH CLEARANCE = 0.8 MM. [1]

In this case, the maximum flow coefficient that has been experimentally investigated is lower than the design flow coefficient because of the reduced pumping capability of the inducer with

respect to the losses in the water loop. If it is desired to investigate higher flow coefficients, it is necessary to use an auxiliary pump within the water loop.

If the results for non-cavitating performance between 3-bladed inducer and 4-bladed inducer are compared, it can be concluded that the DAPAMITO 3 inducer has been designed for higher centrifugal pumping.

With respect to the **cavitating performance**, the low and high pressure taps as the inlet pressure tap are the same than the described in DAPAMITO 3 Subsubsection.

In this case, as commented previously, only low clearance case is analysed but “steady-state” and “continuous” procedures to develop the tests have been employed.

The tests have been performed at Ω = 3000 rpm. and the same flow coefficients than in the case of DAPAMITO 3. However, as the design flow coefficient is different in this case, those values represent 84%, 80% and 76% of the design flow coefficient of DAPAMITO 4. Also, a flow coefficient of 0.050 equivalent to 71% of the design flow coefficient have been used.

For the steady-state tests, the values of the sampling can be seen in Table 2.3 since the values are the same than the ones used for DAPAMITO 3.

In Figure 2.34 it is represented a summary of the DAPAMITO 4 cavitating performance with different flow coefficients by the “steady-state” tests.

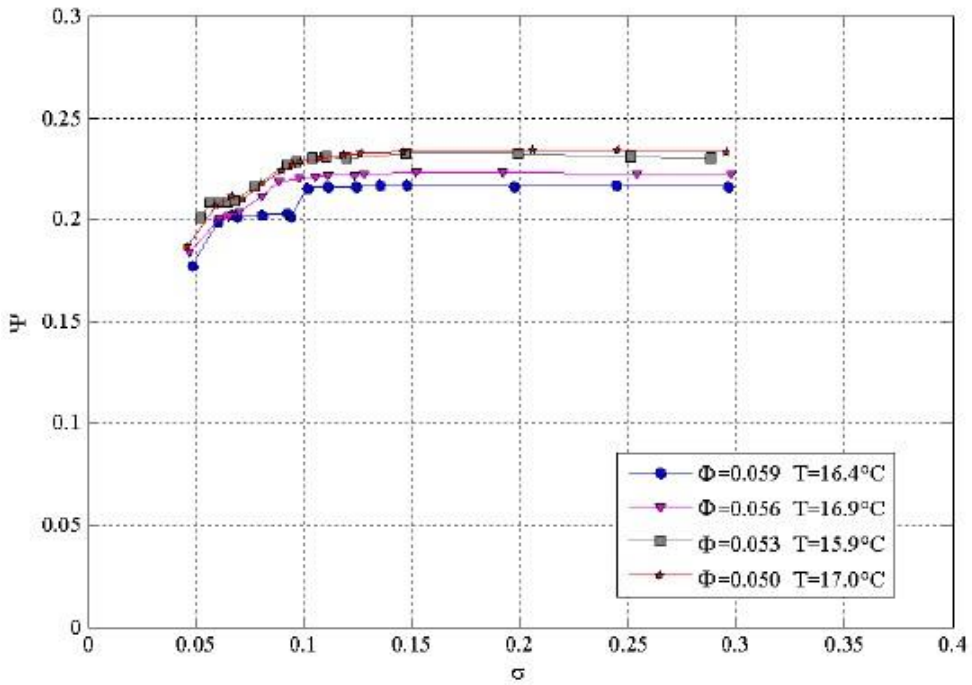

FIGURE 2.34: CAVITATING PERFORMANCE OF DAPAMITO 4 INDUCER WITH STEADY-STATE TEST AND LOW CLEARANCE [1]

For the higher flow coefficients (ϕ = 0.059 and ϕ = 0.056), it is difficult to keep a constant value of flow rate at lowest cavitation numbers since a high level of cavitation tends to decrease the flow rate that should be kept constant opening the flow regulating valve and the full stroke could be reached.

Repeating the procedure from DAPAMITO 3, now some Figures showing the appearance of cavitation for different cavitation numbers and for each flow coefficient used for the tests.

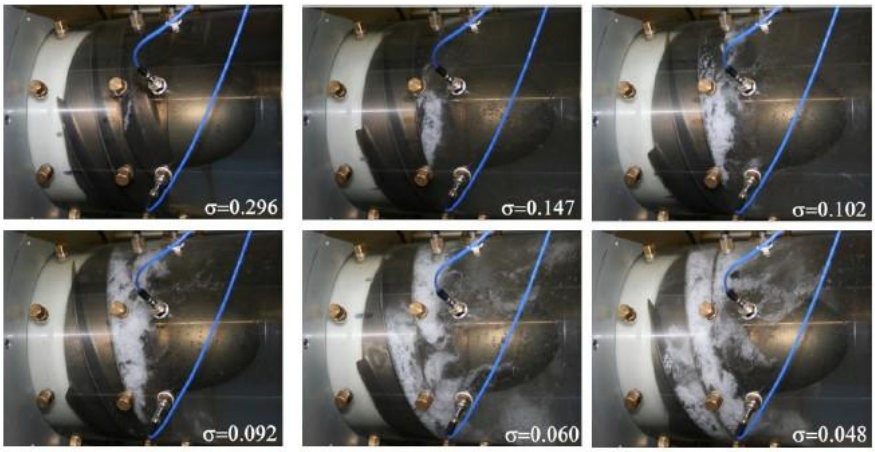

FIGURE 2.35: CAVITATION IN THE DAPAMITO 4 AT Ω=3000 RPM, T = 16.4 ºC, Φ = 0.059 AND CLEARANCE = 0.8 MM. [1]

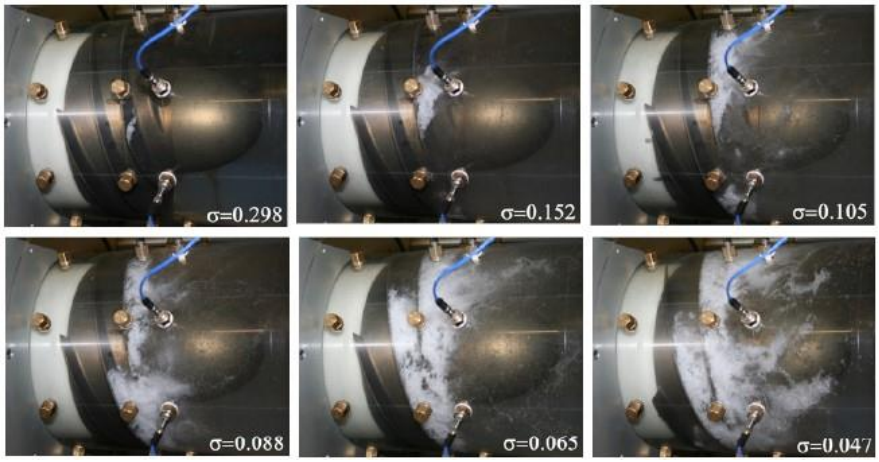

FIGURE 2.36: CAVITATION IN THE DAPAMITO 4 AT Ω=3000 RPM, T = 16.9 ºC, Φ = 0.056 AND CLEARANCE = 0.8 MM. [1]

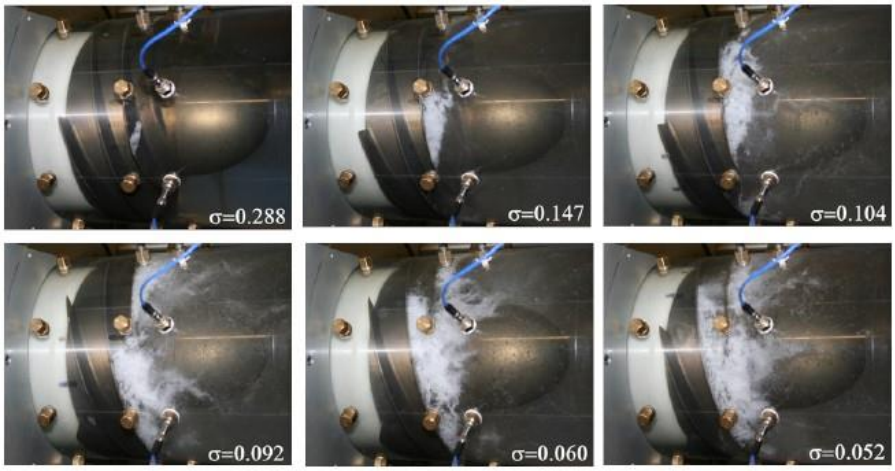

FIGURE 2.37: CAVITATION IN THE DAPAMITO 4 AT Ω=3000 RPM, T = 15.9 ºC, Φ = 0.053 AND CLEARANCE = 0.8 MM. [1]

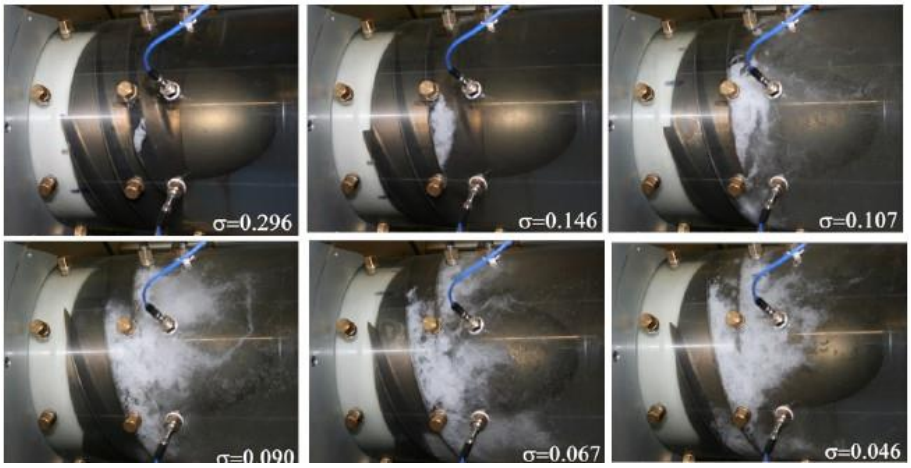

FIGURE 2.38: CAVITATION IN THE DAPAMITO 4 AT Ω=3000 RPM, T = 17.0 ºC, Φ = 0.050 AND CLEARANCE = 0.8 MM. [1]

It can be seen that there is a strong asymmetry of the cavitating regions in every investigated flow coefficient.

For the continuous tests, the values that define the sampling for the data acquisition are the same as the values shown in Table 2.6. However, the duration of the experiment, the mean water temperature, and the maximum gap between nominal flow coefficient and the actual one constant during the run are changed, so the operational parameters for continuous cavitating tests in DAPAMITO 4 inducer are summarized in Table 2.9.

Operational parameters for continuous cavitating tests

Φ [-]	Mean temperature [ºC]	Test time [s]	$\varepsilon^{\Phi}_{\%}$
0.059	15.4	240	8.5
0.056	15.0	240	4.3
0.053	15.2	240	1.2
0.050	15.4	240	0.7
0.044	15.0	240	1.3

TABLE 2.9: OPERATIONAL PARAMETERS FOR CONTINUOUS CAVITATING TESTS OF DAPAMITO 4 WITH LOW CLEARANCE

In Figure 2.39, the cavitating performance differentiating between some flow coefficients of DAPAMITO 4 inducer by the steady-state and continuous tests with low clearance are represented.

It is observed that in this case, the steady-state curves are superimposed to the continuous curves, so the unsteady procedure is validated.

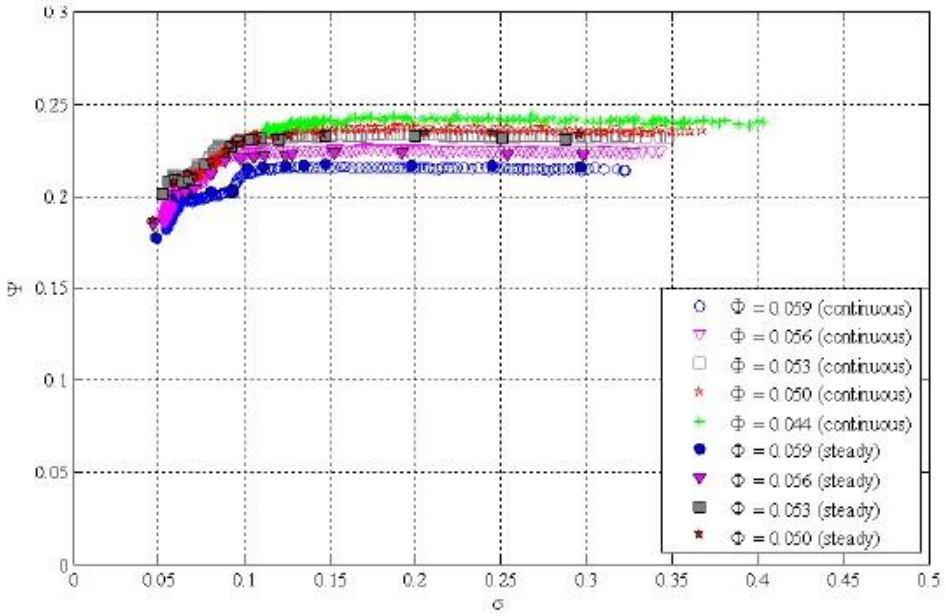

FIGURE 2.39: CAVITATING PERFORMANCE OF DAPAMITO 4 INDUCER WITH STEADY-STATE AND CONTINUOUS TESTS AND LOW CLEARANCE [1]

Finally, it can be concluded that the DAPAMITO 4 inducer has a similar cavitating behaviour than the DAPAMITO 3 inducer. In both cases, the cavitating curves with low clearance show a “one step” shape under breakdown conditions, that consist of an intermediate head drop in which different forms of instabilities as synchronous rotating cavitation may occur.

2.3.3. RAPDUD

The RAPDUD is a three-bladed inducer that has been used in the present activity after being designed and proposed by some authors (d’Agostino [7]). It has been tested in different cavitation experiments in a CPRTF. The shape of the RAPDUD inducer is shown in Figure 2.40.

FIGURE 2.40: RAPDUD INDUCER SIDE VIEW [1]

As for the DAPAMITO inducers, the main geometrical and operational parameters of RAPDUD inducer are summarized in Table 2.10 [5].

Geometrical and operational parameters of RAPDUD inducer	
Design flow coefficient (ϕ_D) [-]	0.070
Number of blades (N) [-]	3
Tip radius (r_T) [mm.]	81.0
Inlet tip blade angle (Υ_{Tle}) [º]	82.80
Inlet hub radius with fully-developed blade (r_{Hle}) [mm.]	45.0
Outlet hub radius (r_{Hte}) [mm.]	58.5
Axial length with fully-developed blade (c_a) [mm.]	69.0
Rotational speed (Ω) [r.p.m.]	1500
Inlet hub radius (r_{Hle}) [mm.]	35.0
Axial length (L) [mm.]	90.0
Diffusion factor (D) [-]	0.25
Incidence and blade angles ratio (α/β_b) [-]	0.197
Tip solidity (σ_T) [-]	2.28
Incidence tip angle at design (α) [º]	1.42
Outlet tip blade angle (Υ_{Tte}) [º]	79.65

TABLE 2.10: GEOEMETRICAL AND OPERATIONAL PARAMETERS OF RAPDUD INDUCER

In the case of RAPDUD inducer, as in the case of DAPAMITO 4, only the low clearance case is studied with a radial clearance value of 0.8 mm.

For the **non-cavitating performance**, as in the DAPAMITO inducers, following the sampling values of Table 2.2. and for rotational speeds of Ω = 2000 rpm., Ω = 2500 rpm. and Ω = 3000 rpm., the Figure 2.41 shows a summary of the results[5]. As it can be seen, the independence of the Reynolds number is confirmed in this case too as the flow is fully turbulent (Re > 10^6).

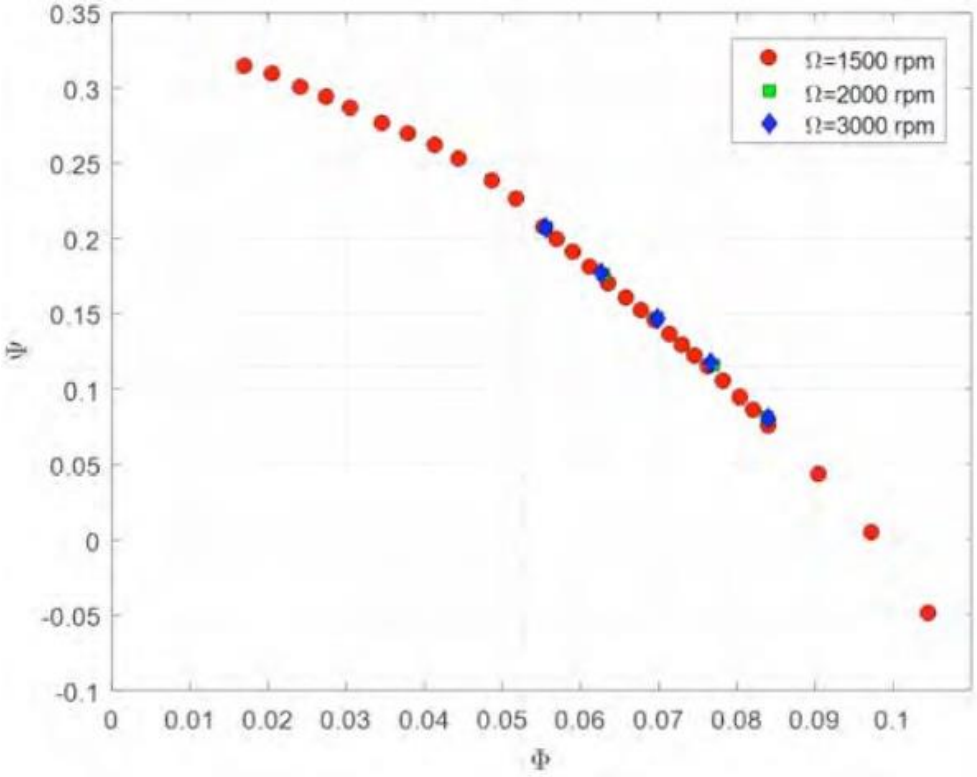

FIGURE 2.41: RAPDUD NON-CAVITATING PERFORMANCE WITH CLEARANCE = 0.8 MM. [1]

For the **cavitating performance**, the relevant data for the spectral analysis for the continuous test, is given in Table 2.11.

Sampling for continuous cavitating tests data acquisition	
Sample rate [sps]	5000
Number of samples [-]	10000
Overall test duration [s]	240
Number of records [-]	4
Overlap % [s]	50

TABLE 2.11: RELEVANT DATA FOR THE SPECTRAL ANALYSIS OF RAPDUD INDUCER

For the test conducted with a rotational speed of Ω = 3000 rpm., the results of the cavitating performance for flow coefficients between 0.056 to 0.084 (from 80% to 120% of the design flow coefficient) are represented in Figure 2.42.

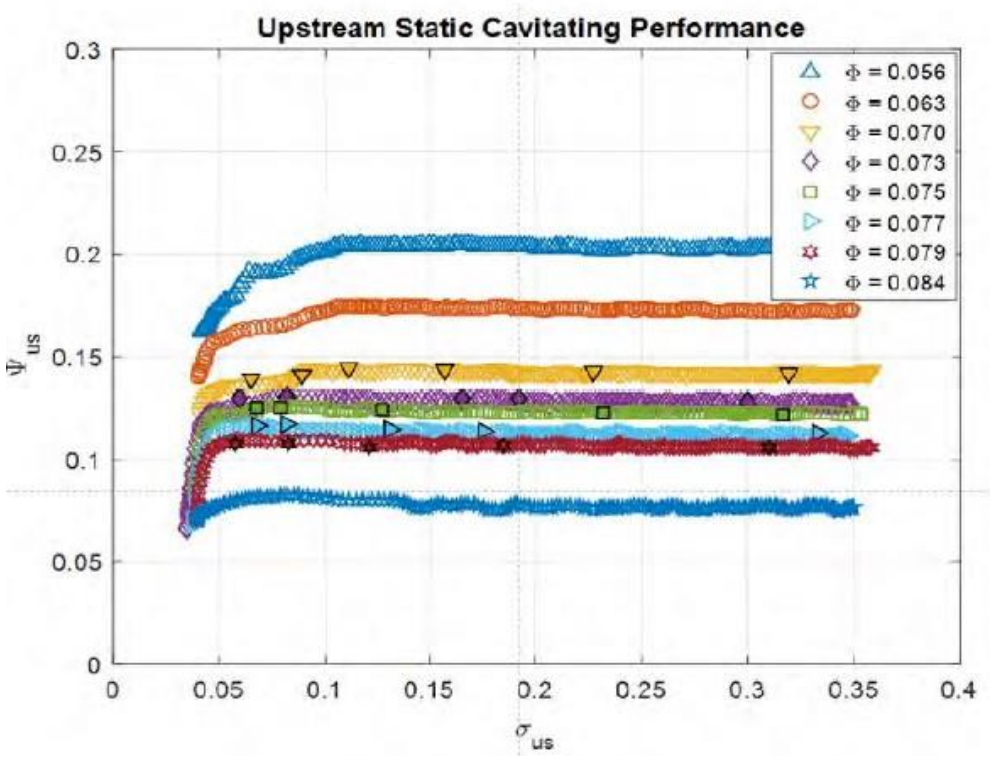

FIGURE 2.42: CAVITATING PERFORMANCE OF RAPDUD INDUCER WITH LOW CLEARANCE [1]

The results are obtained after the unsteady pressure in the blade channels has been measured by PCB S112A22 piezoelectric transducers (0 to 345 kPa pressure range, 7 Pa resolution, 14.5 mV/kPa sensitivity, –73 to +135 °C temperature range) flush-mounted on the inducer casing as shown in Figure 2.43.

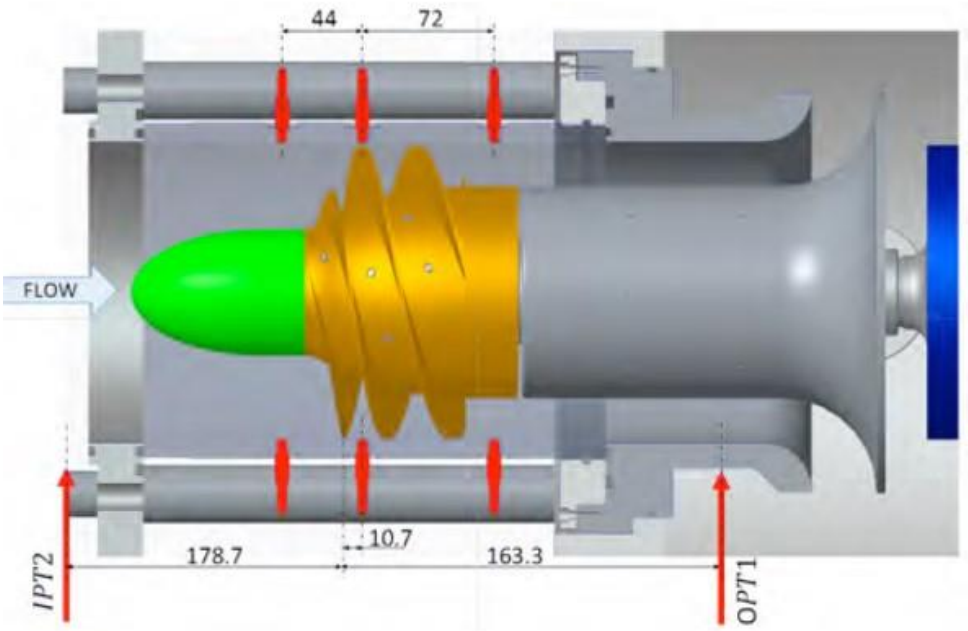

FIGURE 2.43: RAPDUD INDUCER MOUNTED IN CPRTF TEST SECTION WITH POSITIONS OF FIXED PRESSURE TAPS [1]

3. Cavitation-induced flow instabilities

Flow instabilities have been characterized by their frequency, intensity and typology (longitudinal, azimuthal…). For analysing the pressure fluctuations, the inlet section has been equipped with flush-mounted pressure transducers differentiating the cases of high clearance and low clearance. The high and low clearance cases are shown only for the DAPAMITO 3 inducer as it is the only inducer that has been tested with both configurations. For the rest, the disposition of transducers is the same as in the case of the low clearance DAPAMITO 3 as explained in Subsection 3.2.

For organizing this Section, firstly the high clearance and low clearance configurations are studied, taking notice of the location of the pressure transducers. Then, the experimental procedure and reduction techniques used in the project are presented. Finally, different kinds of flow instabilities due to cavitation are analysed, dividing them with their respective characteristics, frequency of appearing and Euler number associated to each flow coefficient studied. Also, some Figures are presented in which the kinds of instability are well-differentiated.

3.1. High clearance case

In Figure 3.1, it is represented the Plexiglas inlet section for the high clearance case, and a frontal view of the DAPAMITO 3 inducer inside the test section[1].

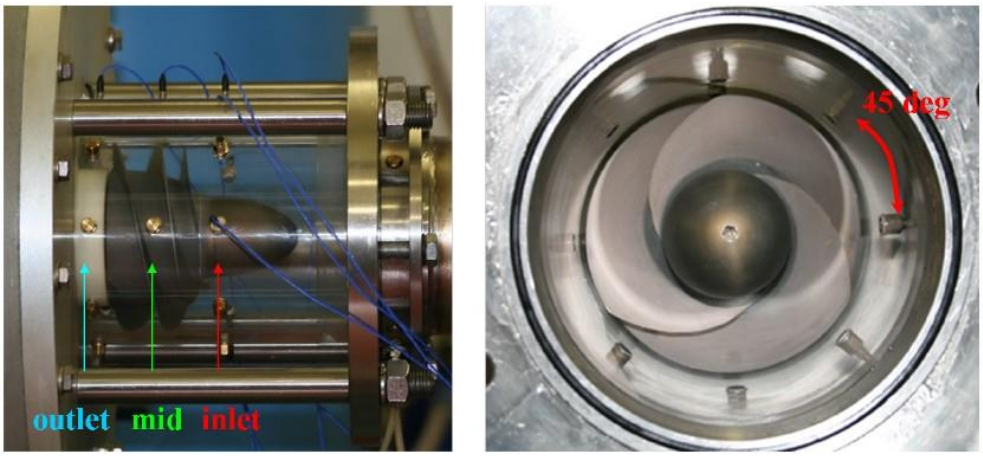

FIGURE 3.1: TRANSPARENT HOUSING WITH HIGH CLEARANCE WITH PIEZOELECTRIC PRESSURE TRANSDUCERS (LEFT) AND FRONTAL VIEW OF DAPAMITO 3 INSIDE THE TEST SECTION (RIGHT) [1]

In the case of high clearance casing, the inlet section made in transparent Plexiglas is equipped with eight piezoelectric pressure inducers, being at 3 axial stations: 6 of them are located at the flow inlet section with a spacing between them of 45º, one at the outlet section and the last one in the inducer blade channels. In Figure 3.2, the location of the PCB transducers in high clearance case is shown:

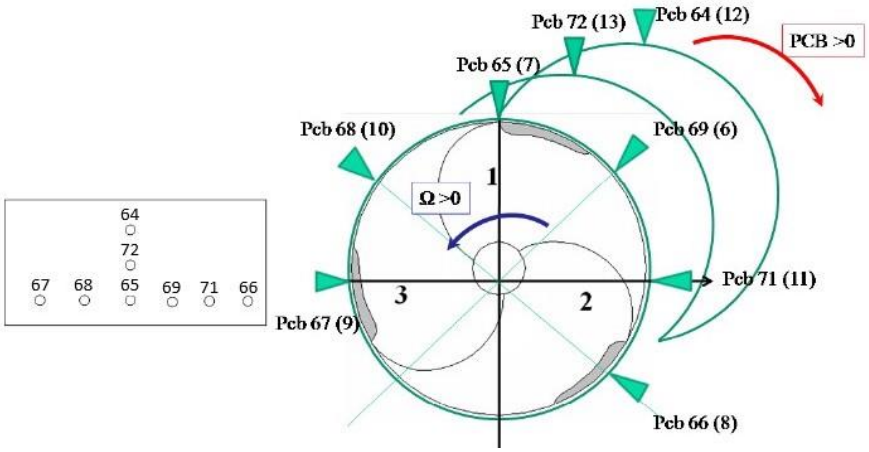

FIGURE 3.2: PCB TRANSDUCERS LOCATION IN HIGH CLEARANCE CASE [1]

In Table 3.1, it is shown the main sampling values and data reduction parameters used for getting the power spectral density of the pressure fluctuations with different cavitation numbers of the DAPAMITO 3 inducer.

Sampling for continuous cavitating tests high clearance	
Sample rate [sps]	1000
Number of samples [-]	240000
Nyquist frequency [Hz]	500
Interval temporal length [s]	4.0
Number of means [-]	2
Spectral temporal length [s]	2.0
Frequency resolution [Hz]	0.5

TABLE 3.1: SAMPLING VALUES AND DATA REDUCTION PARAMETERS IN FLOW INSTABILITIES ANALYSIS IN HIGH CLEARANCE CASE

The data is obtained with a sample rate of 1000 sps, so it is straightforward to know that $\Delta t = 1000^{-1}$ s and the Nyquist frequency is 500 Hz. As it is summarized in Table 3.1, each set of data with temporal length $T_r = 4$ seconds have been divided into 2 blocks with same length in which the inlet pressure is considered as a constant value.

3.2. Low clearance case

As in the case of high clearance, in Figure 3.3, it is represented the Plexiglas inlet section for the low clearance case, and a frontal view of the DAPAMITO 3 inducer inside the test section [1].

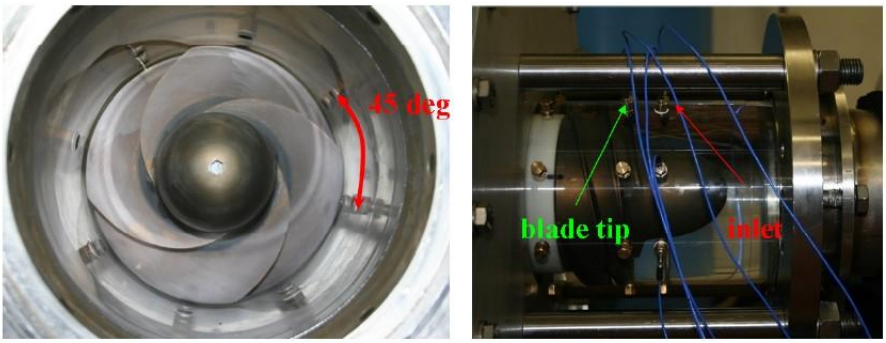

FIGURE 3.3: TRANSPARENT HOUSING WITH LOW CLEARANCE WITH PIEZOELECTRIC PRESSURE TRANSDUCERS (RIGHT) AND FRONTAL VIEW OF DAPAMITO 3 INSIDE THE TEST SECTION (LEFT) [1]

The main differentiation between both cases is the eight flush-mounted piezoelectric pressure transducers. In this case, they are located at two axial stations and not 3 as in the case of high clearance. In this case, the location of the piezoelectric transducers is given by six of them at the flow inlet section with spacing of 45 degrees between them and two of them in correspondence of the blade tip at the leading-edge. The Figure 3.4 represents the configuration that has just been explained:

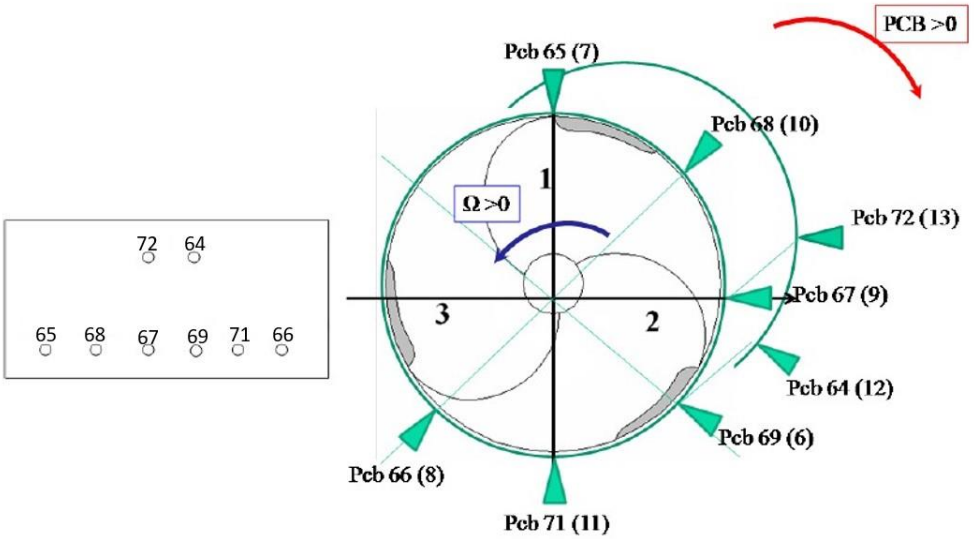

FIGURE 3.4: PCB TRANSDUCERS LOCATION IN HIGH CLEARANCE CASE [1]

It is important to remark that the distance between the transducers placement at the inlet station and the blade tip is the same in both cases (33.7 mm.) allowing the comparison of the results. The objective of this kind of configuration is that the higher-pressure oscillation signals were taken. However, experimentally although in general the pressure signals are amplified, rotor passage just behind the transducer increases the noise level. Due to this limitation of the configuration, the proceed with analysis of the PCB transducers is chosen.

The values of sampling and parameters for obtaining the power spectral density of the pressure fluctuations with different cavitation numbers are the same as the values shown in Table 3.1 for the high clearance case.

3.3. Experimental procedure and reduction techniques

Firstly, it is important to comment that at the inlet axial station, there are at least two transducers mounted with a fixed angular spacing [1]. The objective of this fact is to cross-correlate their signals for coherence and phase analysis.

So, in order to get the axial or azimuthal nature of the detected instabilities, cross-correlation of the pressure signals from different locations is used.

The procedure for the data reduction is described following some steps detailed as:

1. Acquisition of a set of signals from different piezoelectric transducers through a continuous test.

2. The data is divided in several time intervals, in which the inlet pressure is considered as a constant.
3. Each set of data, with a temporal length defined as T_r, is divided into n_d blocks with same time length. In Figure 3.5, it is detailed, for clarification, the division of the temporal length.

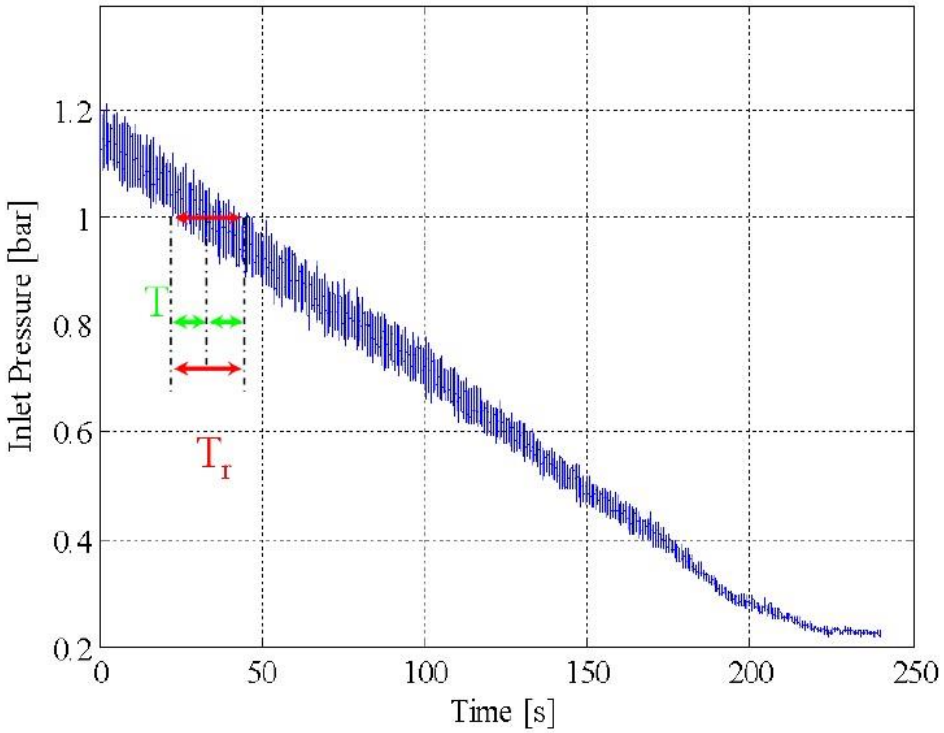

FIGURE 3.5: TIME HISTORY OF INLET PRESSURE DURING A CONTINUOUS TEST [1]

4. Each block of data is windowed through Hanning window to suppress the side-lobe leakage.
5. For each of the n_d blocks, it is done a Fourier transform of the signal x, making use of the following Equation.

$$X_i(f_k) = \Delta t \cdot \sum_{n=0}^{N-1} x_{in} \cdot e^{\frac{-12 \cdot \pi \cdot k \cdot n}{N}} \qquad 3.1$$

Being i = 1, 2, …, n_d , k = 0, 1, …, (N-1) and Δt the sampling interval.

6. X values that have been obtained by the Fourier transform are scaled taking into account the influence of windowing (in the used case of Hanning window, the scale factor is defined as $\sqrt{8/3}$).
7. Power density of auto-correlation of the n_d data blocks is calculated making use of the following Equation.

$$S_{xx}(f_k) = \frac{1}{n_d \cdot N \cdot \Delta t} \cdot \sum_{i=1}^{n_d} |X_i(f_k)|^2 \qquad 3.2$$

8. Power density of cross-correlation between the signals from two different transducers is calculated by a similar Equation to the previous one:

$$S_{xy}(f_k) = \frac{1}{n_d \cdot N \cdot \Delta t} \cdot \sum_{i=1}^{n_d} |X_i(f_k)| \cdot |Y_i(f_k)| \qquad 3.3$$

9. The coherence function is calculated, considering that the value must be near to 1 in order to consider the cross-correlation as acceptable:

$$\Upsilon_{xy}^2 = \frac{\left|S_{xy}(f_k)\right|^2}{S_{xx}(f_k) \cdot S_{yy}(f_k)} \qquad 3.4$$

From these steps, the frequency resolution of the Fourier transform is given by: $df = 1/T$. So, the time length T of each set of data must be chosen as high as possible with the objective of obtaining a better frequency resolution. However, the value of T can not be too high because it will result in an excessive variation of the inlet pressure in the acquisition interval.

Making use of the Nyquist equation, there is an upper limit for the frequency observable (Nyquist frequency) by Fourier transform defined as:

$$f_c = \frac{1}{2\Delta t} \qquad 3.5$$

Being Δt the time interval between two acquisitions from a same transducer.

3.4. Flow instabilities

The chosen way to represent the results that have been obtained by the Fourier analysis of the signals from piezoelectric transducers are “waterfall plots”, in which the power frequency spectra is reported as fa function of the cavitation number given a fixed value for the flow coefficient.

If a frequency peak is observed in the waterfall plots, the nature of the corresponding instability (axial or rotating) is analysed by means of cross-correlation of signals from different transducers. The instability analysis is conducted for same flow coefficients investigated during cavitating performance characterization. The analysis is based in: recognition of oscillating phenomena by analysing pressure fluctuations in the inducer; definition of the most probable nature of the phenomena by analysing the cross-spectra phases φ for different transducers couples at same axial section and angular separation Δθ (axial or rotating and in the case of rotating, number of lobes and direction of rotation); validation of the previous points by the coherence function.

In the case of two transducers at the same longitudinal section with different angular positions, for an axial phenomenon, the phase of cross-correlation between both transducers is 0º. On the other hand, for rotating phenomenon, the ratio between the phase of the cross-correlation and the angular separation between transducers results in the number of rotating cells:

$$n_c = \frac{\varphi}{\Delta\theta} \qquad 3.6$$

Being Ω the detected frequency of the pressure oscillation, the real frequency of the oscillation is:

$$f_r = \Omega \frac{\varphi}{\Delta\theta} = \frac{\Omega}{n_c} \qquad 3.7$$

It can be concluded that real frequency of the oscillation is equal to detected frequency for phenomena with a single rotating cell or axial phenomena.

To sum up, cross-spectra phases close to 0 imply an axial phenomenon while cross-spectra phases close to $\Delta\theta$ or a multiple of that value imply a rotating phenomenon with n (the multiple used with $\Delta\theta$) lobes. In Figure 3.6, there is an example of a waterfall plot of the DAPAMITO 3 inducer with a given flow coefficient with a continuous test.

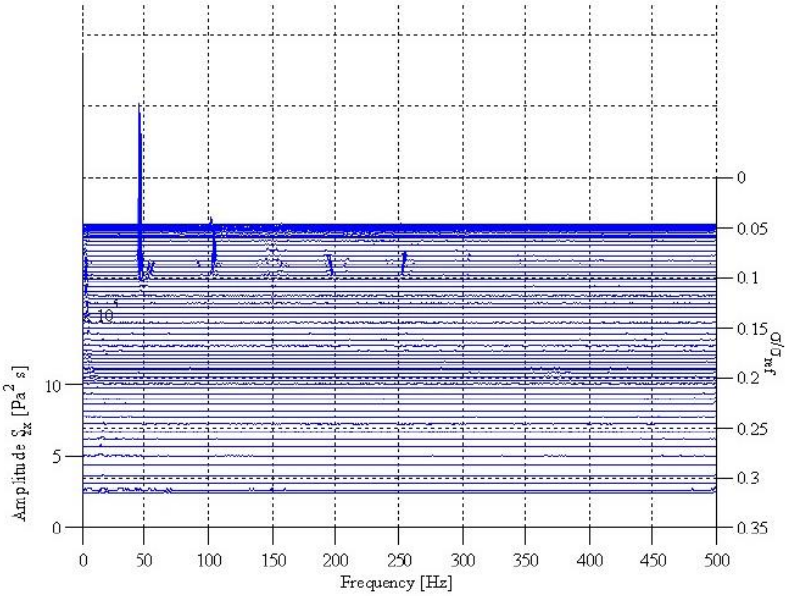

FIGURE 3.6: WATERFALL PLOT OF THE POWER SPECTRUM OF THE INLET PRESSURE FLUCTUATION ON DAPAMITO 3 INDUCER WITH LOW CLEARANCE, Ω = 3000 RPM, T =49.8ºC, AND FILTERED FOR NΩ FREQUENCIES. [1]

Once the theory that lies behind the waterfall plots has been explained, some examples are presented identifying different forms of instabilities.

In Table 3.2, it is shown the flow instabilities detected on inducer DAPAMITO 3 in the case of high clearance (for information about low clearance see [1]). It appears the typology of instability, frequencies range, flow coefficients in which they have been observed, cavitation number range and number of lobes.

The instability called surge is related to 0-th order (axial) instability that corresponds probably to auto-oscillation of the inlet line flow. It appears for all flow coefficients studied except in the case of the lowest value. The instability BO (one lobe co-rotating stability) and AO1 (axial phenomenon) can be seen only with the lowest flow coefficient and with relatively high cavitation numbers. BVI1 is related to a rotating phenomenon with at least four lobes typical of backflow vortices instabilities. It appears with all flow coefficients and appears with very low cavitation numbers, in situations close to performance breakdown. BVI2 is related to a rotating phenomenon with, as minimum, eight lobes and is typical of backflow vortices instabilities. As in the other case, it appears only at very low cavitation numbers. AO2 appears only at highest

flow coefficients and in cases with non-cavitating conditions. It is axial and it probably occurs due to a form of high order surge instability. The rest of instabilities detected at the other detected frequencies are probably caused by non-linear interaction between phenomena BVI1, BVI2 and harmonics of the blade passage (nΩ).

Instability	Characteristics	Frequency [Hz]	σ with different ϕ				
			0.062	0.059	0.056	0.053	0.044
Surge (S)	Axial	8-10	0.08-0.12	0.08-0.12	0.08-0.12	0.08-0.12	
Backflow Oscillation (BO)	Rotating 1 cell	9-10					0.101-0.35
Backflow Vortices Instability 1 (BVI1)	Rotating 4 cell	36.2-37.1	0.04-0.045	0.04-0.048	0.04-0.048	0.04-0.048	
Axial Oscillation 1 (AO1)	Axial	93-95					0.125-0.35
3Ω-BVI1	Counter-rotating 1 cell	112.5-113.7	0.04-0.045	0.04-0.048	0.04-0.048	0.04-0.048	
Backflow Vortices Instability 2 (BVI2)	Rotating 8 cell	163.5	0.04-0.045		0.042-0.048	0.042-0.048	
2Ω+BVI2	Rotating 2 cell	263.8-264	0.04-0.045			0.042-0.048	
Axial Oscillation 2 (AO2)	Axial	355.4-357.5	0.25-0.35				

TABLE 3.2: FLOW INSTABILITIES ON DAPAMITO 3 INDUCER WITH HIGH CLEARANCE

In Figures 3.7 and 3.8, it can be seen the waterfall plot for the high clearance case for different values of flow coefficient as an example and identifying the different forms of instabilities that can be seen.

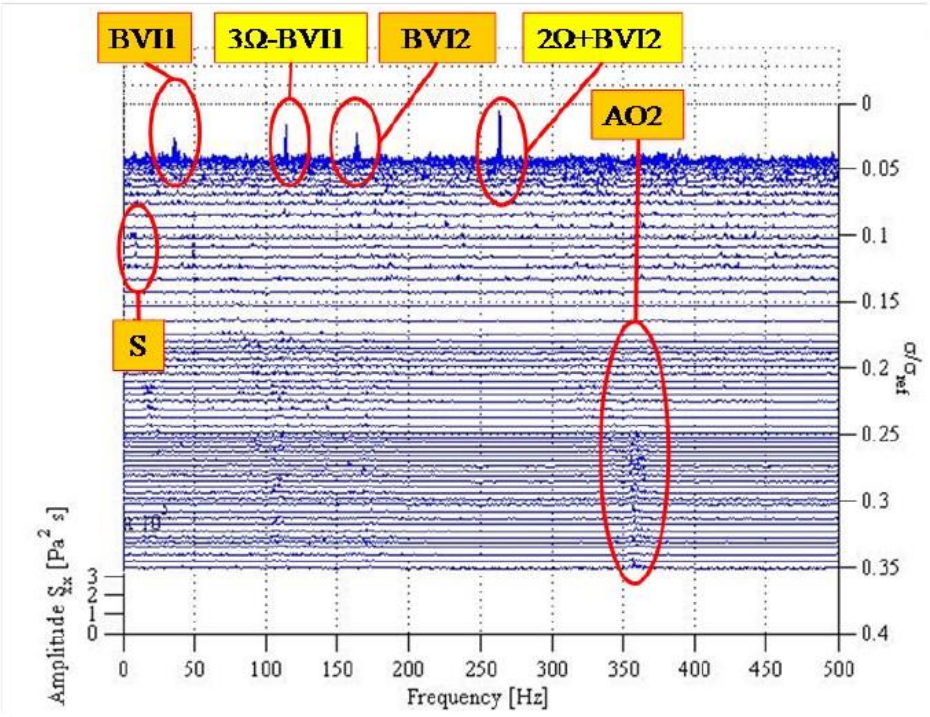

FIGURE 3.7: WATERFALL PLOT OF THE POWER SPECTRUM OF THE INLET PRESSURE FLUCTUATION ON DAPAMITO 3 INDUCER WITH Φ = 0.062, HIGH CLEARANCE, Ω = 3000 RPM, T =14.9ºC, AND FILTERED FOR NΩ FREQUENCIES. [1]

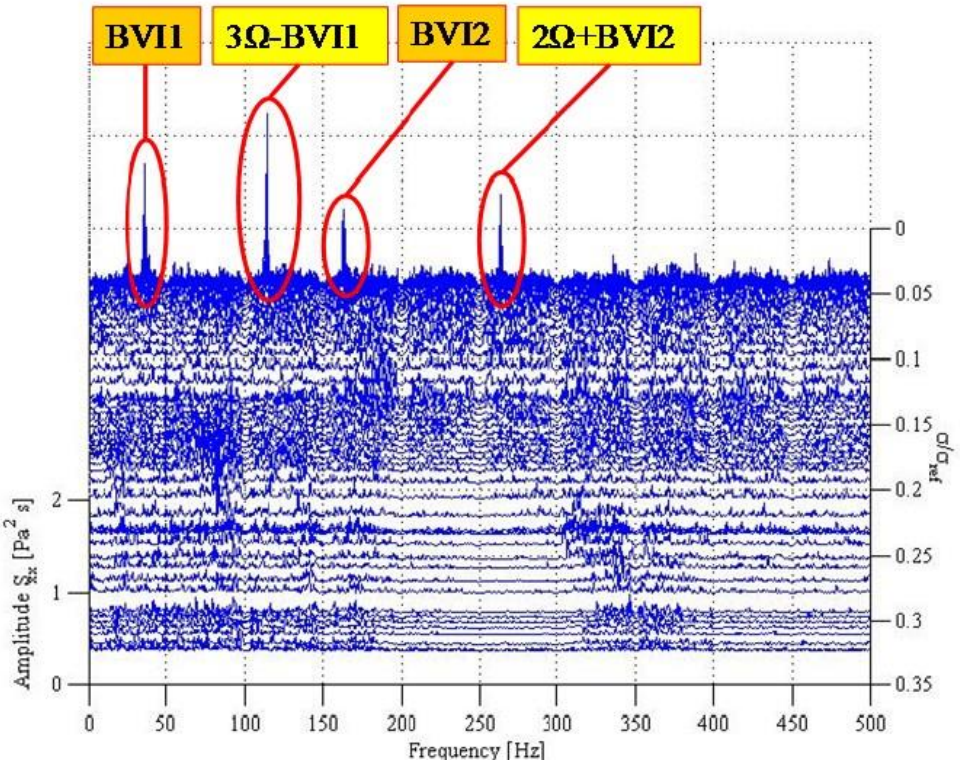

FIGURE 3.8: WATERFALL PLOT OF THE POWER SPECTRUM OF THE INLET PRESSURE FLUCTUATION ON DAPAMITO 3 INDUCER WITH Φ = 0.059, HIGH CLEARANCE, Ω = 3000 RPM, T =14.9ºC, AND FILTERED FOR NΩ FREQUENCIES. [1]

4. Backflow vortex instability

The basis of this Final Master's thesis is the backflow vortex instability. So, from the different kinds of instabilities that have been analysed in the previous Section, in this one, the backflow vortex instability is introduced in detail.

With this objective, firstly some general aspects of the studied phenomenon are shown, analysing the main characteristics and the principal region of influence. Then, the instability model used for the backflow vortex instability is presented, obtaining the velocity potential and pressure predictions from a potential flow, and considering some hypothesis around it. Also, the frequency broadening is analysed due to its importance for the identification process evaluating the results.

4.1. General aspects

It is known that under low flow rates, a backflow occurs at the outer part of pump inlet by the excessive pressure difference across the blades near the leading-edge [3][4][12][13][14][15][16]. The backflow has a high tangential velocity by the angular momentum imparted by the rotation of the blades. The shear layer between the swirling backflow and straight main flow rolls up and forms a backflow vortex structure as can be seen in Figure 4.1.

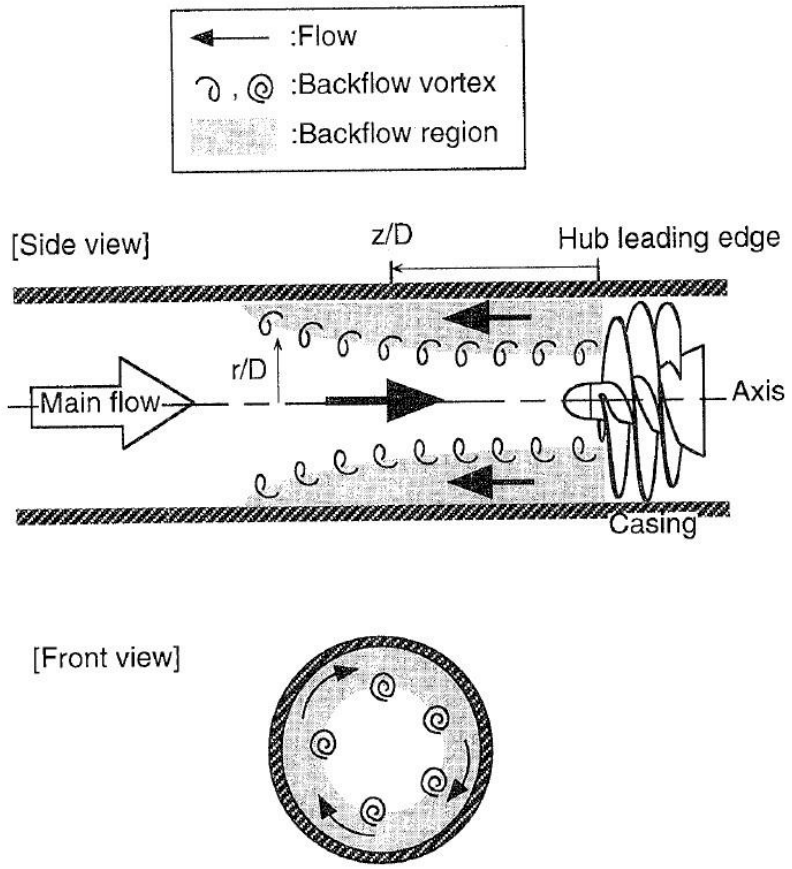

FIGURE 4.1: BACKFLOW VORTEX STRUCTURE AT THE BOUNDARY BETWEEN SWIRLING BACKFLOW AND AXIAL MAIN FLOW [3]

The studied phenomenon of backflow vortex cavitation occurs at the vortex core when the pressure there becomes lower than the vapour pressure, by the effect of centrifugal force on the vorticity and the increase of the main flow velocity by the backflow displacement effect.

The inlet characteristics of backflow in inducers must be understood because the design of the inducers is made with a certain incidence angle securing that the cavitation occurs only on the suction surface preventing breakdown by cavitation on the pressure surface.

In Figure 4.2, it can be seen a photograph of the backflow vortex filament at the inlet of an inducer after an experimental research. It is shown that at least seven inlet backflow cavitating vortex filaments extend from the impeller upstream, and they rotate in the same direction keeping their relative positions. The upstream ends of these vortex cavities seem to attach to the casing and the other ends to the blade.

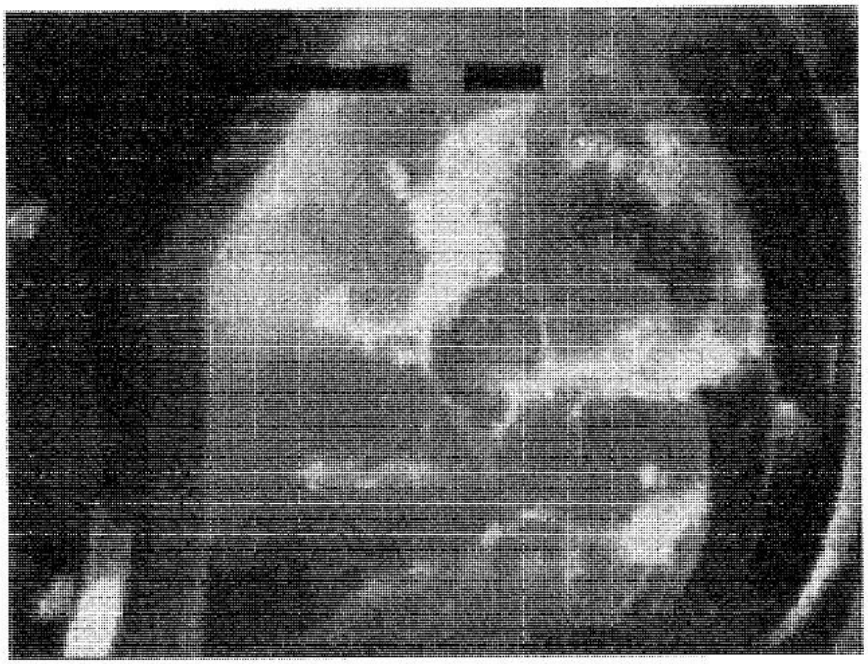

FIGURE 4.2: BACKFLOW VORTEX FILAMENTS AT THE INDUCER INLET [4]

In order to analyse the geometry of the vortex filament, it is necessary to remark that backflow vortex cavitation can be detected from the inlet pressure fluctuation only with extremely large cavities or when the vortex sweeps the pressure transducer.

Studying the voltage proportional to the distance from the sensor to the target it could be seen that a dip in the signal indicates the passage of the cavity vortex filaments as it is shown in Figure 4.3.

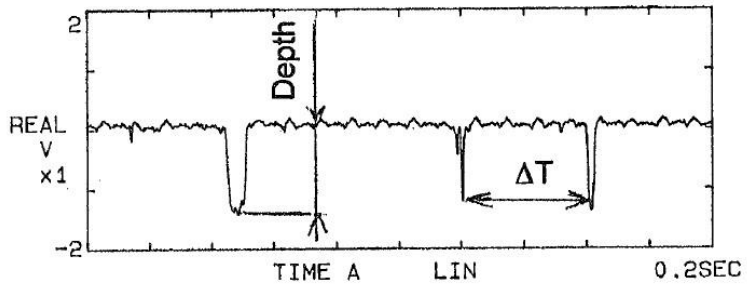

FIGURE 4.3: LASER SENSOR TEMPORAL OUTPUTS [4]

Taking that into account, the radial location of the vortex filaments with respect to the axial locations measured form inducer blade leading-edge to the hub can be obtained and analyse the profile of vortex filaments and the axial length of the vortex filaments.

4.2. Instability model

4.2.1. POTENTIAL FLOW

The first necessary assumption for the instability model studied is the consideration of potential flow [2]. A potential flow is described by means of a velocity potential (ϕ) depending on space and time. In that case, the flow velocity ***u*** is a vector field equal to the gradient of the defined velocity potential:

$$u = \nabla\phi \qquad 4.1$$

As a definition, the curl of the gradient is equal to zero and consequently, the vorticity, that is, the curl of the velocity field is equal to zero too:

$$\begin{gathered}\nabla \times \nabla\phi = 0 \\ \nabla \times \mathrm{u} = 0\end{gathered} \qquad 4.2$$

Taking that into account, it can be said that a potential flow is an irrotational flow. In flow regions with important vorticity, as wakes or boundary layers, potential flow theory is not accurate to be applied to predict the flow. However, as there are large regions of flow where the hypothesis of irrotationality is accurate, the potential flow can be used to predict the flow. In 2D, potential flow is analysed simply with conformal mapping, using transformations of the complex plane. Basically, it consists in using an analytic function ***f*** mapping the physical domain (x,y) to the transformed domain defined by (ϕ, ψ). Defining the complex quantities ***z*** and ***w*** as:

$$\begin{gathered}z = x + iy \\ w = \phi + i\psi\end{gathered} \qquad 4.3$$

Defining now the mapping function ***f***, called complex velocity potential:

$$f\,(x + iy) = f\,(z) = \phi + i\psi = w \qquad 4.4$$

Being ***f*** an analytic function, the Cauchy-Riemman equations must be satisfied:

$$\begin{gathered}\frac{\partial\phi}{\partial x} = \frac{\partial\psi}{\partial y} \\ \frac{\partial\phi}{\partial y} = -\frac{\partial\psi}{\partial x}\end{gathered} \qquad 4.5$$

Now, to obtain the velocity components (u, v) related to the directions (x, y) respectively:

$$\frac{df}{dz} = u - iv \qquad 4.6$$

Calculating, the velocity field ***u*** is defined, taking into account the Cauchy-Riemman equations as:

$$u = \frac{\partial \phi}{\partial x} = \frac{\partial \psi}{\partial y} \qquad 4.7$$

$$v = \frac{\partial \phi}{\partial y} = -\frac{\partial \psi}{\partial x}$$

Then, both ϕ and ψ satisfy the Laplace equation defined as $\nabla^2 \phi = 0$, so:

$$\Delta \phi = \frac{\partial^2 \phi}{\partial x^2} + \frac{\partial^2 \phi}{\partial y^2} = 0 \qquad 4.8$$

$$\Delta \psi = \frac{\partial^2 \psi}{\partial x^2} + \frac{\partial^2 \psi}{\partial y^2} = 0$$

ϕ is identified as velocity potential, being lines with constant ϕ defined as equipotential and ψ as stream function being lines with constant ψ called streamlines.

4.2.2. HYPOTHESIS

When modelling backflow vortex instability, it is assumed an ideal flow with N concentrated vortices in a circular geometry, with the objective of simulating the inlet of the inducer as represented in Figure 4.4 [2].

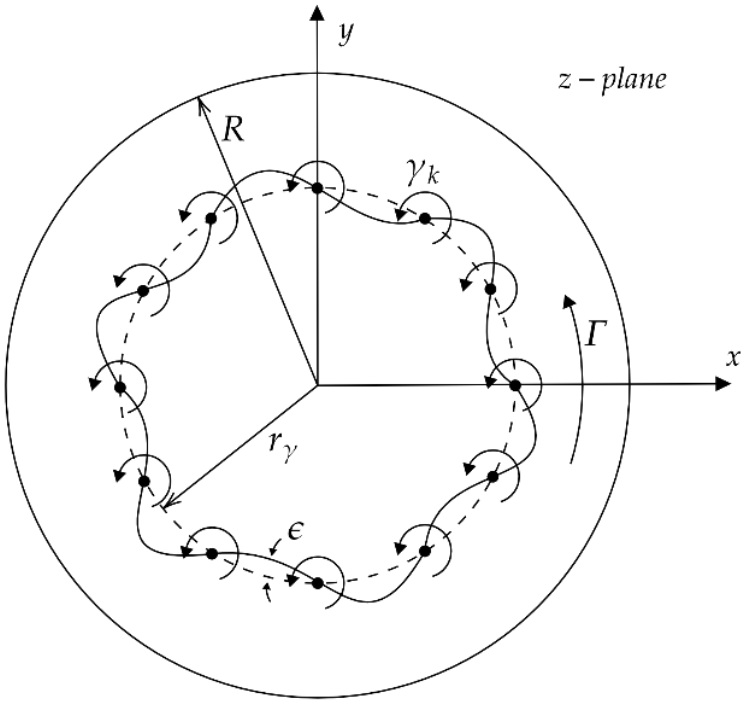

FIGURE 4.4: IDEAL FLOW SCHEME [2]

The vortices are located at:

$$z_k = a \cdot e^{i\theta_k} \qquad 4.9$$

Being the parameter θ_k defined as:

$$\theta_k = \frac{(k-1)\cdot 2\pi}{N} \qquad 4.10$$

The vortex intensity is considered as similar for all the vortices and the N concentrated vortices are co-rotating with angular speed ω_γ.

4.2.3. MILNE-THOMSON THEOREM

The basis of the called "*Circle Theorem*" is a new stream function for a fluid flow when a circular cylinder is placed into the flow. It is the starting point to obtain velocity potential of the flow at the interest location of the inducer, the inlet for the backflow vortex instability.

Theorem: Being $f_k(z)$ the complex potential of an ideal flow with a singularity at z_k in $|z| < R$. In the case that a circular cylinder, typified by its cross-section, the circle $|z| = R$, is placed into that flow, the complex potential of the new flow is the previous complex potential adding a term defined as:

$$f(z) = f_k(z) + \overline{f_k(R^2/\bar{z})} \qquad 4.11$$

With the same singularity as $f_k(z)$ at $\overline{z_k}$ in $|z| > R$.

4.2.4. VELOCITY POTENTIAL AND PRESSURE PREDICTIONS

Making use of the Source-Vortex flow theory, for a vortex with defined intensity $i\Gamma_k$ located at z_k inside the circle $|z| = R$, the complex velocity potential is given by:

$$f_k(z) = -i\frac{\Gamma_k}{2\pi}\ln(z - z_k) \qquad 4.12$$

So, for the circle theorem defined previously, the necessary term is defined as:

$$f_k\left(\frac{R^2}{z}\right) = -i\frac{\Gamma_k}{2\pi}\ln\left(\frac{R^2}{z} - z_k\right), \qquad 4.13$$

$$\overline{f_k\left(\frac{R^2}{z}\right)} = i\frac{\Gamma_k}{2\pi}\ln\left(\frac{R^2}{z} - \overline{z_k}\right)$$

By the Milne-Thomson theorem, the potential for the flow around and inside of the cylinder is:

$$f(z) = f_k(z) + \overline{f_k(R^2/\bar{z})} = -i\frac{\Gamma_k}{2\pi}\ln(z - z_k) + i\frac{\Gamma_k}{2\pi}\ln\left(\frac{R^2}{z} - \overline{z_k}\right) \qquad 4.14$$

Defining also z_k and its complex conjugate:

$$z_k = r_k e^{i\theta_k} = r_k\cdot(\cos\theta_k + i\cdot sin\,\theta_k), \qquad 4.15$$

$$\overline{z_k} = r_k e^{-i\theta_k} = r_k\cdot(\cos\theta_k - i\cdot sin\,\theta_k)$$

It is obtained:

$$f(R) = -i\frac{\Gamma_k}{2\pi}\ln(R - z_k) + i\frac{\Gamma_k}{2\pi}\ln(R - \overline{z_k}) = \; -i\frac{\Gamma_k}{2\pi}\left[\ln(R - z_k) - \ln\overline{(R - z_k)}\right]$$

$$= \; \frac{\Gamma_k}{\pi} Arg\{R - r_k \cdot \cos\theta_k - i \cdot r_k \cdot \sin\theta_k\} \qquad 4.16$$

Being $-\frac{\pi}{2} < Arg\,\{R - z_k\} < \frac{\pi}{2}$ for $r_k > R$:

$$-r_k \cdot \sin\theta_k = (R - \; r_k \cdot \cos\theta_k) \cdot \tan(Arg\{R - z_k\})\,,$$

$$\tan(Arg\{R - z_k\}) = \; Arctan\left(\frac{-r_k \cdot \sin\theta_k}{R - r_k \cdot \cos\theta_k}\right) \qquad 4.17$$

So, finally, substituting the development of the terms in the function $f(R)$:

$$f(R) = \; \frac{\Gamma_k}{\pi} \cdot Arctan\left(\frac{-r_k \cdot \sin\theta_k}{R - r_k \cdot \cos\theta_k}\right) = \phi(R) \qquad 4.18$$

Using the obtained relationship for the N vortices with same intensity and located at z_k:

$$\phi(R) = \; \frac{\Gamma}{\pi} \cdot \sum_{k=1}^{N} Arctan\left(\frac{-a \cdot \sin\theta_k}{R - a \cdot \cos\theta_k}\right) \qquad 4.19$$

Adding also the previously mentioned assumption that the centres of the different vortices rotate counter-clockwise with speed ω_Γ. This contribution is incorporated adding to θ_k the term $\omega_\gamma \cdot t$:

$$\phi(R,t) = \; \frac{\Gamma}{\pi} \cdot \sum_{k=1}^{N} Arctan\left(\frac{-a \cdot \sin(\omega\gamma t \; + \theta_k \;)}{R - a \cdot \cos(\omega\gamma t \; + \theta_k)}\right) \qquad 4.20$$

With this procedure, the velocity potential is differentiable in time. To obtain pressure perturbations, the Bernoulli equation is used in the form linearized to the 1st order in the perturbations for the inlet flow, with steady far-field conditions and no axial velocity perturbations ($w' = 0$):

$$\frac{\partial\phi}{\partial t} + \frac{p'}{\rho} + 0.5\,\boldsymbol{u}\cdot\boldsymbol{u} = B$$

$$\frac{\partial\phi}{\partial t} + \frac{p'}{\rho} + \bar{w}w' = 0 \qquad 4.21$$

Also, p' can be defined as:

$$p'(R,t) = \; -\rho \cdot \frac{\partial\phi(R,t)}{\partial t} \qquad 4.22$$

The needed term $\frac{\partial\phi(R,t)}{\partial t}$ can be computed as:

$$\frac{\partial\phi(R,t)}{\partial t} = \frac{\Gamma}{\pi}\cdot\frac{\partial}{\partial t}\sum_{k=1}^{N} Arctan\left(\frac{-a\cdot\sin(\omega_\gamma t\ +\theta_k\ )}{R-a\cdot\cos(\omega_\gamma t\ +\theta_k)}\right) =$$

$$=\frac{\Gamma}{\pi}\sum_{k=1}^{N}\frac{\partial\ Arctan\left(\frac{-a\cdot\sin(\omega_\gamma t\ +\theta_k\ )}{R-a\cdot\cos(\omega_\gamma t\ +\theta_k)}\right)}{\partial\left(\frac{-a\cdot\sin(\omega_\gamma t\ +\theta_k\ )}{R-a\cdot\cos(\omega_\gamma t\ +\theta_k)}\right)}\cdot\frac{\partial\left(\frac{-a\cdot\sin(\omega_\gamma t\ +\theta_k\ )}{R-a\cdot\cos(\omega_\gamma t\ +\theta_k)}\right)}{\partial t} =$$

$$\frac{\Gamma}{\pi}\sum_{k=1}^{N}\frac{-a}{1+\left(\frac{-a\cdot\sin(\omega_\gamma t\ +\theta_k\ )}{R-a\cdot\cos(\omega_\gamma t\ +\theta_k)}\right)^2}\cdot\frac{\partial\left(\frac{\sin(\omega_\gamma t\ +\theta_k\ )}{R-a\cdot\cos(\omega_\gamma t\ +\theta_k)}\right)}{\partial t} = \qquad 4.23$$

$$\frac{\Gamma}{\pi}\sum_{k=1}^{N}\frac{-a\cdot\left(R-a\cdot\cos(\omega_\gamma t\ +\theta_k)\frac{\partial}{\partial t}\sin(\omega_\gamma t\ +\theta_k\ )-\sin(\omega_\gamma t\ +\theta_k\ )\frac{\partial}{\partial t}(R-a\cdot\cos(\omega_\gamma t\ +\theta_k))\right)}{(R-a\cdot\cos(\omega_\gamma t\ +\theta_k))^2+(-a\cdot\sin(\omega_\gamma t\ +\theta_k\ ))^2} =$$

$$\frac{\Gamma}{\pi}\sum_{k=1}^{N}\frac{a\cdot\omega_\Gamma\cdot\left(R\cdot\cos(\omega_\gamma t\ +\theta_k)-a\cdot\cos^2(\omega_\gamma t\ +\theta_k)-a\cdot\sin^2(\omega_\gamma t\ +\theta_k\ )\right)}{(R-a\cdot\cos(\omega_\gamma t\ +\theta_k))^2+-(a\cdot\sin(\omega_\gamma t\ +\theta_k\ ))^2}$$

Now that the expression of the derivative of the potential velocity has been obtained in the time domain, the next step is moving the potential velocity onto the frequency domain with a Fourier transform as:

$$\hat{\phi}(R,\omega) = \int_{-\infty}^{\infty}\phi(R,t)\cdot e^{-i\omega t}\,dt = \frac{\Gamma}{\pi}\sum_{k=1}^{N}\int_{-\infty}^{\infty} Arctan\left[\frac{-a\cdot sin(\omega_\gamma t\ +\theta_k\ )}{R-a\cdot\cos(\omega_\gamma t\ +\theta_k)}\right]\cdot e^{-i\omega t}\,dt \qquad 4.24$$

And the pressure perturbations in the frequency domain:

$$\hat{p}(R,\omega) = \int_{-\infty}^{\infty}p'(R,t)\cdot e^{-i\omega t}\,dt = \sum_{k=1}^{N}\int_{-\infty}^{\infty}\rho\cdot\frac{\partial\phi}{\partial t}(R,t)\cdot e^{-i\omega t}\,dt\ = -i\omega\rho\hat{\phi}(R,\omega) \qquad 4.25$$

The algorithm used to obtain these transformations computationally is the Cooley-Turkey FFT [17]. The PCB readings are modified before being transformed with the objective of powering the computational speed.

4.2.5. Frequency Broadening

The frequency broadening is applied to this project mainly because the frequency broadening in experimental pressure spectra is expected due to:

1. Spatial resolution of the sensor.
2. Windowing of the sample data ($\Delta\omega\approx 2/T_{sampling}$).
3. Intrinsically noisy nature of the quasi-periodic phenomena observed.

4. Measurement errors (as could be A/D discretization, repeatability…)
5. Fluctuation of the impeller rotational speed Ω and manufacturing imperfections on the impeller blades that could be seen as a fluctuation of the rotational speed ΔΩ with a constant period of revolution.
6. The averaging of the experimental spectra from 4 subsamples with slowly changes of the rotational speed.

Now, commenting the points 1 and 2 on the list, being D_p the diameter of the sensing area of the transducer corresponding to an angular distance along the perimeter of the impeller casing:

$$\theta_p = \frac{D_p}{2\pi r_t} \qquad 4.26$$

Considering the time uncertainty for pressure measurement on an impeller rotating with a given angular speed as:

$$r_p = \frac{\theta_p}{\Omega} \qquad 4.27$$

Time and frequency domains are related by a variable s=ωt, so if it is differentiated with s as a constant:

$$\Delta\omega = \omega \frac{\Delta t}{t} \qquad 4.28$$

Decomposing the terms for an impeller rotating with a given angular speed:

$$\omega = \Omega = \frac{2\pi}{t}$$
$$\frac{\Delta t}{t} = \frac{\tau_p}{T} \qquad 4.29$$

So, finally it is obtained:

$$\Delta\omega = \Omega \frac{\tau_p}{T} = \Omega \frac{\theta_p}{\Omega} \frac{\Omega}{2\pi} = \Omega \frac{\theta_p}{2\pi} = \frac{\Omega}{2\pi} \frac{D_p}{2\pi r_t} = \frac{\Omega D_p}{4\pi^2 r_t} \qquad 4.30$$

Thus, the frequency bandwidth in the acquisition of the pressure fluctuations on the impeller casing is:

$$\Delta\omega_p = \frac{\Delta\omega}{2} = \frac{\Omega D_p}{8\pi^2 r_t} \qquad 4.31$$

The frequency broadening of the experimental pressure spectra is caused principally by the intrinsic noise of the phenomena and the evaluation of the experimental spectra considering the average of spectra obtained by partitioning the sampling time in similar intervals. To consider the frequency broadening, the free parameters in the theoretical spectra are the sum of n terms following a Normal Distribution with equal mean μ but unknown variance σ^2.

$$y = \sum_{i=1}^{n} x_i = n\bar{x} \qquad 4.32$$

Being ***y*** the argument of the generic Dirac function, ***x*** the sample mean and ***n*** the number of independent free parameters.

$$\bar{n} = \frac{1}{n}\sum_{i=1}^{n} x_i \qquad 4.33$$

Being the sample the set of independent free parameters. If the objective is fitting to the experimental data, and for accounting the frequency broadening, a convolution operation must be done between the theoretical pressure perturbation spectra and the assumed Gaussian probability distribution, being the probability distribution a standard Normal distribution with zero mean and unknown standard deviation called σ_g.

$$\hat{G}(\omega, \sigma_g) = \frac{1}{\sqrt{2\pi}\sigma_g}\, e^{\frac{-\omega^2}{2\,\sigma_g}} \qquad 4.34$$

Once the probability distribution is known, the convolution is obtained as:

$$\tilde{p}(R,\omega) = \left(\hat{p} * \hat{G}\right)(\omega) = \int_{-\infty}^{\infty} \hat{p}(\omega, R)\, \hat{G}(\omega - w, \sigma_g) dw =$$

$$\int_{-\infty}^{\infty} \hat{p}(\omega - w, R)\, \hat{G}(\omega, \sigma_g) dw \qquad 4.35$$

5. Backflow vortex identification

In this Section, the computational way of identifying the backflow vortex instability is presented. The identification process has been carried out using MATLAB and can be divided into different parts: system identification and cross-correlation, also presenting the review of the identification procedure

With the objective of organizing this Section, firstly the system identification is studied, dividing between the non-linear least-square method and the evaluation of the error making use of the figure of merit. Then, it is explained the cross-correlation that has been developed with a Bayesian estimator with the power density of auto-correlation and power density of cross-correlation allowing to get the cross-correlation coefficient. Finally, a review of the procedure for the identification is exposed.

5.1. System identification

The first important consideration to take into account is that the system identification is purely data-driven and could be understood as an input-output map of a system that is learned from training data in a representation that generalizes to data that was not in the training set [2][17][18]. In this particular case, it has been used a non-linear least-squares approach for the regression analysis.

5.1.1. Non-linear Least Square Method

Starting from a set of m data points defined as:

$$(x_1, y_1), (x_2, y_2), \ldots, (x_m, y_m) \tag{5.1}$$

and with a curve of function y = f(x, β (n)), that as can be seen, depends on x but also on n due to dependency of $\beta = (\beta_1, \beta_2, \ldots, \beta_n)$ being $m \geq n$.

Vector β must be found with parameters that result with the best possible fit curve to the given data in the least squares senses, that is, the sum of squares:

$$S = \sum_{i=1}^{m} r_i^2 \tag{5.2}$$

This parameter is minimized, and the residuals (in-sample prediction errors) are given by the difference between the data and the equation of the curve as:

$$r_i = y_i - f(x_i, \beta) \tag{5.3}$$

Being i = 1, 2, …, m. The minimum value of S that is being looked for occurs when the gradient is equal to zero. The model contains n parameters, so there are n gradient equations defined as:

$$\frac{\partial S}{\partial \beta_j} = 2 \cdot \sum_i r_i \cdot \frac{\partial r_i}{\partial \beta_j} = 0 \qquad 5.4$$

Being j = 1, 2, …, n. As it is a non-linear system, the term $\frac{\partial r_i}{\partial \beta_j}$ is function of the independent variable but also of the parameters, so in general, the gradient equations do not have a closed solution. The way of solving this is choosing initial values for the parameters. In the case of study in this project, for the backflow vortex instability, the initialization of the frequency value is chosen as the output of the Bayesian estimator. Then, the parameters are changed in an iterative process:

$$\beta_j \approx \beta_j^{k+1} = \beta_j^k + \Delta\beta_j \qquad 5.5$$

K is defined as an iteration number and the vector $\Delta\beta_j$ is called shift vector. The way of acting is that at each iteration, the model is linearized by first-order Taylor polynomial expansion approximation about β^k.

$$f\,(x_i, \beta) \approx f\left(x_i, \beta^k\right) + \sum_i \frac{\partial f\left(x_i, \beta^k\right)}{\partial \beta_j} \cdot \left(\beta_j - \beta_j^k\right) = f\left(x_i, \beta^k\right) + \sum_j J_{ij} \cdot \Delta\beta_{ij} \qquad 5.6$$

The Jacobian term J is function of constants, independent variables and parameters so it is a term that changes from one iteration to the next one. So, in the linearized model is:

$$\frac{\partial r_i}{\partial \beta_j} = -J_{ij} \qquad 5.7$$

And the residuals are calculated as:

$$\Delta y_i = y_i - f(x_i, \beta^k)$$

$$r_i = y_i - f(x_i, \beta) = y_i - f\left(x_i, \beta^k\right) + \left(f\left(x_i, \beta^k\right) - f(x_i, \beta)\right) \approx \triangle y_i - \sum_{s=1}^{n} J_{is} \triangle \beta_s \qquad 5.8$$

Considering these expressions and substituting into the gradient equations defined previously:

$$-2 \sum_{i=1}^{m} J_{ij} \cdot \left(\Delta y_i - \sum_{s=1}^{n} J_{is} \cdot \Delta\beta_s\right) = 0 \qquad 5.9$$

Rearranging, they become n simultaneous linear equations, called *normal equations*:

$$\sum_{i=1}^{m} \sum_{s=1}^{n} J_{ij} \cdot J_{is} \cdot \Delta\beta_s = \sum_{i=1}^{m} J_{ij} \cdot \Delta y_i \qquad 5.10$$

Or written in matrix notation:

$$\left(\boldsymbol{J^T J}\right) \Delta\boldsymbol{\beta} = \boldsymbol{J^T} \Delta \boldsymbol{y}$$

The steps followed conform the basis of the Gauss-Newton algorithm for a non-linear least squares problem.

In the analysed problem in this project, the code that implement least-square methods uses "Levenberg-Marquadt" algorithm (LMA). The "Levenberg-Marquadt" algorithm interpolates between the Gauss-Newton algorithm (GNA) and the method of gradient descent. The LMA shows a bigger robustness than the GNA, so in many cases, it finds a solution even if it starts far from the final minimum. Besides, it seems to be the algorithm that converges the fastest.

Consistently with standard maximum likelihood estimation approach, the best fit to the theoretical power spectra of pressure fluctuations in the absolute frame have been to the relevant experimental data by minimizing the sum of quadratic deviations of two spectra in the multidimensional space of the adjustable free parameters β:

$$\chi^2(\beta) = \sum_k \left[S_{xx\,exp}(\omega) - S_{xx\,th}(\omega,\beta)\right] \qquad 5.11$$

Considering the pressure perturbation of the backflow vortex instability as: 5.12

$$\hat{p}(R,\omega) = -i\omega\rho\hat{\phi}\,(R,\omega) = \frac{-i\omega\rho\Gamma}{\pi}\sum_{k=1}^{N}\int_{-\infty}^{\infty} tan^{-1}\left[\frac{-a\,\sin\,(\omega_\gamma t + \theta_k)}{R - a\,\mathrm{cps}\,(\omega_\gamma t + \theta_k)}\right]\cdot e^{-i\omega t}dt$$

And adding the frequency broadening filter:

$$\tilde{p} = \int_{-\infty}^{\infty}[\hat{p}(R,\omega)]\,\hat{G}\big(\omega - w,\sigma_g\big)d\omega \qquad 5.13$$

Defining as Γ the vortex intensity, ω_Γ the angular velocity of the vortices, a as the radial position of the vortices and σ_g as the square root of the variance of the Gaussian.

As it was commented before, it is necessary to choose initial values for the parameters, giving a initial state vector that could be expressed as:

$$\beta = \left[\Gamma_0\ \omega_{\gamma 0}\ \ a_0\ \ \sigma_{g0}\right] \qquad 5.14$$

5.1.2. EVALUATION OF THE ERROR

As an advantage of the developed method, it is possible to find the covariance matrix of χ^2 with respect to the vector β as the Equation presented previously. It is based on the standard approximation to the Hessian of a nonlinear least-squares problem used by GNA and LMA.

Considering the non-linear least-square problem in form:

$$\min_{x\in R^n} f(x) = 0.5\cdot\ r_i(x)^2 \qquad 5.15$$

Being the functions r_i (x) the residual between a model function and a measured value.

The value of the gradient of "f", $\nabla f(x)$, can be derived with the chain rule as:

$$\nabla f\ (x) = \nabla r(x)\, r(x) = J(x)^T\, r(x) \qquad 5.16$$

For the Hessian, the chain rule is used again, and it is obtained:

$$\nabla^2 f\ (x) = \nabla r(x)\, \nabla r(x)^T + \sum_{i=1}^{m} r_i(x)\, \nabla^2 r_i\ (x) = J(x)^T \cdot J(x) + Q(x) \qquad 5.17$$

In the case that the residual of the problem is equal to zero, the term Q(x) is small close to the solution.

Being an output of the code the value of the squared 2-norm of the residual at x, the value of the residuals and the Jacobian at the solution; the covariance matrix can be calculated as:

$$D = \widehat{\sigma^2}(\nabla^2 f(x))^{-1} = \hat{\sigma}^2 (J^T J)^{-1} \qquad 5.18$$

The diagonal elements d_{ii} correspond to the variance of the parameter x_i, and the off-diagonal elements d_{ij} correspond to the covariance between parameters x_i and x_j. The term $\hat{\sigma}^2$ is defined as the result of the norm divided by a term "m-n" being m the number of observations and n the number of parameters.

Upon convergence, the principal diagonal elements of the covariance matrix yield the variances of the estimated parameters, so, they can be used to measure how accurate is the identification. When the standard errors of the estimated parameters (ε_i) are obtained, Γ, ω_Γ and a are normalized and the figure of merit is evaluated (ε_{Total}). The figure of merit for the project is the harmonic mean of the relative standard errors:

$$\frac{1}{\varepsilon_{TOT}} = \frac{1}{\varepsilon_\Gamma} + \frac{1}{\varepsilon_{\omega\Gamma}} + \frac{1}{\varepsilon_a} \qquad 5.19$$

There are some considerations to make about the figure of merit. As the pressure transducer is located on the transparent casing defined in Section 3, the distance from the centre of the vortex has a lot of uncertainty, moreover, due to rotating pressure perturbations.

With the figure of merit, tends to mitigate the impact of large outliers and aggravate the impact of the small ones, so the error on the vortex radial distance that has a huge impact is weighted less than the real value in the obtention of the figure of merit.

5.2. Cross-correlation

The initialization of the unstable frequencies of the parameters characterizing the instabilities of interest is a crucial aspect in the convergence of the iterative minimization of χ^2 (β). In order to explain the problem, the identification of a specific form of instability at frequency ω_Γ is carried out by making use of a Bayesian estimator.

The Bayesian estimator consists in minimizing the posterior expected value of a loss function. The prior distribution (p) has been assumed as a true probability distribution:

$$\int p(\theta)\, d\theta = 1 \qquad 5.20$$

By that, the posterior distribution can be defined as:

$$p(\theta|x) = \frac{p(x|\theta)\, p(\theta)}{\int p\,(x|\theta)\, p(\theta)\, d\theta} \qquad 5.21$$

Now, with the Bayesian estimator, the objective is to cross-correlate the experimental power density of auto-correlation and the theoretical.

5.2.1. BAYESIAN ESTIMATOR

The experimental power density of auto-correlation is defined as:

$$S_{xx\,th}(\omega_k) = \frac{1}{n_d \cdot N \cdot \Delta t} \cdot \sum_{i=1}^{n_d} |\tilde{p}(R, \omega)|^2 \qquad 5.22$$

The power density of the cross-correlation between experimental and theoretical spectra for each angular frequency ω_k is defined as:

$$S_{xx\,exp-th} = S_{xx\,exp} \cdot S_{xx\,th} \qquad 5.23$$

Now, the cross-correlation coefficient is introduced and with its value, the most correlated frequency used for the components of the initial state vector for the non-linear least-square method could be indicated.

$$r_{Sexp\,Sth}(\omega_k) = \frac{\int_0^\infty S_{xx\,exp}(\omega)\, S_{xx\,th}(\omega,\, \omega_\Gamma)}{\sqrt{\int_0^\infty S_{xx\,exp}^2\,(\omega)\; d\omega} \cdot \sqrt{\int_0^\infty S_{xx\,th}^2\,(\omega,\, \omega_\Gamma)}} \qquad 5.24$$

It is important to consider that in order to put the theory into practice, as it is not possible to have an infinitesimal frequency resolution, the correlation coefficient is calculated replacing the integrals with summations.

The most significant peak of $r_{Sexp\,Sth}$ as a function of frequency ω provides an effective method for the preliminary identification of the occurrence of the backflow vortex instability. The significance of the peaks can be assessed from the values of $r_{Sexp\,Sth}$. Generally, in order to have a strong correlation between experimental auto-correlation spectrum and theoretical one, the statistical significative value of the correlation coefficient must be higher than 0.7, however it is not an exact value and lower values of correlation coefficients have been considered for the present project.

5.3. Identification procedure review

To identify backflow vortex instability, the procedure followed can be summarised in the following steps:

1. **Creation of the experimental auto-correlation spectrum**: The experimental auto-correlation spectra are created as a function of the clearance, the flow coefficient, the Euler number and the reading of the PCBs.
2. **Analysis of the experimental auto-correlation spectrum**: The variation of the spectrum as a function of the amplitude and reduced frequency (ω/Ω) is studied to analyse if the backflow vortex instability is affecting it. From the spectral analysis applied to pressure signal provided by PCB3 transducer, 60 single-sided Fourier Spectra were obtained, corresponding each of them to a particular value of cavitation number. The frequency domain is numerically a vector of 2048 equally spaced points with extreme values of 0 to 500 Hz.

   In order to simplify, this spectrum is designated as complete experimental auto-correlation pressure spectrum, and it is plotted as a function of the reduced frequency. The minimum value of the reduced frequency is zero because only single-sided spectra were considered. On the other hand, the maximum value is 10 as the maximum value of the frequency is 500 Hz and the rotational speed of the inducer was 50 Hz.

   The backflow vortex instability is very localized in terms of reduced frequency, being the speed of the backflow at maximum equal to the rotational speed of the inducer. So, the maximum intensity of the phenomenon is subsynchronous in any case (ω < Ω).

3. **Cross-correlation through the Bayesian Estimator**: The experimental spectrum obtained is cross-correlated with the theoretical spectrum generated by the backflow vortex instability.

   It is very important to take into account that the predictive model of pressure perturbations is discrete. In fact, only after the number of vortices (N) is chosen, the cross-correlation can be carried out. So, the procedure in the project was to execute multiple cross-correlations.

   The objective is the evaluation of the correlation coefficient $r_{Sexp\,Sth}$ of the experimental pressure power density spectrum with the theoretical spectrum as a function of the reduced frequency. Particularly, the range of frequencies ω_Γ depends on the number of vortices used for carrying out the cross-correlation. In the project, the frequency ω_Γ was adapted to values between 0.03Ω and 0.3Ω.

   Taking this into account, the experimental frequency range used to construct Bayesian estimator is $\omega_i = N \cdot \omega_\Gamma$ being N the number of vortices.

4. **Parametric identification and error evaluation**: The maximum likelihood parametric identification of the backflow vortex instability in the proximity of the most correlated frequency ω_i is accomplished through the non-linear least-squares method. As outputs result the estimate of the parametric vector and the standard errors. The parametric vector concerning the backflow vortex instability is composed of four elements: vortex intensity (Γ), vortex angular velocity (ω_Γ), vortex radial position (a), and variance of

gaussian distribution used for broadening the frequency ($\hat{\sigma}_g$). To estimate the accuracy of the estimation of each parameter, the standard errors are used.

The results from identifications are compared in terms of the calculated value of the figure of merit ε_{Total}. For computing the figure of merit, the standard errors have been normalized, defined as the ratio between the standard deviation and some normalization constant. By that, the normalized standard error is expressed in relation to the parameters characterizing the problem:

$$\begin{aligned} \varepsilon_\Gamma &= \frac{d_{11}}{2\pi\Omega r_T^2/N} \\ \varepsilon_{\omega\Gamma} &= \frac{d_{22}}{\Omega} \\ \varepsilon_a &= \frac{d_{33}}{r_T} \end{aligned} \qquad 5.25$$

Normalization constants chosen for d_{22} and d_{33} are the errors relative to a rotation measurement and a position measurement respectively. For the first normalization constant, it is more complicated. In potential flow of a fluid with a region of vorticity, all closed curves that enclose the vorticity have the same circulation value, the normalization constant chosen is the circulation about the closed circle that is described by the tip radius and related to the number of vortices. The circulation is defined as:

$$\Gamma = \int_A w \cdot n \, dA = \int_c u \, dS = \int_0^{2\pi} \Omega \cdot r_T^2 \, d\lambda = 2\Omega\pi r_T^2 \qquad 5.26$$

Being w the vorticity vector, n a normal vector to the surface A, formed by taking a cross-section of the vortex-tube with elemental area dA, u the velocity vector on the closed curve c, bounding the surface A. Finally, the error relating to the variance of the frequency broadening is not considered in the figure of merit.

6. Evaluation

The objective of this chapter is the illustration of the analytical results of the predictive backflow vortex instability due to cavitation in the used inducers that were detailed previously. The results obtained of the identifications of the pressure oscillations have been done for different flow conditions in each case. In total there are 11 cases divided by: 2 flow coefficients studied in DAPAMITO 3 inducer with low clearance and 3 with high clearance; 3 cases studied in the DAPAMITO 4 inducer; and 3 different configurations in the RAPDUD inducer. Carrying out these identifications, it is studied the effect of the clearance and the flow coefficient in the obtained results. Also, each studied configuration has been analysed for several fixed Euler number values, representing in this case only 3 Euler numbers for each configuration. However, in the identification process of the present thesis many more cases have been studied shifting the Euler number. Those cases are not explained in detail here because the basis of the analysis is the same. However, a Table with the choice for each situation can be seen for each of the presented identifications.

Thus, the organization of this Section is to explain how the results are organized and then present the results obtained for some fixed Euler numbers in the studied cases for each inducer.

6.1. Organization of results

There are some Figures and some Tables for each studied case. For a value of clearance and flow coefficient, a Table with all the set of Euler numbers and the choice of the number of vortices minimizing the figure of merit is presented giving a general review of the studied configuration. Then, the attention is fixed in some values of Euler numbers arbitrarily chosen, in which, the analysis is presented in detail, presenting the experimental auto-correlation pressure spectrum, the comparison between the experimental auto-correlation spectrum and the full theoretical one and the full theoretical auto-correlation pressure spectrum. These Figures are referenced to the number of vortices chosen because the figure of merit is the minimum from all the studied cases. Also, a Figure representing the evolution of the figure of merit with the number of vortices is presented. Finally, a Table representing for each number of cells, the reduced frequency obtained as the Bayes Estimator output, the figure of merit and the identified parameters $\boldsymbol{\Gamma}$, $\boldsymbol{\alpha}$, and $\boldsymbol{\sigma_g}$, highlighting the choice of the number of cells based on the minimum figure of merit.

6.2. DAPAMITO 3

6.2.1. $\Phi = \Phi_D$ AND CLEARANCE = 2 MM.

Firstly, it is important to comment that, in the case that in the cross-correlation there are several peaks to consider, because the correlation coefficient has been interpreted as high enough comparing to the rest of the peaks, every one of them have been analysed, obtaining the figure of merit of each one of them. Finally, it has been chosen the minimum figure of merit from the results obtained for each Euler number studied.

In this case, it is presented in Table 6.1, the 11 different Euler numbers studied with the number of vortices that has resulted as the minimum figure of merit.

σ	N	ω/Ω	ε_{TOT}	Γ	ω_γ [rad/s]	a (%R)	σ_g
0.1309	7	0.141602	8.02E-5	0.01812	44.53	0.66712	0.19948
0.1423	7	0.0488281	1.25E-4	0.02342	15.36	0.71482	0.199
0.1842	3	0.13916	1.58E-4	0.00474	43.76	0.74793	0.20027
0.214	9	0.0415039	3.19E-5	0.02366	13.05	0.83281	0.19911
0.2282	9	0.0439453	6.47E-5	0.02709	13.82	0.77551	0.19859
0.2377	3	0.158691	1.30E-4	0.00138	49.91	0.96797	0.20078
0.2482	7	0.0683594	1.27E-4	0.02755	21.50	0.66613	0.19856
0.2629	9	0.131836	4.64E-5	0.02172	41.46	0.70818	0.19917
0.2709	10	0.0463867	6.90E-5	0.03328	14.59	0.75115	0.19779
0.2825	10	0.0463867	4.84E-5	0.03153	14.59	0.76464	0.19809
0.2969	7	0.109863	1.23E-4	0.02689	34.55	0.61701	0.1988

TABLE 6.1: IDENTIFICATION ASSESSMENT ASSOCIATED WITH BACKFLOW INSTABILITIES ON DAPAMITO 3 INDUCER, DESIGN FLOW COEFFICIENT AND HIGH CLEARANCE

Now, in order to clarify the process, some of the Euler numbers selected are explained in detail but it is important to consider that the process have been done for every Euler number presented in Table 6.1.

For the waterfall plot obtained, taking a line with a fixed flow coefficient corresponds to a value of the Euler number. So, the procedure followed was to get the auto-spectrum to study by fixing an Euler number.

- **σ = 0.1423**

The experimental power density of the auto-correlation in this case is represented in Figure 6.1.

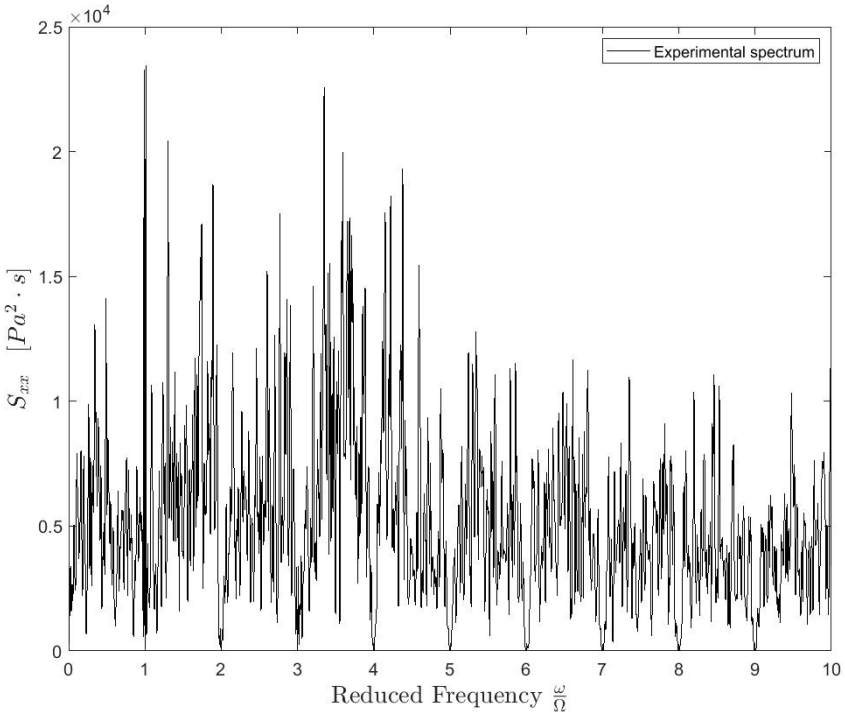

FIGURE 6.1: EXPERIMENTAL AUTO-CORRELATION PRESSURE SPECTRUM FOR DAPAMITO 3 WITH Φ = Φ_D, EULER NUMBER = 0.1423 AND CLEARANCE = 2 MM.

The spectrum is filtered from the blade passage frequencies by the application of a notch filter. The reason why the filter has been applied is because the amplitude of these phenomena is very high and makes impossible to see the presence of lower spectrum amplitude related to other phenomena. Based on the characteristics of the different cavitation-induced flow instabilities, the studied phenomenon that can be seen is a rotating phenomenon evident with strongly cavitating regime and with minimum four lobes.

Taking into account that for the cross-correlation of two transducer for studying the number of lobes, if the angular separation is 45º, phenomena with more than four lobes can not be differentiated. The solution is to space PCBs with an angular separation not equal to a constant value of 45º.

From the auto-spectrum, the $\omega_{\Gamma 0}$ is calculated by the Bayesian estimator However, the final output is not straight-forward. The model is discrete, so for each case there are several cross-correlations. Since the backflow is a non-linear, unsteady phenomenon extremely simplified in this project, for a certain number of vortices is possible that the correlation is not sufficient. On the other hand, if it is well cross-correlated, the model is extremely powerful predicting the backflow vortex phenomenon. Also, during the identification process, it has been seen that the correlation peaks in terms of the correlation coefficient tend to be much more pronounced while the range of the frequency ω_{Γ} is between 0.03Ω and 0.3Ω, so the model increases its reliability. Then, the output of the Bayesian estimator for N = 7 vortices is obtained, the chosen N for the studied case as will be seen in Table 6.2. Knowing $\omega_{\gamma 0}$ for a fixed number of vortices, the identifications are processed. As output, it can be found the estimation of the parameters and the figure of merit.

In Figure 6.2, the full theoretical auto-correlation pressure spectrum for the studied case with 7 vortices is presented.

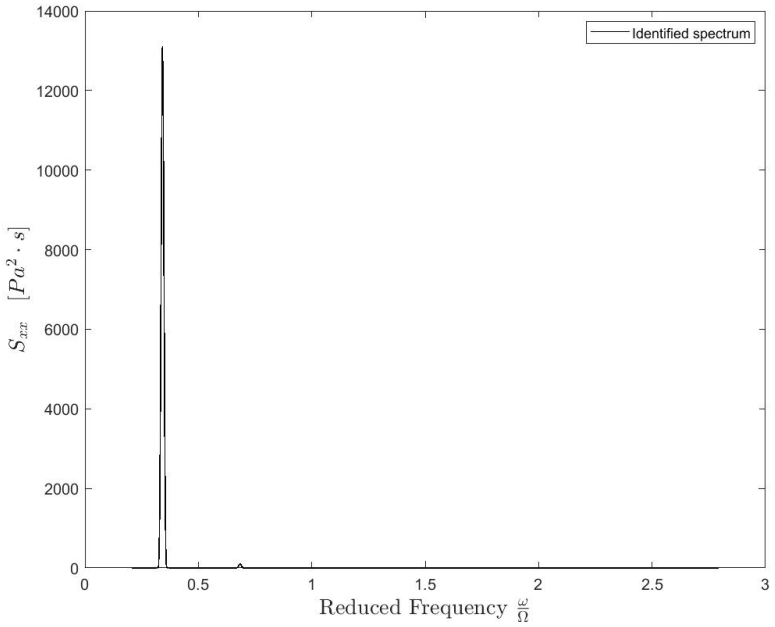

FIGURE 6.2: FULL-THEORETICAL AUTO-CORRELATION PRESSURE SPECTRUM FOR DAPAMITO 3 WITH $\Phi = \Phi_D$, EULER NUMBER = 0.1423, N = 7 VORTICES AND CLEARANCE = 2 MM.

The comparison between the experimental auto-correlation pressure spectrum and the full-theoretical auto-correlation pressure spectrum is shown in Figure 6.3:

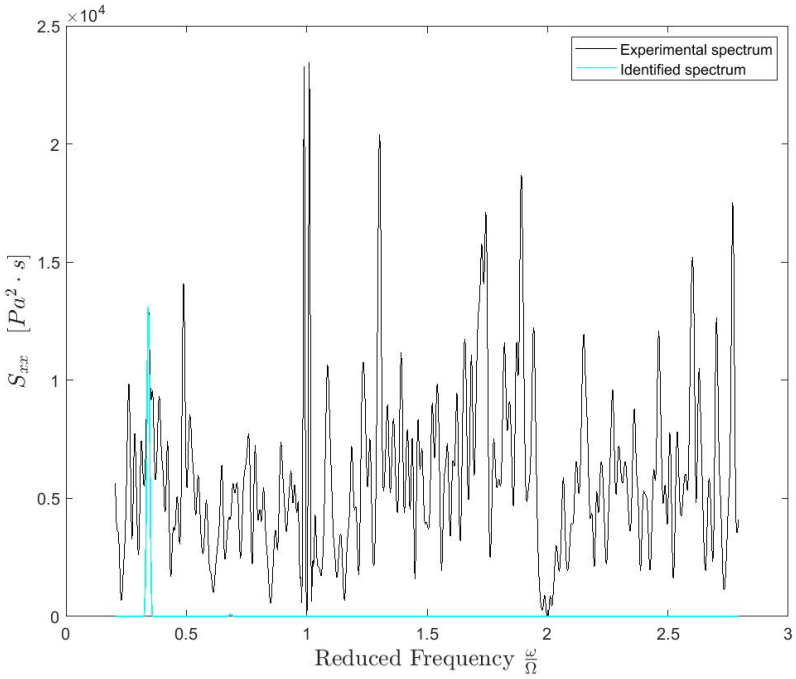

FIGURE 6.3: COMPARISON BETWEEN EXPERIMENTAL AUTO-CORRELATION SPECTRUM AND FULL-THEORETICAL SPECTRUM FOR DAPAMITO 3 WITH $\Phi = \Phi_D$, EULER NUMBER = 0.1423, N = 7 VORTICES AND CLEARANCE = 2 MM.

Choosing the case with the lowest figure of merit (in this case was N=7 vortices), the needed parameters are obtained as represented in Table 6.1. The existence of minimum four rotating phenomena is theoretically confirmed but also, the number of lobes characterizing the phenomenon is also studied. In Figure 6.4, it is represented the variation of the figure of merit with the number of vortices studied. It is important to consider that some values of the number of vortices are repeated due to the fact commented previously (if there are several important intensities for the number of vortices studied, each one of them will be studied and analysed). As there are several peaks of the correlation coefficient bigger than the rest, all of them have been studied obtaining the correspondent figure of merit. It is important to consider that the number of vortices in the extremes are the limits in which correlation can be found. With a number of vortices lower than 3 or bigger than 7 in this case, there is a no-correlation zone, so it is not represented in the Figure.

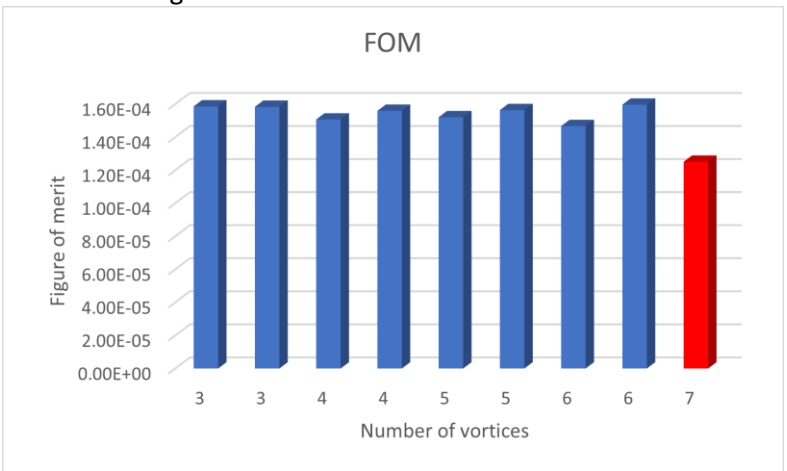

FIGURE 6.4: EVALUATION OF THE FIGURE OF MERIT WITH RESPECT TO THE NUMBER OF VORTICES FOR DAPAMITO 3 WITH $\Phi = \Phi_D$, EULER NUMBER = 0.1423 AND CLEARANCE = 2 MM.

Finally, in Table 6.2, it is presented the identification assessment associated with backflow vortex instability for the different number of vortices that have been studied in this case.

N	ω/Ω	ε_{TOT}	Γ	ω_γ [rad/s]	a (%R)	σ_g
3	0.114746	1.59E-04	0.01485	36.09	0.53183	0.19974
3	0.163574	1.58E-04	0.00552	51.44	0.65636	0.2002
4	0.0854492	1.51E-04	0.02569	26.87	0.54302	0.199
4	0.12207	1.56E-04	0.0235	38.39	0.506	0.19933
5	0.0683594	1.52E-04	0.02212	21.50	0.63182	0.19916
5	0.0976562	1.56E-04	0.02249	30.71	0.58478	0.19916
6	0.0585937	1.47E-04	0.03538	18.43	0.62252	0.19764
6	0.0805664	1.60E-04	0.03408	25.34	0.59019	0.19814
7	0.0488281	1.25E-04	0.02342±4.42	15.36±1.25E-4	0.71482±0.58	0.199

TABLE 6.2: IDENTIFICATION ASSESSMENT ASSOCIATED WITH BACKFLOW INSTABILITIES ON DAPAMITO 3 INDUCER, DESIGN FLOW COEFFICIENT, EULER NUMBER = 0.1423 AND HIGH CLEARANCE

- **σ = 0.2282**

The explanation developed in the previous reported case are the same than for this case. The only variation is the Euler number, so there is another auto-spectrum to study following the same procedure studied before. Firstly, in Figure 6.5, it is shown the experimental auto-correlation pressure spectrum.

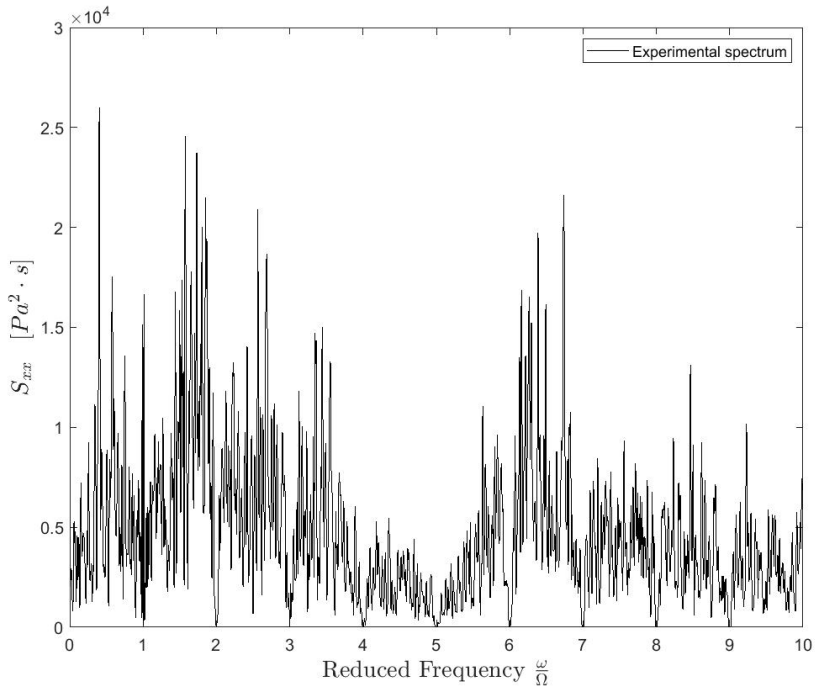

FIGURE 6.5: EXPERIMENTAL AUTO-CORRELATION PRESSURE SPECTRUM FOR DAPAMITO 3 WITH Φ = Φ_D, EULER NUMBER = 0.2282 AND CLEARANCE = 2 MM.

Now, in Figures 6.6 and 6.7, it is represented the full theoretical auto-correlation and the comparison between experimental and theoretical auto-correlations for the studied configuration:

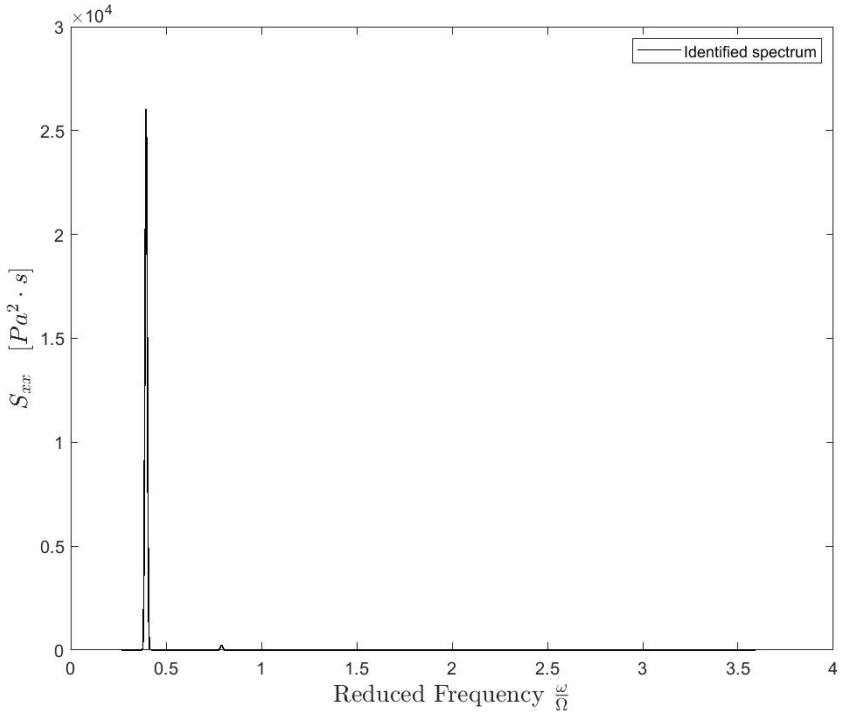

FIGURE 6.6: FULL-THEORETICAL AUTO-CORRELATION PRESSURE SPECTRUM FOR DAPAMITO 3 WITH $\Phi = \Phi_D$, EULER NUMBER = 0.2282, N = 9 VORTICES AND CLEARANCE = 2 MM.

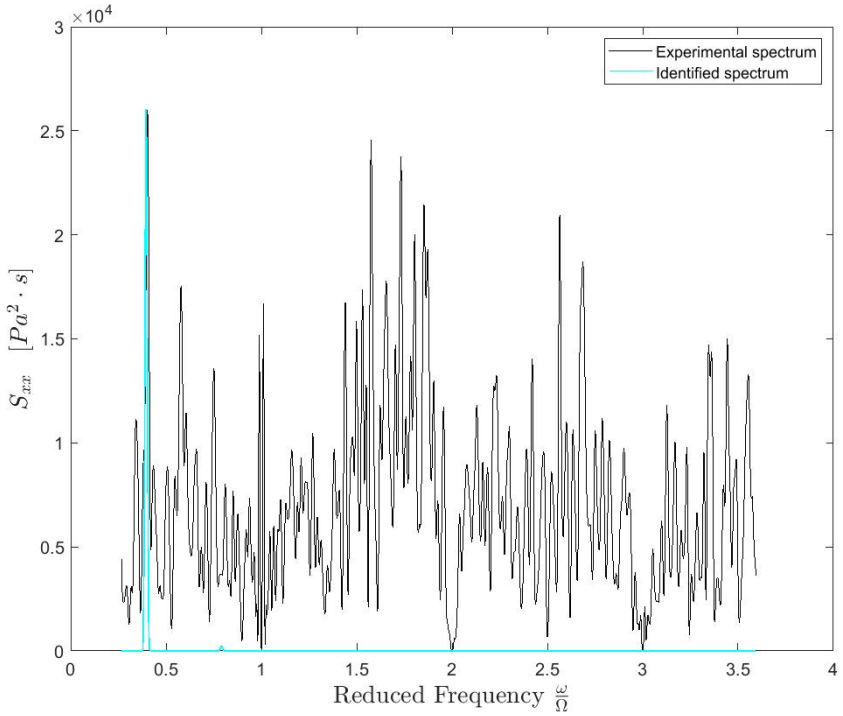

FIGURE 6.7: COMPARISON BETWEEN EXPERIMENTAL AUTO-CORRELATION SPECTRUM AND FULL-THEORETICAL SPECTRUM FOR DAPAMITO 3 WITH $\Phi = \Phi_D$, EULER NUMBER = 0.2282, N = 9 VORTICES AND CLEARANCE = 2 MM.

In Figure 6.8, the evolution of the figure of merit with the number of vortices that have been analysed is presented:

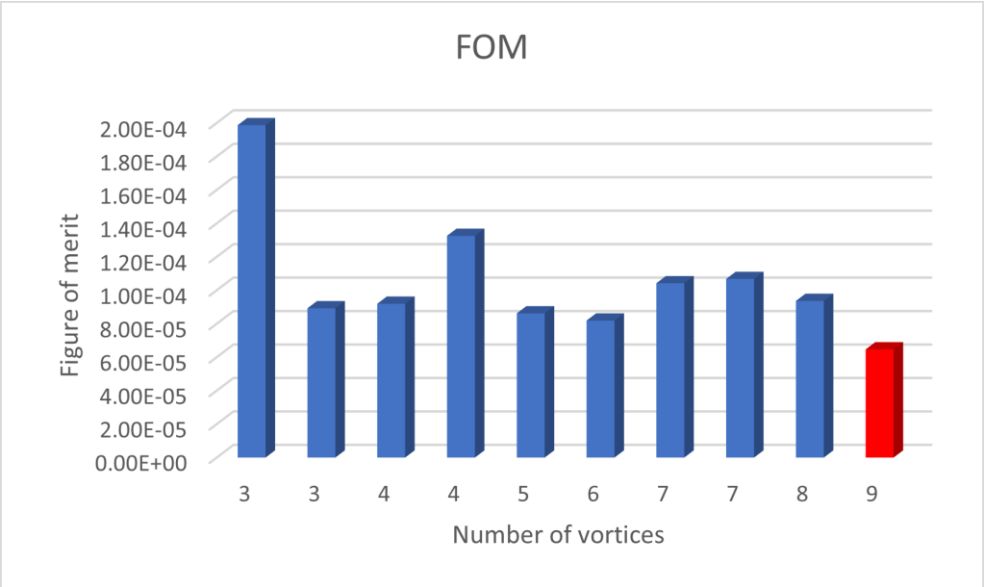

FIGURE 6.8: EVALUATION OF THE FIGURE OF MERIT WITH RESPECT TO THE NUMBER OF VORTICES FOR DAPAMITO 3 WITH $\Phi = \Phi_D$, EULER NUMBER = 0.2282 AND CLEARANCE = 2 MM.

Finally, the Table 6.3 presents the identification assessment associated with backflow vortex instability for the different number of vortices that have been studied in this case.

N	ω/Ω	ε_{TOT}	Γ	ω_γ [rad/s]	a (%R)	σ_g
3	0.114746	1.99E-04	0.01738	36.09	0.50	0.19964
3	0.134277	8.92E-05	0.01894	42.23	0.51925	0.19952
4	0.100098	9.19E-05	0.02231	31.48	0.58596	0.19916
4	0.144043	1.33E-04	0.01666	45.30	0.55227	0.19963
5	0.0805664	8.62E-05	0.03191	25.34	0.61249	0.19813
6	0.065918	8.19E-05	0.04533	20.73	0.62543	0.19659
7	0.0585937	1.04E-04	0.03511	18.43	0.67596	0.19762
7	0.0830078	1.07E-04	0.02848	26.11	0.66212	0.19855
8	0.0512695	9.36E-05	0.03791	16.12	0.70314	0.1973
9	0.0439453	6.47E-05	0.02709±4.49	13.82±6.47E-5	0.77551±0.29	0.19859

TABLE 6.3: IDENTIFICATION ASSESSMENT ASSOCIATED WITH BACKFLOW INSTABILITIES ON DAPAMITO 3 INDUCER, DESIGN FLOW COEFFICIENT, EULER NUMBER = 0.2282 AND HIGH CLEARANCE

- **σ = 0.2825**

Following the same procedure as in the previous case, the representative Figures and Tables characterizing this configuration are presented. In Figure 6.9 it can be seen the experimental power density of auto-correlation for the analysed case.

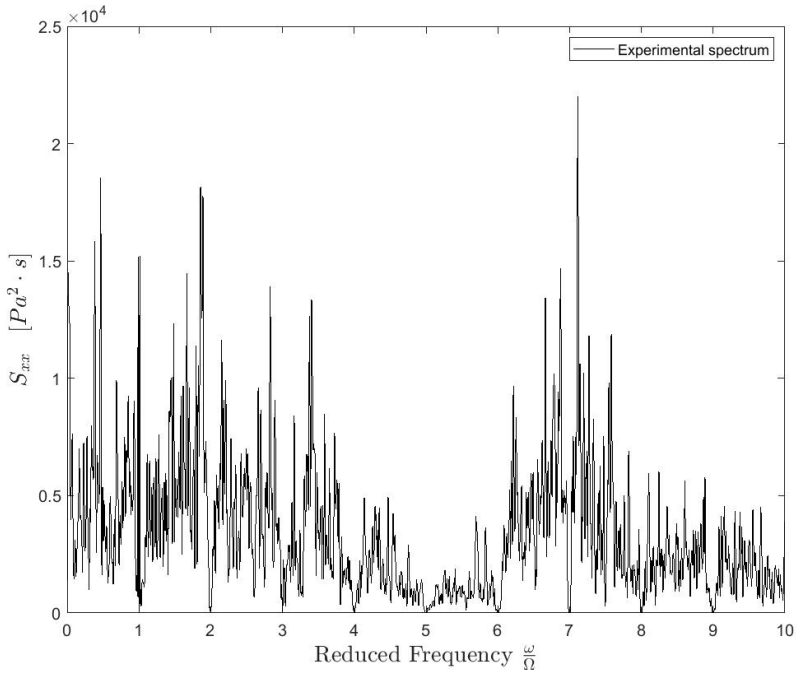

FIGURE 6.9: EXPERIMENTAL AUTO-CORRELATION PRESSURE SPECTRUM FOR DAPAMITO 3 WITH Φ = Φ_D, EULER NUMBER = 0.2825 AND CLEARANCE = 2 MM.

In Figures 6.10 and 6.11, it is represented respectively he full theoretical auto-correlation pressure spectrum for the number of vortices in this case (N= 10) and the comparison between experimental and full-theoretical auto-correlation. It can be observed that the peak of the identified spectrum and the experimental spectrum coincides, indicating the strength of this tool for identifying backflow vortex instability.

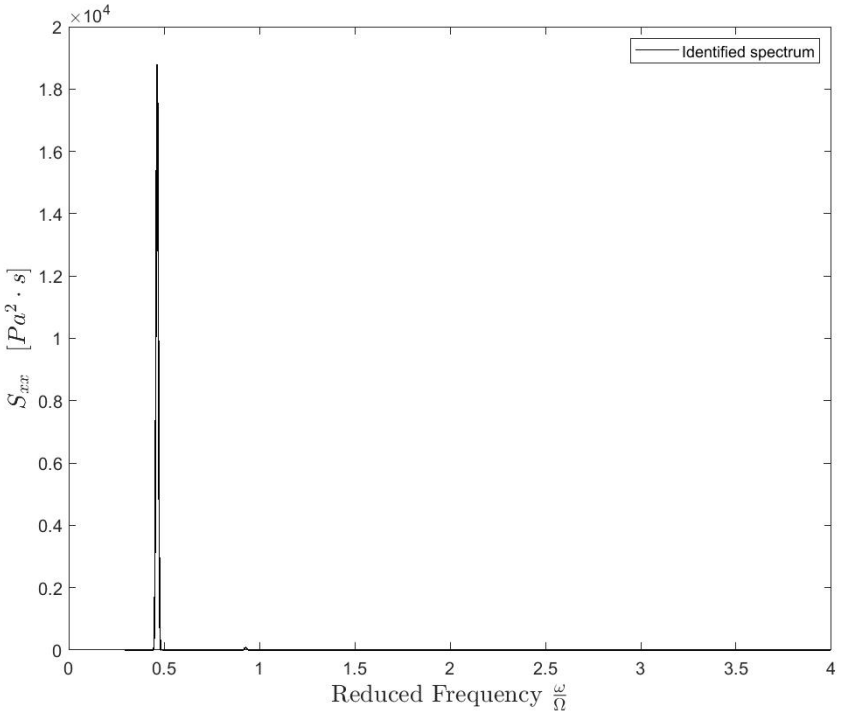

FIGURE 6.10: FULL-THEORETICAL AUTO-CORRELATION PRESSURE SPECTRUM FOR DAPAMITO 3 WITH Φ = Φ_D, EULER NUMBER = 0.2825, N = 10 VORTICES AND CLEARANCE = 2 MM.

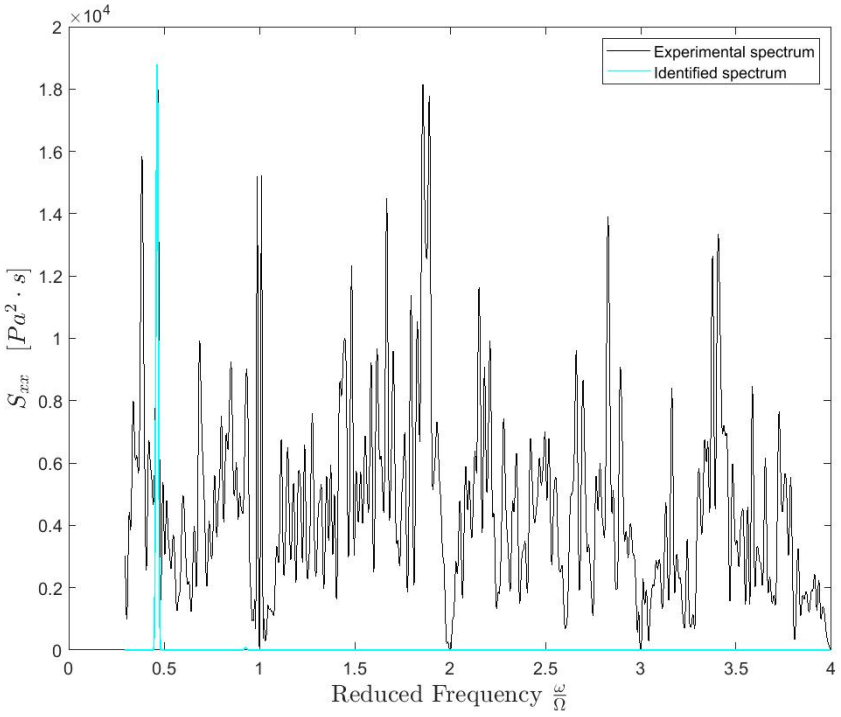

FIGURE 6.11: COMPARISON BETWEEN EXPERIMENTAL AUTO-CORRELATION SPECTRUM AND FULL-THEORETICAL SPECTRUM FOR DAPAMITO 3 WITH Φ = Φ_D, EULER NUMBER = 0.2825, N = 10 VORTICES AND CLEARANCE = 2 MM.

Finally, for a quantitative summary of this studied case, it is represented in Figure 6.12 the evolution of the figure of merit with the number of vortices analysed and in Table 6.4 the parameters obtained for each studied case, highlighting the selected as reference due to the low figure of merit value.

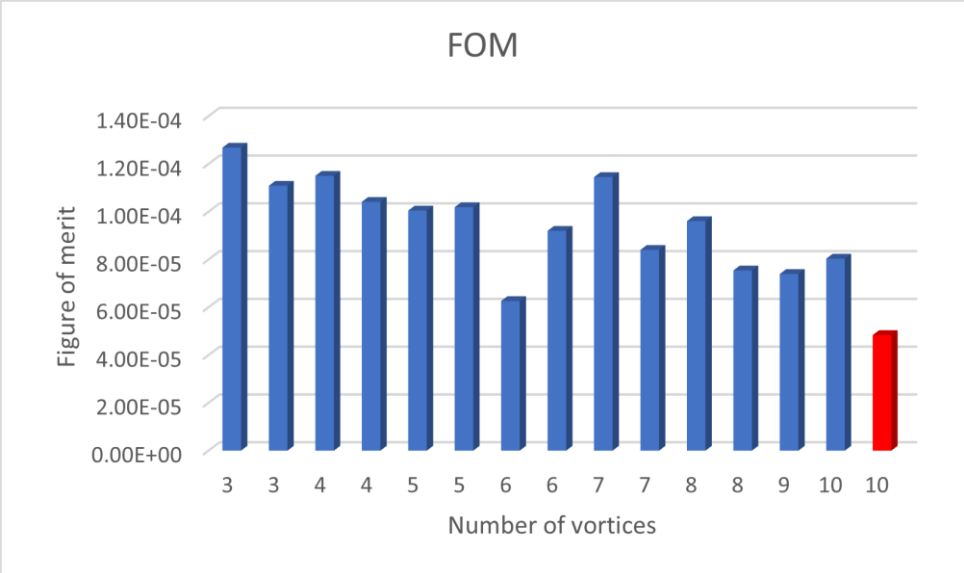

FIGURE 6.12: EVALUATION OF THE FIGURE OF MERIT WITH RESPECT TO THE NUMBER OF VORTICES FOR DAPAMITO 3 WITH Φ = Φ_D, EULER NUMBER = 0.2825 AND CLEARANCE = 2 MM.

N	ω/Ω	ε_{TOT}	Γ	ω_γ [rad/s]	a (%R)	σ_g
3	0.126953	1.27E-04	0.01474	39.93	0.52644	0.19975
3	0.15625	1.11E-04	0.00755	49.14	0.6259	0.20016
4	0.0952148	1.15E-04	0.02835	29.95	0.52391	0.19988
4	0.117187	1.04E-04	0.0281	36.86	0.050438	0.19912
5	0.0756836	1.00E-04	0.0216	23.80	0.64062	0.19926
5	0.0927734	1.02E-04	0.02667	29.18	0.58781	0.19875
6	0.0634766	6.26E-05	0.03172	19.96	0.6656	0.19836
6	0.078125	9.20E-05	0.04534	24.57	0.58518	0.19672
7	0.0537109	1.15E-04	0.02678	16.89	0.68854	0.19865
7	0.065918	8.40E-05	0.02555	20.73	0.68785	0.19876
8	0.0488281	9.61E-05	0.02831	15.36	0.71655	0.19851
8	0.0585937	7.54E-05	0.03581	18.43	0.68984	0.19773
9	0.0512695	7.40E-05	0.02466	16.12	0.74953	0.19887
10	0.0390625	8.04E-05	0.02237	12.29	0.78562	0.19917
10	0.0463867	4.84E-05	0.03153±4.99	14.59±4.84E-5	0.76464±0.47	0.19809

TABLE 6.4: IDENTIFICATION ASSESSMENT ASSOCIATED WITH BACKFLOW INSTABILITIES ON DAPAMITO 3 INDUCER, DESIGN FLOW COEFFICIENT, EULER NUMBER = 0.2825 AND HIGH CLEARANCE

6.2.2. $\Phi = 0.9 \cdot \Phi_D$ AND CLEARANCE = 2 MM.

The next studied case is for the same inducer, maintaining the value of the clearance but changing the flow coefficient. Also, in this case 3 Euler numbers are presented but for all the studied cases, the choice for each Euler number is presented in Table 6.5, together with the parameters obtained for each one of them. The main idea in this evaluation is to apply a comparison between cases with different clearances and similar Euler numbers (as it will be seen in Subsubsection 6.2.3 with respect to this one). Also, another comparison, that can be seen in this particular case, is to study with the same clearance, a more loaded inducer, so the intensity of the searched instability is greater than in the previous case.

σ	N	ω/Ω	ε_{TOT}	Γ	ω_γ [rad/s]	a (%R)	σ_g
0.1313	6	0.0366211	7.42E-05	0.03264	11.52	0.83992	0.1978
0.1425	7	0.0317383	4.85E-05	0.03508	9.98	0.87137	0.19762
0.1835	5	0.0317383	6.30E-05	0.04588	9.98	0.82729	0.19554
0.2127	6	0.0341797	7.18E-05	0.0354	10.75	0.8332	0.1975
0.2265	9	0.0463867	4.32E-05	0.02989	14.59	0.83948	0.19818
0.2379	9	0.0366211	5.48E-05	0.03437	11.52	0.83867	0.1979
0.2499	8	0.0463867	4.32E-05	0.03591	14.59	0.81843	0.19738
0.2628	9	0.0463867	4.67E-05	0.03164	14.59	0.8261	0.19798
0.2700	9	0.0415039	5.65E-05	0.03697	13.05	0.80616	0.1973
0.2834	6	0.0463867	6.53E-05	0.02933	14.59	0.80634	0.19836
0.2965	7	0.0585937	4.40E-05	0.0315	18.43	0.80133	0.19799

TABLE 6.5: IDENTIFICATION ASSESSMENT ASSOCIATED WITH BACKFLOW INSTABILITIES ON DAPAMITO 3 INDUCER, 90% OF DESIGN FLOW COEFFICIENT AND HIGH CLEARANCE

- **σ = 0.1425**

The small differences between the Euler number values for which the phenomenon has been studied could be related to the averages carried out over a certain period of time made to obtain the different rows of the waterfall plot. As in previous cases, in Figure 6.13 it can be seen the experimental power density of auto-correlation for σ = 0.1425 at $\phi = 0.9 \cdot \phi_D$.

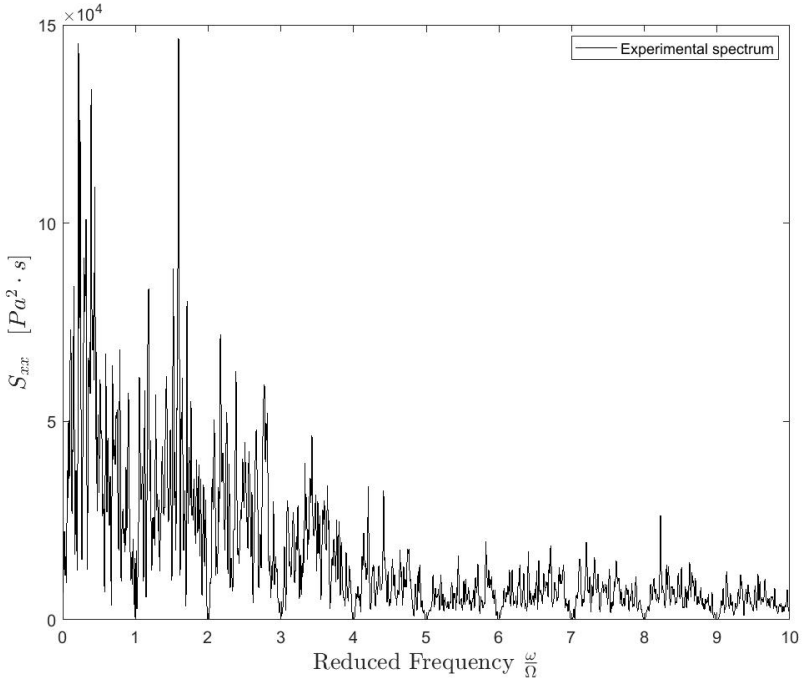

FIGURE 6.13: EXPERIMENTAL AUTO-CORRELATION PRESSURE SPECTRUM FOR DAPAMITO 3 WITH Φ =0.9 Φ_D, EULER NUMBER = 0.1425 AND CLEARANCE = 2 MM.

In Figure 6.14 the theoretical auto-correlation and finally in Figure 6.15 the comparison between experimental and full-theoretical auto-correlation spectrum identified.

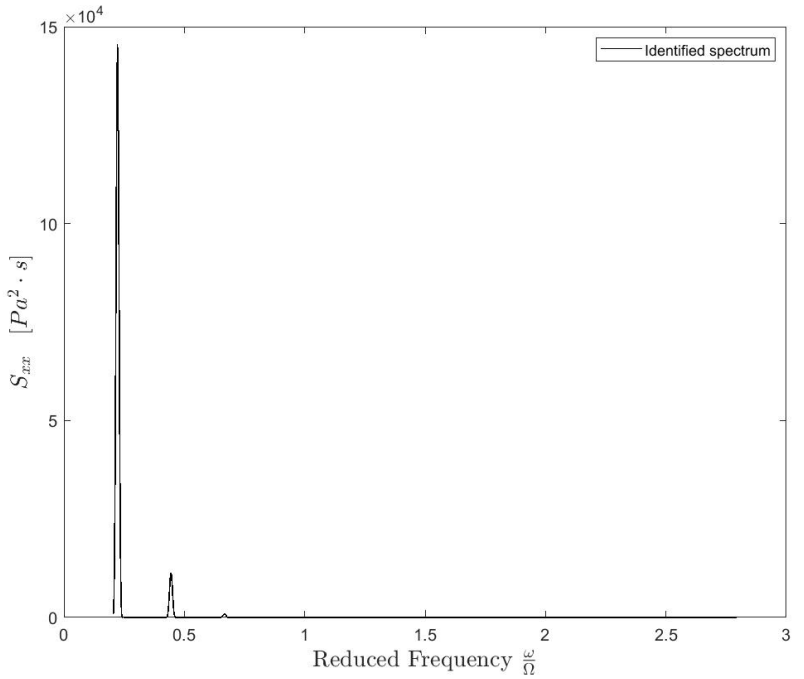

FIGURE 6.14: FULL-THEORETICAL AUTO-CORRELATION PRESSURE SPECTRUM FOR DAPAMITO 3 WITH Φ = 0.9 Φ_D, EULER NUMBER = 0.1425, N = 7 VORTICES AND CLEARANCE = 2 MM.

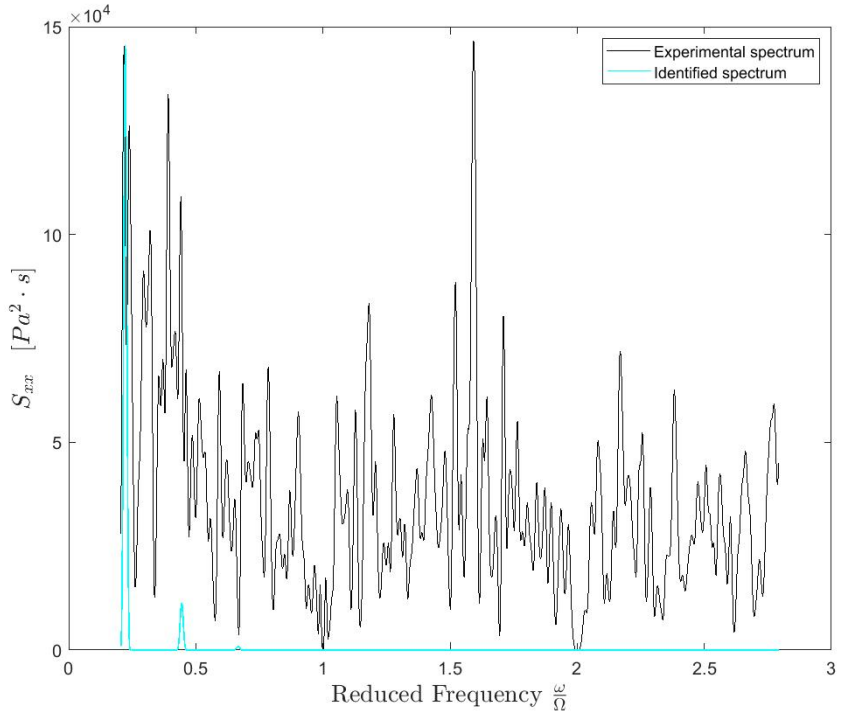

FIGURE 6.15: COMPARISON BETWEEN EXPERIMENTAL AUTO-CORRELATION SPECTRUM AND FULL-THEORETICAL SPECTRUM FOR DAPAMITO 3 WITH $\Phi = 0.9\ \Phi_D$, EULER NUMBER = 0.1425, N = 7 VORTICES AND CLEARANCE = 2 MM.

The evolution of the figure of merit with the different number of vortices and the correlation coefficients studied is presented on Figure 6.16, marking as red the figure of merit of the evaluated case.

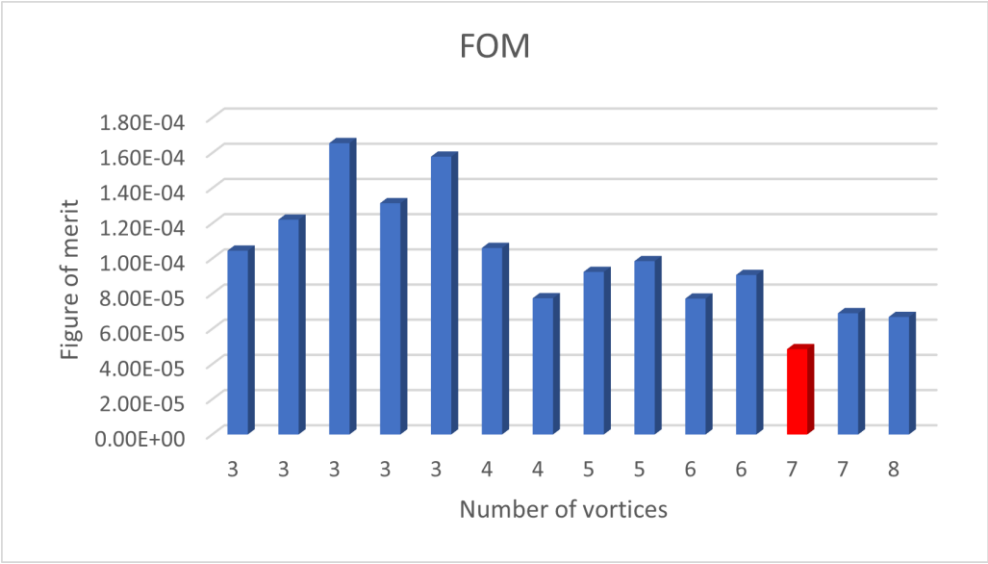

FIGURE 6.16: EVALUATION OF THE FIGURE OF MERIT WITH RESPECT TO THE NUMBER OF VORTICES FOR DAPAMITO 3 WITH $\Phi = 0.9\ \Phi_D$, EULER NUMBER = 0.1425 AND CLEARANCE = 2 MM.

Finally, a quantitative summary of the simulations is presented in Table 6.6.

N	ω/Ω	ε_{TOT}	Γ	ω_γ [rad/s]	a (%R)	σ_g
3	0.0732422	1.04E-04	0.04708	23.03	0.64116	0.19658
3	0.078125	1.22E-04	0.04701	24.57	0.61309	0.19668
3	0.10498	1.66E-04	0.03059	33.02	0.61196	0.19827
3	0.131836	1.31E-04	0.02562	41.46	0.62461	0.19893
3	0.146484	1.58E-04	0.02396	46.07	0.59994	0.19907
4	0.0537109	1.06E-04	0.02973	16.89	0.78765	0.19845
4	0.0976562	7.74E-05	0.03988	30.71	0.65956	0.19745
5	0.0439453	9.24E-05	0.03937	13.82	0.77786	0.19727
5	0.078125	9.85E-05	0.02741	24.57	0.74253	0.19864
6	0.0366211	7.72E-05	0.03506	11.52	0.82915	0.19756
6	0.065918	9.07E-05	0.03445	20.73	0.74595	0.1978
7	0.0317383	4.85E-05	0.03508±2.91	9.98±4.86E-5	0.87137±0.017	0.19762
7	0.0561523	6.89E-05	0.02842	17.66	0.8096	0.19841
8	0.0488281	6.68E-05	0.03242	15.36	0.81206	0.19788

TABLE 6.6: IDENTIFICATION ASSESSMENT ASSOCIATED WITH BACKFLOW INSTABILITIES ON DAPAMITO 3 INDUCER, 90% OF DESIGN FLOW COEFFICIENT, EULER NUMBER = 0.1425 AND HIGH CLEARANCE

- **σ = 0.2127**

For this case, also it has been analysed the Euler numbers of σ = 0.2127 and σ = 0.2834, organizing the information as in the commented case, so the different Figures obtained as result of each case are presented, together with the quantitative summary in form of Table of the Euler numbers studied.

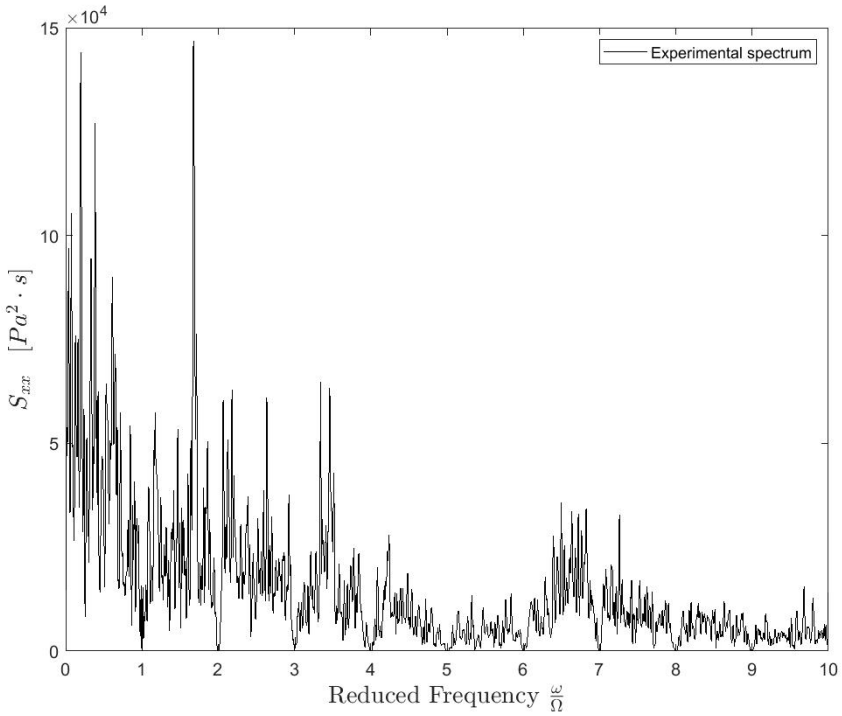

FIGURE 6.17: EXPERIMENTAL AUTO-CORRELATION PRESSURE SPECTRUM FOR DAPAMITO 3 WITH Φ =0.9 Φ_D, EULER NUMBER = 0.2127 AND CLEARANCE = 2 MM.

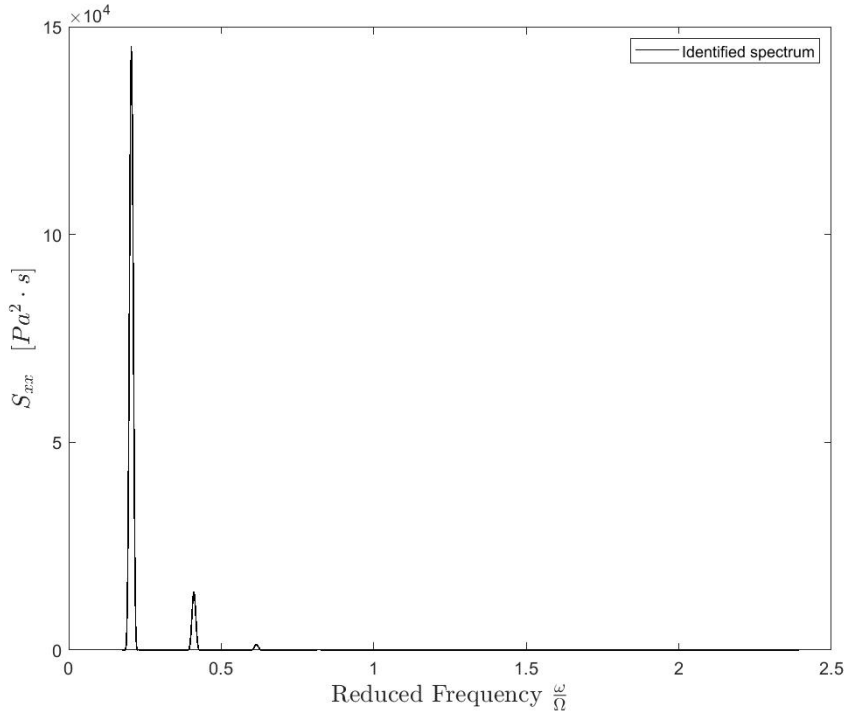

FIGURE 6.18: FULL-THEORETICAL AUTO-CORRELATION PRESSURE SPECTRUM FOR DAPAMITO 3 WITH $\Phi = 0.9\ \Phi_D$, EULER NUMBER = 0.2127, N = 6 VORTICES AND CLEARANCE = 2 MM.

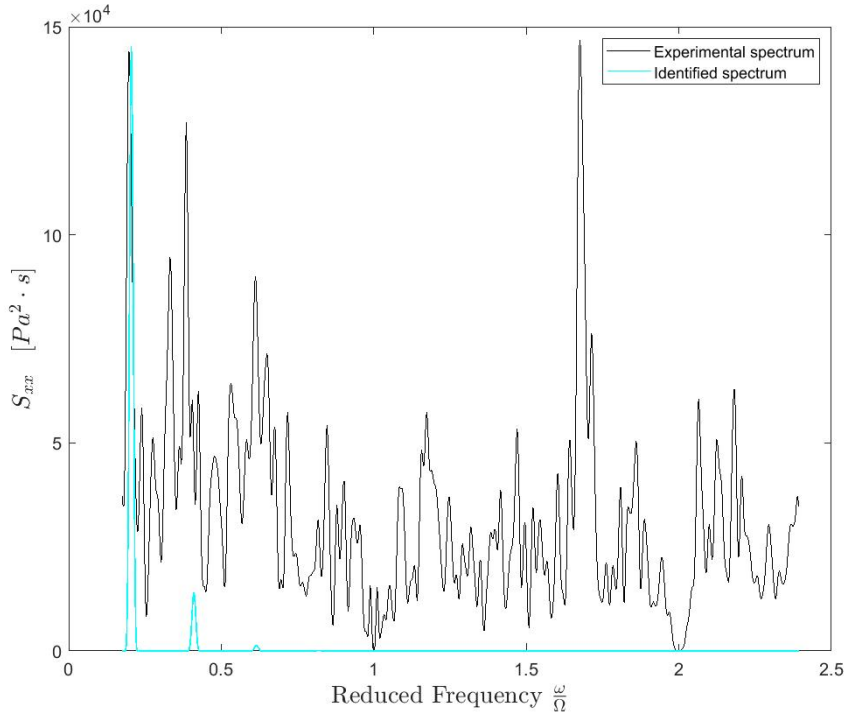

FIGURE 6.19: COMPARISON BETWEEN EXPERIMENTAL AUTO-CORRELATION SPECTRUM AND FULL-THEORETICAL SPECTRUM FOR DAPAMITO 3 WITH $\Phi = 0.9\ \Phi_D$, EULER NUMBER = 0.2127, N = 6 VORTICES AND CLEARANCE = 2 MM.

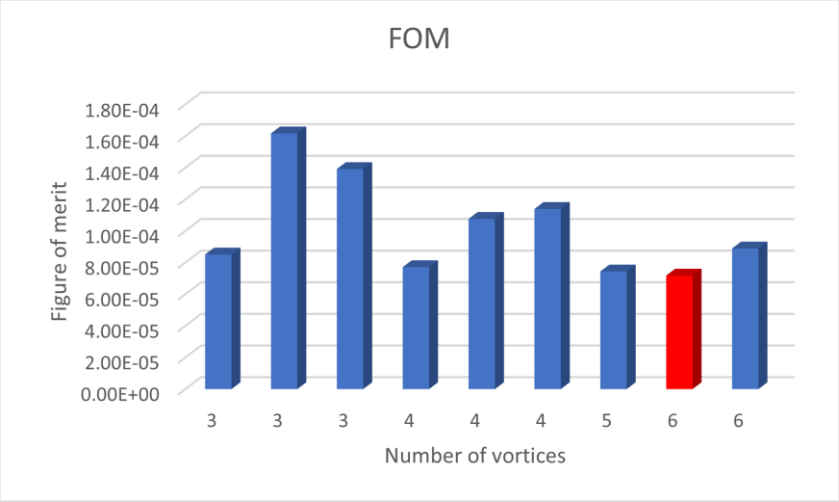

FIGURE 6.20: EVALUATION OF THE FIGURE OF MERIT WITH RESPECT TO THE NUMBER OF VORTICES FOR DAPAMITO 3 WITH Φ =0.9 Φ_D, EULER NUMBER = 0.2127 AND CLEARANCE = 2 MM.

N	ω/Ω	ε_{TOT}	Γ	ω_γ [rad/s]	a (%R)	σ_g
3	0.065918	8.51E-05	0.04587	20.73	0.67604	0.19662
3	0.109863	1.62E-04	0.02904	34.55	0.60465	0.19845
3	0.129395	1.39E-04	0.02515	40.69	0.61495	0.19894
4	0.0488281	7.71E-05	0.03793	15.36	0.76964	0.19733
4	0.0830078	1.08E-04	0.03561	26.11	0.66333	0.19758
4	0.0952148	1.14E-04	0.03631	29.95	0.63284	0.19778
5	0.0390625	7.44E-05	0.04568	12.29	0.77801	0.19581
6	0.0341797	7.18E-05	0.0354±3.17	10.75±7.19E-5	0.8332±0.032	0.1975
6	0.0634766	8.89E-05	0.03333	19.96	0.74823	0.19787

TABLE 6.7: IDENTIFICATION ASSESSMENT ASSOCIATED WITH BACKFLOW INSTABILITIES ON DAPAMITO 3 INDUCER, 90% OF DESIGN FLOW COEFFICIENT, EULER NUMBER = 0.2127 AND HIGH CLEARANCE

- **σ = 0.2834**

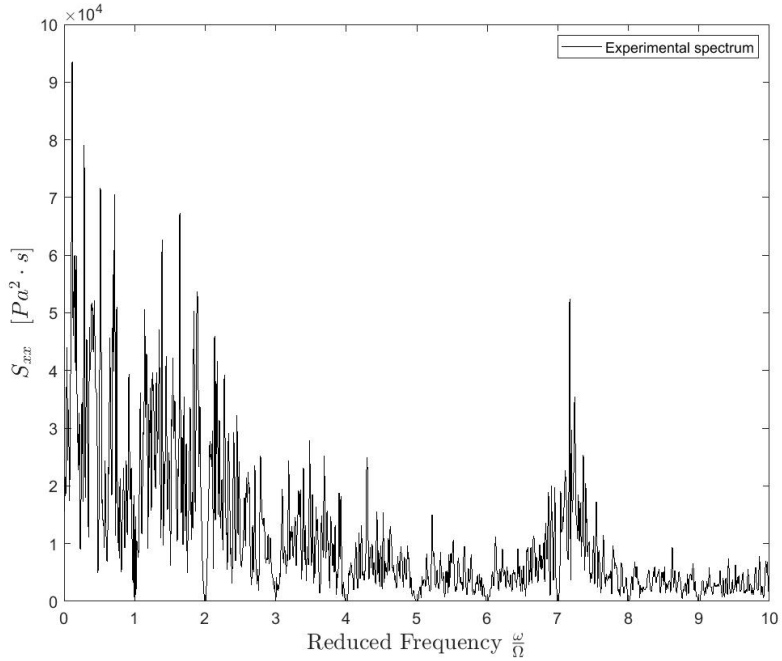

FIGURE 6.21: EXPERIMENTAL AUTO-CORRELATION PRESSURE SPECTRUM FOR DAPAMITO 3 WITH Φ =0.9 Φ_D, EULER NUMBER = 0.2834 AND CLEARANCE = 2 MM.

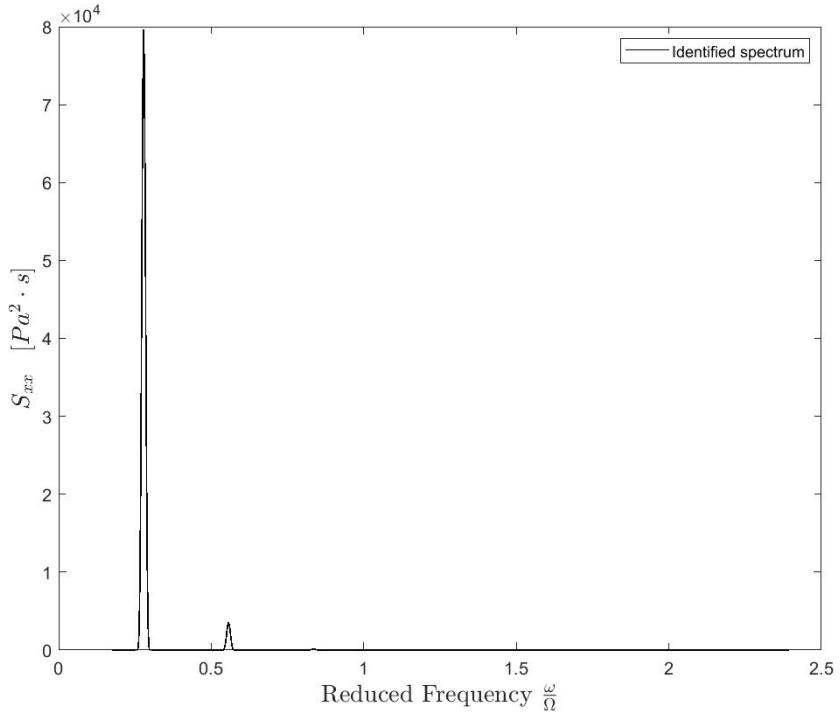

FIGURE 6.22: FULL-THEORETICAL AUTO-CORRELATION PRESSURE SPECTRUM FOR DAPAMITO 3 WITH $\Phi = 0.9\ \Phi_D$, EULER NUMBER = 0.2834, N = 6 VORTICES AND CLEARANCE = 2 MM.

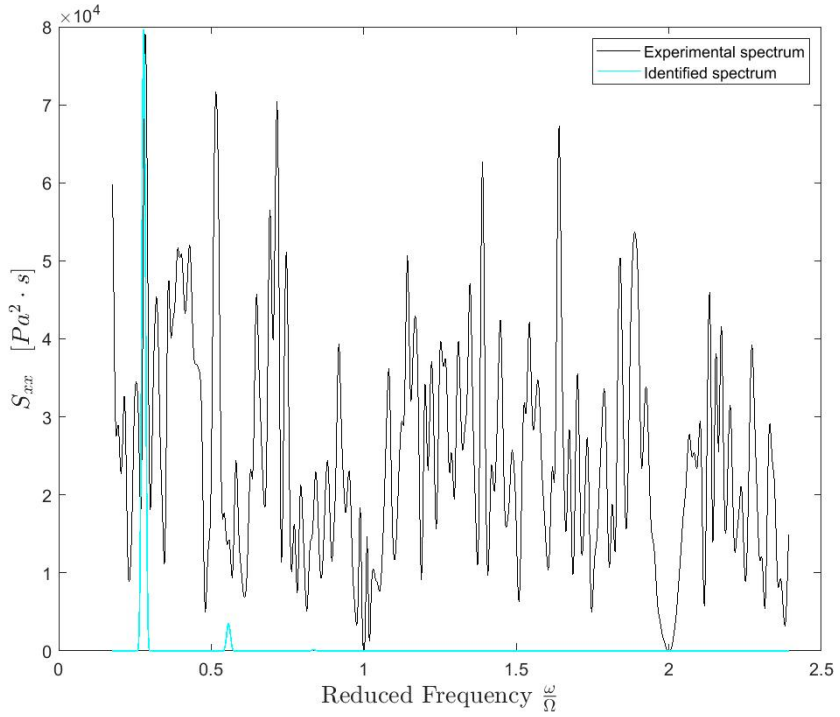

FIGURE 6.23: COMPARISON BETWEEN EXPERIMENTAL AUTO-CORRELATION SPECTRUM AND FULL-THEORETICAL SPECTRUM FOR DAPAMITO 3 WITH $\Phi = 0.9\ \Phi_D$, EULER NUMBER = 0.2834, N = 6 VORTICES AND CLEARANCE = 2 MM.

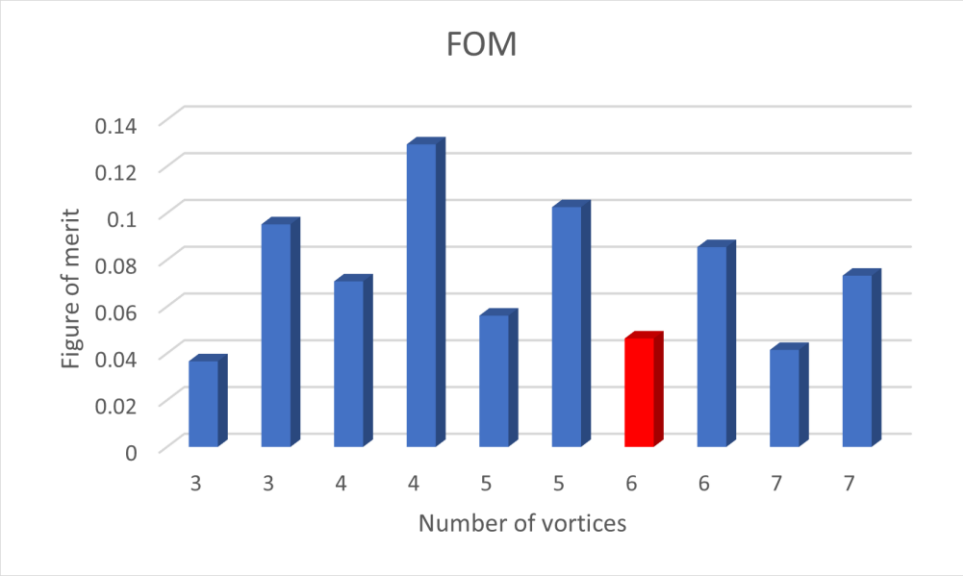

FIGURE 6.24: EVALUATION OF THE FIGURE OF MERIT WITH RESPECT TO THE NUMBER OF VORTICES FOR DAPAMITO 3 WITH Φ =0.9 Φ_D, EULER NUMBER = 0.2834 AND CLEARANCE = 2 MM.

N	ω/Ω	ε_{TOT}	Γ	ω_γ [rad/s]	a (%R)	σ_g
3	0.0366211	1.16E-04	0.04107	11.52	0.76563	0.19642
3	0.0952148	1.65E-04	0.0363	29.95	0.55833	0.19815
4	0.0708008	1.34E-04	0.02695	22.27	0.69832	0.19879
4	0.129395	1.28E-04	0.03457	40.69	0.56782	0.1982
5	0.0561523	1.21E-04	0.0373	17.66	0.70018	0.19747
5	0.102539	1.20E-04	0.02569	32.25	0.67053	0.19884
6	0.0463867	6.53E-05	0.02933±2.24	14.59±6.54E-5	0.80634±0.041	0.19836
6	0.0854492	9.20E-05	0.03431	26.87	0.68903	0.19784
7	0.0415039	1.04E-04	0.03848	13.05	0.76085	0.19695
7	0.0732422	7.77E-05	0.0353	23.03	0.72515	0.19752

TABLE 6.8: IDENTIFICATION ASSESSMENT ASSOCIATED WITH BACKFLOW INSTABILITIES ON DAPAMITO 3 INDUCER, 90% OF DESIGN FLOW COEFFICIENT, EULER NUMBER = 0.2834 AND HIGH CLEARANCE

As a conclusion, as this case is more loaded, the intensity of the instability is greater as can be analysed by comparing both presented cases. Now, the objective is to compare with the same flow coefficient the case with reduced clearance to analyse the effects of this change in the results.

6.2.3. $\Phi = 0.9 \cdot \Phi_D$ AND CLEARANCE = 0.8 MM.

As it has been said, in this case the same flow coefficient is studied for the same inducer, but the clearance is decreased. The recirculation area (R - a), from a physical point of view is thicker in the case of high clearance due to the greater leakage appearing in this case. Due to the studied parameter radial position **a**, the thickness of the recirculation zone can be compared. Also, with a reduction of the thickness of the recirculation zone, a higher number of vortices can be expected because it has been proved that a larger number of vortices could exist stably if they are located closer to the casing. In Table 6.9, it can be seen the parameters and number of vortices of the evaluated cases for the configuration of $\phi = 0.9\ \phi_D$ and low clearance.

σ	N	ω/Ω	ε_{TOT}	Γ	ω_γ [rad/s]	a (%R)	σ_g
0.1262	7	0.0341797	6.74E-05	0.03162	10.75	0.89512	0.19799
0.1433	7	0.0366211	4.63E-05	0.03159	11.52	0.89632	0.19798
0.1804	9	0.0585937	7.25E-05	0.02586	18.43	0.83819	0.1988
0.2056	8	0.0366211	6.61E-05	0.03364	11.52	0.85541	0.19768
0.2178	3	0.114746	6.09E-05	0.03125	36.09	0.70919	0.1984
0.2282	5	0.100098	1.12E-04	0.02888	31.48	0.69993	0.19841
0.2408	7	0.0708008	6.66E-05	0.02574	22.27	0.82536	0.19893
0.2554	4	0.0952148	7.07E-05	0.03884	29.95	0.66208	0.19757
0.2629	8	0.0439453	5.99E-05	0.03366	13.82	0.84561	0.19785
0.2770	5	0.0805664	3.52E-05	0.02879	25.34	0.08057	0.19866
0.2921	6	0.0830078	6.74E-05	0.0452	26.11	0.7177	0.19647

TABLE 6.9: IDENTIFICATION ASSESSMENT ASSOCIATED WITH BACKFLOW INSTABILITIES ON DAPAMITO 3 INDUCER, 90% OF DESIGN FLOW COEFFICIENT AND LOW CLEARANCE

- **σ = 0.1433**

For each analysed case, the results are presented with a Figure representing the experimental power density of auto-correlation for the analysed case, the theoretical auto-correlation for the analysed case, a comparison between experimental and full theoretical auto-correlation (in which it can be seen that the identified and experimental auto-correlation coincides) and finally a graph showing the evolution of the figure of merit with the number of vortices. Also, a Table with the important information about the analysed case, summarizing the parameters obtained as a result for each number of vortices considered in which there exist correlation.

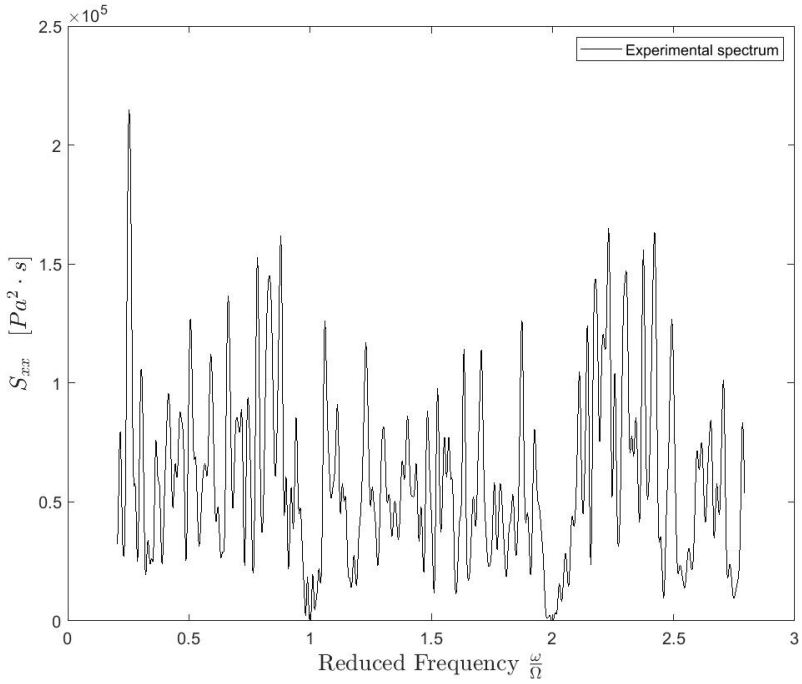

FIGURE 6.25: EXPERIMENTAL AUTO-CORRELATION PRESSURE SPECTRUM FOR DAPAMITO 3 WITH Φ =0.9 Φ_D, EULER NUMBER = 0.1433 AND CLEARANCE = 0.8 MM.

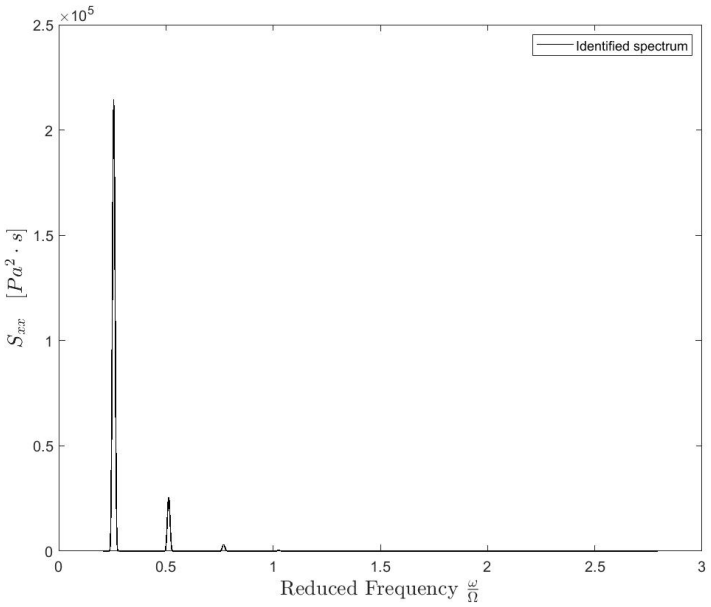

FIGURE 6.26: FULL-THEORETICAL AUTO-CORRELATION PRESSURE SPECTRUM FOR DAPAMITO 3 WITH $\Phi = 0.9\ \Phi_D$, EULER NUMBER = 0.1433, N = 7 VORTICES AND CLEARANCE = 0.8 MM.

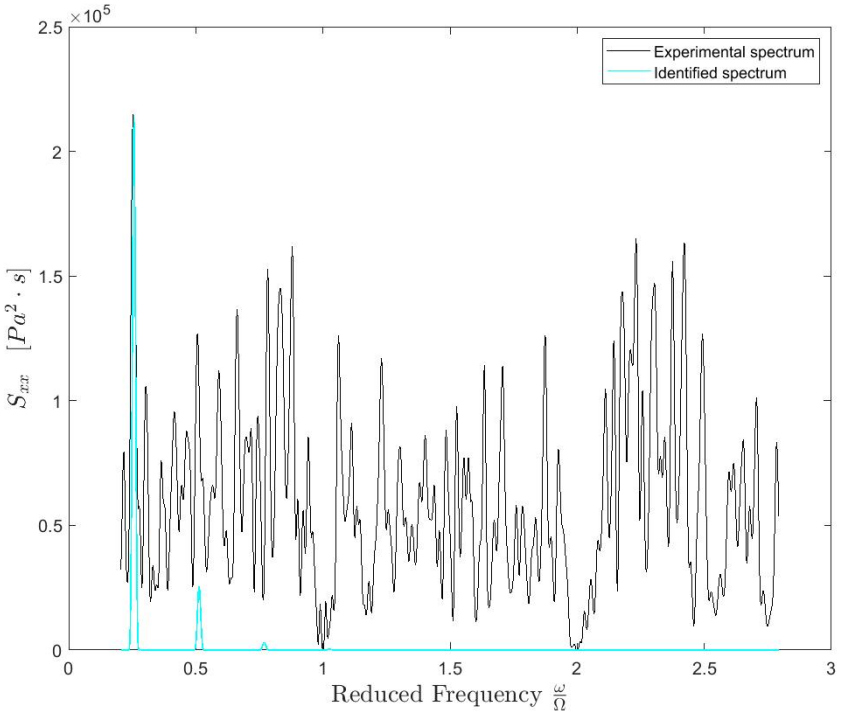

FIGURE 6.27: COMPARISON BETWEEN EXPERIMENTAL AUTO-CORRELATION SPECTRUM AND FULL-THEORETICAL SPECTRUM FOR DAPAMITO 3 WITH $\Phi = 0.9\ \Phi_D$, EULER NUMBER = 0.1433, N = 7 VORTICES AND CLEARANCE = 0.8 MM.

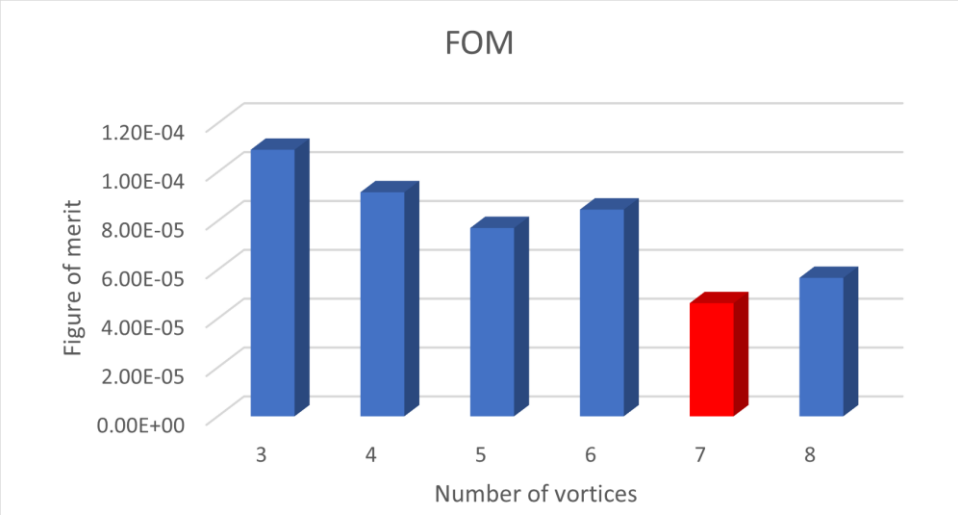

FIGURE 6.28: EVALUATION OF THE FIGURE OF MERIT WITH RESPECT TO THE NUMBER OF VORTICES FOR DAPAMITO 3 WITH Φ =0.9 Φ_D, EULER NUMBER = 0.1433 AND CLEARANCE = 0.8 MM.

N	ω/Ω	ε_{TOT}	Γ	ω_γ [rad/s]	a (%R)	σ_g
3	0.0854492	1.09E-04	0.03413	26.87	0.71038	0.19773
4	0.0634766	9.17E-05	0.04112	19.96	0.74096	0.19677
5	0.0512695	7.71E-05	0.03353	16.12	0.8189	0.19776
6	0.0415039	8.46E-05	0.04127	13.05	0.81484	0.19644
7	0.0366211	4.63E-05	0.03159±2.62	11.52±4.65E-5	0.89632±0.012	0.19798
8	0.0317383	5.67E-05	0.02756	9.98	0.90892	0.1987

TABLE 6.10: IDENTIFICATION ASSESSMENT ASSOCIATED WITH BACKFLOW INSTABILITIES ON DAPAMITO 3 INDUCER, 90% OF DESIGN FLOW COEFFICIENT, EULER NUMBER = 0.1433 AND LOW CLEARANCE

- **σ = 0.2282**

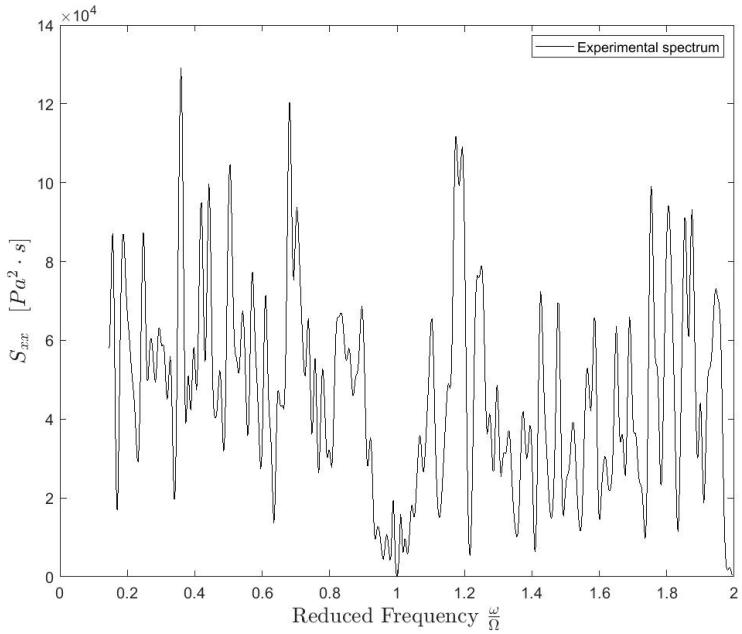

FIGURE 6.29: EXPERIMENTAL AUTO-CORRELATION PRESSURE SPECTRUM FOR DAPAMITO 3 WITH Φ =0.9 Φ_D, EULER NUMBER = 0.2282 AND CLEARANCE = 0.8 MM.

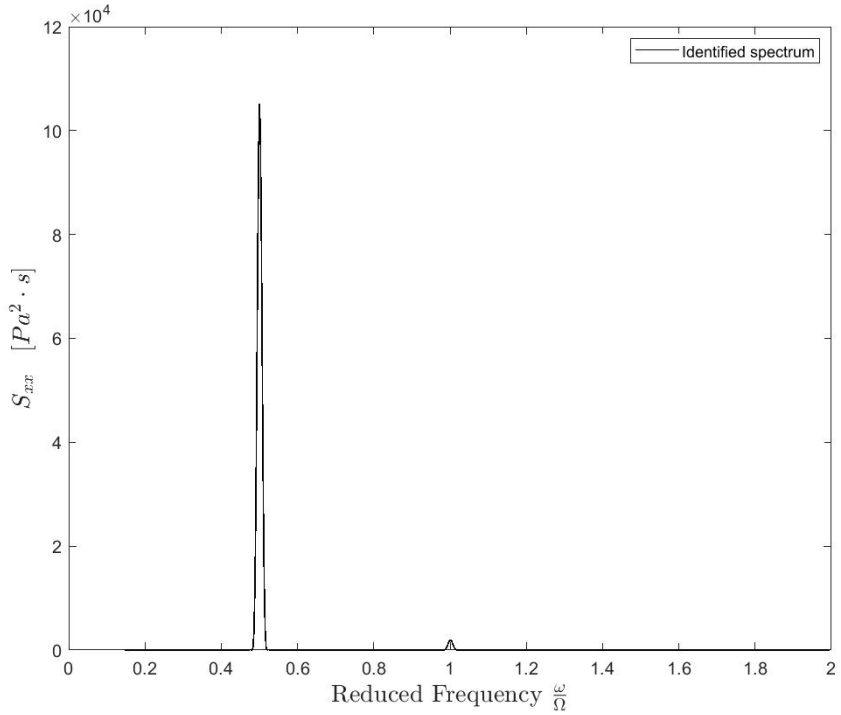

FIGURE 6.30: FULL-THEORETICAL AUTO-CORRELATION PRESSURE SPECTRUM FOR DAPAMITO 3 WITH Φ = 0.9 Φ_D, EULER NUMBER = 0.2282, N =5 VORTICES AND CLEARANCE = 0.8 MM.

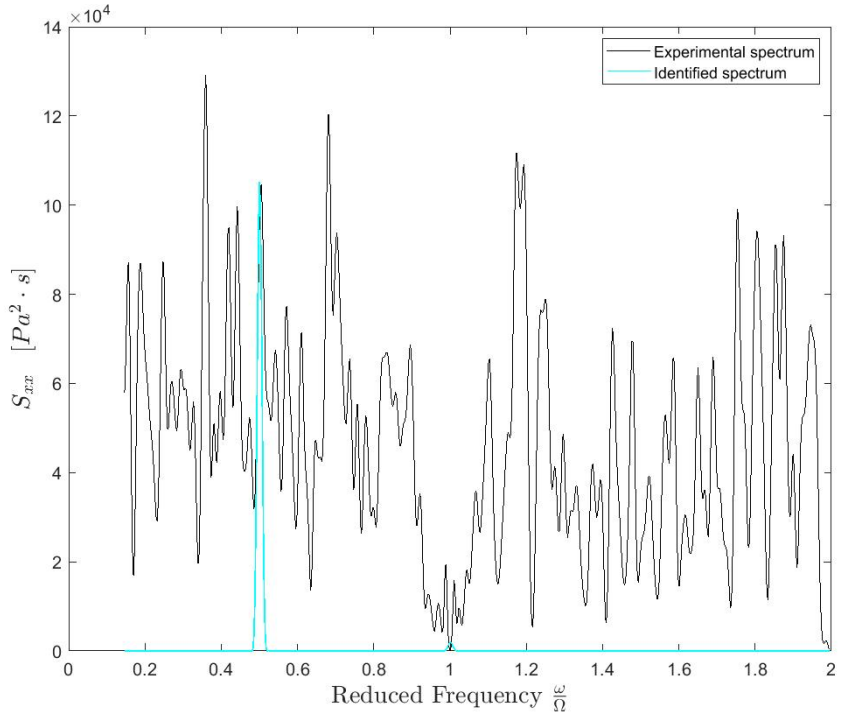

FIGURE 6.31: COMPARISON BETWEEN EXPERIMENTAL AUTO-CORRELATION SPECTRUM AND FULL-THEORETICAL SPECTRUM FOR DAPAMITO 3 WITH Φ = 0.9 Φ_D, EULER NUMBER = 0.2282, N =5 VORTICES AND CLEARANCE = 0.8 MM.

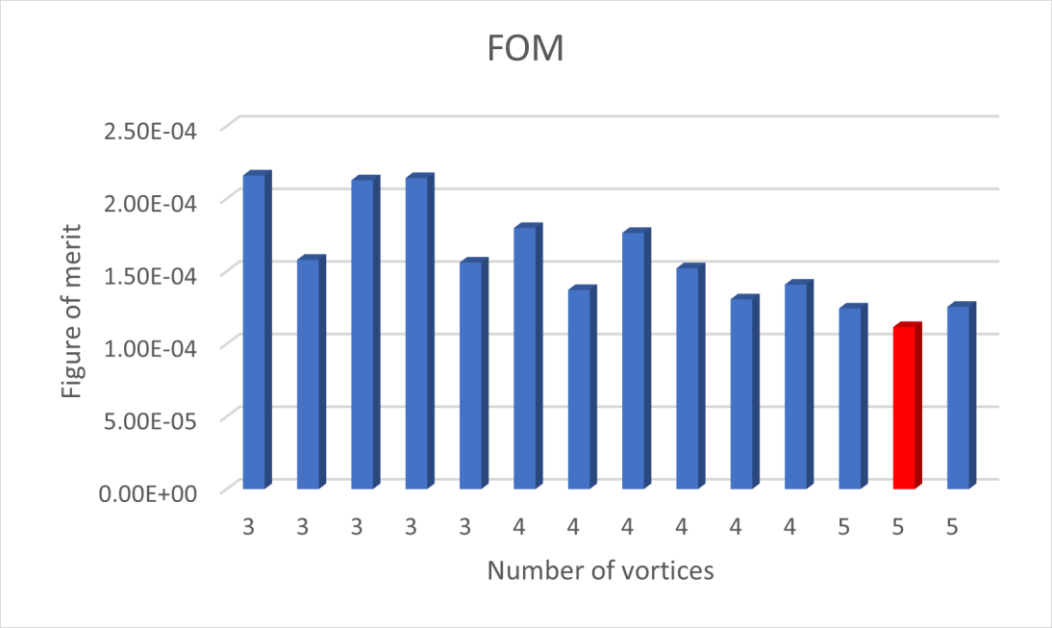

FIGURE 6.32: EVALUATION OF THE FIGURE OF MERIT WITH RESPECT TO THE NUMBER OF VORTICES FOR DAPAMITO 3 WITH Φ =0.9 Φ_D, EULER NUMBER = 0.2282 AND CLEARANCE = 0.8 MM.

N	ω/Ω	ε_{TOT}	Γ	ω_γ [rad/s]	a (%R)	σ_g
3	0.0634766	2.16E-04	0.03897	19.96	0.64947	0.19713
3	0.119629	1.58E-04	0.02613	37.62	0.63333	0.19884
3	0.13916	2.13E-04	0.0228	43.77	0.60202	0.19916
3	0.146484	2.14E-04	0.02274	46.07	0.59172	0.19917
3	0.168457	1.56E-04	0.024	52.98	0.5846	0.19909
4	0.0463867	1.80E-04	0.05111	14.59	0.67868	0.19652
4	0.090332	1.37E-04	0.03712	28.41	0.64396	0.19761
4	0.10498	1.76E-04	0.03408	33.02	0.61525	0.19815
4	0.109863	1.52E-04	0.03597	34.55	0.61132	0.19797
4	0.126953	1.31E-04	0.04327	39.93	0.5732	0.19731
4	0.170898	1.41E-04	0.02208	53.75	0.62458	0.19923
5	0.0708008	1.24E-04	0.02717	22.27	0.7503	0.19864
5	0.100098	1.12E-04	0.02888±2.66	31.48±1.12E-4	0.69993±0.16	0.19841
5	0.136719	1.25E-04	0.03223	43.00	0.63532	0.19827

TABLE 6.11: IDENTIFICATION ASSESSMENT ASSOCIATED WITH BACKFLOW INSTABILITIES ON DAPAMITO 3 INDUCER, 90% OF DESIGN FLOW COEFFICIENT, EULER NUMBER = 0.2282 AND LOW CLEARANCE

- **σ = 0.277**

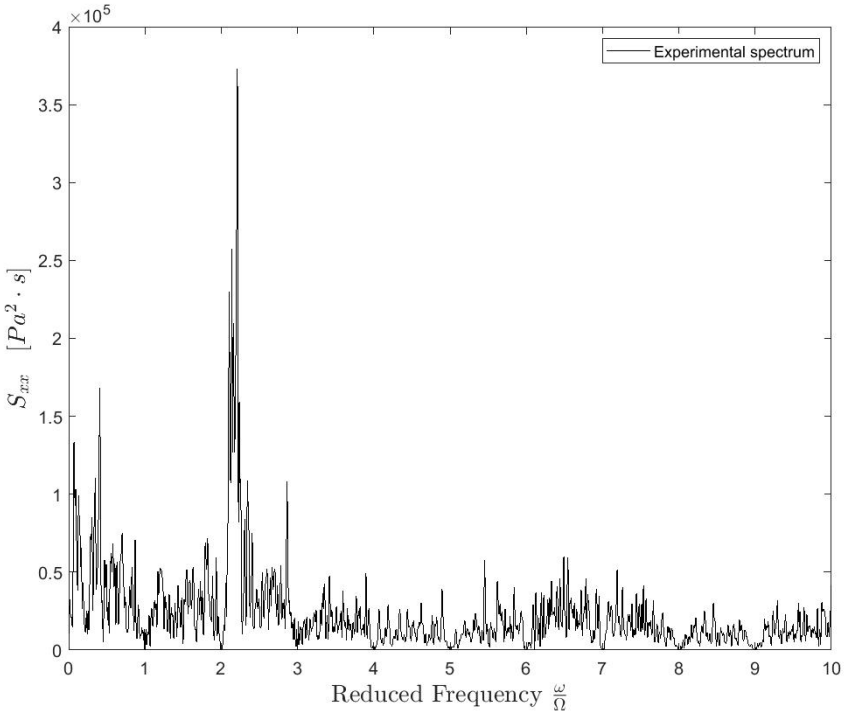

FIGURE 6.33: EXPERIMENTAL AUTO-CORRELATION PRESSURE SPECTRUM FOR DAPAMITO 3 WITH Φ =0.9 Φ_D, EULER NUMBER = 0.277 AND CLEARANCE = 0.8 MM.

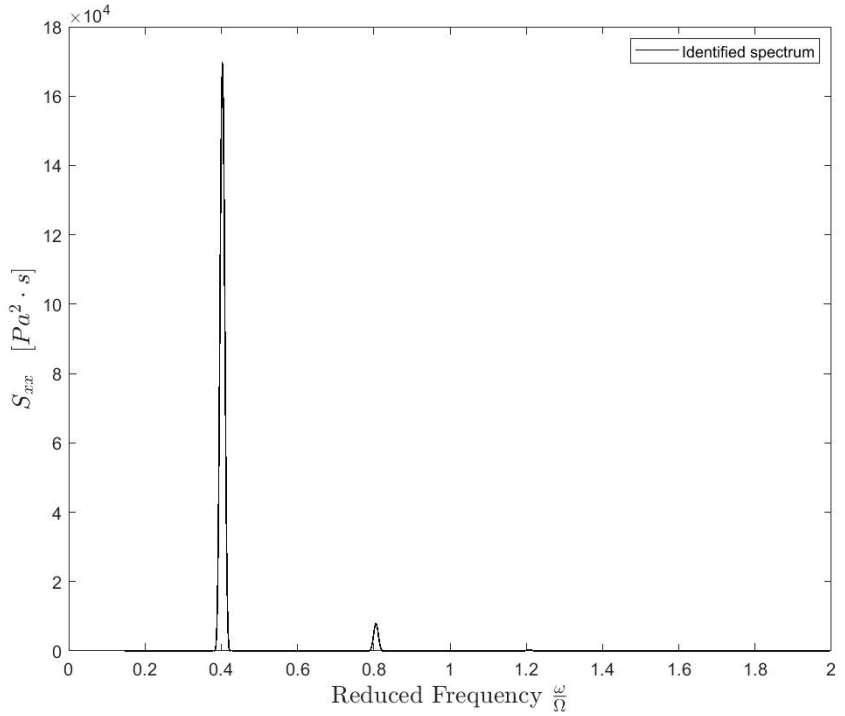

FIGURE 6.34: FULL-THEORETICAL AUTO-CORRELATION PRESSURE SPECTRUM FOR DAPAMITO 3 WITH Φ = 0.9 Φ_D, EULER NUMBER = 0.277, N =5 VORTICES AND CLEARANCE = 0.8 MM.

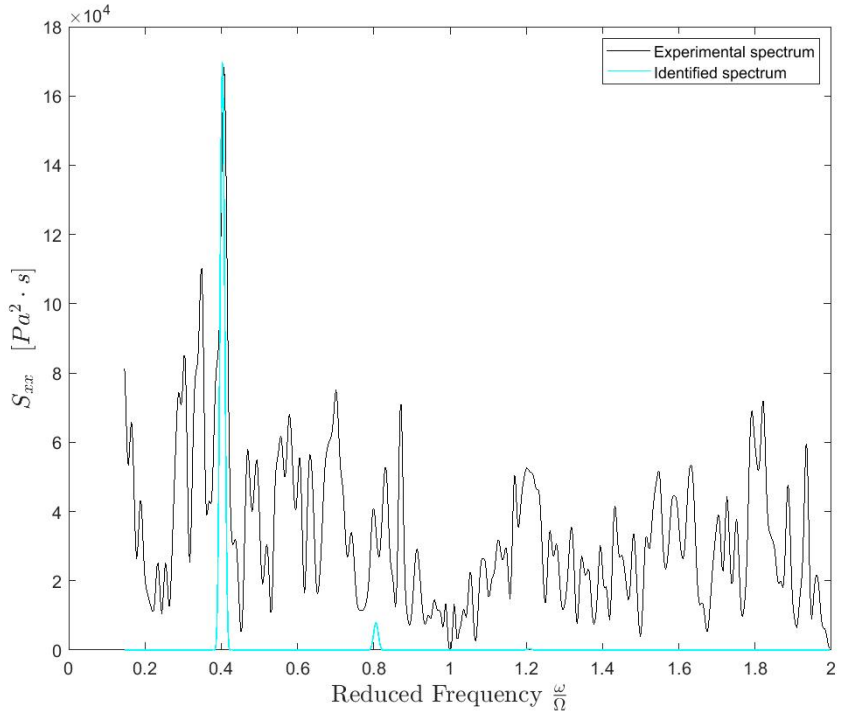

FIGURE 6.35: COMPARISON BETWEEN EXPERIMENTAL AUTO-CORRELATION SPECTRUM AND FULL-THEORETICAL SPECTRUM FOR DAPAMITO 3 WITH $\Phi = 0.9\ \Phi_D$, EULER NUMBER = 0.277, N =5 VORTICES AND CLEARANCE = 0.8 MM.

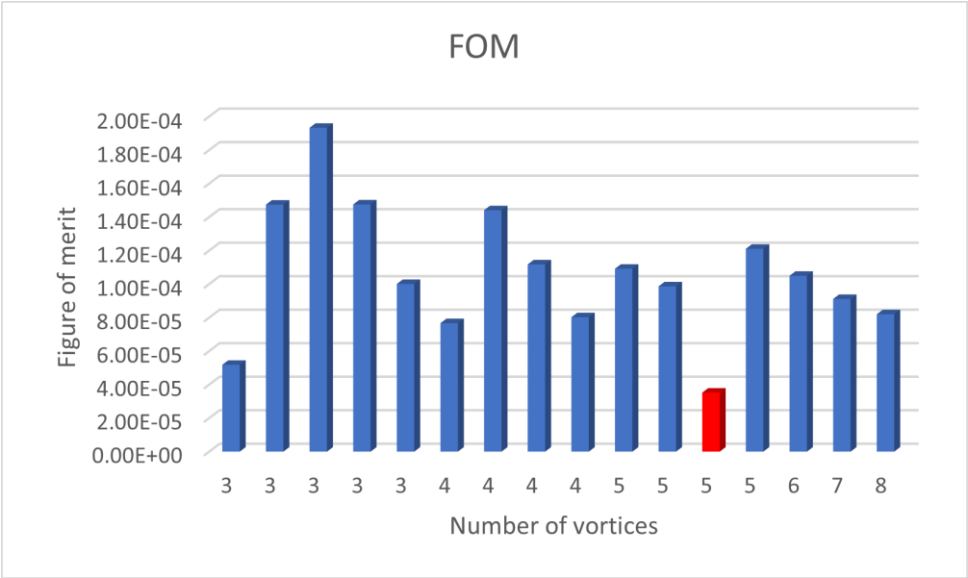

FIGURE 6.36: EVALUATION OF THE FIGURE OF MERIT WITH RESPECT TO THE NUMBER OF VORTICES FOR DAPAMITO 3 WITH $\Phi = 0.9\ \Phi_D$, EULER NUMBER = 0.277 AND CLEARANCE = 0.8 MM.

N	ω/Ω	ε_{TOT}	Γ	ω_γ [rad/s]	a (%R)	σ_g
3	0.0317383	5.18E-05	0.05013	9.98	0.87158	0.19802
3	0.0439453	1.47E-04	0.03863	13.82	0.75303	0.19725
3	0.100098	1.93E-04	0.04299	31.48	0.53553	0.19758
3	0.114746	1.48E-04	0.02852	36.09	0.6125	0.19854
3	0.134277	1.00E-04	0.02809	42.23	0.61854	0.1986
4	0.0341797	7.67E-05	0.04450	10.75	0.81232	0.19666
4	0.0756836	1.44E-04	0.0313	23.80	0.68	0.19813
4	0.0854492	1.12E-04	0.03876	26.87	0.64399	0.19719
4	0.102539	8.02E-05	0.05085	32.25	0.5953	0.19594
5	0.0585937	1.09E-04	0.04375	18.43	0.69801	0.19663
5	0.0683594	9.87E-05	0.02807	21.50	0.7471	0.19845
5	0.0805664	3.52E-05	0.02879±0.84	25.34±3.53E-5	0.79852±0.016	0.19866
5	0.13916	1.21E-04	0.03106	43.77	0.62354	0.19821
6	0.0683594	1.05E-04	0.04113	21.50	0.73378	0.19697
7	0.0585937	9.11E-05	0.02782	17.57	0.81245	0.19853
8	0.0512695	8.20E-05	0.03408	16.12	0.81208	0.19777

TABLE 6.12: IDENTIFICATION ASSESSMENT ASSOCIATED WITH BACKFLOW INSTABILITIES ON DAPAMITO 3 INDUCER, 90% OF DESIGN FLOW COEFFICIENT, EULER NUMBER = 0.277 AND LOW CLEARANCE

As the clearance decreases, there is a confirmation of the increase in the number of vortices for most of the cases as the case of σ = 0.1835 with N = 5 for the DAPAMITO 3, with flow coefficient $\phi = 0.9 \cdot \phi_D$ with clearance 2 mm and the case of σ = 0.1804 with N = 9 for the DAPAMITO 3, with flow coefficient $\phi = 0.9 \cdot \phi_D$ with clearance 0.8 mm. The values of the parameters for each case can be seen in Tables 6.5 and 6.9 respectively.

This is true in most of the cases, in some of them, the number of vortices of the selected case, in which there is the minimum value of the figure of merit is equal or even lower in the case of low clearance. This could be explained due to the hypothesis and simplifications introduced in the model, whose results must be understood as approximations and analysed experimentally.

6.2.4. $\Phi = 0.75 \cdot \Phi_D$ AND CLEARANCE = 2 MM.

The fourth analysed case is for high clearance, reducing the flow coefficient until a 75% of the design flow coefficient. Also, this case has been analysed for different Euler numbers (Table 6.13), close to the rest of the DAPAMITO 3 evaluations in order to ease the comparation.

σ	N	ω/Ω	ε_{TOT}	Γ	ω_γ [rad/s]	a (%R)	σ_g
0.1319	7	0.0317383	1.72E-05	0.04014	9.98	0.93473	0.19667
0.1426	7	0.0317383	3.85E-05	0.0372	9.98	0.90026	0.1971
0.1841	7	0.0317383	2.89E-05	0.04629	9.98	0.89612	0.20223
0.2134	6	0.0317383	1.63E-05	0.03269	9.98	0.96016	0.1983
0.2267	8	0.0317383	3.22E-05	0.03904	9.98	0.89371	0.19688
0.2383	6	0.0317383	2.77E-05	0.06885	9.98	0.8487	0.19138
0.2493	6	0.0439453	3.36E-05	0.03837	13.82	0.87573	0.19713
0.2629	7	0.0341797	3.72E-05	0.03863	10.75	0.8851	0.19683
0.2701	8	0.0366211	4.04E-05	0.03547	11.52	0.88046	0.19758
0.2839	8	0.0537109	2.58E-05	0.02821	16.89	0.88849	0.19852
0.2972	8	0.0488281	3.49E-05	0.03724	15.36	0.83642	0.19745

TABLE 6.13: IDENTIFICATION ASSESSMENT ASSOCIATED WITH BACKFLOW INSTABILITIES ON DAPAMITO 3 INDUCER, 75% OF DESIGN FLOW COEFFICIENT AND HIGH CLEARANCE

For this case, the same can be said, the results are presented in Figures analysing the experimental pressure spectrum, the full-theoretical auto-correlation, and the comparison between identified and experimental spectrum for the method to identify backflow vortex instability. Finally, a Table with quantitative analysis of the studied case and a Figure describing the evolution of the figure of merit for the number of vortices studied of peaks in which the correlation-coefficient is high is presented.

- **σ = 0.1426**

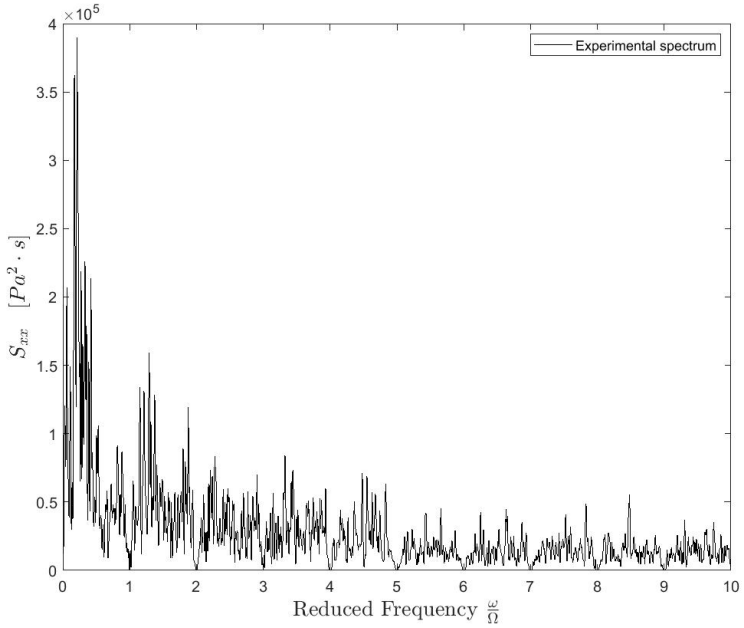

FIGURE 6.37: EXPERIMENTAL AUTO-CORRELATION PRESSURE SPECTRUM FOR DAPAMITO 3 WITH Φ =0.75 Φ_D, EULER NUMBER = 0.1426 AND CLEARANCE = 2 MM.

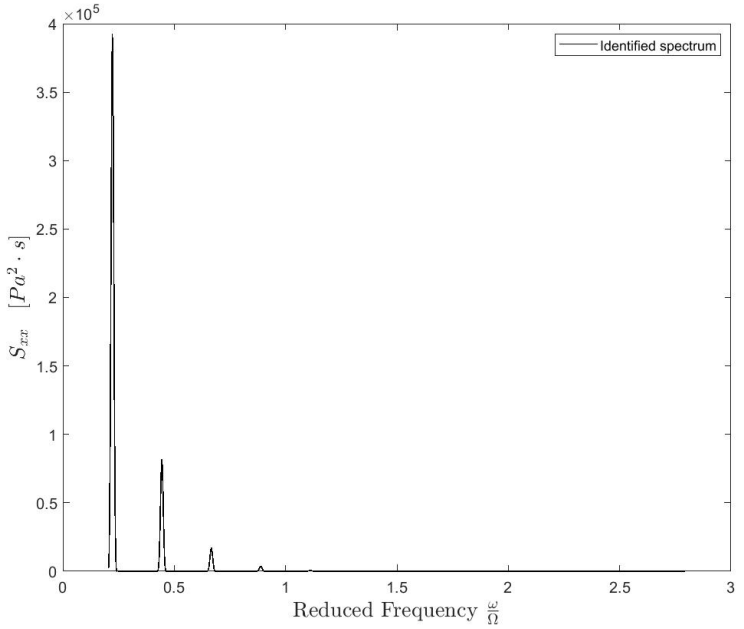

FIGURE 6.38: FULL-THEORETICAL AUTO-CORRELATION PRESSURE SPECTRUM FOR DAPAMITO 3 WITH Φ = 0.75 Φ_D, EULER NUMBER = 0.1426, N =7 VORTICES AND CLEARANCE = 2 MM.

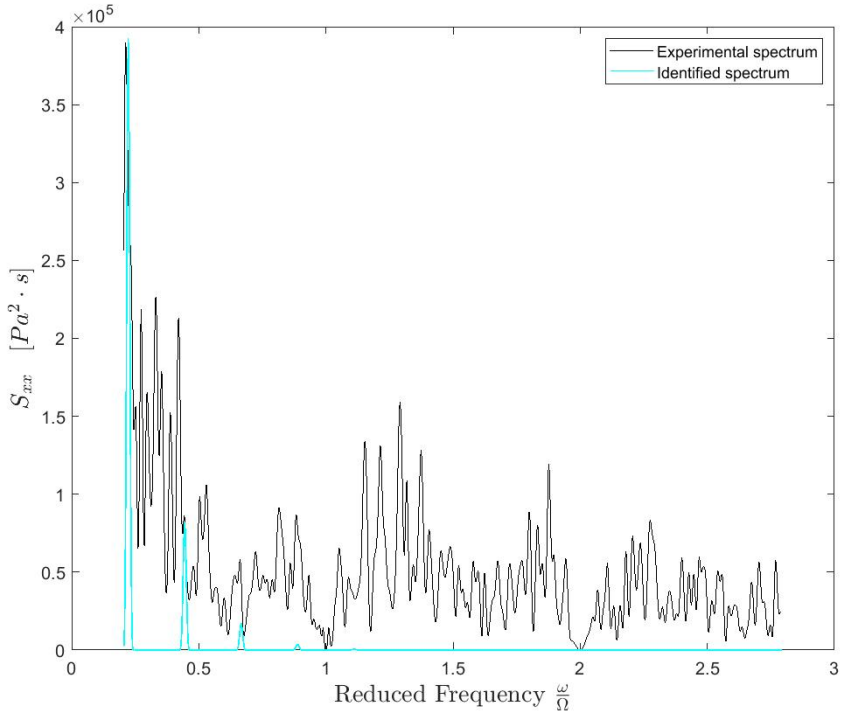

FIGURE 6.39: COMPARISON BETWEEN EXPERIMENTAL AUTO-CORRELATION SPECTRUM AND FULL-THEORETICAL SPECTRUM FOR DAPAMITO 3 WITH $\Phi = 0.75\ \Phi_D$, EULER NUMBER = 0.1426, N =7 VORTICES AND CLEARANCE = 2 MM.

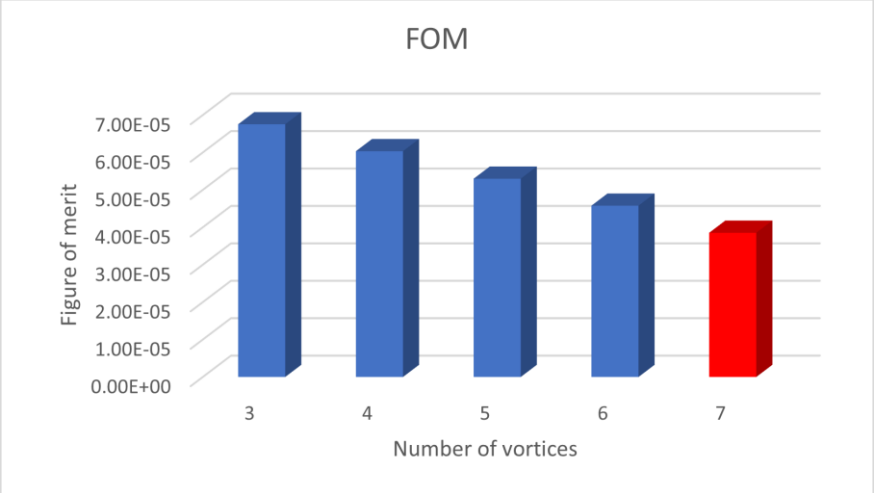

FIGURE 6.40: EVALUATION OF THE FIGURE OF MERIT WITH RESPECT TO THE NUMBER OF VORTICES FOR DAPAMITO 3 WITH $\Phi = 0.75\ \Phi_D$, EULER NUMBER = 0.1426 AND CLEARANCE = 2 MM.

N	ω/Ω	ε_{TOT}	Γ	ω_γ [rad/s]	a (%R)	σ_g
3	0.0708008	6.75E-05	0.0374	22.27	0.81352	0.1974
4	0.0537109	6.03E-05	0.04329	16.89	0.82237	0.19683
5	0.0439453	5.30E-05	0.03621	13.82	0.87432	0.19731
6	0.0366211	4.58E-05	0.04471	11.52	0.86319	0.19586
7	0.0317383	3.85E-05	0.0372±2.67	9.98±3.87E-5	0.90026±0.0092	0.1971

TABLE 6.14: IDENTIFICATION ASSESSMENT ASSOCIATED WITH BACKFLOW INSTABILITIES ON DAPAMITO 3 INDUCER, 75% OF DESIGN FLOW COEFFICIENT, EULER NUMBER = 0.1426 AND HIGH CLEARANCE

- **σ = 0.2267**

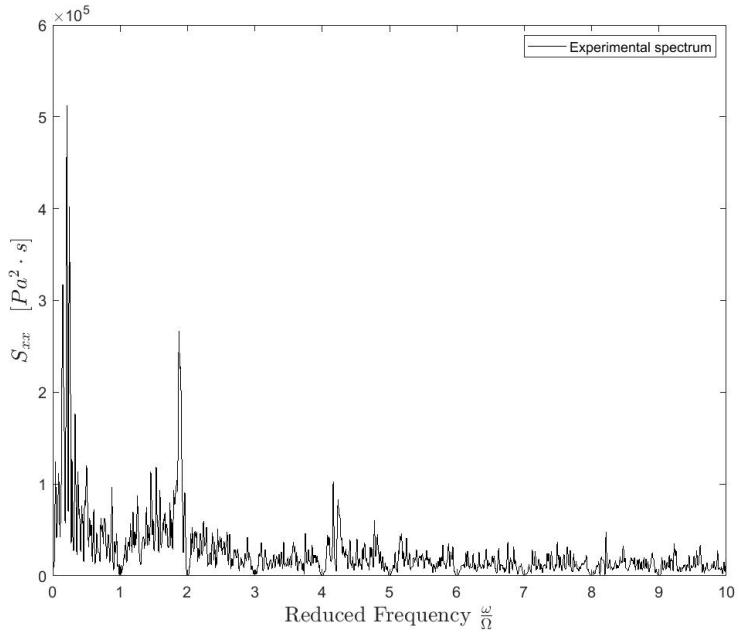

FIGURE 6.41: EXPERIMENTAL AUTO-CORRELATION PRESSURE SPECTRUM FOR DAPAMITO 3 WITH Φ =0.75 Φ_D, EULER NUMBER = 0.2267 AND CLEARANCE = 2 MM.

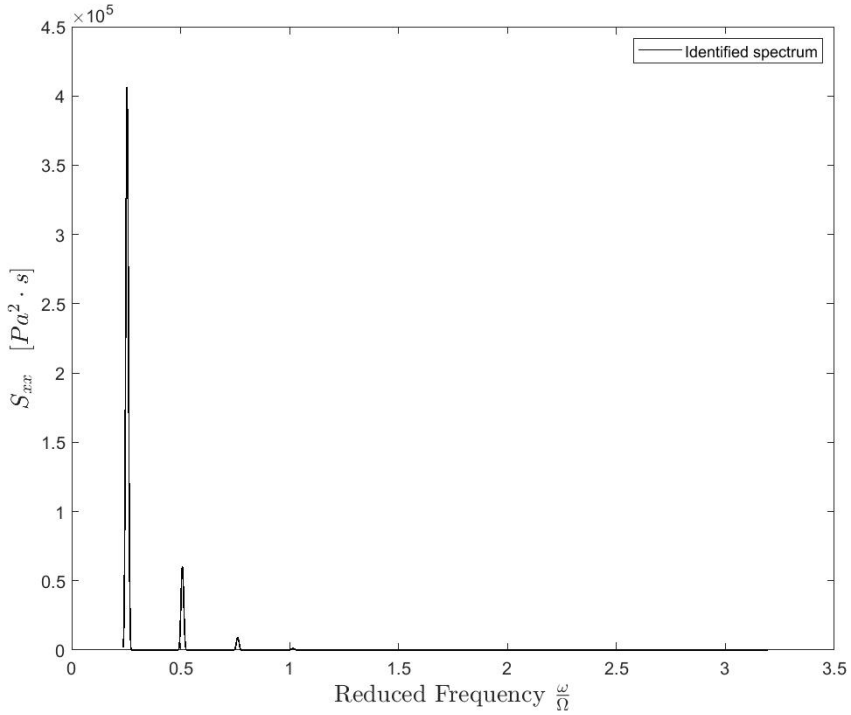

FIGURE 6.42: FULL-THEORETICAL AUTO-CORRELATION PRESSURE SPECTRUM FOR DAPAMITO 3 WITH Φ = 0.75 Φ_D, EULER NUMBER = 0.2267, N =8 VORTICES AND CLEARANCE = 2 MM.

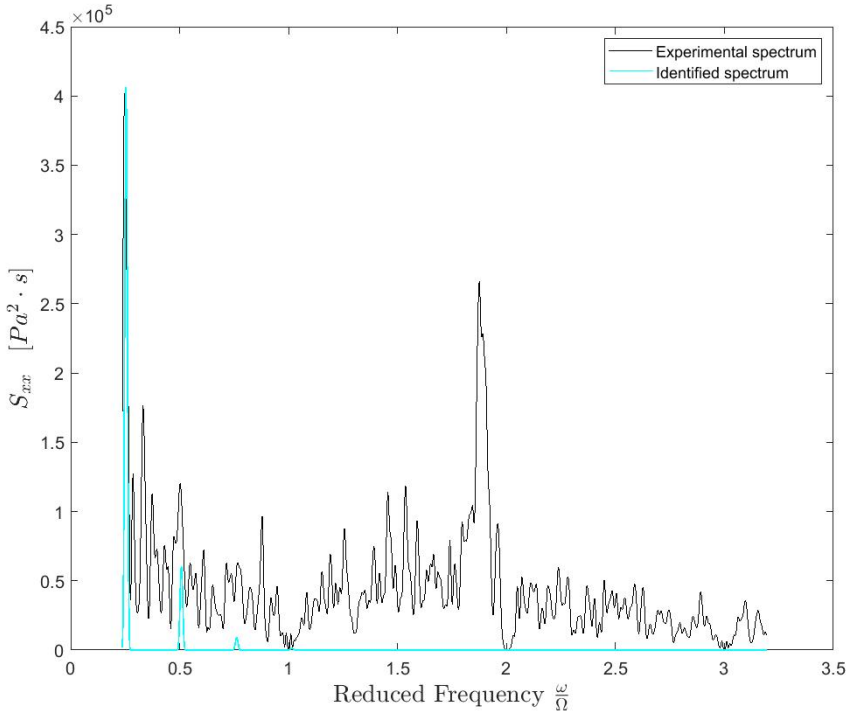

FIGURE 6.43: COMPARISON BETWEEN EXPERIMENTAL AUTO-CORRELATION SPECTRUM AND FULL-THEORETICAL SPECTRUM FOR DAPAMITO 3 WITH $\Phi = 0.75\ \Phi_D$, EULER NUMBER = 0.2267, N =8 VORTICES AND CLEARANCE = 2 MM.

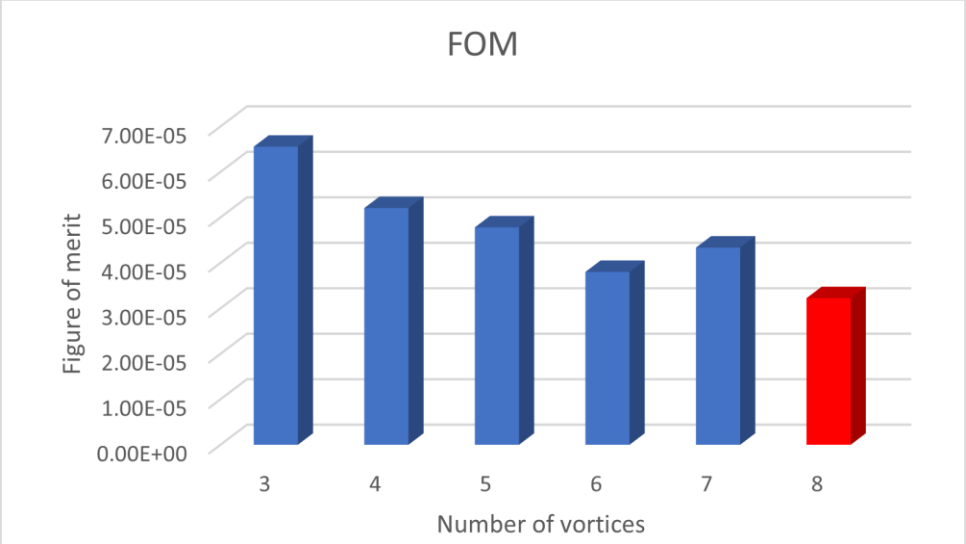

FIGURE 6.44: EVALUATION OF THE FIGURE OF MERIT WITH RESPECT TO THE NUMBER OF VORTICES FOR DAPAMITO 3 WITH $\Phi = 0.75\ \Phi_D$, EULER NUMBER = 0.2267 AND CLEARANCE = 2 MM.

N	ω/Ω	ε_{TOT}	Γ	ω_γ [rad/s]	a (%R)	σ_g
3	0.0708008	6.55E-05	0.06669	22.27	0.69113	0.19764
4	0.0512695	5.20E-05	0.06532	16.12	0.75639	0.19177
5	0.0415039	4.78E-05	0.06487	13.05	0.79997	0.19063
6	0.0341797	3.80E-05	0.06589	10.75	0.82795	0.19012
7	0.0292969	4.34E-05	0.06293	9.21	0.85454	0.19198
8	0.0317383	3.22E-05	0.03904±2.98	9.98±3.23E-5	0.89371±0.011	0.19688

TABLE 6.15: IDENTIFICATION ASSESSMENT ASSOCIATED WITH BACKFLOW INSTABILITIES ON DAPAMITO 3 INDUCER, 75% OF DESIGN FLOW COEFFICIENT, EULER NUMBER = 0.2267 AND HIGH CLEARANCE

- **σ = 0.2839**

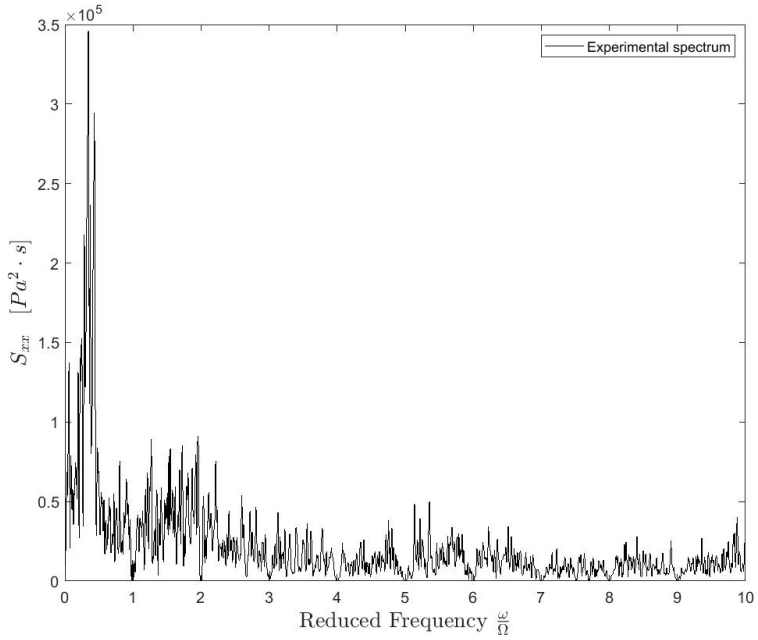

FIGURE 6.45: EXPERIMENTAL AUTO-CORRELATION PRESSURE SPECTRUM FOR DAPAMITO 3 WITH Φ =0.75 Φ_D, EULER NUMBER = 0.2839 AND CLEARANCE = 2 MM.

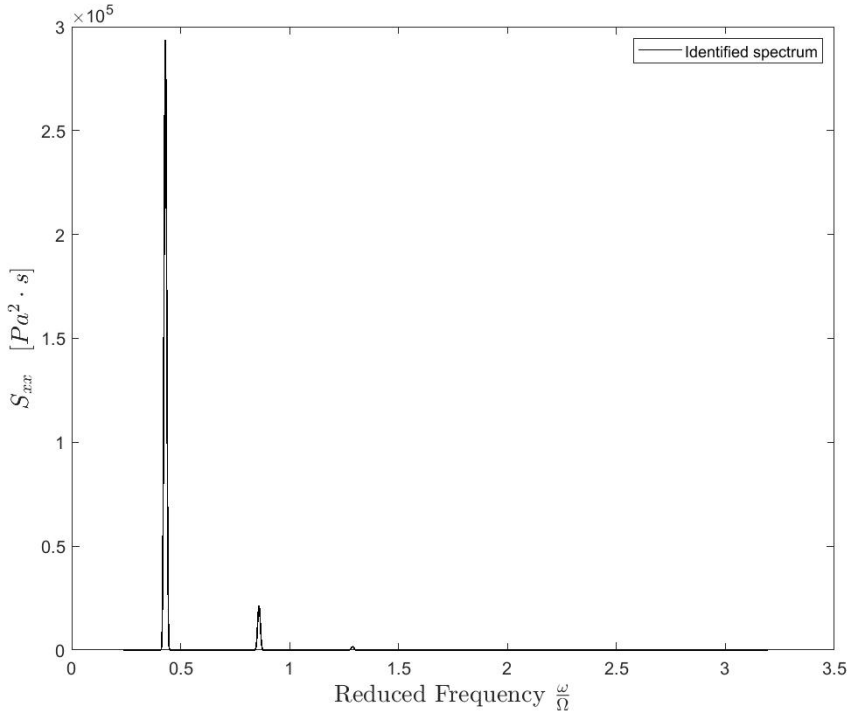

FIGURE 6.46: FULL-THEORETICAL AUTO-CORRELATION PRESSURE SPECTRUM FOR DAPAMITO 3 WITH Φ = 0.75 Φ_D, EULER NUMBER = 0.2839, N =8 VORTICES AND CLEARANCE = 2 MM.

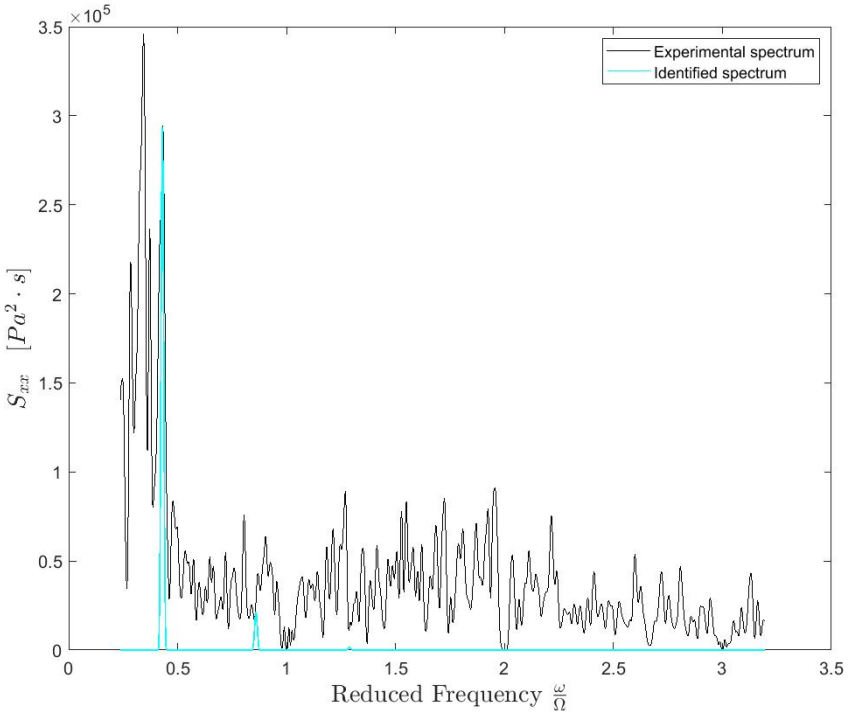

FIGURE 6.47: COMPARISON BETWEEN EXPERIMENTAL AUTO-CORRELATION SPECTRUM AND FULL-THEORETICAL SPECTRUM FOR DAPAMITO 3 WITH $\Phi = 0.75\ \Phi_D$, EULER NUMBER = 0.2839, N =8 VORTICES AND CLEARANCE = 2 MM.

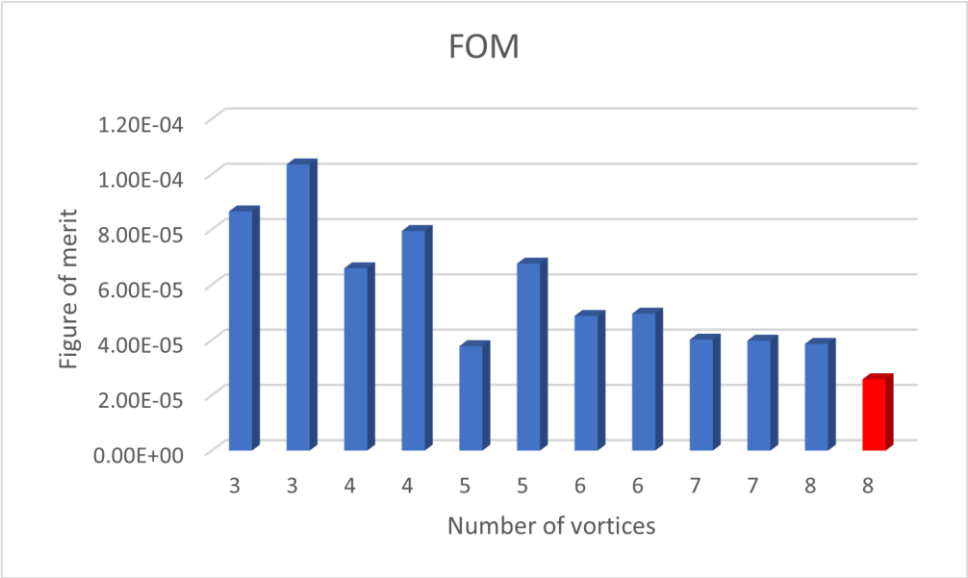

FIGURE 6.48: EVALUATION OF THE FIGURE OF MERIT WITH RESPECT TO THE NUMBER OF VORTICES FOR DAPAMITO 3 WITH $\Phi = 0.75\ \Phi_D$, EULER NUMBER = 0.2839 AND CLEARANCE = 2 MM.

N	ω/Ω	ε_{TOT}	Γ	ω_γ [rad/s]	a (%R)	σ_g
3	0.114746	8.66E-05	0.04322	36.09	0.64172	0.1966
3	0.144043	1.04E-04	0.04094	45.30	0.59269	0.19744
4	0.0854492	6.60E-05	0.04659	26.87	0.71933	0.21092
4	0.107422	7.95E-05	0.03378	33.78	0.7109	0.19787
5	0.0683594	3.78E-05	0.04095	21.50	0.8083	0.19661
5	0.0854492	6.77E-05	0.04172	26.87	0.72903	0.1967
6	0.0561523	4.87E-05	0.05298	17.66	0.77591	0.19533
6	0.0708008	4.96E-05	0.03739	22.27	0.79317	0.19716
7	0.0488281	4.02E-05	0.04419	15.37	0.82858	0.20021
7	0.0610352	3.98E-05	0.03492	19.20	0.83091	0.19755
8	0.0415039	3.86E-05	0.03659	13.05	0.04151	0.19765
8	0.0537109	2.58E-05	0.02821±1.54	16.89±2.59E-5	0.88849±0.0091	0.19852

TABLE 6.16: IDENTIFICATION ASSESSMENT ASSOCIATED WITH BACKFLOW INSTABILITIES ON DAPAMITO 3 INDUCER, 75% OF DESIGN FLOW COEFFICIENT, EULER NUMBER = 0.2839 AND HIGH CLEARANCE

6.2.5. $\Phi = 0.75 \cdot \Phi_D$ AND CLEARANCE = 0.8 MM.

The last case of DAPAMITO 3 inducer studied is the one with the same flow coefficient than the last one but reducing the clearance to study its effect as it has been done before with $\phi = 0.9 \cdot \phi_D$. So, to sum up, in this case it is studied DAPAMITO 3 inducer with flow coefficient $\phi = 0.75 \cdot \phi_D$ but, with a reduction of the clearance (0.8 mm.). The Table 6.17 represents the selected number of vortices with the different Euler numbers, allowing the comparison with Table 6.13 in order to report the effect of the clearance in the results.

σ	N	ω/Ω	ε_{TOT}	Γ	ω_γ [rad/s]	a (%R)	σ_g
0.1267	4	0.0341797	8.29E-05	0.04069	10.75	0.85961	0.19644
0.1437	4	0.0390625	7.55E-05	0.03739	12.29	0.88031	0.19736
0.1807	4	0.0585937	1.19E-04	0.04488	18.43	0.72524	0.19582
0.2062	4	0.0878906	1.09E-04	0.05047	27.64	0.6357	0.19575
0.2169	5	0.0390625	4.89E-05	0.03956	12.29	0.87816	0.19695
0.2289	4	0.0512695	7.07E-05	0.03337	16.12	0.82998	0.19822
0.2409	5	0.0488281	8.20E-05	0.03454	15.36	0.8225	0.19754
0.2555	3	0.0708008	8.69E-05	0.04955	22.27	0.66027	0.1962
0.2626	6	0.0341797	7.36E-05	0.04563	10.75	0.85576	0.19557
0.2769	4	0.0537109	5.72E-05	0.03379	16.89	0.83939	0.19818
0.2923	3	0.0610352	7.51E-05	0.04852	19.20	0.7225	0.19617

TABLE 6.17: IDENTIFICATION ASSESSMENT ASSOCIATED WITH BACKFLOW INSTABILITIES ON DAPAMITO 3 INDUCER, 75% OF DESIGN FLOW COEFFICIENT AND LOW CLEARANCE

Again, the Figures and Tables used to present the results are the same for flow coefficients close to the Euler numbers studied in the rest of the cases and can be seen in following paragraphs.

- **σ = 0.1437**

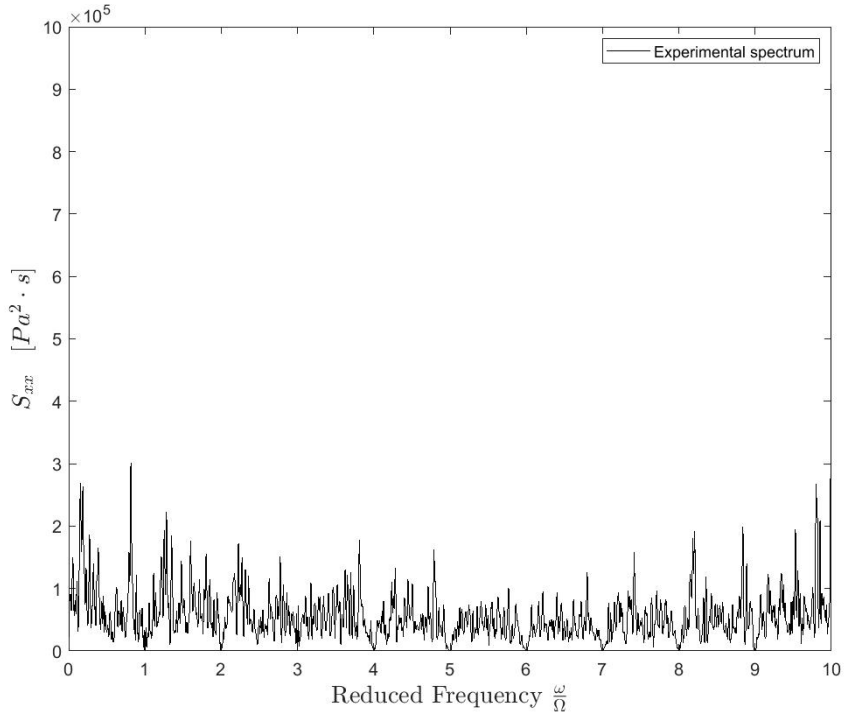

FIGURE 6.49: EXPERIMENTAL AUTO-CORRELATION PRESSURE SPECTRUM FOR DAPAMITO 3 WITH Φ =0.75 Φ_D, EULER NUMBER = 0.1437 AND CLEARANCE = 0.8 MM.

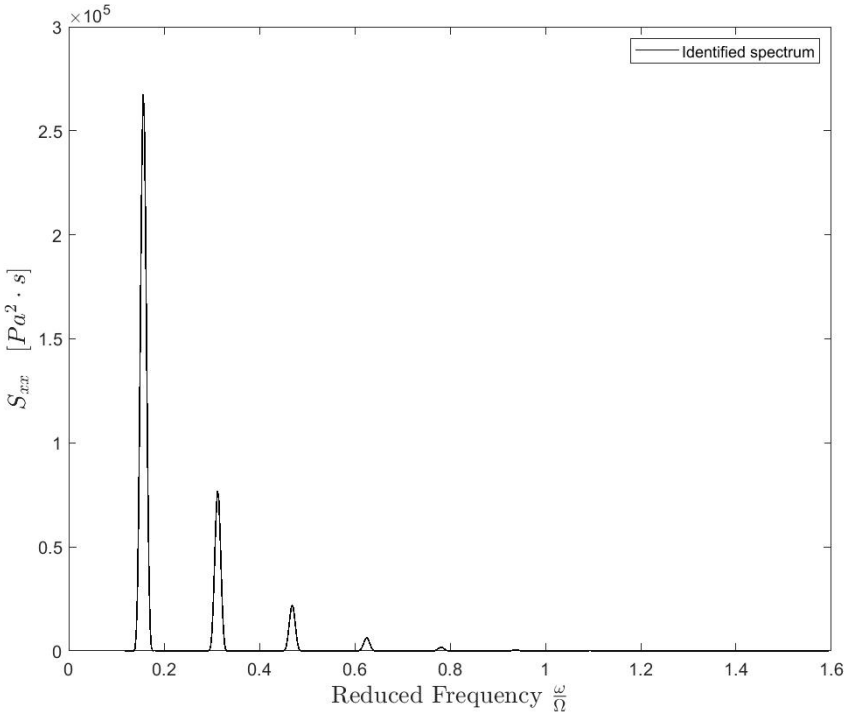

FIGURE 6.50: FULL-THEORETICAL AUTO-CORRELATION PRESSURE SPECTRUM FOR DAPAMITO 3 WITH Φ = 0.75 Φ_D, EULER NUMBER = 0.1437, N =4 VORTICES AND CLEARANCE = 0.8 MM.

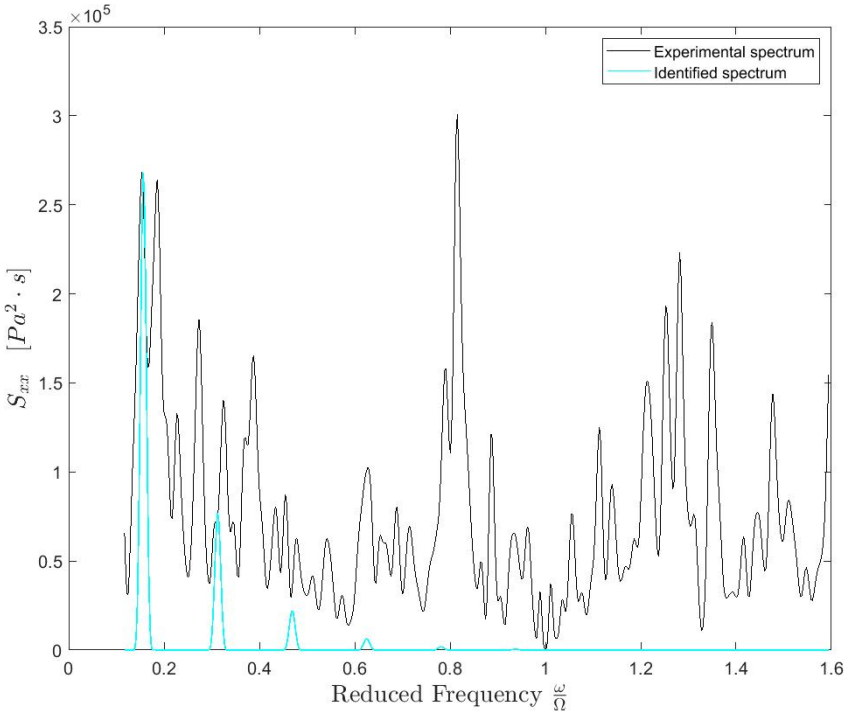

FIGURE 6.51: COMPARISON BETWEEN EXPERIMENTAL AUTO-CORRELATION SPECTRUM AND FULL-THEORETICAL SPECTRUM FOR DAPAMITO 3 WITH $\Phi = 0.75\ \Phi_D$, EULER NUMBER = 0.1437, N =4 VORTICES AND CLEARANCE = 0.8 MM.

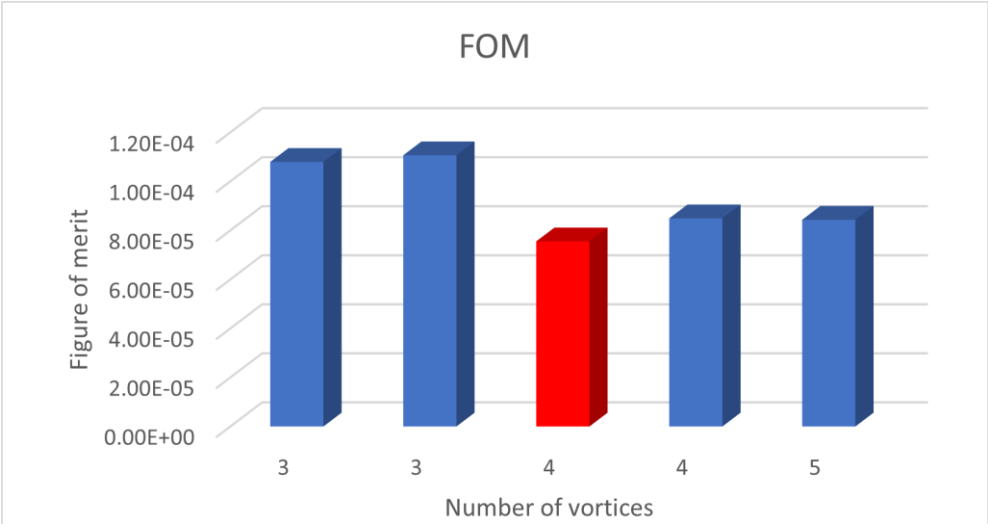

FIGURE 6.52: EVALUATION OF THE FIGURE OF MERIT WITH RESPECT TO THE NUMBER OF VORTICES FOR DAPAMITO 3 WITH $\Phi = 0.75\ \Phi_D$, EULER NUMBER = 0.1437 AND CLEARANCE = 0.8 MM.

N	ω/Ω	ε_{TOT}	Γ	ω_γ [rad/s]	a (%R)	σ_g
3	0.0512695	1.08E-04	0.06119	16.12	0.71482	0.1932
3	0.0610352	1.11E-04	0.05981	19.20	0.68104	0.1952
4	0.0390625	7.55E-05	0.03739±1.95	12.29±7.6E-5	0.88031±0.012	0.19736
4	0.0463867	8.49E-05	0.03884	14.59	0.8384	0.19702
5	0.0366211	8.43E-05	0.05919	11.52	0.79541	0.19336

TABLE 6.18: IDENTIFICATION ASSESSMENT ASSOCIATED WITH BACKFLOW INSTABILITIES ON DAPAMITO 3 INDUCER, 75% OF DESIGN FLOW COEFFICIENT, EULER NUMBER = 0.1437 AND LOW CLEARANCE

- **σ = 0.2169**

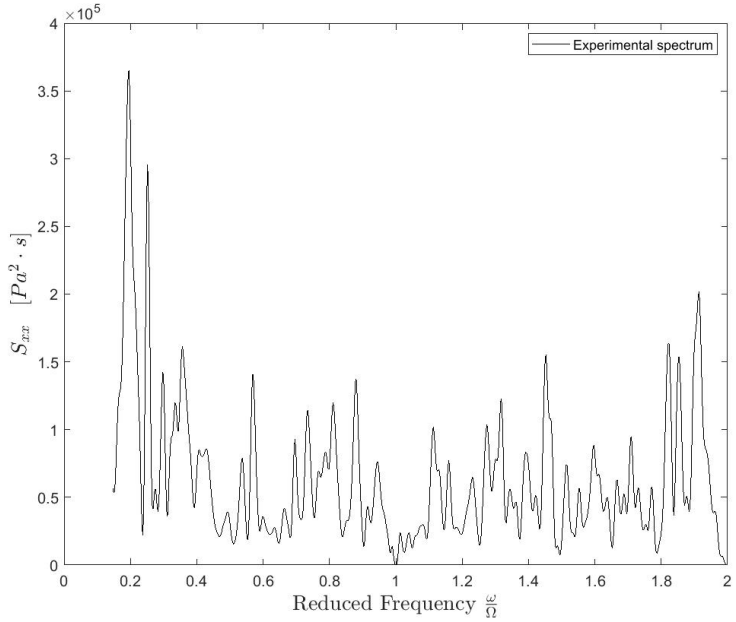

FIGURE 6.53: EXPERIMENTAL AUTO-CORRELATION PRESSURE SPECTRUM FOR DAPAMITO 3 WITH Φ =0.75 Φ_D, EULER NUMBER = 0.2169 AND CLEARANCE = 0.8 MM.

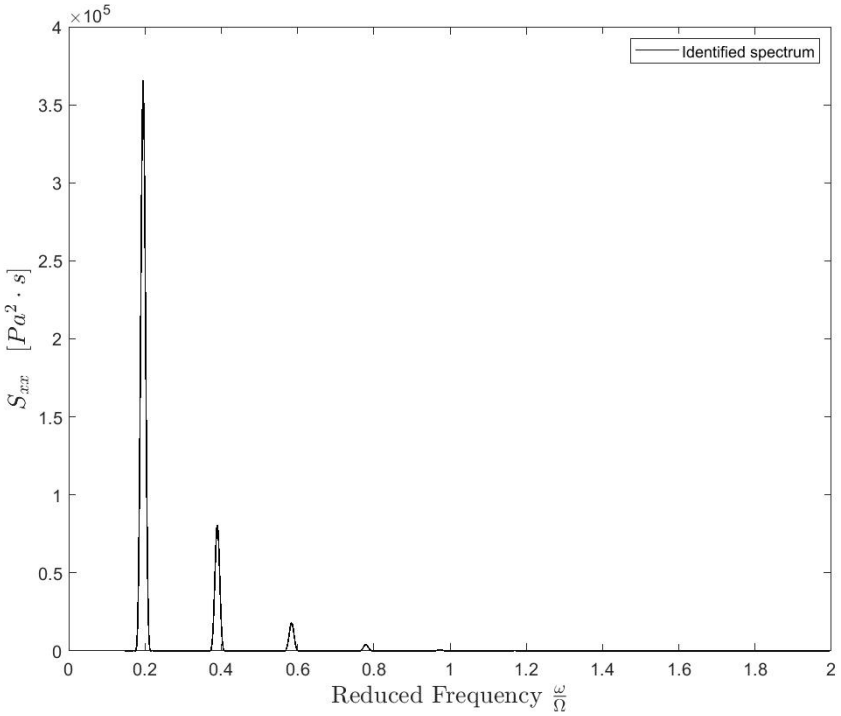

FIGURE 6.54: FULL-THEORETICAL AUTO-CORRELATION PRESSURE SPECTRUM FOR DAPAMITO 3 WITH Φ = 0.75 Φ_D, EULER NUMBER = 0.2169, N =5 VORTICES AND CLEARANCE = 0.8 MM.

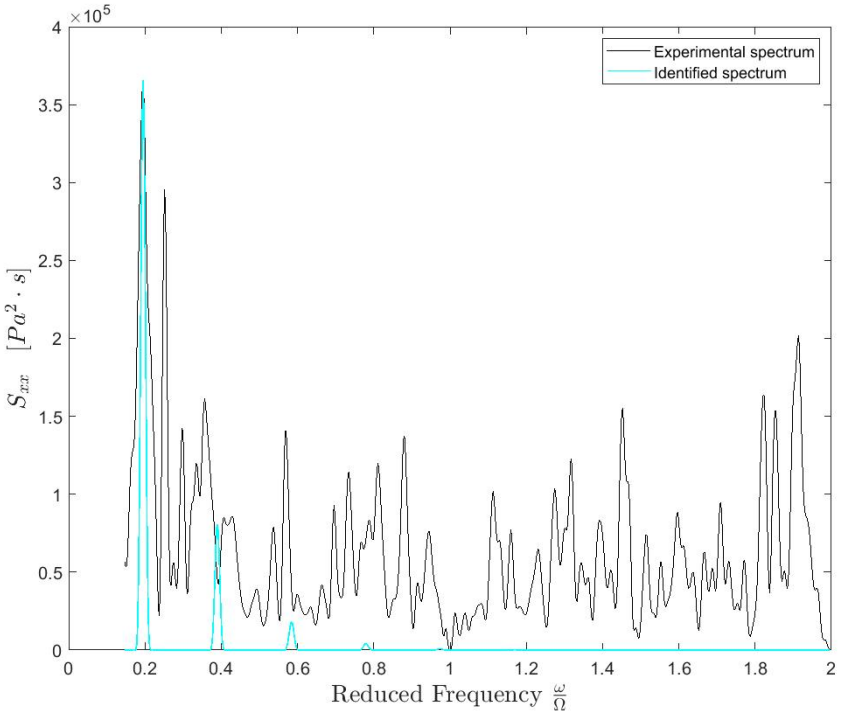

FIGURE 6.55: COMPARISON BETWEEN EXPERIMENTAL AUTO-CORRELATION SPECTRUM AND FULL-THEORETICAL SPECTRUM FOR DAPAMITO 3 WITH Φ = 0.75 Φ_D, EULER NUMBER = 0.2169, N =5 VORTICES AND CLEARANCE = 0.8 MM.

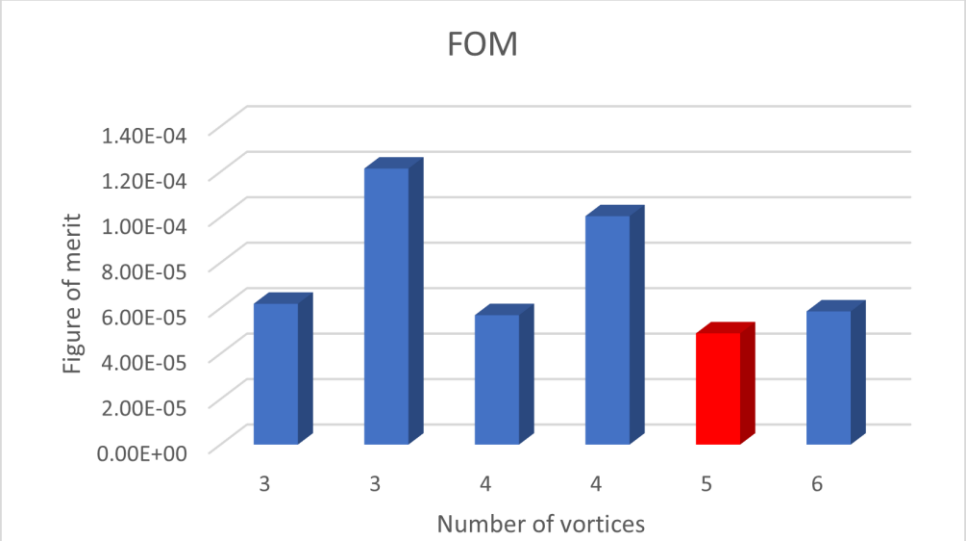

FIGURE 6.56: EVALUATION OF THE FIGURE OF MERIT WITH RESPECT TO THE NUMBER OF VORTICES FOR DAPAMITO 3 WITH Φ =0.75 Φ_D, EULER NUMBER = 0.2169 AND CLEARANCE = 0.8 MM.

N	ω/Ω	ε_{TOT}	Γ	ω_γ [rad/s]	a (%R)	σ_g
3	0.0634766	6.19E-05	0.03949	19.96	0.8136	0.19682
3	0.0830078	1.21E-04	0.03407	26.11	0.72756	0.19782
4	0.0488281	5.69E-05	0.04598	15.36	0.81852	0.19584
4	0.0634766	1.00E-04	0.04201	19.96	0.74463	0.19679
5	0.0390625	4.89E-05	0.03956±1.98	12.29±4.92E-5	0.87816±0.0097	0.19695
6	0.0317383	5.86E-05	0.04912	9.98	0.86988	0.19486

TABLE 6.19: IDENTIFICATION ASSESSMENT ASSOCIATED WITH BACKFLOW INSTABILITIES ON DAPAMITO 3 INDUCER, 75% OF DESIGN FLOW COEFFICIENT, EULER NUMBER = 0.2169 AND LOW CLEARANCE

- **σ = 0.2769**

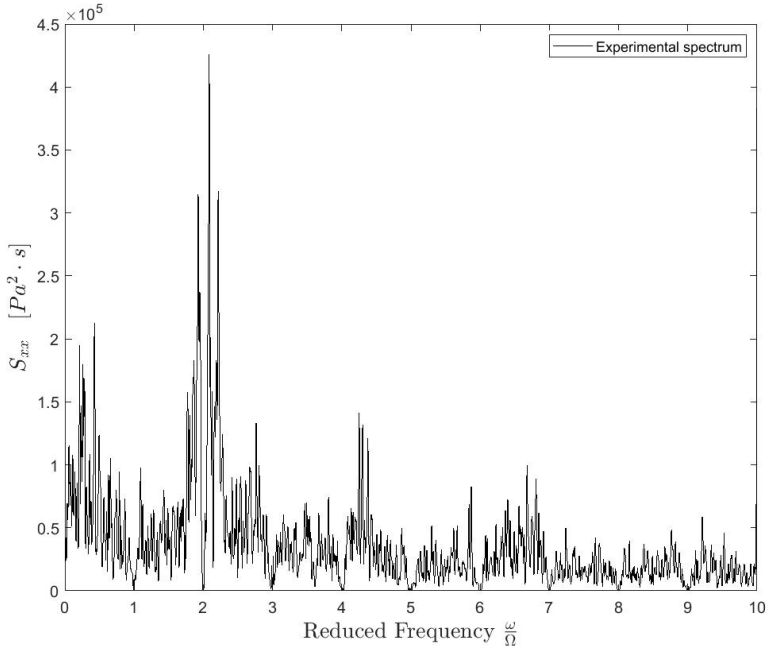

FIGURE 6.57: EXPERIMENTAL AUTO-CORRELATION PRESSURE SPECTRUM FOR DAPAMITO 3 WITH Φ =0.75 Φ_D, EULER NUMBER = 0.2769 AND CLEARANCE = 0.8 MM.

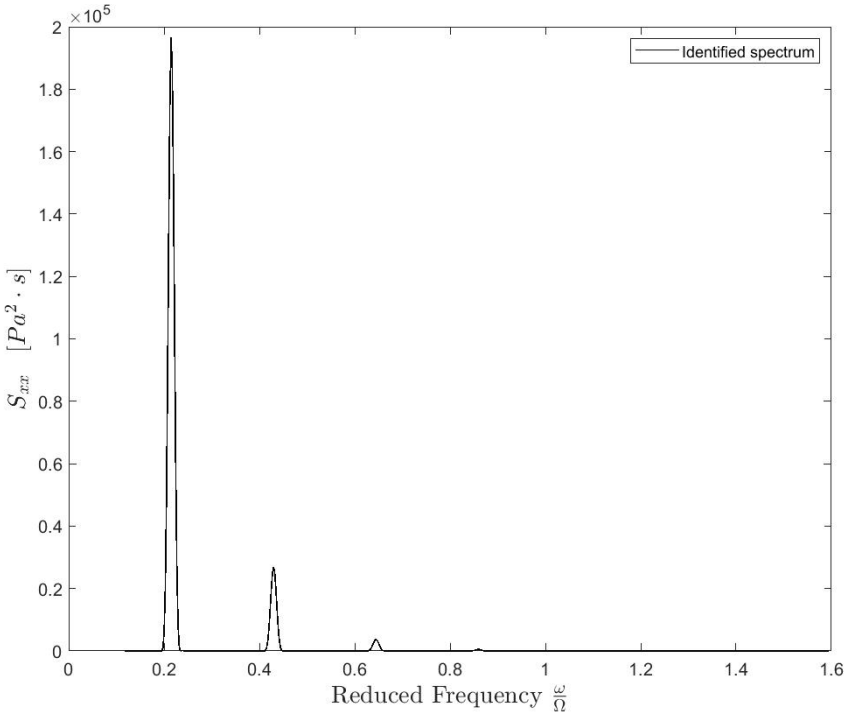

FIGURE 6.58: FULL-THEORETICAL AUTO-CORRELATION PRESSURE SPECTRUM FOR DAPAMITO 3 WITH Φ = 0.75 Φ_D, EULER NUMBER = 0.2769, N =4 VORTICES AND CLEARANCE = 0.8 MM.

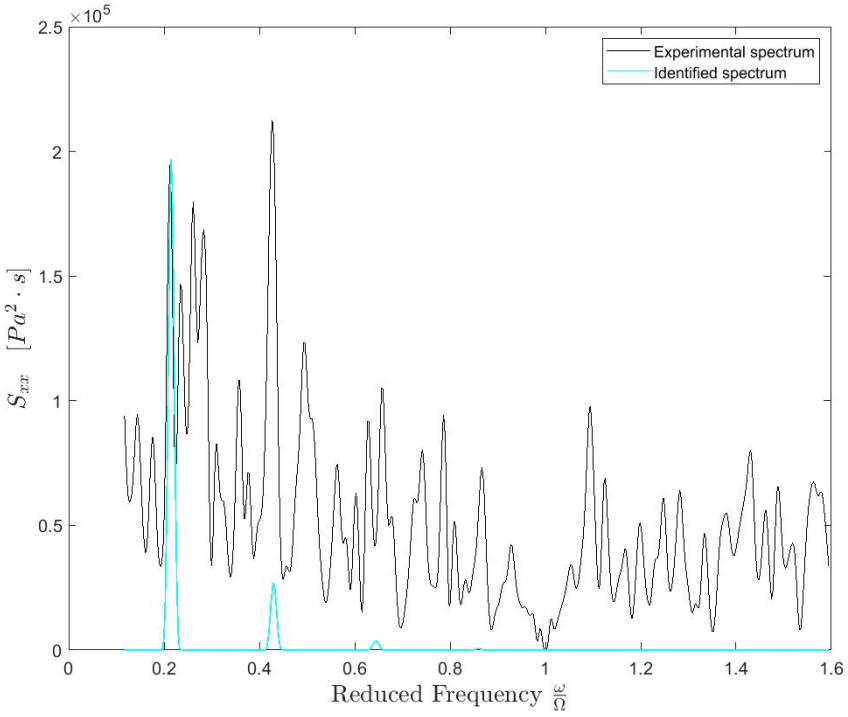

FIGURE 6.59: COMPARISON BETWEEN EXPERIMENTAL AUTO-CORRELATION SPECTRUM AND FULL-THEORETICAL SPECTRUM FOR DAPAMITO 3 WITH $\Phi = 0.75\ \Phi_D$, EULER NUMBER = 0.2769, N =4 VORTICES AND CLEARANCE = 0.8 MM.

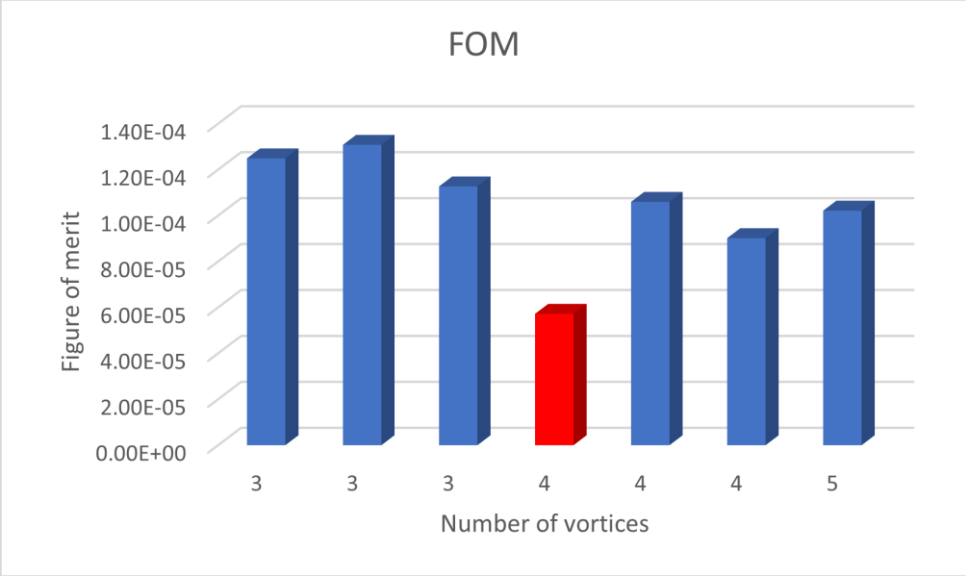

FIGURE 6.60: EVALUATION OF THE FIGURE OF MERIT WITH RESPECT TO THE NUMBER OF VORTICES FOR DAPAMITO 3 WITH $\Phi = 0.75\ \Phi_D$, EULER NUMBER = 0.2769 AND CLEARANCE = 0.8 MM.

N	ω/Ω	ε_{TOT}	Γ	ω_γ [rad/s]	a (%R)	σ_g
3	0.0708008	1.25E-04	0.05115	22.27	0.64285	0.19649
3	0.0878906	1.31E-04	0.03069	27.64	0.7038	0.1982
3	0.141602	1.13E-04	0.03393	44.53	0.5958	019801
4	0.0537109	5.72E-05	0.03379±1.14	16.89±5.75E-5	0.83939±0.012	0.19818
4	0.065918	1.06E-04	0.03745	20.73	0.73008	0.19731
4	0.107422	9.02E-05	0.02866	33.78	0.70492	0.19843
5	0.0854492	1.02E-04	0.04376	26.87	0.69616	0.19616

TABLE 6.20: IDENTIFICATION ASSESSMENT ASSOCIATED WITH BACKFLOW INSTABILITIES ON DAPAMITO 3 INDUCER, 75% OF DESIGN FLOW COEFFICIENT, EULER NUMBER = 0.2769 AND LOW CLEARANCE

Again, it can be seen that in the fourth Figure appearing in each studied case, the comparison between experimental auto-correlation spectrum and full-theoretical spectrum results in a very similar identified and experimental pressure spectrum. This is a proof of the importance of the method and its efficiency. However, it is important to stand out that the method developed takes some assumptions in order to be able to obtain robust identifications and the results must be analysed carefully. Also, it is observed that the confidence level relative to the rotational speed of the vortices is very small due to the initialization of the relative component in the initial parametric vector, which is set by the Bayesian estimator. However, for the vortex intensity the confidence interval values are very high and, although the nominal values seem acceptable, a detailed analysis must be performed.

6.3. DAPAMITO 4

Now, a similar study is developed for DAPAMITO 4 inducer. As it was said before, for the 4-bladed inducer, there is only a clearance of 0.8 mm. since the effect of the clearance is considered as analysed in DAPAMITO 3 inducer. In this case, the flow coefficients analysed are 84%, 76% and 63% of the design flow coefficient of the DAPAMITO 4 inducer (see Table 2.8).

6.3.1. $\Phi = 0.84 \cdot \Phi D$

It could be noted that in some of the configurations presented, there is a lower Euler of numbers that have been simulated. This is due to the fact that some Euler numbers because not meaningful identifications were found. The rest of them are presented in Table 6.21 for a flow coefficient 84% of the design flow coefficient.

σ	N	ω/Ω	ε_{TOT}	Γ	ω_γ [rad/s]	a (%R)	σ_g
0.1439	5	0.0415039	7.54E-05	0.04076	13.05	0.82419	0.19719
0.158	5	0.0317383	3.66E-05	0.04359	9.98	0.89572	0.19677
0.1969	7	0.0488281	3.14E-05	0.02782	15.36	0.88882	0.19875
0.2471	8	0.0341797	6.46E-05	0.02935	10.75	0.87539	0.19838
0.2662	8	0.0488281	5.09E-05	0.03954	15.36	0.81237	0.19686
0.3183	8	0.0439453	4.24E-05	0.03548	13.82	0.85033	0.19769

TABLE 6.21: IDENTIFICATION ASSESSMENT ASSOCIATED WITH BACKFLOW INSTABILITIES ON DAPAMITO 4 INDUCER, 84% OF DESIGN FLOW COEFFICIENT

- **σ = 0.1439**

The results are presented in Figures analysing the experimental pressure spectrum (Figure 6.61), the full-theoretical auto-correlation (Figure 6.62), and the comparison between identified and experimental spectrum to analyse if the method is able to identify backflow vortex instability (Figure 6.63). Finally, a Table with quantitative analysis of the studied case (Table 6.22) and a Figure describing the evolution of the figure of merit for the number of vortices studied of peaks in which the correlation-coefficient is high is presented (Figure 6.64).

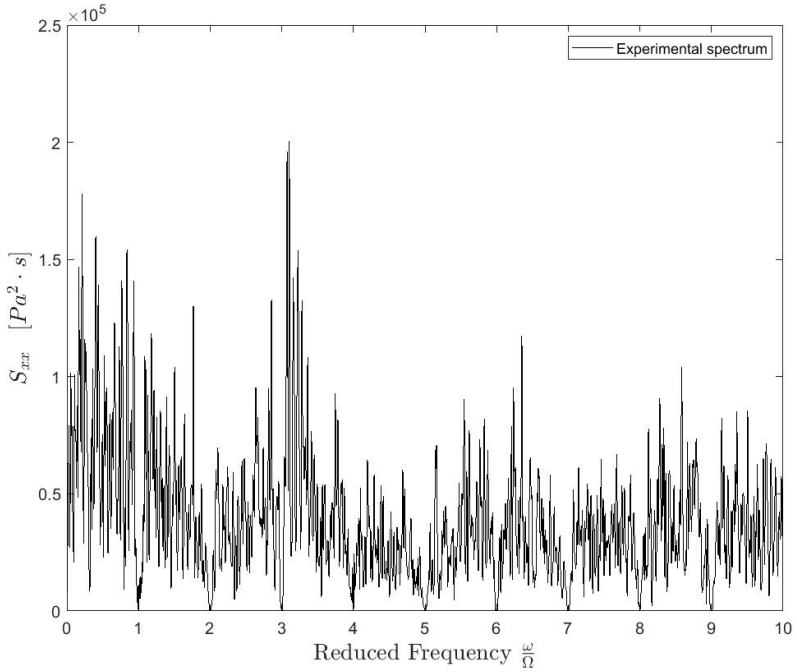

FIGURE 6.61: EXPERIMENTAL AUTO-CORRELATION PRESSURE SPECTRUM FOR DAPAMITO 4 WITH Φ =0.84 Φ_D, EULER NUMBER = 0.1439.

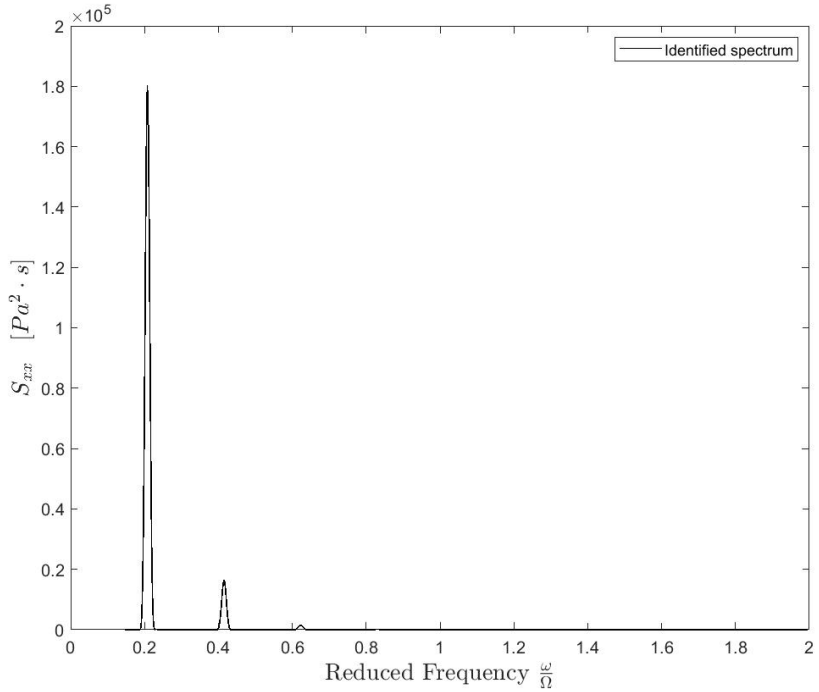

FIGURE 6.62: FULL-THEORETICAL AUTO-CORRELATION PRESSURE SPECTRUM FOR DAPAMITO 4 WITH Φ = 0.84 Φ_D, EULER NUMBER = 0.1439, N =5 VORTICES

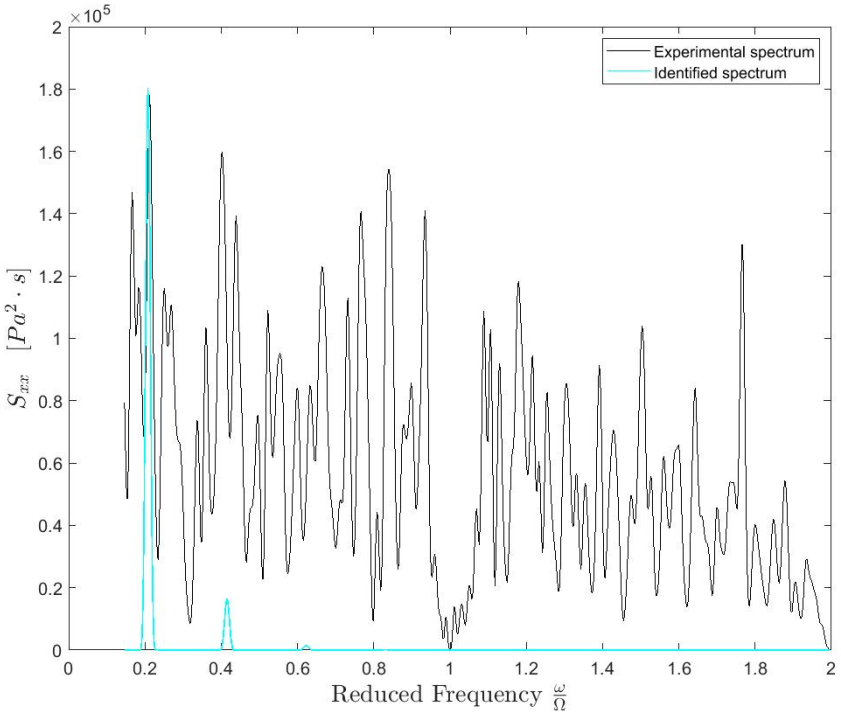

FIGURE 6.63: COMPARISON BETWEEN EXPERIMENTAL AUTO-CORRELATION SPECTRUM AND FULL-THEORETICAL SPECTRUM FOR DAPAMITO 4 WITH $\Phi = 0.84\ \Phi_D$, EULER NUMBER = 0.1439, N =5 VORTICES

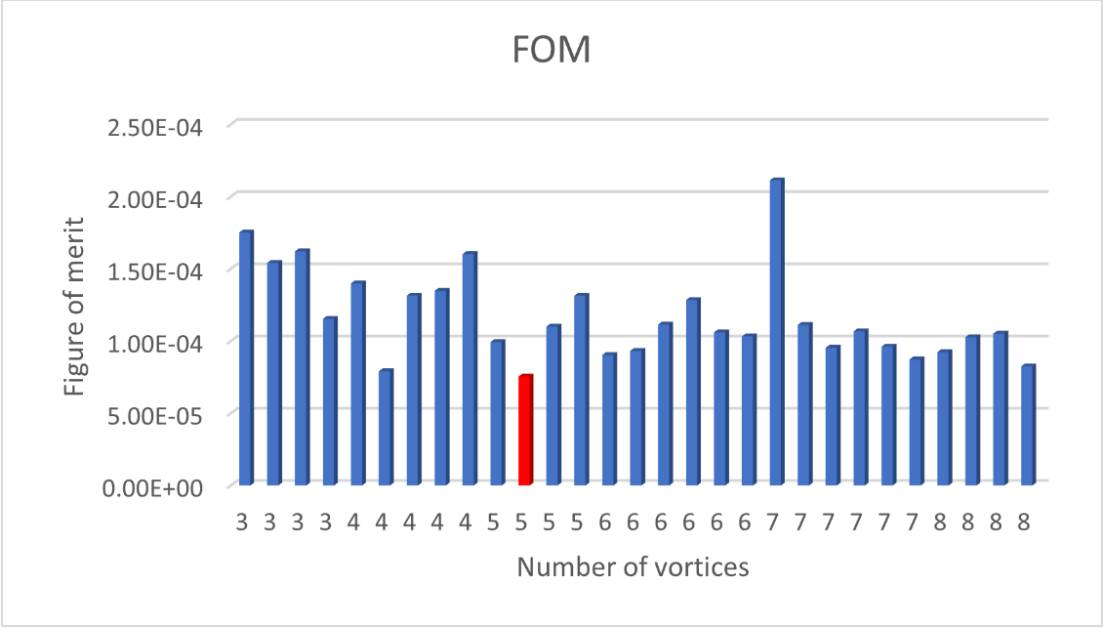

FIGURE 6.64: EVALUATION OF THE FIGURE OF MERIT WITH RESPECT TO THE NUMBER OF VORTICES FOR DAPAMITO 4 WITH $\Phi = 0.84\ \Phi_D$, EULER NUMBER = 0.1439

N	ω/Ω	ε_{TOT}	Γ	ω_γ [rad/s]	a (%R)	σ_g
3	0.0561523	1.75E-04	0.04018	17.66	0.72469	0.19713
3	0.0708008	1.54E-04	0.05743	22.27	0.60908	0.19496
3	0.134277	1.62E-04	0.02872	42.23	0.61861	0.19854
3	0.146484	1.15E-04	0.02801	46.07	0.64332	0.19872
4	0.0415039	1.40E-04	0.03636	13.05	0.80752	0.19721
4	0.0537109	7.91E-05	0.03328	16.89	0.82793	0.19823
4	0.0634766	1.31E-04	0.03509	19.96	0.74418	0.19759
4	0.100098	1.35E-04	0.05183	31.48	0.59946	0.19576
4	0.109863	1.60E-04	0.04982	34.55	0.57976	0.1962
5	0.0341797	9.93E-05	0.03974	10.75	0.83654	0.19681
5	0.0415039	7.54E-05	0.04076±2.84	13.05±7.56E-5	0.82419±0.026	0.19719
5	0.0805664	1.10E-04	0.03768	25.33	0.70883	0.19715
5	0.0878906	1.31E-04	0.03531	27.64	0.69416	0.19753
6	0.0341797	9.03E-05	0.0378	10.75	0.83949	0.19701
6	0.065918	9.32E-05	0.03524	20.73	0.76197	0.19792
6	0.0732422	1.11E-04	0.0405	23.03	0.72055	0.19714
6	0.109863	1.28E-04	0.03084	34.55	0.69739	0.19816
6	0.129395	1.06E-04	0.02345	40.69	0.72219	0.19912
6	0.13916	1.03E-04	0.02681	43.77	0.69867	0.19866
7	0.0292969	2.11E-04	0.04421	9.21	0.85017	0.1958
7	0.0366211	1.11E-04	0.03992	11.52	0.8103	0.19693
7	0.0585937	9.54E-05	0.03139	18.43	0.7933	0.19805
7	0.0634766	1.07E-04	0.03362	19.96	0.7706	0.19777
7	0.109863	9.62E-05	0.03829	34.55	0.70425	0.19725
7	0.119629	8.73E-05	0.04404	37.62	0.68614	0.1965
8	0.0512695	9.24E-05	0.03735	16.12	0.79858	0.19718
8	0.0830078	1.03E-04	0.02759	26.11	0.77665	0.19853
8	0.0952148	1.05E-04	0.02513	29.95	0.77137	0.1988
8	0.10498	8.25E-05	0.02375	33.02	0.77891	0.19906

TABLE 6.22: IDENTIFICATION ASSESSMENT ASSOCIATED WITH BACKFLOW INSTABILITIES ON DAPAMITO 4 INDUCER, 84% OF DESIGN FLOW COEFFICIENT, EULER NUMBER = 0.1439

- **σ = 0.2471**

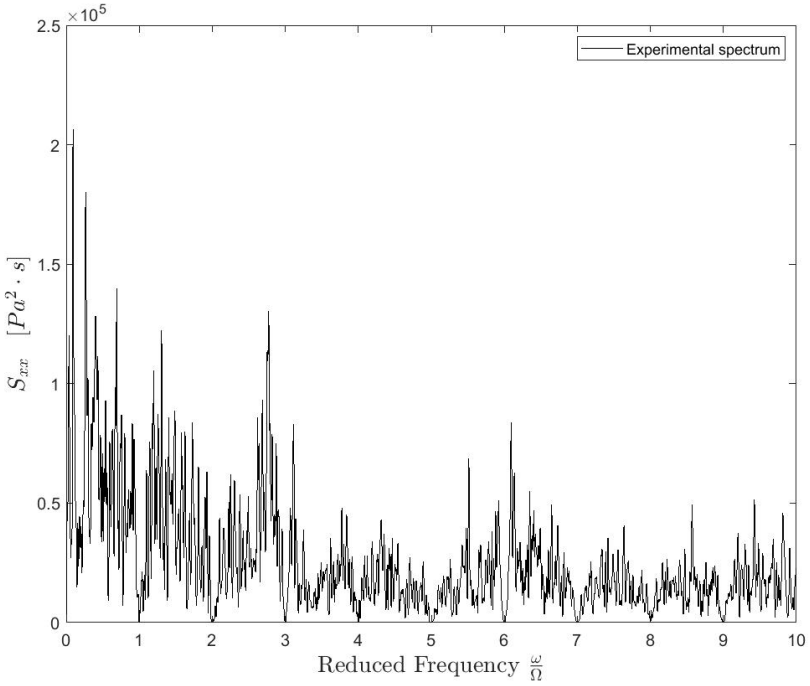

FIGURE 6.65: EXPERIMENTAL AUTO-CORRELATION PRESSURE SPECTRUM FOR DAPAMITO 4 WITH Φ =0.84 Φ_D, EULER NUMBER = 0.2471.

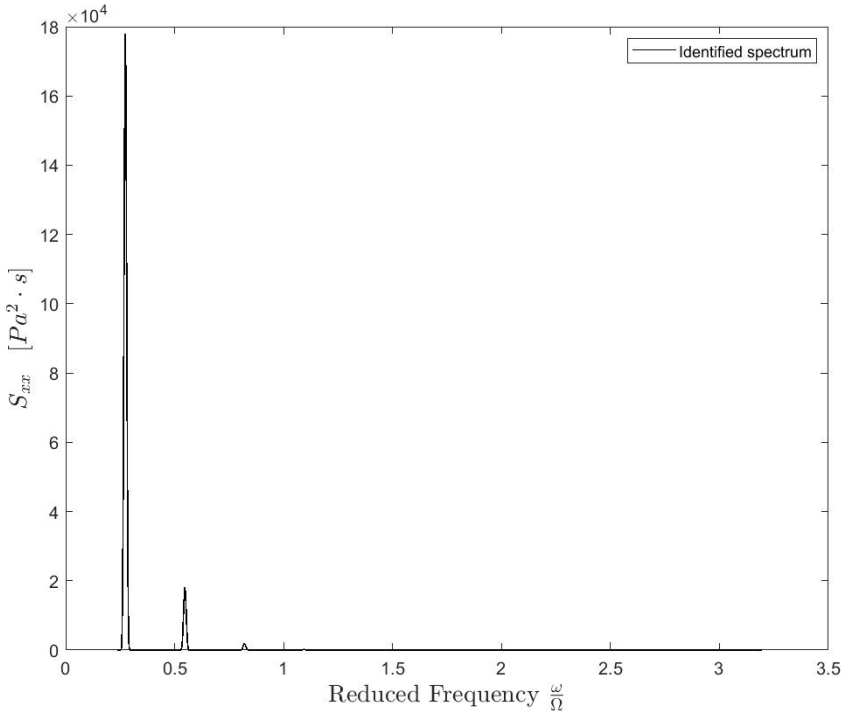

FIGURE 6.66: FULL-THEORETICAL AUTO-CORRELATION PRESSURE SPECTRUM FOR DAPAMITO 4 WITH Φ = 0.84 Φ_D, EULER NUMBER = 0.2471, N =8 VORTICES

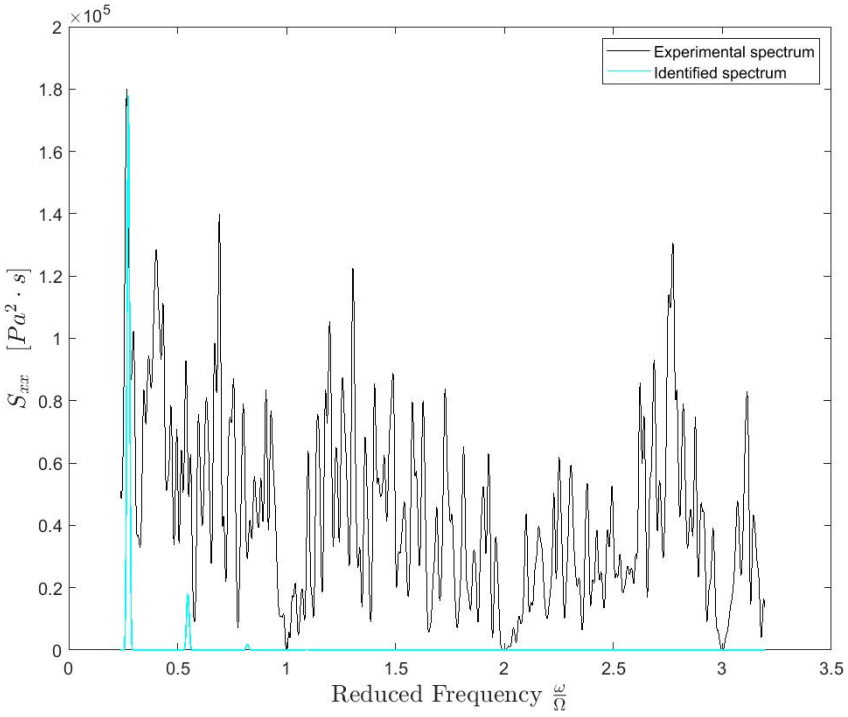

FIGURE 6.67: COMPARISON BETWEEN EXPERIMENTAL AUTO-CORRELATION SPECTRUM AND FULL-THEORETICAL SPECTRUM FOR DAPAMITO 4 WITH $\Phi = 0.84\ \Phi_D$, EULER NUMBER = 0.2471, N =8 VORTICES

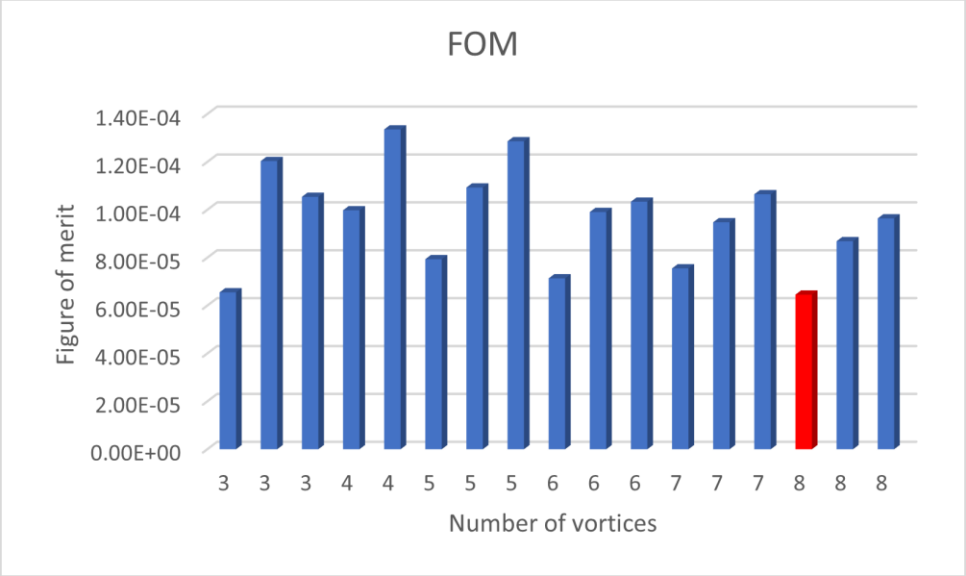

FIGURE 6.68: EVALUATION OF THE FIGURE OF MERIT WITH RESPECT TO THE NUMBER OF VORTICES FOR DAPAMITO 4 WITH $\Phi = 0.84\ \Phi_D$, EULER NUMBER = 0.2471

N	ω/Ω	ε_{TOT}	Γ	ω_γ [rad/s]	a (%R)	σ_g
3	0.0317383	6.55E-05	0.04399	9.98	0.88993	0.19607
3	0.0878906	1.20E-04	0.02977	27.64	0.71465	0.19835
3	0.134277	1.05E-04	0.02799	42.23	0.65437	0.19871
4	0.065918	9.98E-05	0.03672	20.73	0.73652	0.19748
4	0.100098	1.34E-04	0.04427	31.48	0.61291	0.19694
5	0.0537109	7.94E-05	0.03305	16.89	0.80014	0.19777
5	0.0805664	1.09E-04	0.02673	25.34	0.74928	0.19833
5	0.136719	1.29E-04	0.03206	43.00	0.64019	0.19833
6	0.0439453	7.14E-05	0.03962	13.82	0.80528	0.19678
6	0.065918	9.91E-05	0.03475	20.73	0.75108	0.19788
6	0.114746	1.03E-04	0.02559	36.09	0.71882	0.19879
7	0.0390625	7.55E-05	0.05054	12.29	0.79113	0.19522
7	0.0585937	9.48E-05	0.02737	18.43	0.80429	0.19857
7	0.0976562	1.07E-04	0.03023	30.71	0.73134	0.19828
8	0.0341797	6.46E-05	0.02935±4.10	10.75±6.47E-5	0.87539±0.028	0.19838
8	0.0512695	8.69E-05	0.0346	16.12	0.8018	0.19762
8	0.0854492	9.64E-05	0.02778	26.87	0.76878	0.19847

TABLE 6.23: IDENTIFICATION ASSESSMENT ASSOCIATED WITH BACKFLOW INSTABILITIES ON DAPAMITO 4 INDUCER, 84% OF DESIGN FLOW COEFFICIENT, EULER NUMBER = 0.2471

- **σ = 0.3183**

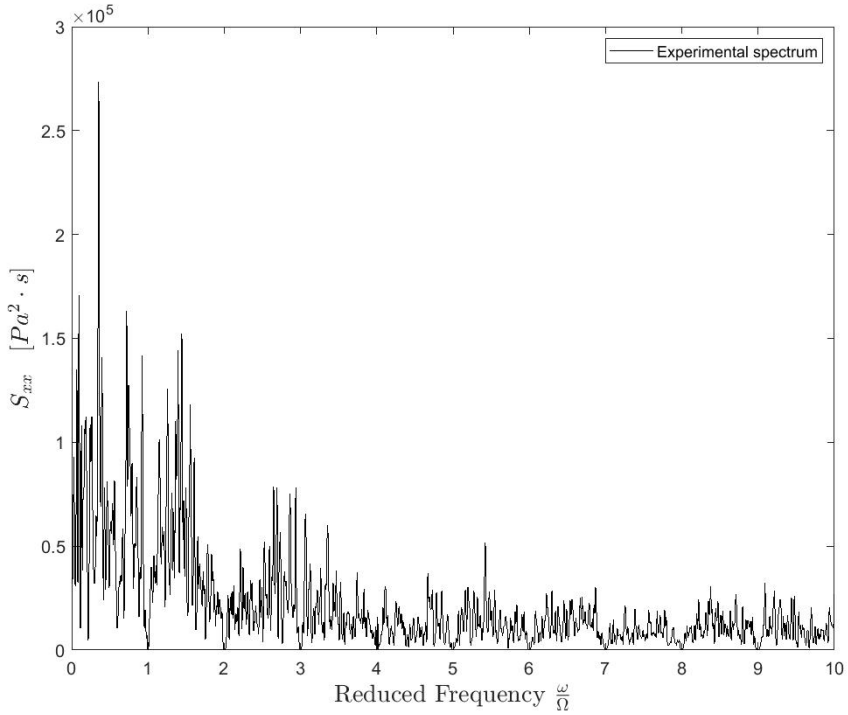

FIGURE 6.69: EXPERIMENTAL AUTO-CORRELATION PRESSURE SPECTRUM FOR DAPAMITO 4 WITH Φ =0.84 Φ_D, EULER NUMBER = 0.3183.

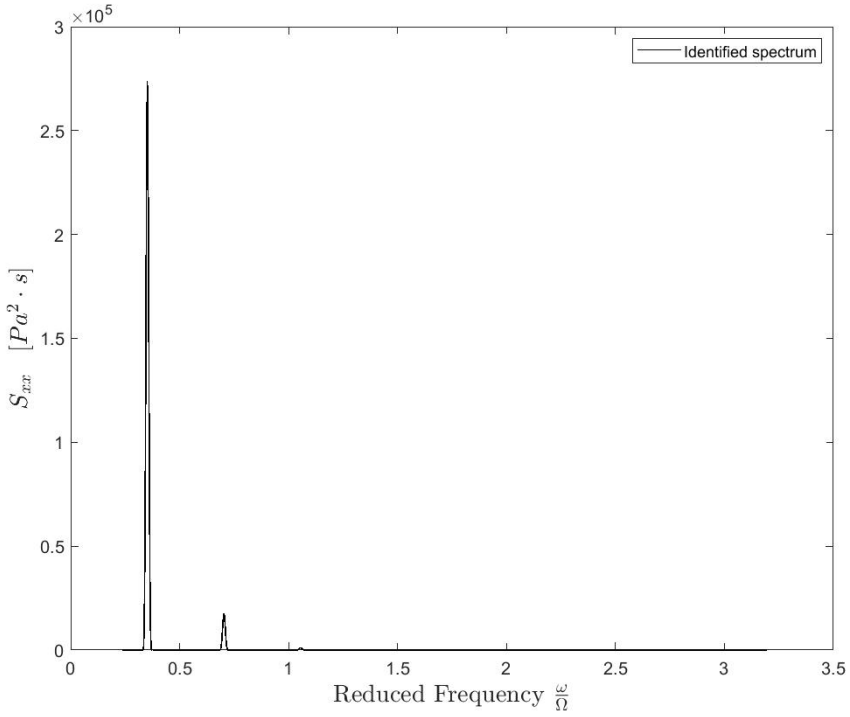

FIGURE 6.70: FULL-THEORETICAL AUTO-CORRELATION PRESSURE SPECTRUM FOR DAPAMITO 4 WITH Φ = 0.84 Φ_D, EULER NUMBER = 0.3183, N =8 VORTICES

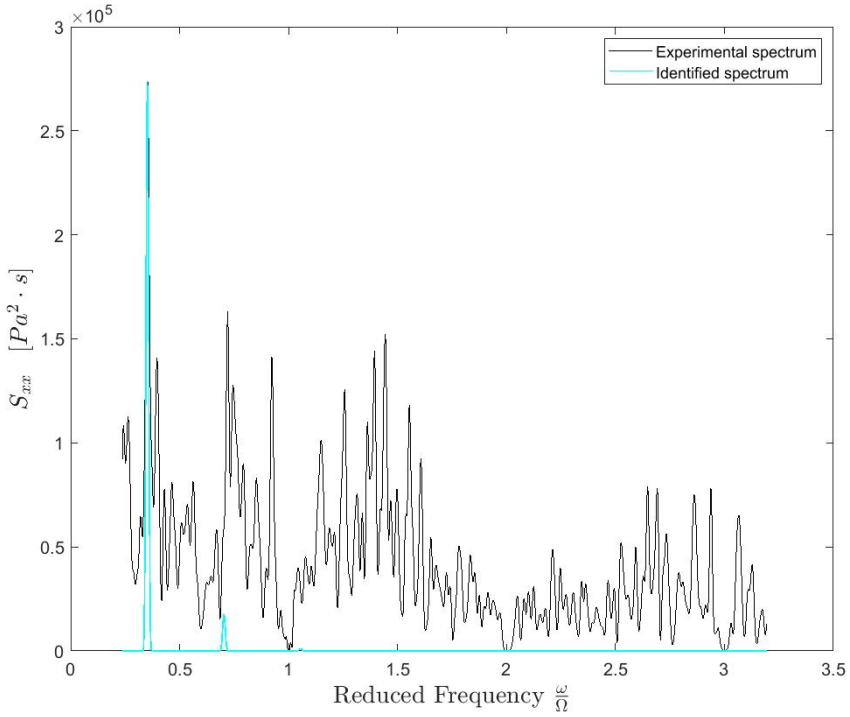

FIGURE 6.71: COMPARISON BETWEEN EXPERIMENTAL AUTO-CORRELATION SPECTRUM AND FULL-THEORETICAL SPECTRUM FOR DAPAMITO 4 WITH Φ = 0.84 Φ_D, EULER NUMBER = 0.3183, N =8 VORTICES

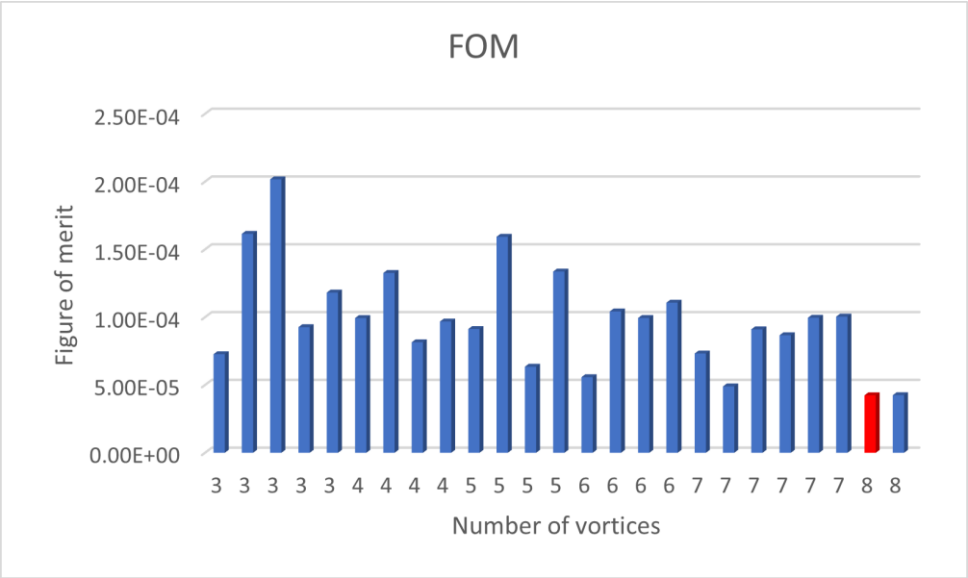

FIGURE 6.72: EVALUATION OF THE FIGURE OF MERIT WITH RESPECT TO THE NUMBER OF VORTICES FOR DAPAMITO 4 WITH Φ =0.84 Φ_D, EULER NUMBER = 0.3183

N	ω/Ω	ε_{TOT}	Γ	ω_γ [rad/s]	a (%R)	σ_g
3	0.0317383	7.27E-05	0.04245	9.98	0.89586	0.19643
3	0.0585937	1.61E-04	0.04045	18.43	0.71624	0.19698
3	0.0878906	2.02E-04	0.05057	27.64	0.56402	0.19652
3	0.117187	9.26E-05	0.03726	36.86	0.63744	0.19738
3	0.131836	1.18E-04	0.02799	41.46	0.65676	0.19871
4	0.0439453	9.94E-05	0.03298	13.82	0.8434	0.19779
4	0.065918	1.33E-04	0.03591	20.73	0.7325	0.19749
4	0.0878906	8.15E-05	0.05227	27.64	0.65483	0.19646
4	0.0976562	9.68E-05	0.04115	30.71	0.66878	0.1973
5	0.0366211	9.12E-05	0.04008	11.39	0.83018	0.19675
5	0.0488281	1.59E-04	0.04368	15.36	0.73233	0.19651
5	0.0708008	6.35E-05	0.03302	22.27	0.78356	0.19788
5	0.078125	1.34E-04	0.02629	24.57	0.75203	0.19882
6	0.0585937	5.58E-05	0.05081	18.43	0.75636	0.19524
6	0.065918	1.04E-04	0.03415	20.73	0.75714	0.19805
6	0.119629	9.94E-05	0.02431	37.62	0.72891	0.19902
6	0.124512	1.11E-04	0.02293	39.16	0.72499	0.19918
7	0.0366211	7.32E-05	0.03652	11.52	0.84213	0.19749
7	0.0512695	4.90E-05	0.02864	16.12	0.85225	0.19849
7	0.0561523	9.10E-05	0.0267	17.66	0.81641	0.19865
7	0.102539	8.67E-05	0.03214	32.25	0.73213	0.19821
7	0.107422	9.96E-05	0.03171	33.78	0.7218	0.19824
7	0.131836	1.00E-04	0.04335	41.46	0.66923	0.19666
8	0.0439453	4.24E-05	0.03548±3.36	13.82±4.24E-5	0.85033±0.029	0.19769
8	0.090332	4.25E-05	0.02603	28.41	0.81168	0.19873

TABLE 6.24: IDENTIFICATION ASSESSMENT ASSOCIATED WITH BACKFLOW INSTABILITIES ON DAPAMITO 4 INDUCER, 84% OF DESIGN FLOW COEFFICIENT, EULER NUMBER = 0.3183

6.3.2. $\Phi = 0.76 \cdot \Phi_D$

For the analysed case of flow coefficient 76% of the design flow coefficient, again similar values of Euler number are analysed to make easy for the reader to compare between the different cases of the DAPAMITO 4 inducer. In Table 6.25 is shown the Euler number studied which granted a meaningful identification and 3 Euler numbers are presented in detail for the evaluated case.

σ	N	ω/Ω	ε_{TOT}	Γ	ω_γ [rad/s]	a (%R)	σ_g
0.1226	6	0.0366211	5.44E-05	0.02863	11.52	0.89547	0.19868
0.1341	5	0.0317383	4.70E-05	0.05153	9.98	0.86575	0.1952
0.143	6	0.0317383	4.59E-05	0.03185	9.98	0.91567	0.19826
0.158	4	0.0512695	5.49E-05	0.04088	16.12	0.84006	0.19671
0.2458	5	0.0488281	8.26E-05	0.05141	15.36	0.75564	0.19537
0.3224	7	0.0390625	4.14E-05	0.03123	12.29	0.88458	0.19803
0.3393	6	0.0292969	3.16E-05	0.03393	9.21	0.94345	0.1978

TABLE 6.25: IDENTIFICATION ASSESSMENT ASSOCIATED WITH BACKFLOW INSTABILITIES ON DAPAMITO 4 INDUCER, 76% OF DESIGN FLOW COEFFICIENT

In each simulation of a fixed Euler number, it is presented the information as in the previous cases, through 4 Figures representing auto-correlations and comparison between identified and experimental auto-correlations as well as the evolution of the figure of merit with the number of vortices analysed. Also, there is a Table with a quantitative summary of the parameters found for the studied configuration.

- **σ = 0.143**

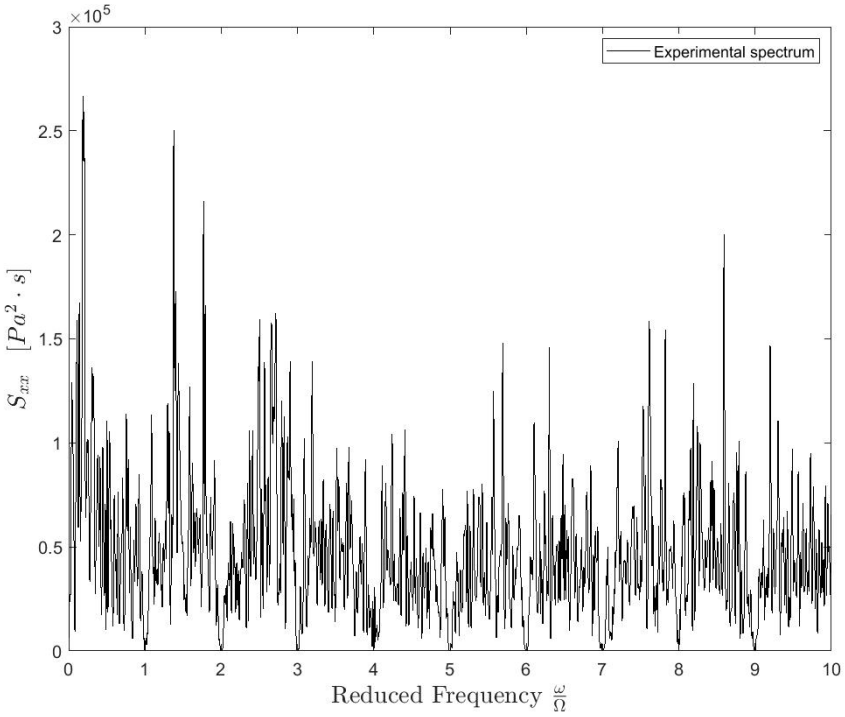

FIGURE 6.73: EXPERIMENTAL AUTO-CORRELATION PRESSURE SPECTRUM FOR DAPAMITO 4 WITH $\Phi = 0.76\ \Phi_D$, EULER NUMBER = 0.143.

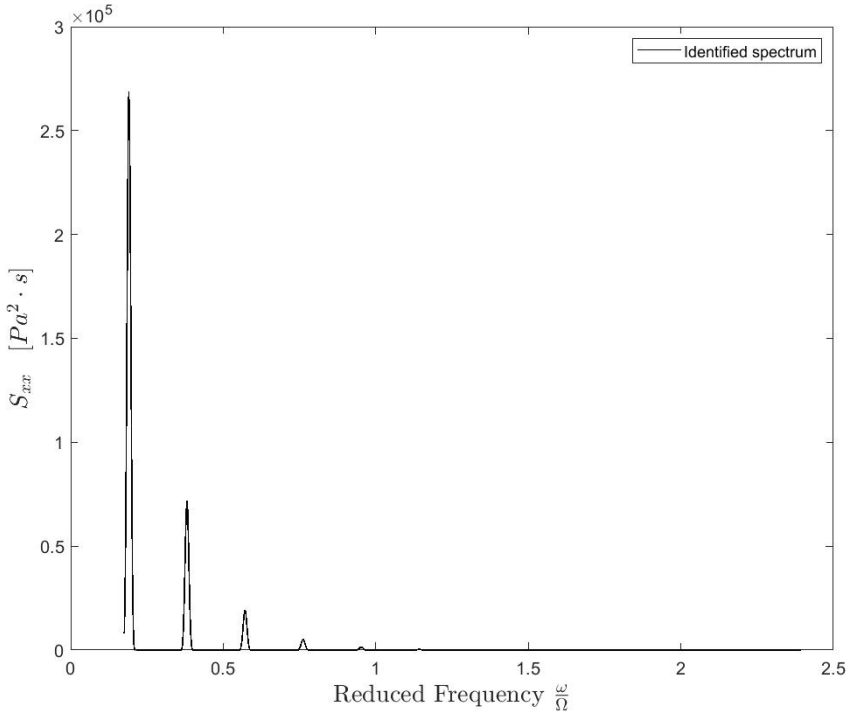

FIGURE 6.74: FULL-THEORETICAL AUTO-CORRELATION PRESSURE SPECTRUM FOR DAPAMITO 4 WITH Φ = 0.76 Φ_D, EULER NUMBER = 0.143, N =6 VORTICES

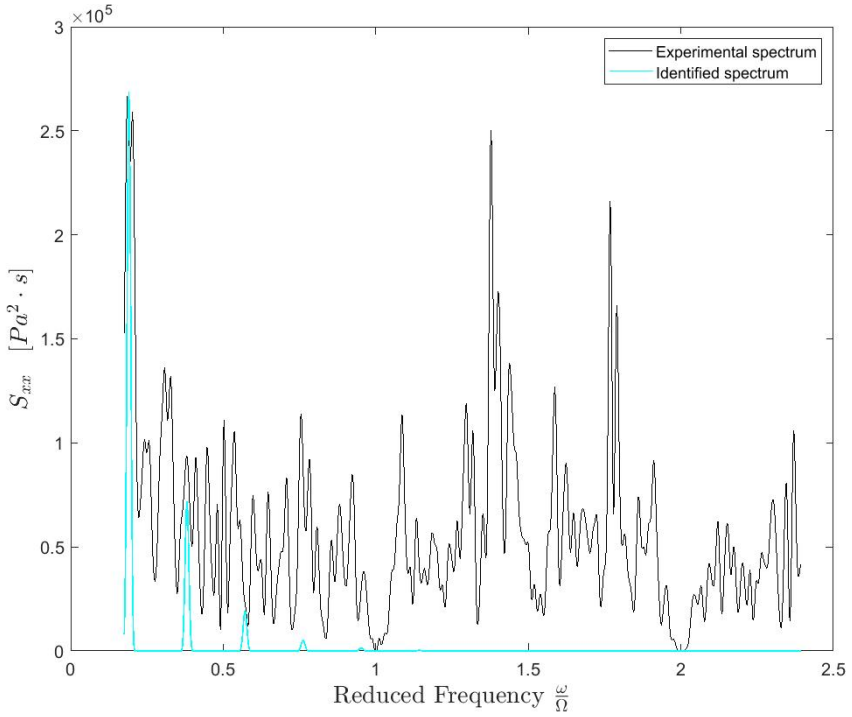

FIGURE 6.75: COMPARISON BETWEEN EXPERIMENTAL AUTO-CORRELATION SPECTRUM AND FULL-THEORETICAL SPECTRUM FOR DAPAMITO 4 WITH Φ = 0.76 Φ_D, EULER NUMBER = 0.143, N =6 VORTICES

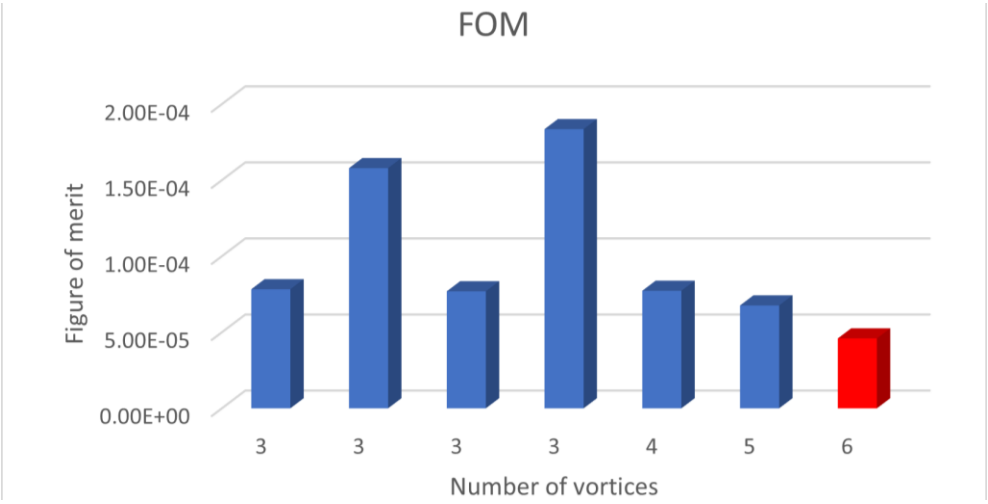

FIGURE 6.76: EVALUATION OF THE FIGURE OF MERIT WITH RESPECT TO THE NUMBER OF VORTICES FOR DAPAMITO 4 WITH Φ =0.76 Φ_D, EULER NUMBER = 0.143

N	ω/Ω	ε_{TOT}	Γ	ω_γ [rad/s]	a (%R)	σ_g
3	0.0366211	7.83E-05	0.03962	11.52	0.88484	0.19719
3	0.0463867	1.58E-04	0.04341	14.59	0.76015	0.19628
3	0.0634766	7.69E-05	0.04091	19.96	0.77368	0.19645
3	0.102539	1.84E-04	0.02769	32.25	0.67099	0.19862
4	0.0488281	7.73E-05	0.05088	15.36	0.77155	0.1946
5	0.0390625	6.76E-05	0.05582	12.29	0.79816	0.19488
6	0.0317383	4.59E-05	0.03185±2.12	9.98±4.62E-5	0.91567±0.0076	0.19826

TABLE 6.26: IDENTIFICATION ASSESSMENT ASSOCIATED WITH BACKFLOW INSTABILITIES ON DAPAMITO 4 INDUCER, 76% OF DESIGN FLOW COEFFICIENT, EULER NUMBER = 0.143

- **σ = 0.2458**

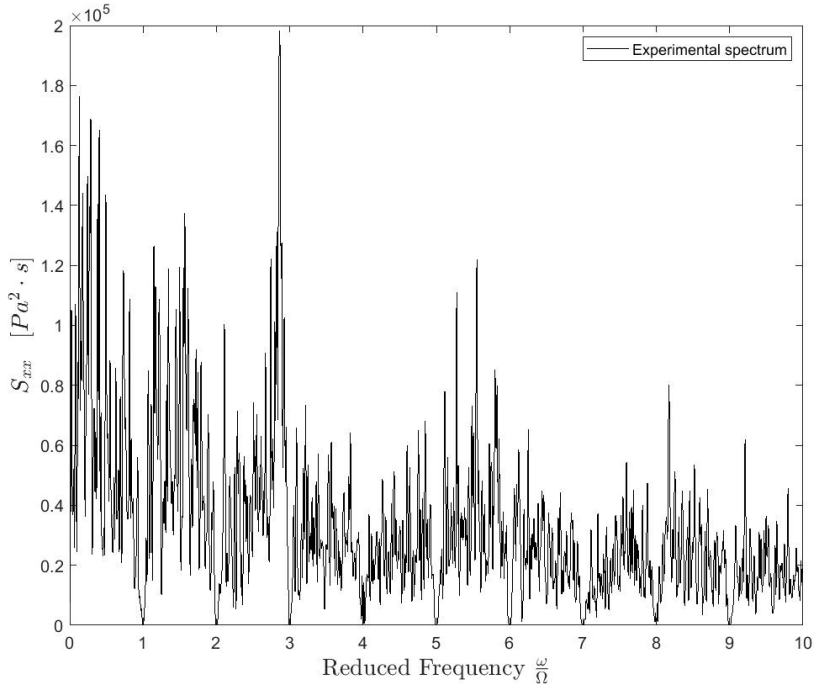

FIGURE 6.77: EXPERIMENTAL AUTO-CORRELATION PRESSURE SPECTRUM FOR DAPAMITO 4 WITH Φ =0.76 Φ_D, EULER NUMBER = 0.2458.

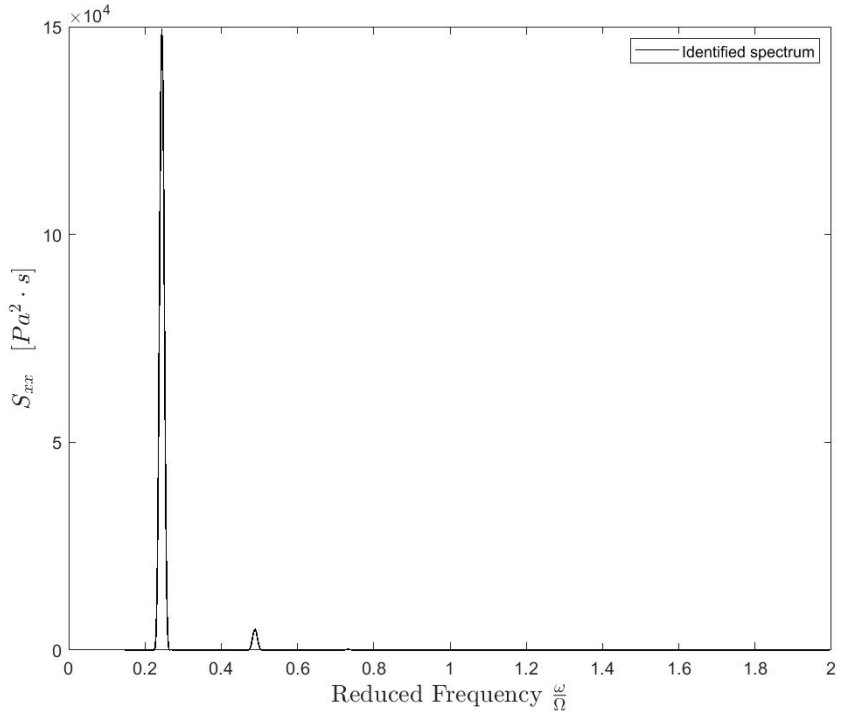

FIGURE 6.78: FULL-THEORETICAL AUTO-CORRELATION PRESSURE SPECTRUM FOR DAPAMITO 4 WITH Φ = 0.76 Φ_D, EULER NUMBER = 0.2458, N =5 VORTICES

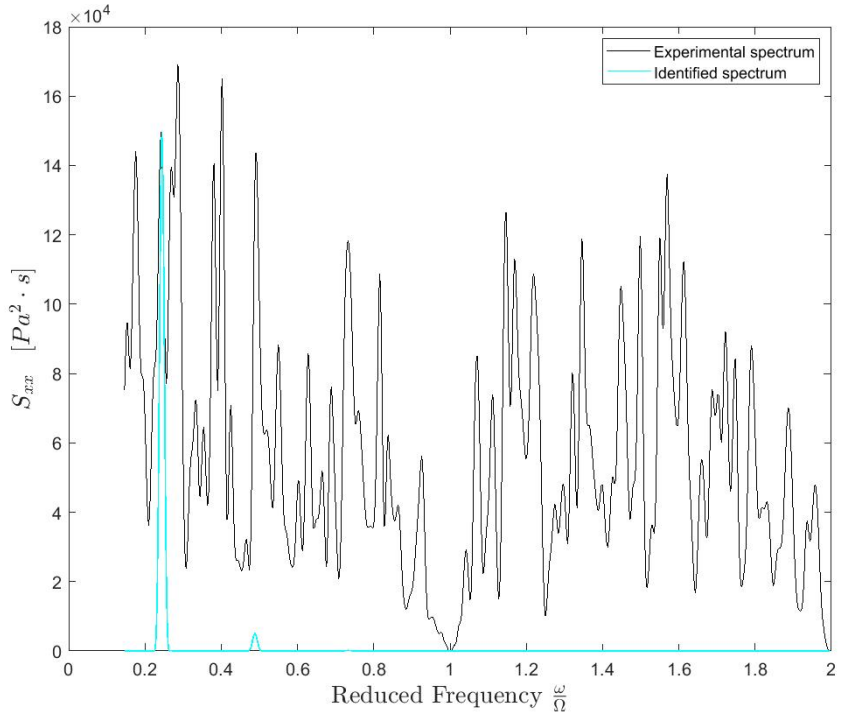

FIGURE 6.79: COMPARISON BETWEEN EXPERIMENTAL AUTO-CORRELATION SPECTRUM AND FULL-THEORETICAL SPECTRUM FOR DAPAMITO 4 WITH Φ = 0.76 Φ_D, EULER NUMBER = 0.2458, N =5 VORTICES

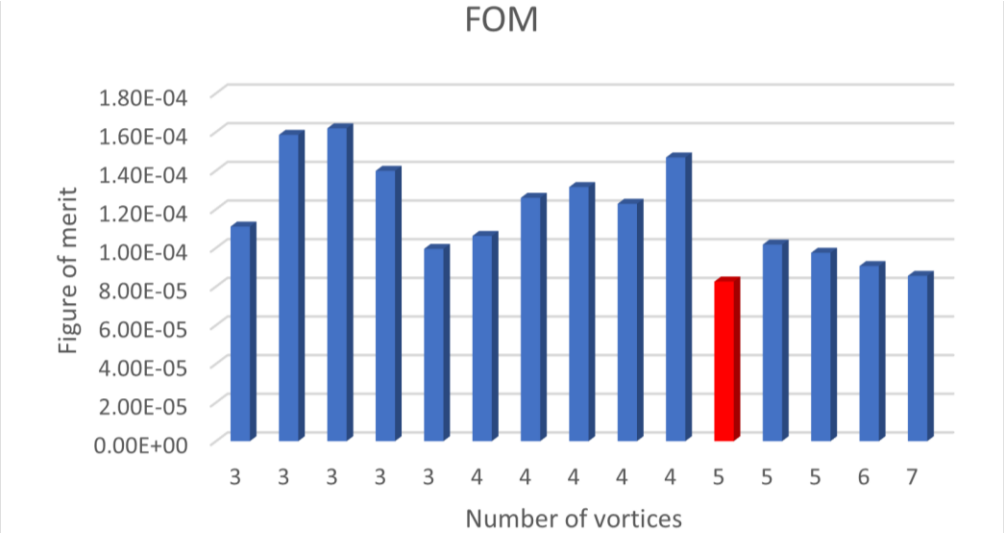

FIGURE 6.80: EVALUATION OF THE FIGURE OF MERIT WITH RESPECT TO THE NUMBER OF VORTICES FOR DAPAMITO 4 WITH $\Phi = 0.76\ \Phi_D$, EULER NUMBER = 0.2458

N	ω/Ω	ε_{TOT}	Γ	ω_γ [rad/s]	a (%R)	σ_g
3	0.0439453	1.11E-04	0.04357	13.82	0.79676	0.19622
3	0.0585937	1.59E-04	0.04084	18.43	0.71294	0.19721
3	0.0805664	1.62E-04	0.04946	25.34	0.60262	0.19727
3	0.0952148	1.40E-04	0.03	29.95	0.68776	0.19834
3	0.134277	9.95E-05	0.02872	42.23	0.66291	0.19864
4	0.0317383	1.06E-04	0.05214	9.98	0.8123	0.19562
4	0.0439453	1.26E-04	0.03559	13.82	0.80881	0.19752
4	0.0610352	1.31E-04	0.03432	19.20	0.75229	0.19764
4	0.0708008	1.23E-04	0.03776	22.27	0.71419	0.1974
4	0.100098	1.47E-04	0.04826	31.48	0.60299	0.19622
5	0.0488281	8.26E-05	0.05141±4.33	15.36±8.27E-5	0.75564±0.061	0.19537
5	0.0561523	1.02E-04	0.03236	17.66	0.78964	0.19789
5	0.0805664	9.75E-05	0.02731	25.34	0.76527	0.19879
6	0.0463867	9.06E-05	0.04547	14.59	0.77357	0.19566
7	0.0390625	8.55E-05	0.04749	12.29	0.7968	0.19584

TABLE 6.27: IDENTIFICATION ASSESSMENT ASSOCIATED WITH BACKFLOW INSTABILITIES ON DAPAMITO 4 INDUCER, 76% OF DESIGN FLOW COEFFICIENT, EULER NUMBER = 0.2458

- **σ = 0.3393**

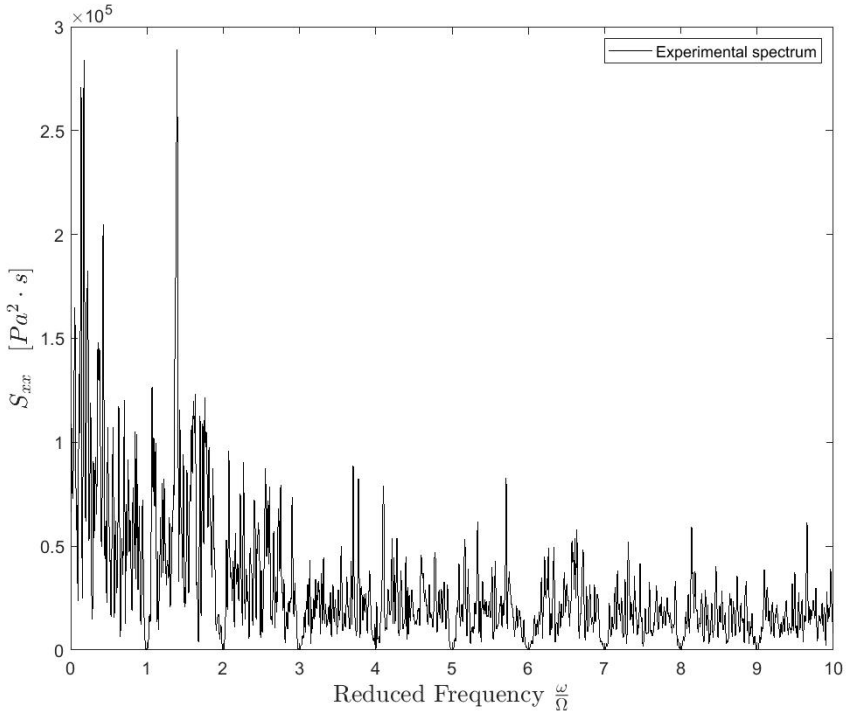

FIGURE 6.81: EXPERIMENTAL AUTO-CORRELATION PRESSURE SPECTRUM FOR DAPAMITO 4 WITH Φ =0.76 Φ_D, EULER NUMBER = 0.3393.

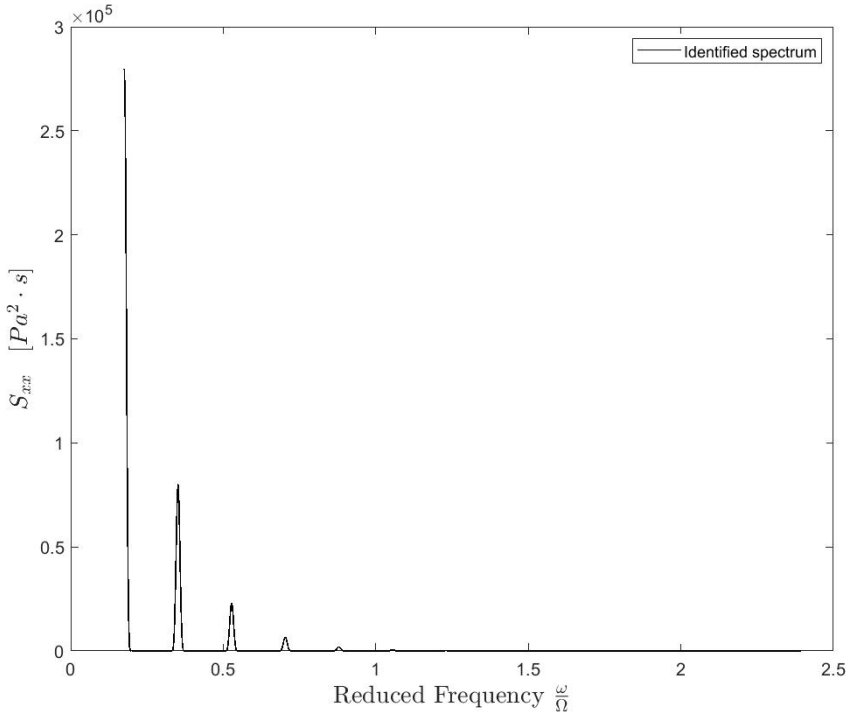

FIGURE 6.82: FULL-THEORETICAL AUTO-CORRELATION PRESSURE SPECTRUM FOR DAPAMITO 4 WITH Φ = 0.76 Φ_D, EULER NUMBER = 0.3393, N =6 VORTICES

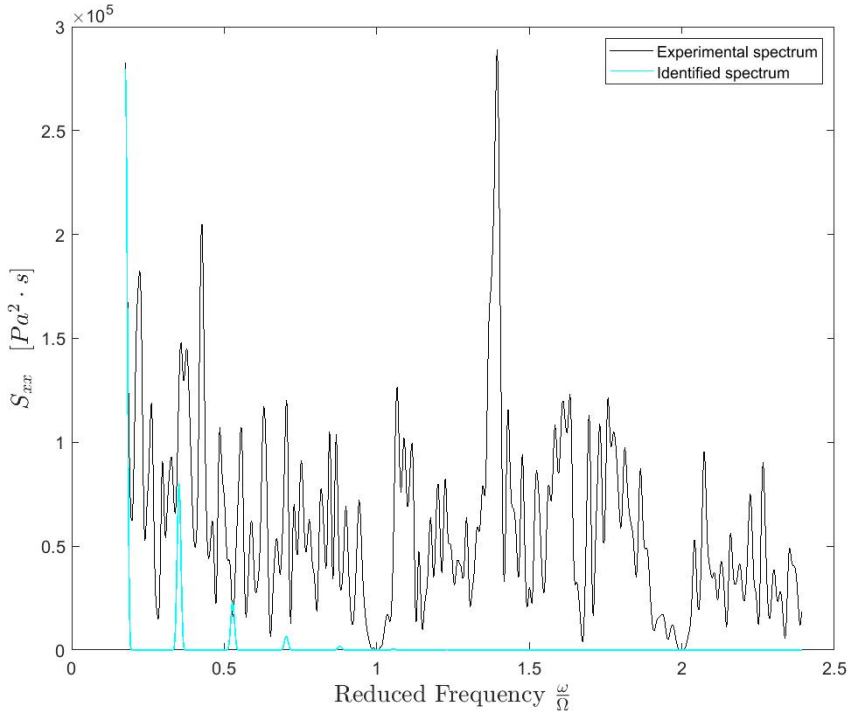

FIGURE 6.83: COMPARISON BETWEEN EXPERIMENTAL AUTO-CORRELATION SPECTRUM AND FULL-THEORETICAL SPECTRUM FOR DAPAMITO 4 WITH $\Phi = 0.76\ \Phi_D$, EULER NUMBER = 0.3393, N =6 VORTICES

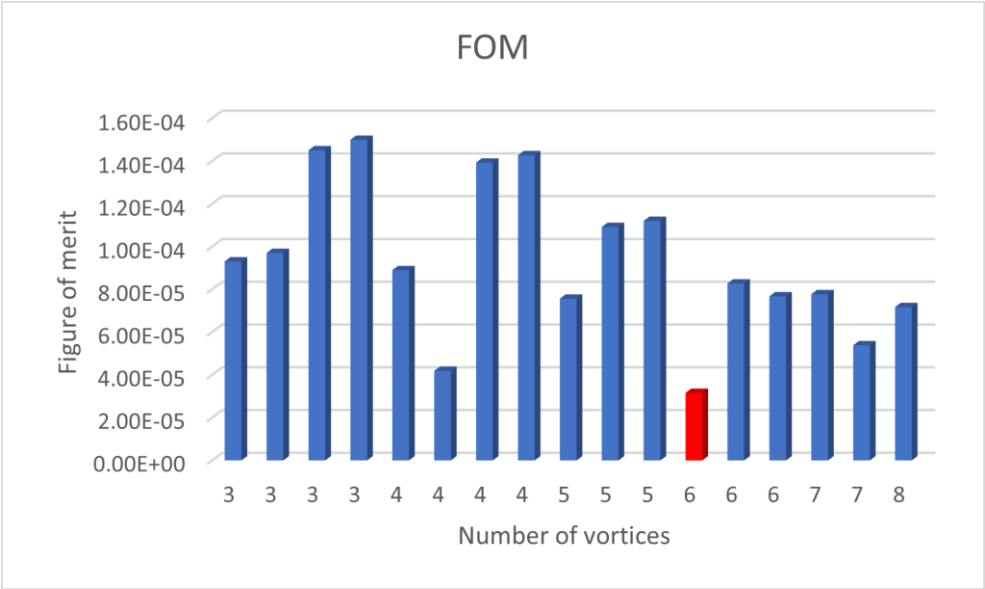

FIGURE 6.84: EVALUATION OF THE FIGURE OF MERIT WITH RESPECT TO THE NUMBER OF VORTICES FOR DAPAMITO 4 WITH $\Phi = 0.76\ \Phi_D$, EULER NUMBER = 0.3393

N	ω/Ω	ε_{TOT}	Γ	ω_γ [rad/s]	a (%R)	σ_g
3	0.0439453	9.31E-05	0.049	13.82	0.80661	0.19539
3	0.0585937	9.70E-05	0.05792	18.43	0.70203	0.19524
3	0.0732422	1.45E-04	0.04384	23.03	0.67592	0.19624
3	0.141602	1.50E-04	0.03194	44.53	0.60335	0.19828
4	0.0341797	8.89E-05	0.04635	10.75	0.85033	0.19539
4	0.0439453	4.19E-05	0.0367	13.82	0.90242	0.19788
4	0.0561523	1.39E-04	0.03714	17.66	0.7666	0.1973
4	0.107422	1.43E-04	0.05116	33.78	0.60197	0.19705
5	0.0341797	7.56E-05	0.04819	10.75	0.83913	0.19572
5	0.0439453	1.09E-04	0.04795	13.82	0.77608	0.19628
5	0.0854492	1.12E-04	0.03963	26.87	0.70531	0.19684
6	0.0292969	3.16E-05	0.03393±2.16	9.21±3.18E-5	0.94345±0.0036	0.1978
6	0.0366211	8.27E-05	0.0322	11.52	0.86887	0.19812
6	0.0708008	7.67E-05	0.04273	22.27	0.75145	0.19729
7	0.0317383	7.77E-05	0.03893	9.98	0.85854	0.1973
7	0.0610352	5.38E-05	0.02655	19.20	0.84956	0.19886
8	0.0537109	7.17E-05	0.03441	16.89	0.81631	0.19798

TABLE 6.28: IDENTIFICATION ASSESSMENT ASSOCIATED WITH BACKFLOW INSTABILITIES ON DAPAMITO 4 INDUCER, 76% OF DESIGN FLOW COEFFICIENT, EULER NUMBER = 0.3393

6.3.3. $\Phi = 0.63 \cdot \Phi D$

Finally, for detailing DAPAMITO 4 inducer, the case with flow coefficient equal to a 63% of the design flow coefficient is analysed. The results are presented as in previous case and there are considered as self-explanatory once the previous cases have been explained in detail, since the appearing information and the organization is strictly the same.

σ	N	ω/Ω	ε_{TOT}	Γ	ω_γ [rad/s]	a (%R)	σ_g
0.1234	5	0.0463867	3.72E-05	0.03449	14.59	0.89808	0.19789
0.1333	5	0.0463867	1.80E-05	0.1387	14.59	0.70894	0.14794
0.1438	5	0.0463867	2.85E-05	0.05804	14.59	0.85127	0.19254
0.1581	5	0.0439453	3.29E-05	0.07851	13.82	0.81467	0.18607
0.1976	5	0.0439453	2.92E-05	0.09369	13.82	0.7922	0.18342
0.2219	5	0.0463867	3.65E-05	0.06827	14.59	0.81689	0.20314
0.2461	5	0.0463867	4.06E-05	0.0467	14.59	0.86784	0.19537
0.2668	5	0.0463867	4.01E-05	0.04704	14.59	0.88097	0.19536
0.295	5	0.0463867	1.93E-05	0.11646	14.59	0.76615	0.16585
0.322	4	0.0585937	1.53E-05	0.03864	18.43	0.94643	0.19768
0.3392	4	0.0561523	3.29E-05	0.03993	17.66	0.90594	0.19687

TABLE 6.29: IDENTIFICATION ASSESSMENT ASSOCIATED WITH BACKFLOW INSTABILITIES ON DAPAMITO 4 INDUCER, 63% OF DESIGN FLOW COEFFICIENT

- **σ = 0.1438**

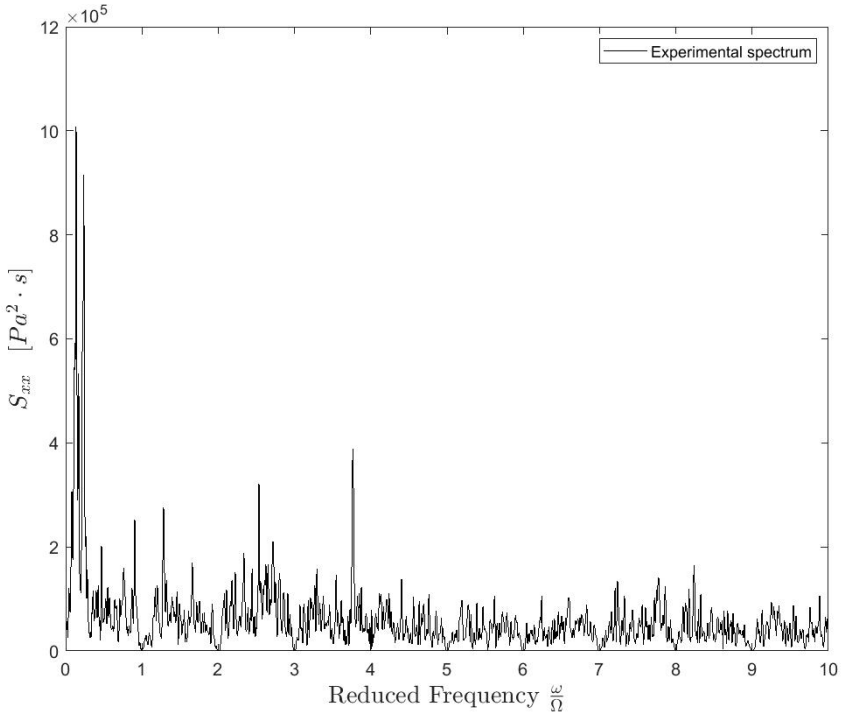

FIGURE 6.85: EXPERIMENTAL AUTO-CORRELATION PRESSURE SPECTRUM FOR DAPAMITO 4 WITH Φ =0.63 Φ_D, EULER NUMBER = 0.1438.

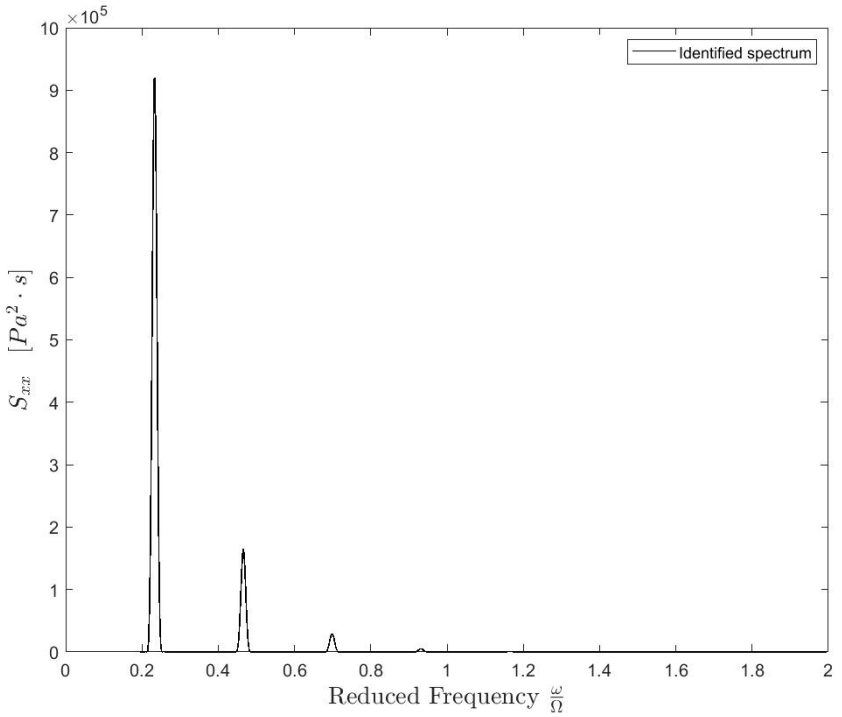

FIGURE 6.86: FULL-THEORETICAL AUTO-CORRELATION PRESSURE SPECTRUM FOR DAPAMITO 4 WITH Φ = 0.63 Φ_D, EULER NUMBER = 0.1438, N =5 VORTICES

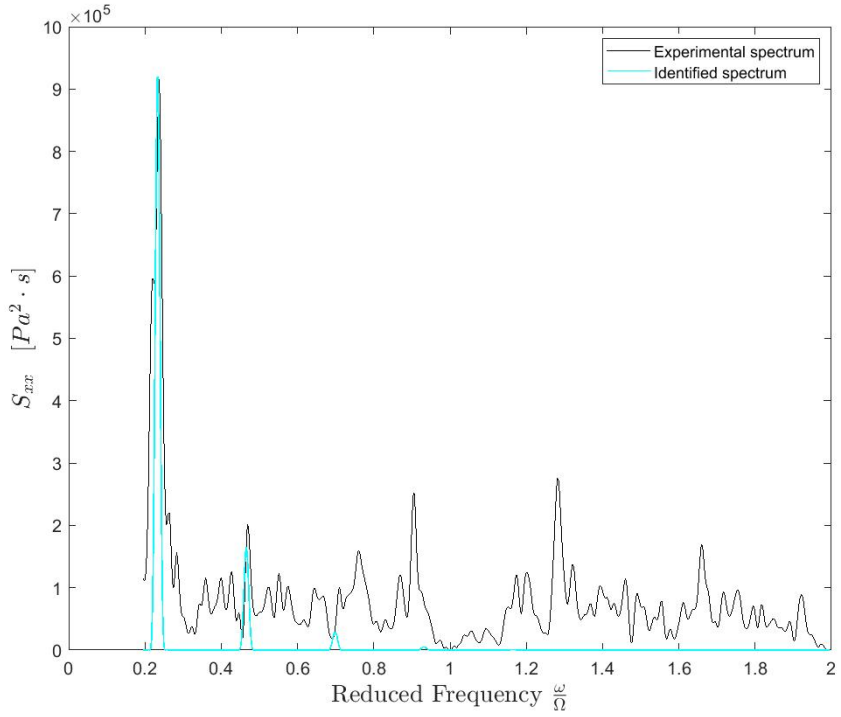

FIGURE 6.87: COMPARISON BETWEEN EXPERIMENTAL AUTO-CORRELATION SPECTRUM AND FULL-THEORETICAL SPECTRUM FOR DAPAMITO 4 WITH $\Phi = 0.63\ \Phi_D$, EULER NUMBER = 0.1438, N =5 VORTICES

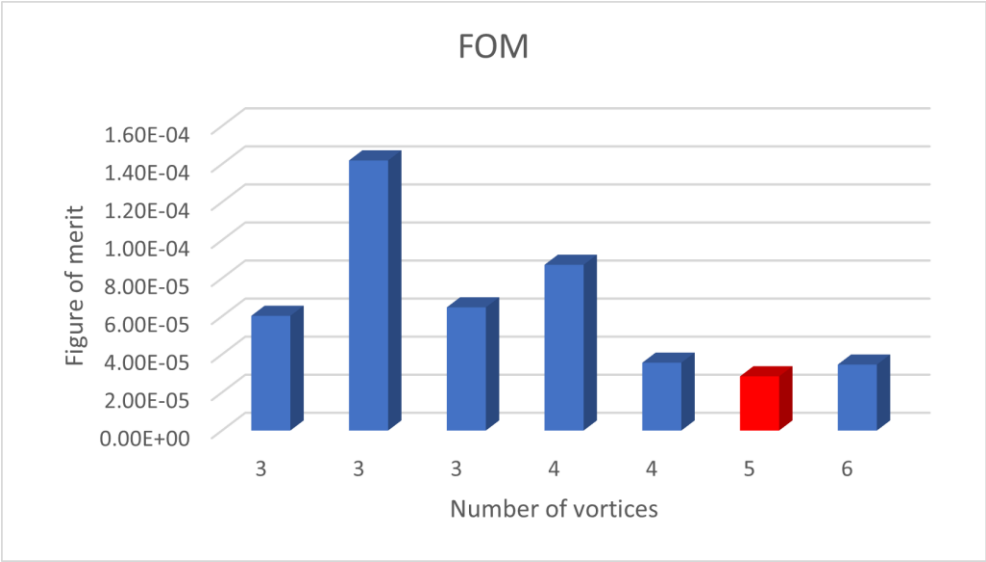

FIGURE 6.88: EVALUATION OF THE FIGURE OF MERIT WITH RESPECT TO THE NUMBER OF VORTICES FOR DAPAMITO 4 WITH $\Phi = 0.63\ \Phi_D$, EULER NUMBER = 0.1438

N	ω/Ω	ε_{TOT}	Γ	ω_γ [rad/s]	a (%R)	σ_g
3	0.0463867	6.03E-05	0.09591	14.59	0.76468	0.17816
3	0.0561523	1.42E-04	0.06995	17.66	0.74561	0.20882
3	0.078125	6.47E-05	0.05495	24.57	0.78795	0.20019
4	0.0415039	8.71E-05	0.06622	13.05	0.79479	0.1909
4	0.0585937	3.56E-05	0.0542	18.43	0.83712	0.19823
5	0.0463867	2.85E-05	0.05804±2.18	14.59±2.86E-5	0.85127±0.0073	0.19254
6	0.0390625	3.47E-05	0.05299	12.29	0.8955	0.19405

TABLE 6.30: IDENTIFICATION ASSESSMENT ASSOCIATED WITH BACKFLOW INSTABILITIES ON DAPAMITO 4 INDUCER, 63% OF DESIGN FLOW COEFFICIENT, EULER NUMBER = 0.1438

- **σ = 0.2461**

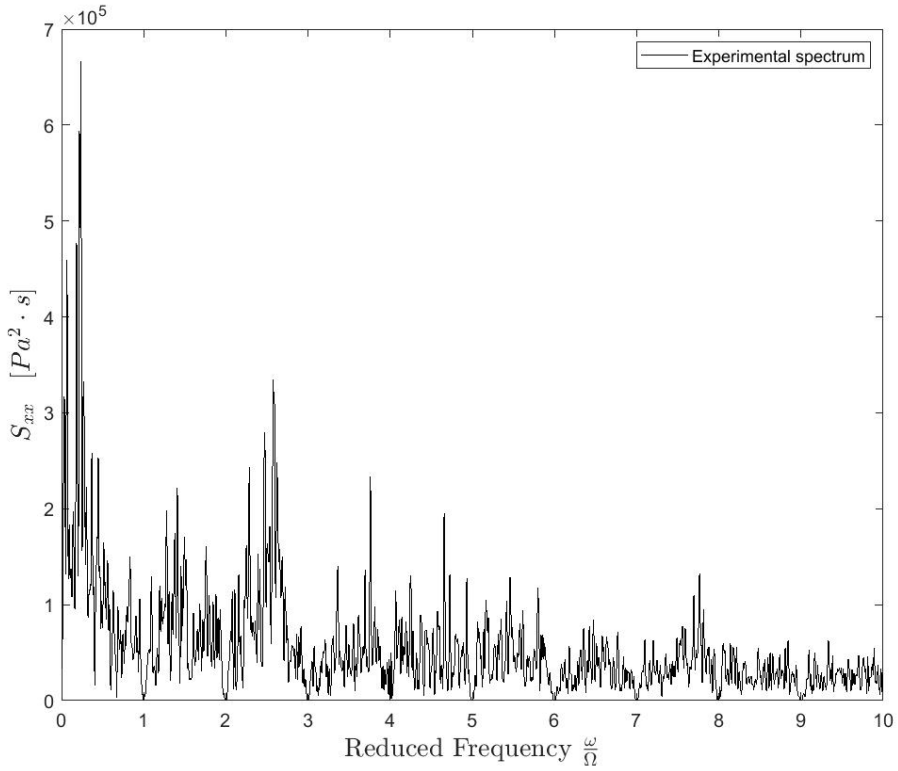

FIGURE 6.89: EXPERIMENTAL AUTO-CORRELATION PRESSURE SPECTRUM FOR DAPAMITO 4 WITH Φ =0.63 Φ_D, EULER NUMBER = 0.2461.

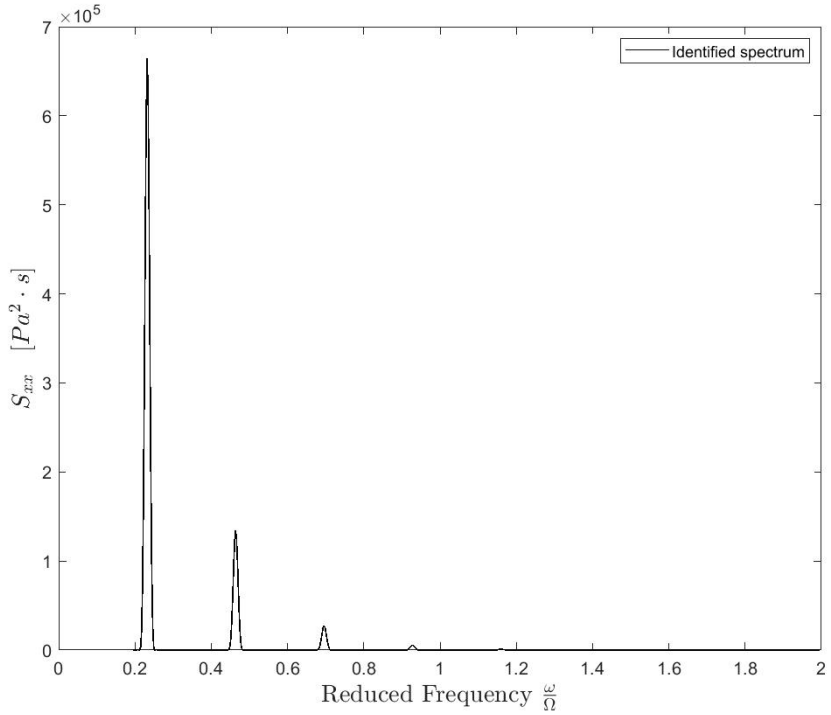

FIGURE 6.90: FULL-THEORETICAL AUTO-CORRELATION PRESSURE SPECTRUM FOR DAPAMITO 4 WITH Φ = 0.63 Φ_D, EULER NUMBER = 0.2461, N =5 VORTICES

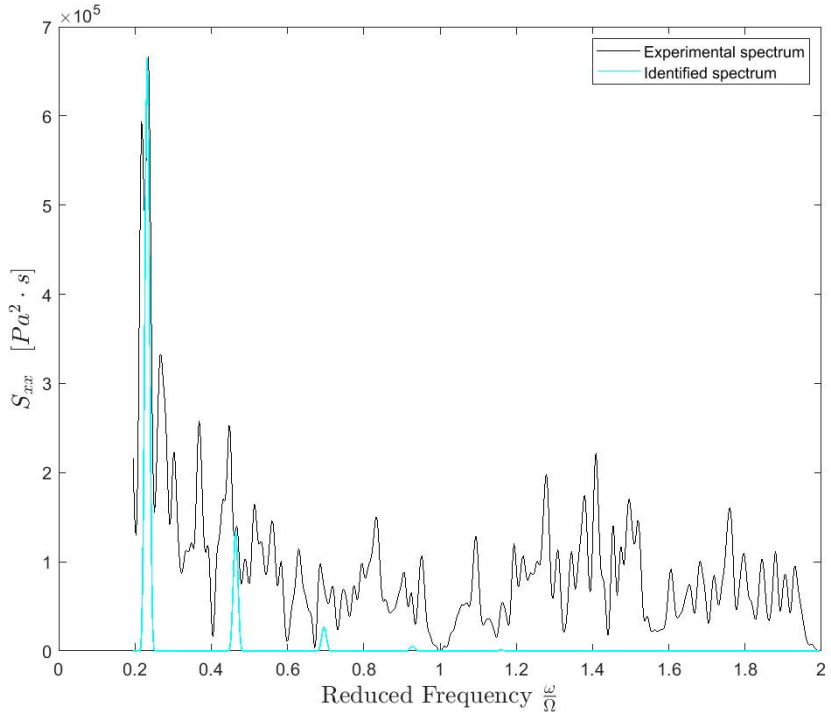

FIGURE 6.91: COMPARISON BETWEEN EXPERIMENTAL AUTO-CORRELATION SPECTRUM AND FULL-THEORETICAL SPECTRUM FOR DAPAMITO 4 WITH Φ = 0.63 Φ_D, EULER NUMBER = 0.2461, N =5 VORTICES

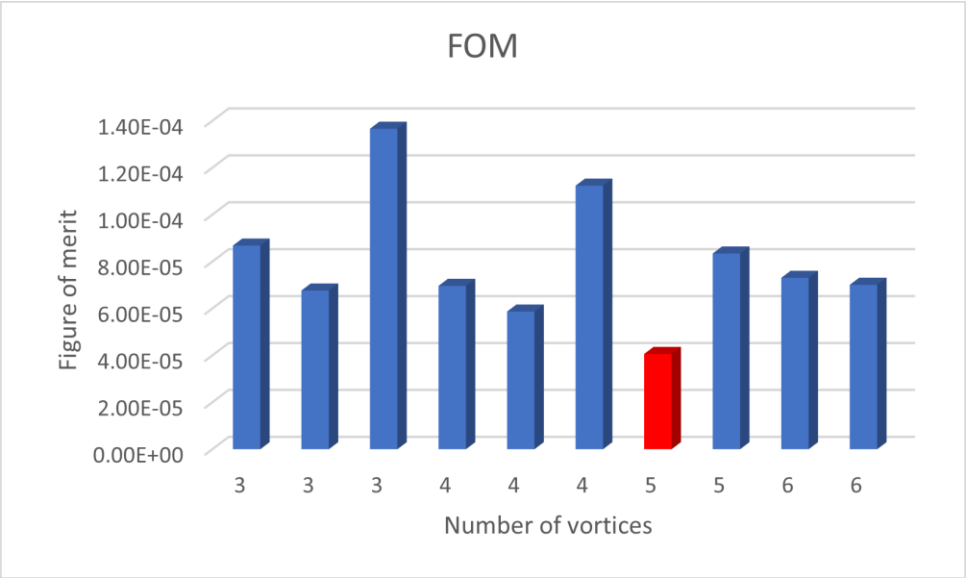

FIGURE 6.92: EVALUATION OF THE FIGURE OF MERIT WITH RESPECT TO THE NUMBER OF VORTICES FOR DAPAMITO 4 WITH Φ =0.63 Φ_D, EULER NUMBER = 0.2461

N	ω/Ω	ε_{TOT}	Γ	ω_γ [rad/s]	a (%R)	σ_g
3	0.0610352	8.68E-05	0.04765	19.20	0.81084	0.1953
3	0.078125	6.77E-05	0.04738	24.57	0.77983	0.19542
3	0.090332	1.37E-04	0.03952	28.41	0.72444	0.19694
4	0.0463867	6.96E-05	0.04629	14.59	0.85803	0.19581
4	0.0585937	5.87E-05	0.06147	18.43	0.7777	0.19473
4	0.0683594	1.12E-04	0.05786	21.50	0.71114	0.19422
5	0.0463867	4.06E-05	0.0467±2.11	14.59±4.08E-5	0.86784±0.0089	0.19537
5	0.0537109	8.34E-05	0.03279	16.89	0.8557	0.19808
6	0.0390625	7.31E-05	0.04569	12.29	0.88662	0.19552
6	0.0439453	7.01E-05	0.03966	13.82	0.84849	0.1971

TABLE 6.31: IDENTIFICATION ASSESSMENT ASSOCIATED WITH BACKFLOW INSTABILITIES ON DAPAMITO 4 INDUCER, 63% OF DESIGN FLOW COEFFICIENT, EULER NUMBER = 0.2461

- **σ = 0.322**

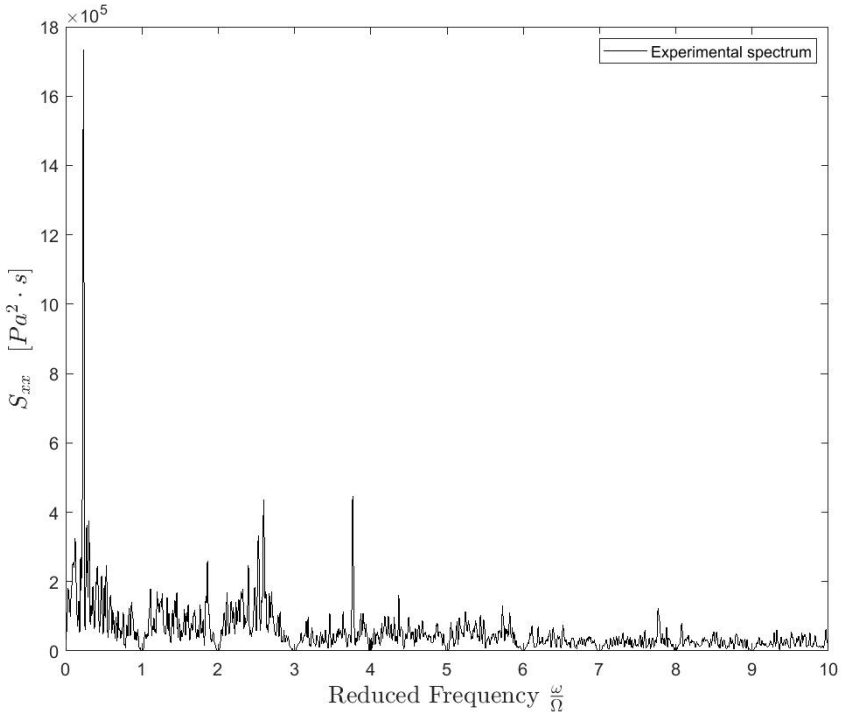

FIGURE 6.93: EXPERIMENTAL AUTO-CORRELATION PRESSURE SPECTRUM FOR DAPAMITO 4 WITH Φ =0.63 Φ_D, EULER NUMBER = 0.322.

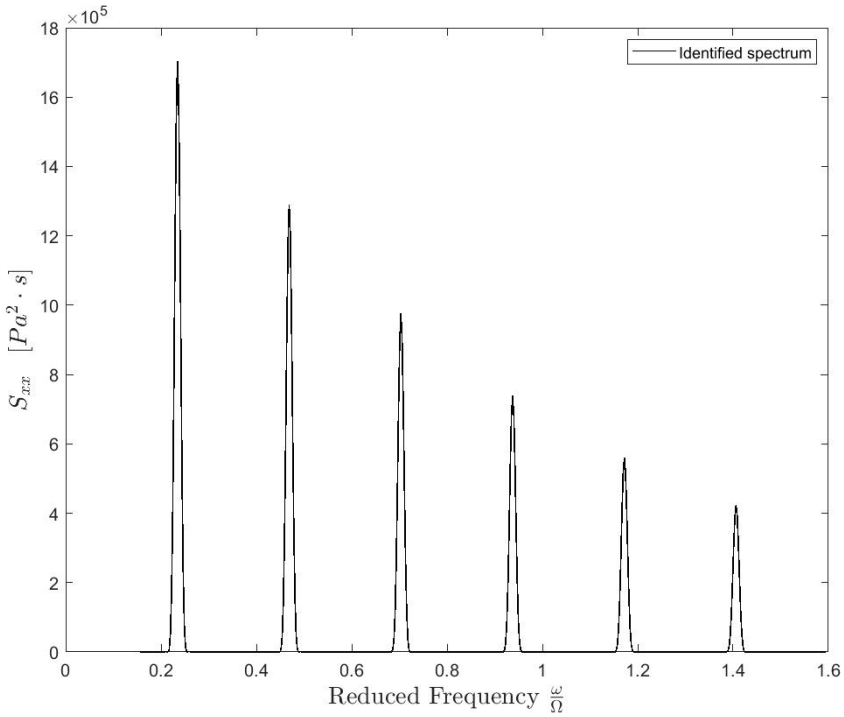

FIGURE 6.94: FULL-THEORETICAL AUTO-CORRELATION PRESSURE SPECTRUM FOR DAPAMITO 4 WITH Φ = 0.63 Φ_D, EULER NUMBER = 0.322, N =4 VORTICES

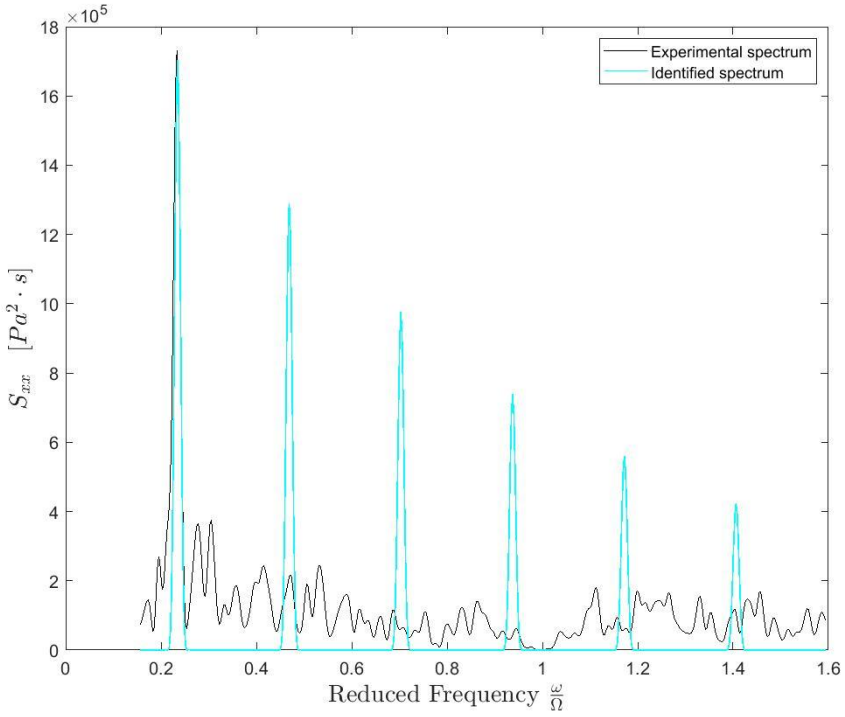

FIGURE 6.95: COMPARISON BETWEEN EXPERIMENTAL AUTO-CORRELATION SPECTRUM AND FULL-THEORETICAL SPECTRUM FOR DAPAMITO 4 WITH $\Phi = 0.63\ \Phi_D$, EULER NUMBER = 0.322, N =4 VORTICES

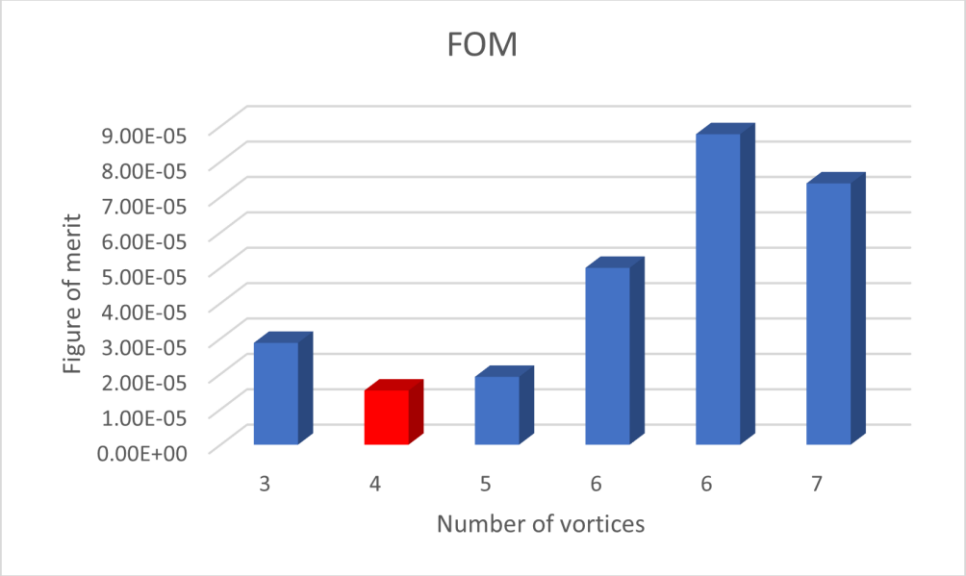

FIGURE 6.96: EVALUATION OF THE FIGURE OF MERIT WITH RESPECT TO THE NUMBER OF VORTICES FOR DAPAMITO 4 WITH $\Phi = 0.63\ \Phi_D$, EULER NUMBER = 0.322

N	ω/Ω	ε_{TOT}	Γ	ω_γ [rad/s]	a (%R)	σ_g
3	0.078125	2.88E-05	0.09696	24.57	0.72334	0.2021
4	0.0585937	1.53E-05	0.03864±0.65	18.43±1.55E-5	0.94643±0.0017	0.19768
5	0.0463867	1.92E-05	0.08763	14.59	0.82331	0.18245
6	0.0390625	5.00E-05	0.07489	12.29	0.86405	0.18771
6	0.0463867	8.78E-05	0.04471	14.59	0.82796	0.19637
7	0.0439453	7.39E-05	0.03506	13.82	0.8648	0.19756

TABLE 6.32: IDENTIFICATION ASSESSMENT ASSOCIATED WITH BACKFLOW INSTABILITIES ON DAPAMITO 4 INDUCER, 63% OF DESIGN FLOW COEFFICIENT, EULER NUMBER = 0.322

6.4. RAPDUD

The last inducer that was evaluated with the method explained in this document is RAPDUD inducer. For analysing it, different configurations have been analysed. With a clearance of 0.8 mm., the design flow coefficient, a 90% of the design flow coefficient and a 80% of the design flow coefficient have been evaluated. For each case, as it was done in all the previous cases, different Euler numbers were studied, presenting 3 of them for each case. The Euler numbers selected to show the results are as similar as possible between them with the aim of the comparison between cases.

6.4.1. $\Phi = \Phi_D$

The first analysed case, as reference, is the flow coefficient equal to the design flow coefficient, being the information of the selected cases presented in Table 6.33, with the parameters obtained in each identification.

σ	N	ω/Ω	ε_{TOT}	Γ	ω_γ [rad/s]	a (%R)	σ_g
0.1157	10	0.0305176	1.08E-05	0.01168	9.60	0.85938	0.20009
0.1308	10	0.0305176	1.63E-05	0.02447	9.60	0.80581	0.19885
0.2064	11	0.0396729	7.40E-06	0.03234	12.48	0.78885	0.19814
0.2186	10	0.0366211	8.49E-06	0.02206	11.52	0.82021	0.19922
0.2355	9	0.0488281	1.36E-05	0.02307	15.36	0.76966	0.19903
0.2537	8	0.0518799	9.52E-06	0.04488	16.32	0.71219	0.1964
0.2692	10	0.0396729	7.22E-06	0.03192	9.33	0.79655	0.19795
0.2968	9	0.0457764	1.34E-05	0.02449	14.40	0.78103	0.19888

TABLE 6.33: IDENTIFICATION ASSESSMENT ASSOCIATED WITH BACKFLOW INSTABILITIES ON RAPDUD INDUCER, DESIGN FLOW COEFFICIENT

Again, it is repeated as in the previous cases, the same procedure to present the results between different cases with Euler numbers: σ = 0.1308; σ = 0.2537 and σ = 0.2968.

- **σ = 0.1308**

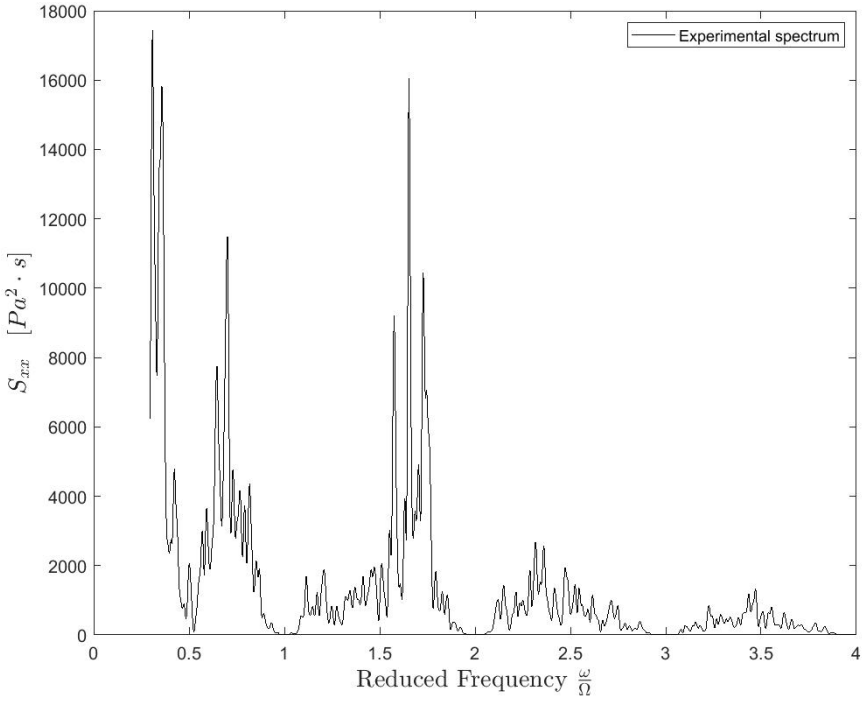

FIGURE 6.97: EXPERIMENTAL AUTO-CORRELATION PRESSURE SPECTRUM FOR RAPDUD WITH Φ = Φ_D, EULER NUMBER = 0.1308.

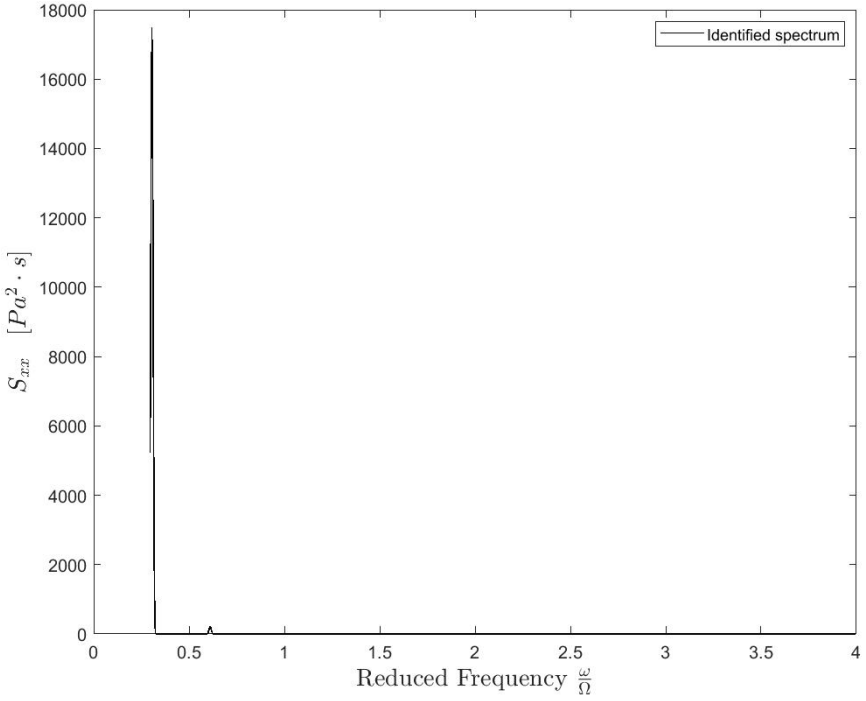

FIGURE 6.98: FULL-THEORETICAL AUTO-CORRELATION PRESSURE SPECTRUM FOR RAPDUD WITH Φ = Φ_D, EULER NUMBER = 0.1308, N =10 VORTICES

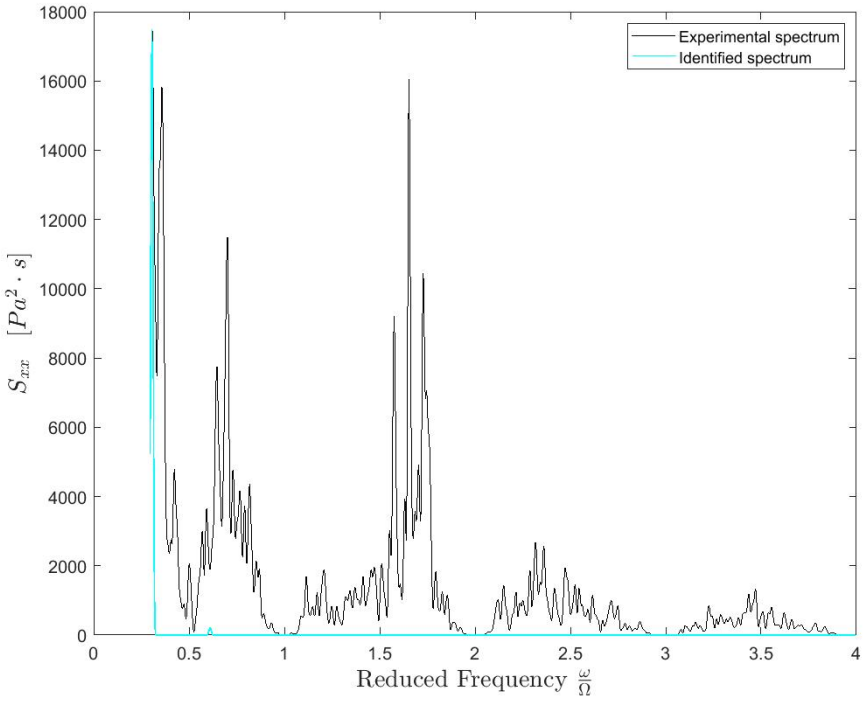

FIGURE 6.99: COMPARISON BETWEEN EXPERIMENTAL AUTO-CORRELATION SPECTRUM AND FULL-THEORETICAL SPECTRUM FOR RAPDUD WITH $\Phi = \Phi_D$, EULER NUMBER = 0.1308, N =10 VORTICES

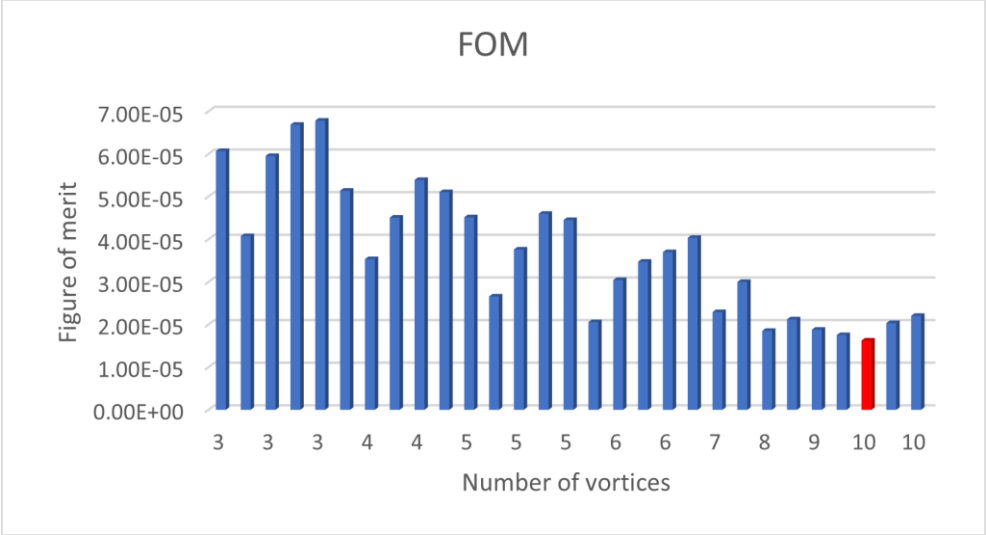

FIGURE 6.100: EVALUATION OF THE FIGURE OF MERIT WITH RESPECT TO THE NUMBER OF VORTICES FOR RAPDUD WITH $\Phi = \Phi_D$, EULER NUMBER = 0.1308

N	ω/Ω	ε_{TOT}	Γ	ω_γ [rad/s]	a (%R)	σ_g
3	0.0518799	6.07E-05	0.02838	16.32	0.59146	0.19872
3	0.0671387	4.07E-05	0.03841	21.12	0.51844	0.1982
3	0.0854492	5.95E-05	0.02887	26.87	0.5	0.19906
3	0.10376	6.69E-05	0.01707	32.63	0.54926	0.19958
3	0.119019	6.78E-05	0.01578	37.43	0.53748	0.19968
4	0.0396729	5.14E-05	0.4707	12.48	0.58289	0.19751
4	0.0488281	3.53E-05	0.02913	15.36	0.65024	0.19834
4	0.0640869	4.51E-05	0.02641	20.16	0.60713	0.19879
4	0.0762939	5.39E-05	0.02735	23.99	0.56471	0.19872
4	0.088501	5.11E-05	0.02771	27.83	0.54585	0.19885
5	0.0305176	4.52E-05	0.02719	9.60	0.7374	0.19869
5	0.0396729	2.66E-05	0.04485	12.48	0.65429	0.19656
5	0.0518799	3.76E-05	0.04236	16.32	0.60952	0.19766
5	0.0610352	4.60E-05	0.04405	19.20	0.57484	0.19771
5	0.0701904	4.45E-05	0.02231	22.07	0.6433	0.19915
6	0.0335693	2.06E-05	0.02579	10.56	0.76999	0.19889
6	0.0427246	3.04E-05	0.02793	13.44	0.71015	0.19847
6	0.0518799	3.47E-05	0.03535	16.32	0.6541	0.19751
6	0.0579834	3.70E-05	0.02951	18.24	0.65904	0.19839
7	0.0305176	4.03E-05	0.03649	9.60	0.7107	0.1973
7	0.0366211	2.29E-05	0.03876	11.52	0.71151	0.1973
7	0.0518799	3.00E-05	0.02665	16.32	0.70277	0.19859
8	0.0335693	1.85E-05	0.0147	10.56	0.83911	0.19986
8	0.0396729	2.12E-05	0.02557	12.48	0.77085	0.19918
9	0.0335693	1.88E-05	0.03068	10.56	0.7656	0.19834
9	0.0396729	1.75E-05	0.0256	12.48	0.77045	0.1987
10	0.0305176	1.63E-05	0.02447±47.54	9.60±1.63E-5	0.80581±0.057	0.19885
10	0.0366211	2.04E-05	0.02343	11.52	0.78591	0.199
10	0.0701904	2.21E-05	0.02774	22.07	0.72161	0.19873

TABLE 6.34: IDENTIFICATION ASSESSMENT ASSOCIATED WITH BACKFLOW INSTABILITIES ON RAPDUD INDUCER, DESIGN FLOW COEFFICIENT, EULER NUMBER = 0.1308

- **σ = 0.2537**

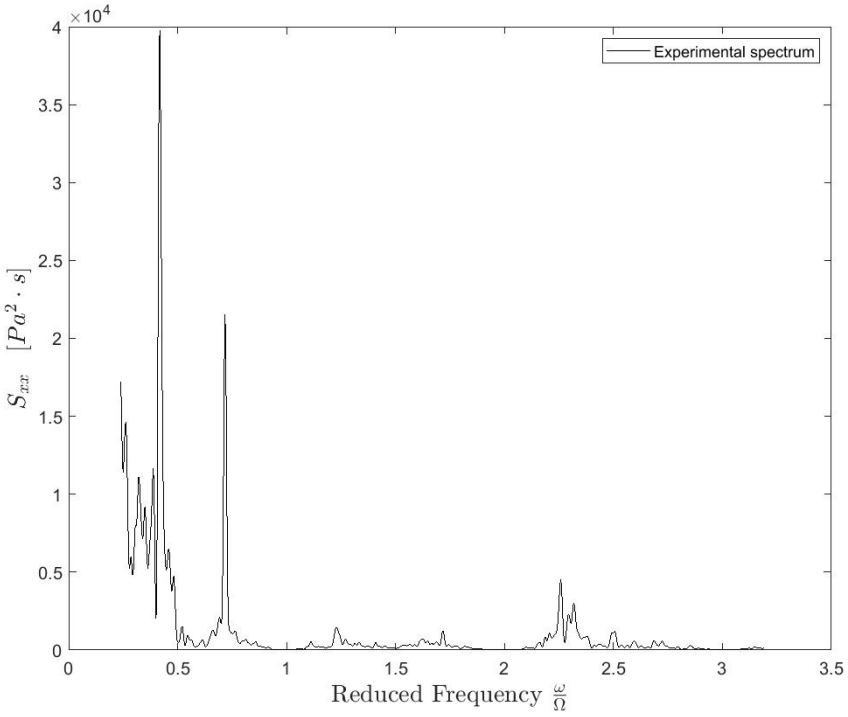

FIGURE 6.101: EXPERIMENTAL AUTO-CORRELATION PRESSURE SPECTRUM FOR RAPDUD WITH $\Phi = \Phi_D$, EULER NUMBER = 0.2537.

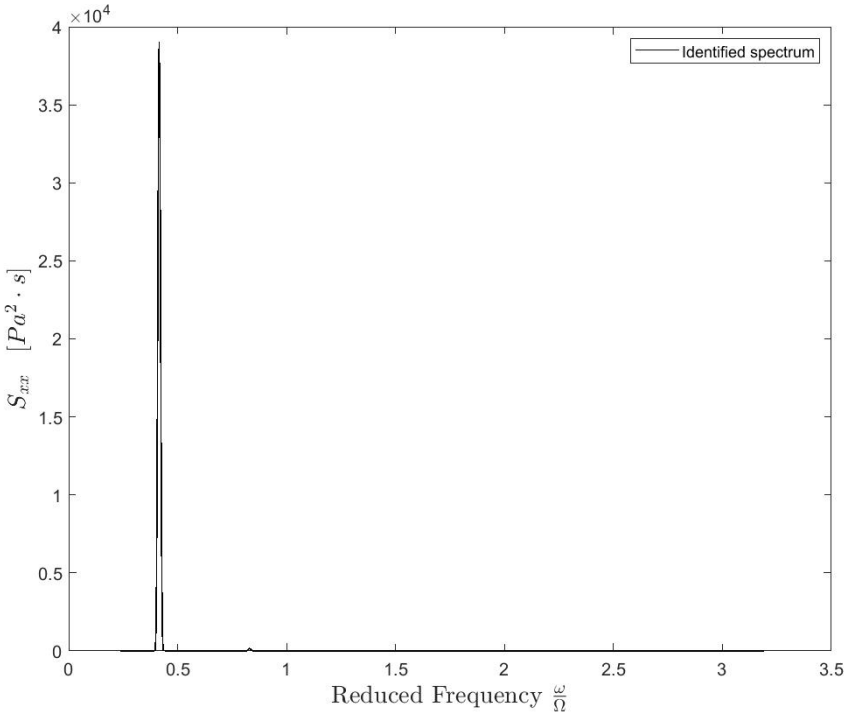

FIGURE 6.102: FULL-THEORETICAL AUTO-CORRELATION PRESSURE SPECTRUM FOR RAPDUD WITH $\Phi = \Phi_D$, EULER NUMBER = 0.2537, N =8 VORTICES

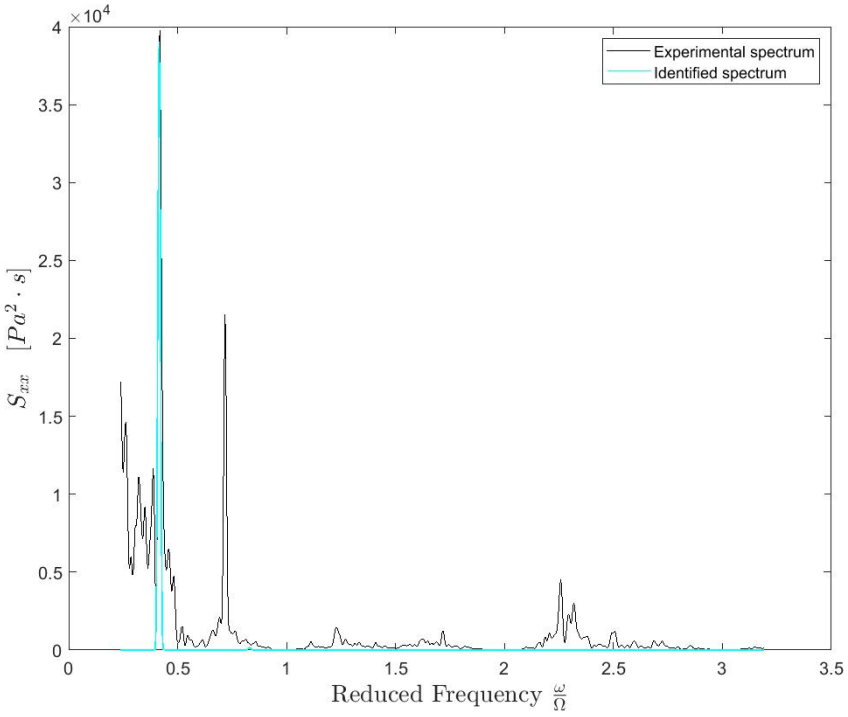

FIGURE 6.103: COMPARISON BETWEEN EXPERIMENTAL AUTO-CORRELATION SPECTRUM AND FULL-THEORETICAL SPECTRUM FOR RAPDUD WITH $\Phi = \Phi_D$, EULER NUMBER = 0.2537, N =8 VORTICES

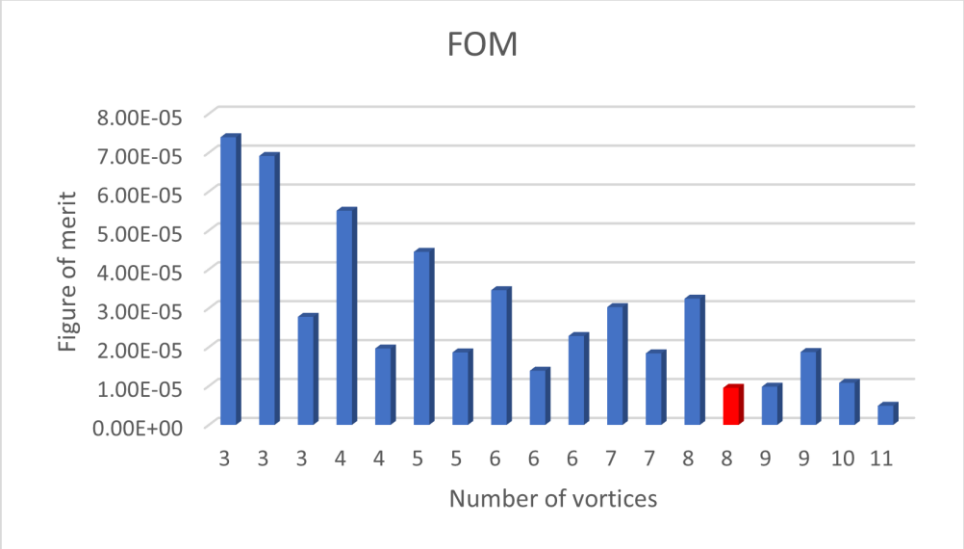

FIGURE 6.104: EVALUATION OF THE FIGURE OF MERIT WITH RESPECT TO THE NUMBER OF VORTICES FOR RAPDUD WITH $\Phi = \Phi_D$, EULER NUMBER = 0.2537

N	ω/Ω	ε_{TOT}	Γ	ω_γ [rad/s]	a (%R)	σ_g
3	0.0732422	7.40E-05	0.02581	23.03	0.53183	0.19915
3	0.0793457	6.91E-05	0.02713	24.95	0.51431	0.19913
3	0.140381	2.78E-05	0.02132	44.15	0.52001	0.19938
4	0.0610352	5.51E-05	0.02495	19.20	0.61175	0.19888
4	0.10376	1.96E-05	0.02731	32.63	0.57809	0.19858
5	0.0488281	4.45E-05	0.03989	15.36	0.61279	0.1974
5	0.0823975	1.86E-05	0.03232	25.91	0.62116	0.19804
6	0.0396729	3.46E-05	0.02421	12.48	0.73057	0.19902
6	0.0701904	1.39E-05	0.02706	22.07	0.69227	0.19858
6	0.119019	2.29E-05	0.02033	37.43	0.6495	0.19935
7	0.0335693	3.03E-05	0.03246	10.56	0.73209	0.19807
7	0.0610352	1.84E-05	0.02547	19.20	0.71806	0.19879
8	0.0305176	3.25E-05	0.02619	9.60	0.77352	0.19863
8	0.0518799	9.52E-06	0.04488±39.59	16.32±9.52E-6	0.71219±0.092	0.1964
9	0.0457764	9.81E-06	0.02358	14.40	0.78935	0.19901
9	0.0793457	1.87E-05	0.0265	24.95	0.71337	0.19867
10	0.0427246	1.08E-05	0.03111	13.44	0.77664	0.19814
11	0.0396729	4.91E-06	0.03702	12.48	0.79648	0.19722

TABLE 6.35: IDENTIFICATION ASSESSMENT ASSOCIATED WITH BACKFLOW INSTABILITIES ON RAPDUD INDUCER, DESIGN FLOW COEFFICIENT, EULER NUMBER = 0.2537

- **σ = 0.2968**

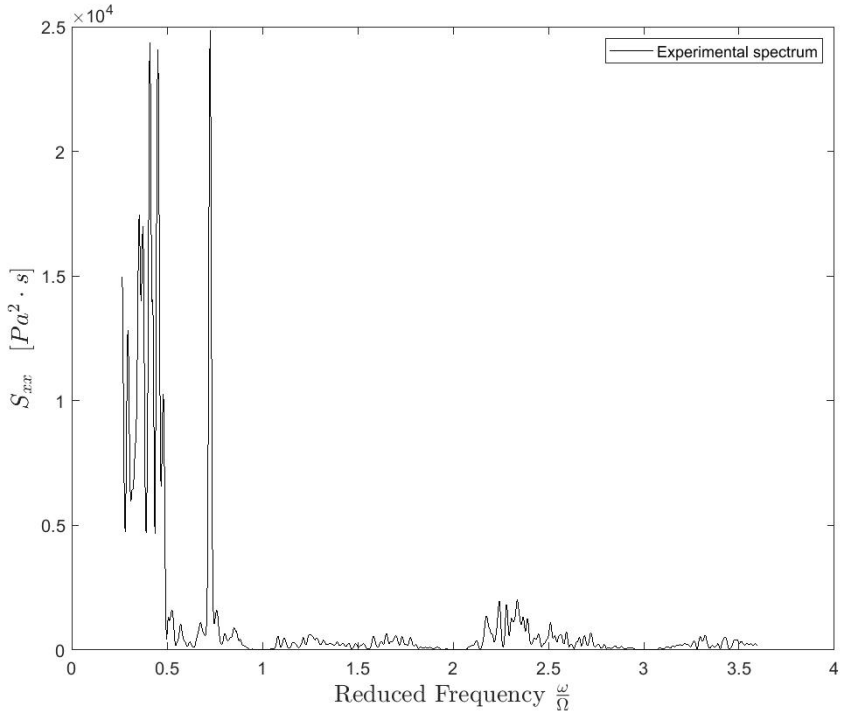

FIGURE 6.105: EXPERIMENTAL AUTO-CORRELATION PRESSURE SPECTRUM FOR RAPDUD WITH Φ = Φ_D, EULER NUMBER = 0.2968.

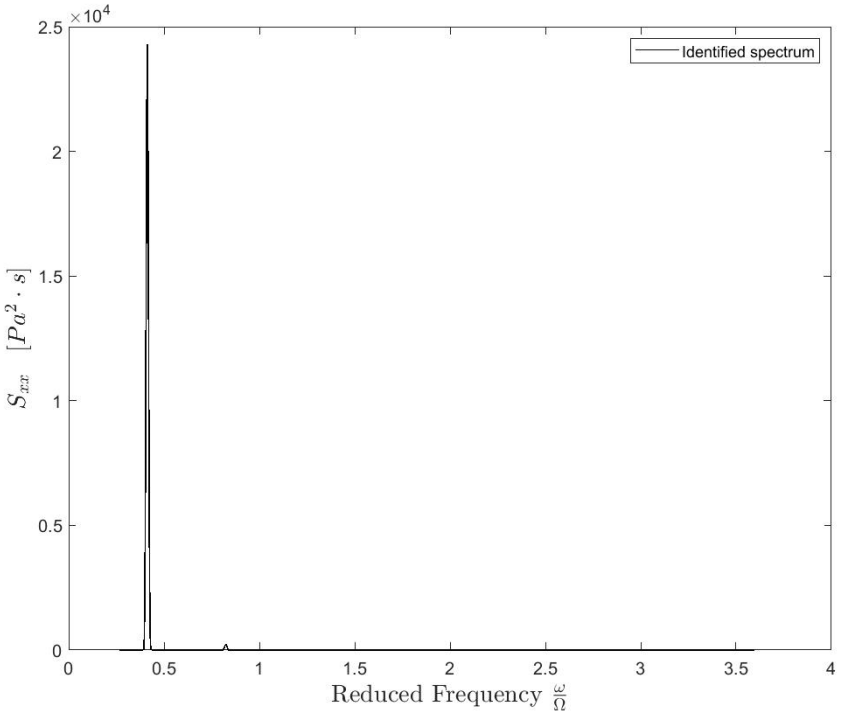

FIGURE 6.106: FULL-THEORETICAL AUTO-CORRELATION PRESSURE SPECTRUM FOR RAPDUD WITH Φ = Φ_D, EULER NUMBER = 0.2968, N =9 VORTICES

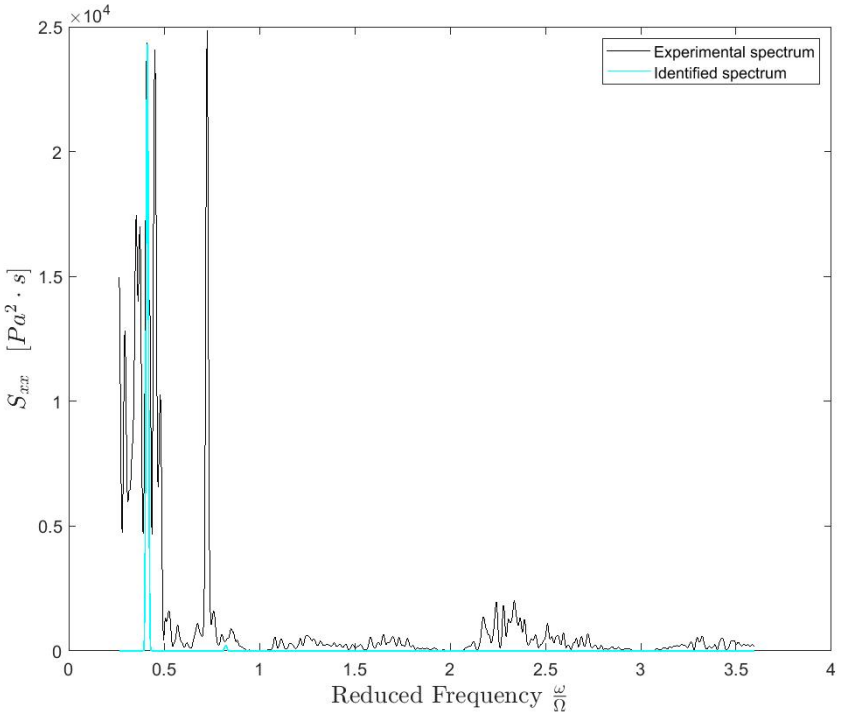

FIGURE 6.107: COMPARISON BETWEEN EXPERIMENTAL AUTO-CORRELATION SPECTRUM AND FULL-THEORETICAL SPECTRUM FOR RAPDUD WITH Φ = Φ_D, EULER NUMBER = 0.2968, N =9 VORTICES

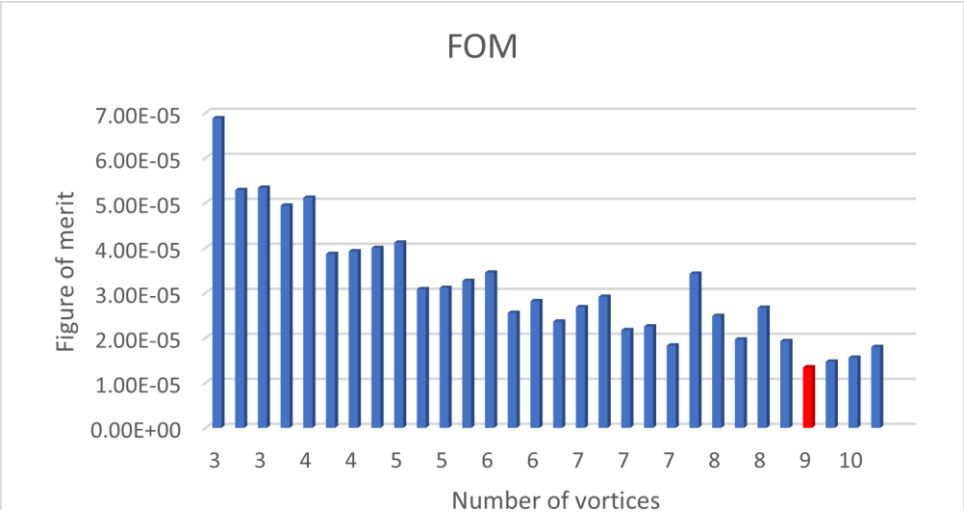

FIGURE 6.108: EVALUATION OF THE FIGURE OF MERIT WITH RESPECT TO THE NUMBER OF VORTICES FOR RAPDUD WITH $\Phi = \Phi_D$, EULER NUMBER = 0.2968

N	ω/Ω	ε_{TOT}	Γ	ω_γ [rad/s]	a (%R)	σ_g
3	0.0854492	6.73E-05	0.02857	26.87	0.5	0.19907
3	0.119019	6.88E-05	0.01569	37.43	0.54535	0.1997
3	0.137329	5.28E-05	0.01755	43.19	0.52148	0.19985
3	0.149536	5.34E-05	0.03426	47.03	0.45315	0.28369
4	0.0640869	4.94E-05	0.02633	20.16	0.60652	0.19879
4	0.088501	5.11E-05	0.02912	27.83	0.54347	0.19873
4	0.10376	3.86E-05	0.01785	32.63	0.61167	0.20073
4	0.112915	3.92E-05	0.03338	35.51	0.50879	0.19885
5	0.0518799	4.00E-05	0.04867	16.32	0.58885	0.1962
5	0.0732422	4.12E-05	0.02159	23.03	0.64691	0.19925
5	0.0823975	3.08E-05	0.02637	25.91	0.62239	0.19874
5	0.0915527	3.11E-05	0.02452	28.79	0.61959	0.19902
6	0.0427246	3.27E-05	0.02789	13.44	0.70946	0.19847
6	0.0610352	3.45E-05	0.03054	19.20	0.65577	0.19839
6	0.0671387	2.56E-05	0.03295	21.12	0.64937	0.19826
6	0.0762939	2.82E-05	0.04341	23.99	0.60471	0.19689
6	0.12207	2.36E-05	0.02026	38.39	0.64754	0.19936
7	0.0366211	2.68E-05	0.03844	11.52	0.71302	0.19734
7	0.0518799	2.91E-05	0.03209	16.32	0.69265	0.19799
7	0.0579834	2.17E-05	0.01885	18.24	0.74876	0.19957
7	0.0640869	2.25E-05	0.02736	20.16	0.69918	0.19854
7	0.10376	1.83E-05	0.03451	32.63	0.64103	0.19793
8	0.0305176	3.42E-05	0.02569	9.60	0.77617	0.19869
8	0.0457764	2.49E-05	0.02981	14.40	0.7312	0.19824
8	0.0518799	1.96E-05	0.03222	16.32	0.72219	0.19814
8	0.0915527	2.67E-05	0.02288	28.79	0.69076	0.19903
9	0.0396729	1.93E-05	0.02313	12.48	0.78385	0.19903
9	0.0457764	1.34E-05	0.02429±29.23	14.40±1.35E-5	0.78103±0.053	0.19888
10	0.0366211	1.47E-05	0.02767	11.52	0.79192	0.19848
10	0.0457764	1.56E-05	0.0301	14.40	0.76494	0.19822
10	0.0732422	1.80E-05	0.02491	23.03	0.73975	0.19881

TABLE 6.36: IDENTIFICATION ASSESSMENT ASSOCIATED WITH BACKFLOW INSTABILITIES ON RAPDUD INDUCER, DESIGN FLOW COEFFICIENT, EULER NUMBER = 0.2968

6.4.2. $\Phi = 0.9 \cdot \Phi_D$

The next set of cases studied is the one with flow coefficient equal to the 90% of the design flow coefficient. The selected number of vortices for each evaluation are presented in Table 6.37.

σ	N	ω/Ω	ε_{TOT}	Γ	ω_γ [rad/s]	a (%R)	σ_g
0.1159	6	0.0335693	1.49E-05	0.03428	10.56	0.7535	0.19765
0.1319	8	0.0305176	1.04E-05	0.02859	9.60	0.81755	0.19837
0.1404	6	0.0427246	2.15E-05	0.02471	13.44	0.75202	0.19901
0.1618	6	0.0427246	1.32E-05	0.03439	13.44	0.74365	0.19774
0.1745	8	0.0335693	1.13E-05	0.03732	10.56	0.78862	0.19711
0.2061	4	0.0518799	4.14E-05	0.02306	16.32	0.63092	0.19906
0.2187	10	0.0305176	1.82E-05	0.02508	9.60	0.80777	0.19885
0.2358	5	0.0640869	2.43E-05	0.0407	20.16	0.58616	0.19754
0.2544	10	0.0427246	1.41E-05	0.02671	13.44	0.78067	0.19864
0.2693	8	0.0335693	1.11E-05	0.02944	10.56	0.79019	0.19827
0.2969	9	0.0488281	1.99E-05	0.03607	15.36	0.71606	0.19778

TABLE 6.37: IDENTIFICATION ASSESSMENT ASSOCIATED WITH BACKFLOW INSTABILITIES ON RAPDUD INDUCER, 90% OF DESIGN FLOW COEFFICIENT

For presenting the information, there are Figures representing experimental spectrum, the full theoretical spectrum and the comparison between identified and experimental auto-correlation and a Table related to the fixed Euler number with the information obtained for each one of the analysed cases with backflow vortex instability. Also, there are Figures representing the evolution of the figure of merit with the studied number of vortices for each case, as in previous analysis.

- **σ = 0.1319**

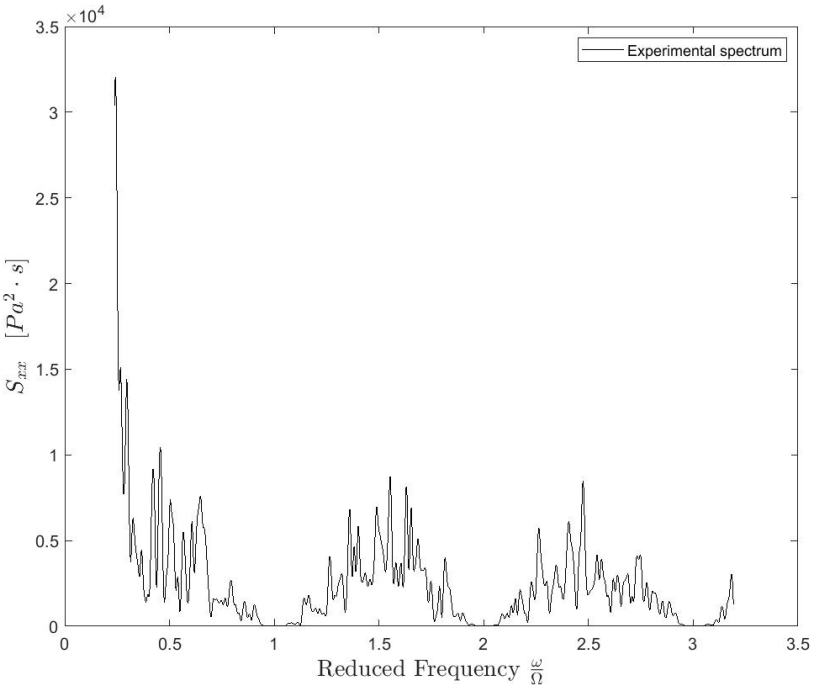

FIGURE 6.109: EXPERIMENTAL AUTO-CORRELATION PRESSURE SPECTRUM FOR RAPDUD WITH $\Phi = 0.9\ \Phi_D$, EULER NUMBER = 0.1319.

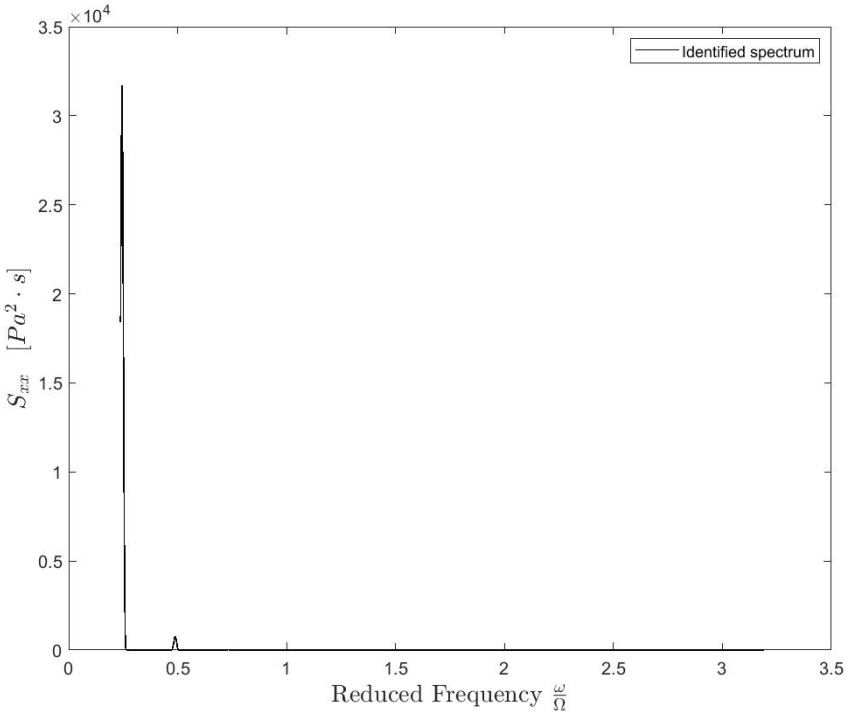

FIGURE 6.110: FULL-THEORETICAL AUTO-CORRELATION PRESSURE SPECTRUM FOR RAPDUD WITH Φ = 0.9 Φ_D, EULER NUMBER = 0.1319, N =8 VORTICES

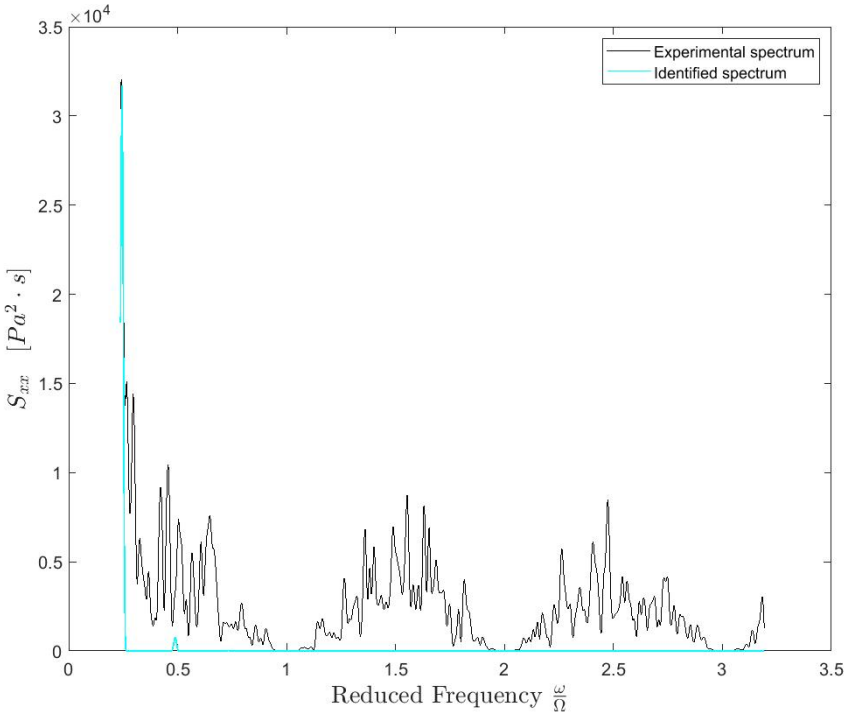

FIGURE 6.111: COMPARISON BETWEEN EXPERIMENTAL AUTO-CORRELATION SPECTRUM AND FULL-THEORETICAL SPECTRUM FOR RAPDUD WITH Φ =0.9 Φ_D, EULER NUMBER = 0.1319, N =8 VORTICES

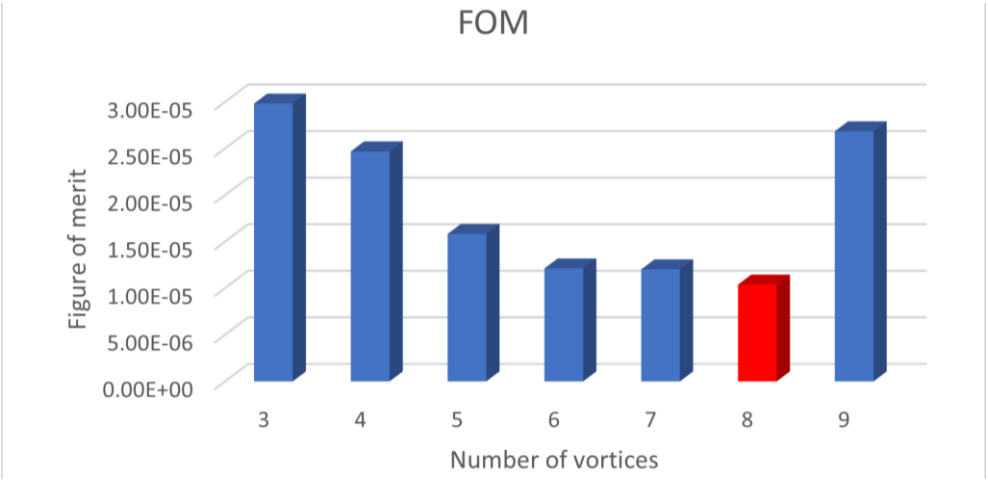

FIGURE 6.112: EVALUATION OF THE FIGURE OF MERIT WITH RESPECT TO THE NUMBER OF VORTICES FOR RAPDUD WITH $\Phi = 0.9\ \Phi_D$, EULER NUMBER = 0.1319

N	ω/Ω	ε_{TOT}	Γ	ω_γ [rad/s]	a (%R)	σ_g
3	0.0793457	2.98E-05	0.02409	24.95	0.59467	0.19899
4	0.0610352	2.47E-05	0.03435	19.20	0.61415	0.19799
5	0.0488281	1.58E-05	0.02911	15.36	0.71988	0.19837
6	0.0396729	1.21E-05	0.03557	12.48	0.74475	0.19746
7	0.0335693	1.20E-05	0.0436	10.56	0.7482	0.19688
8	0.0305176	1.04E-05	0.02859±25.62	9.60±1.04E-5	0.81755±0.011	0.19837
9	0.0335693	2.68E-05	0.02969	10.56	0.75801	0.19831

TABLE 6.38: IDENTIFICATION ASSESSMENT ASSOCIATED WITH BACKFLOW INSTABILITIES ON RAPDUD INDUCER, 90% OF DESIGN FLOW COEFFICIENT, EULER NUMBER = 0.1319

- **σ = 0.2544**

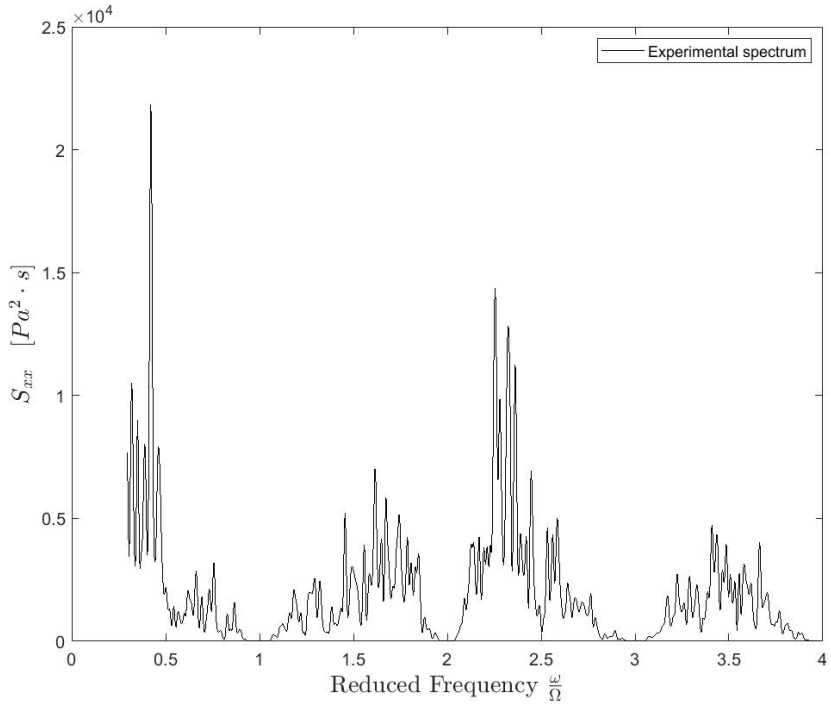

FIGURE 6.113: EXPERIMENTAL AUTO-CORRELATION PRESSURE SPECTRUM FOR RAPDUD WITH $\Phi = 0.9\ \Phi_D$, EULER NUMBER = 0.2544.

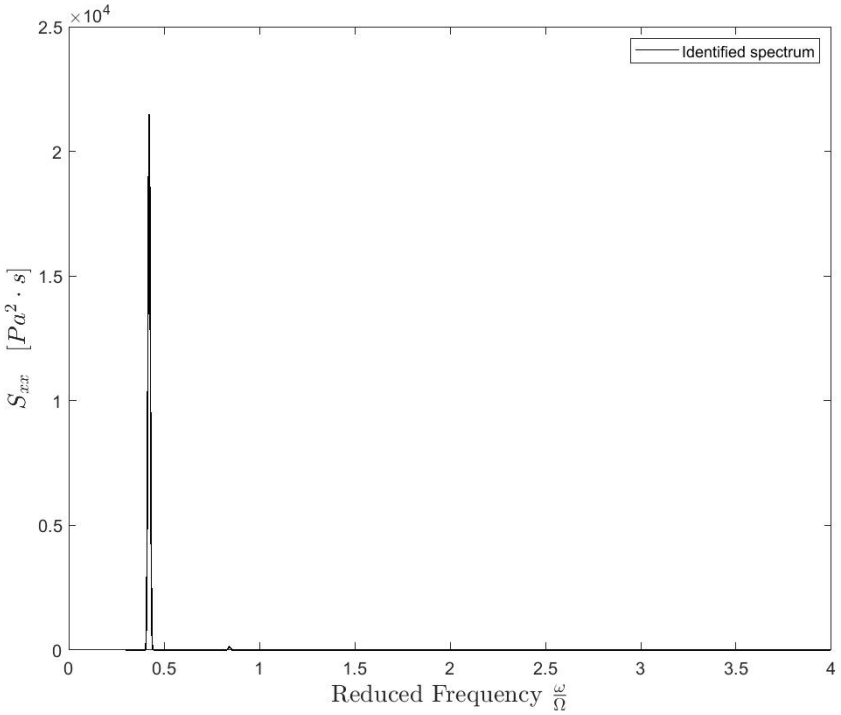

FIGURE 6.114: FULL-THEORETICAL AUTO-CORRELATION PRESSURE SPECTRUM FOR RAPDUD WITH Φ = 0.9 Φ_D, EULER NUMBER = 0.2544, N =10 VORTICES

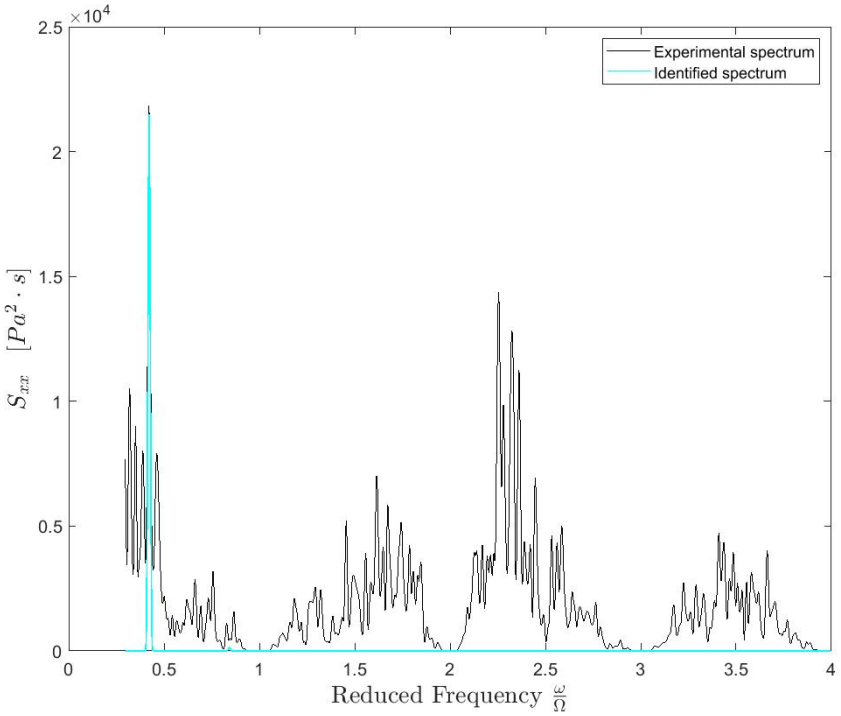

FIGURE 6.115: COMPARISON BETWEEN EXPERIMENTAL AUTO-CORRELATION SPECTRUM AND FULL-THEORETICAL SPECTRUM FOR RAPDUD WITH Φ =0.9 Φ_D, EULER NUMBER = 0.2544, N =10 VORTICES

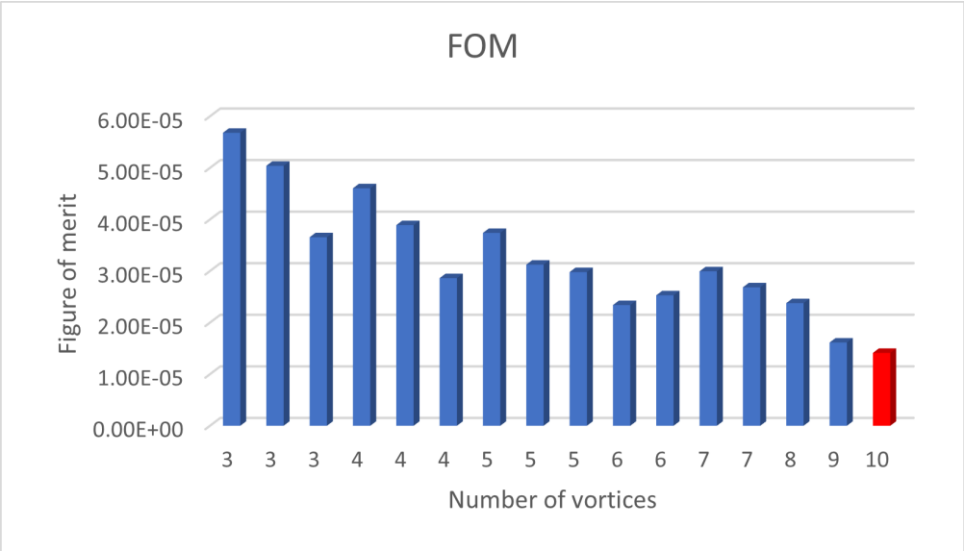

FIGURE 6.116: EVALUATION OF THE FIGURE OF MERIT WITH RESPECT TO THE NUMBER OF VORTICES FOR RAPDUD WITH $\Phi = 0.9\,\Phi_D$, EULER NUMBER = 0.2544

N	ω/Ω	ε_{TOT}	Γ	$\omega_{\gamma\,\Gamma}$ [rad/s]	a (%R)	σ_g
3	0.0732422	5.68E-05	0.02404	23.03	0.53233	0.19922
3	0.0854492	5.04E-05	0.02519	26.87	0.50593	0.19923
3	0.140381	3.66E-05	0.01625	44.15	0.51805	0.19966
4	0.0549316	4.61E-05	0.02351	17.28	0.62285	0.19905
4	0.0640869	3.89E-05	0.02488	20.16	0.60169	0.1989
4	0.106812	2.86E-05	0.02292	33.59	0.55951	0.19966
5	0.0427246	3.74E-05	0.03112	13.44	0.65335	0.19834
5	0.0518799	3.12E-05	0.04424	16.32	0.59411	0.19683
5	0.0854492	2.98E-05	0.02361	26.87	0.6134	0.199
6	0.0427246	2.34E-05	0.02418	13.44	0.73934	0.19905
6	0.0701904	2.53E-05	0.03902	22.07	0.62123	0.19746
7	0.0366211	3.00E-05	0.0317	11.52	0.72211	0.1983
7	0.0610352	2.68E-05	0.0238	19.20	0.70468	0.19899
8	0.0518799	2.38E-05	0.03234	16.32	0.70829	0.19796
9	0.0457764	1.61E-05	0.01513	14.40	0.80954	0.19979
10	0.0427246	1.41E-05	0.02671±42.75	13.44±1.41E-5	0.78067±0.092	0.19864

TABLE 6.39: IDENTIFICATION ASSESSMENT ASSOCIATED WITH BACKFLOW INSTABILITIES ON RAPDUD INDUCER, 90% OF DESIGN FLOW COEFFICIENT, EULER NUMBER = 0.2544

- **σ = 0.2969**

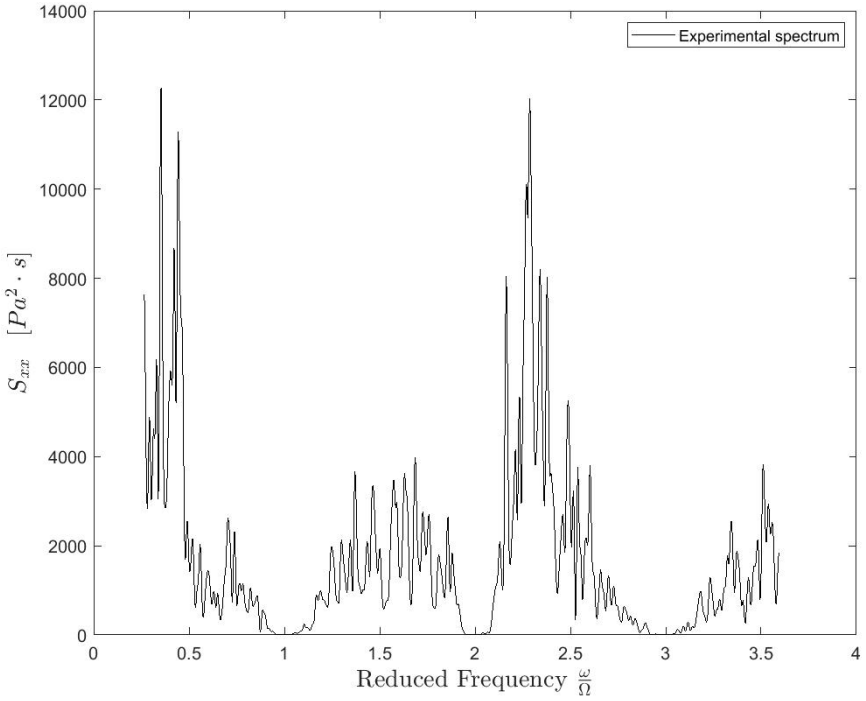

FIGURE 6.117: EXPERIMENTAL AUTO-CORRELATION PRESSURE SPECTRUM FOR RAPDUD WITH Φ = 0.9 Φ_D, EULER NUMBER = 0.2969.

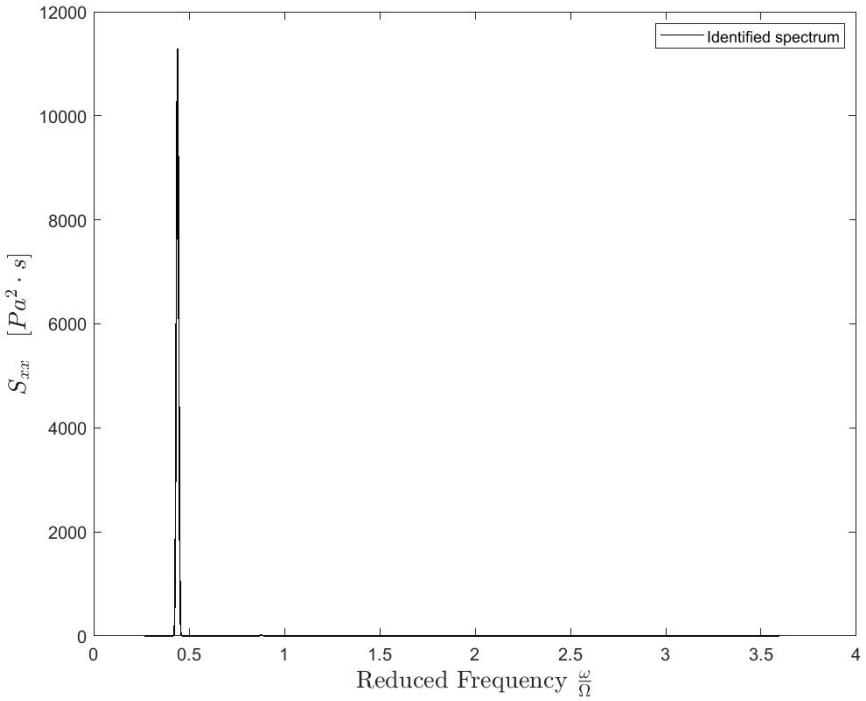

FIGURE 6.118: FULL-THEORETICAL AUTO-CORRELATION PRESSURE SPECTRUM FOR RAPDUD WITH Φ = 0.9 Φ_D, EULER NUMBER = 0.2969, N =9 VORTICES

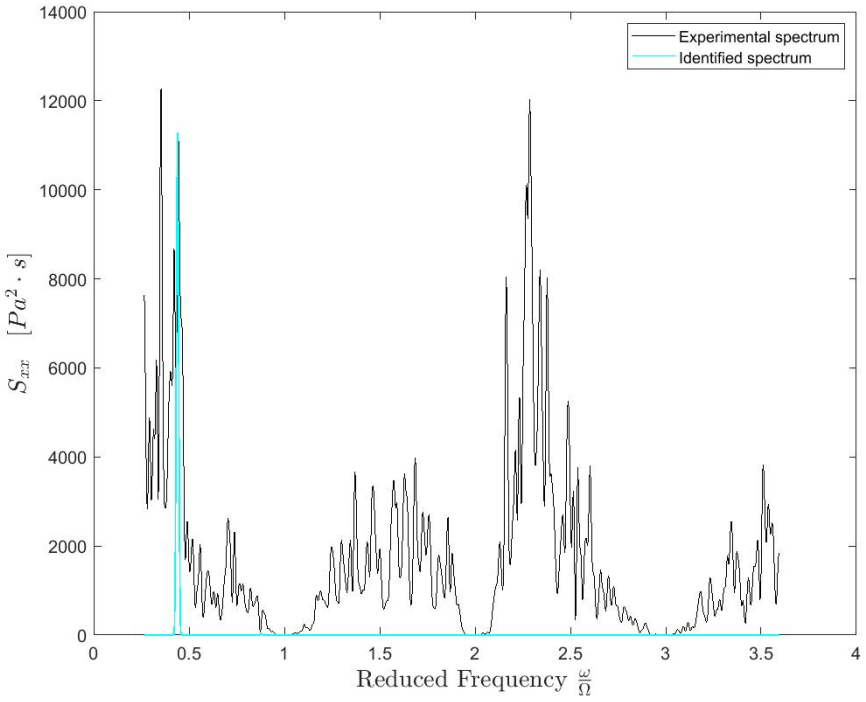

FIGURE 6.119: COMPARISON BETWEEN EXPERIMENTAL AUTO-CORRELATION SPECTRUM AND FULL-THEORETICAL SPECTRUM FOR RAPDUD WITH Φ =0.9 Φ_D, EULER NUMBER = 0.2969, N =9 VORTICES

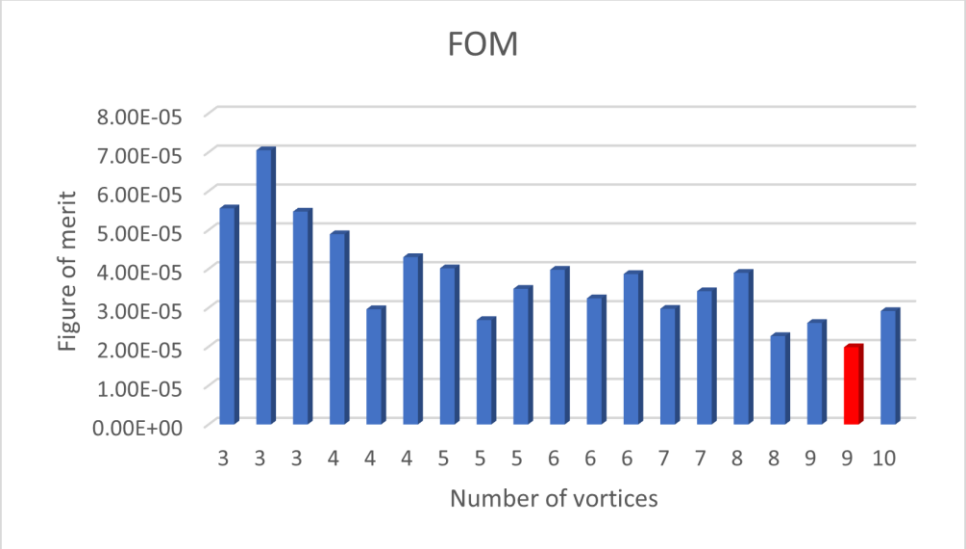

FIGURE 6.120: EVALUATION OF THE FIGURE OF MERIT WITH RESPECT TO THE NUMBER OF VORTICES FOR RAPDUD WITH Φ = 0.9 Φ_D, EULER NUMBER = 0.2969

N	ω/Ω	ε_{TOT}	Γ	ω_γ [rad/s]	a (%R)	σ_g
3	0.0823975	6.07E-05	0.01948	25.91	0.51673	0.19949
3	0.119019	5.56E-05	0.0155	37.43	0.5	0.19973
3	0.140381	7.05E-05	0.00488	44.15	0.67009	0.20021
3	0.149536	5.47E-05	0.01242	47.03	0.5	0.19988
4	0.0610352	4.89E-05	0.01204	19.20	0.68752	0.20007
4	0.088501	2.96E-05	0.02224	27.83	0.57127	0.19925
4	0.109863	4.30E-05	0.02044	34.55	0.528	0.19942
5	0.0488281	4.01E-05	0.03258	15.36	0.60709	0.19804
5	0.0701904	2.68E-05	0.04315	22.07	0.55449	0.19737
5	0.088501	3.49E-05	0.01238	27.83	0.66319	0.20001
6	0.0427246	3.98E-05	0.02434	13.44	0.69244	0.1989
6	0.0579834	3.24E-05	0.02847	18.24	0.65159	0.19848
6	0.0732422	3.87E-05	0.0317	23.03	0.60627	0.19814
7	0.0366211	2.97E-05	0.03755	11.52	0.69319	0.19713
7	0.0640869	3.43E-05	0.02516	20.16	0.67085	0.19881
8	0.0305176	3.90E-05	0.04382	9.60	0.70348	0.19642
8	0.0549316	2.27E-05	0.02258	17.28	0.72881	0.19915
9	0.0396729	2.61E-05	0.02946	12.48	0.73814	0.19845
9	0.0488281	1.99E-05	0.03607±72.20	15.36±1.99E-5	0.71606±0.34	0.19778
10	0.0457764	2.92E-05	0.02159	14.40	0.75799	0.1992

TABLE 6.40: IDENTIFICATION ASSESSMENT ASSOCIATED WITH BACKFLOW INSTABILITIES ON RAPDUD INDUCER, 90% OF DESIGN FLOW COEFFICIENT, EULER NUMBER = 0.2969

6.4.3. $\Phi = 0.8 \cdot \Phi_D$

The last evaluated case in this project with meaningful identifications is an 80% of the design flow coefficient in RAPDUD inducer. The different selected cases for each fixed value of the Euler number are presented in Table 6.41, while the detailed results are presented for Euler numbers of σ = 0.1318, σ = 0.2539 and σ = 0.2971.

σ	N	ω/Ω	ε_{TOT}	Γ	ω_γ [rad/s]	a (%R)	σ_g
0.116	6	0.036	1.87E-05	0.02975	11.32	0.90944	0.19856
0.1318	5	0.0427	1.64E-05	0.05064	13.43	0.83968	0.19606
0.1399	6	0.036	2.68E-05	0.0325	11.32	0.88473	0.19803
0.1616	5	0.0457764	2.08E-05	0.0367	14.40	0.84721	0.19711
0.1751	5	0.0457764	2.79E-05	0.05789	14.40	0.76434	0.19436
0.2063	5	0.0457764	3.53E-05	0.05055	14.40	0.75932	0.1953
0.2191	5	0.0457764	2.23E-05	0.03469	14.40	0.8621	0.19749
0.2359	5	0.0335693	2.64E-05	0.04836	10.56	0.82929	0.19511
0.2539	5	0.0640869	3.67E-05	0.03402	20.16	0.76655	0.19765
0.2696	5	0.0457764	2.03E-05	0.04887	14.40	0.79787	0.19639
0.283	5	0.0488281	2.55E-05	0.03663	15.36	0.82696	0.19713
0.2971	5	0.0335693	3.30E-05	0.04092	10.56	0.85493	0.19652

TABLE 6.41: IDENTIFICATION ASSESSMENT ASSOCIATED WITH BACKFLOW INSTABILITIES ON RAPDUD INDUCER, 80% OF DESIGN FLOW COEFFICIENT

- **σ = 0.1318**

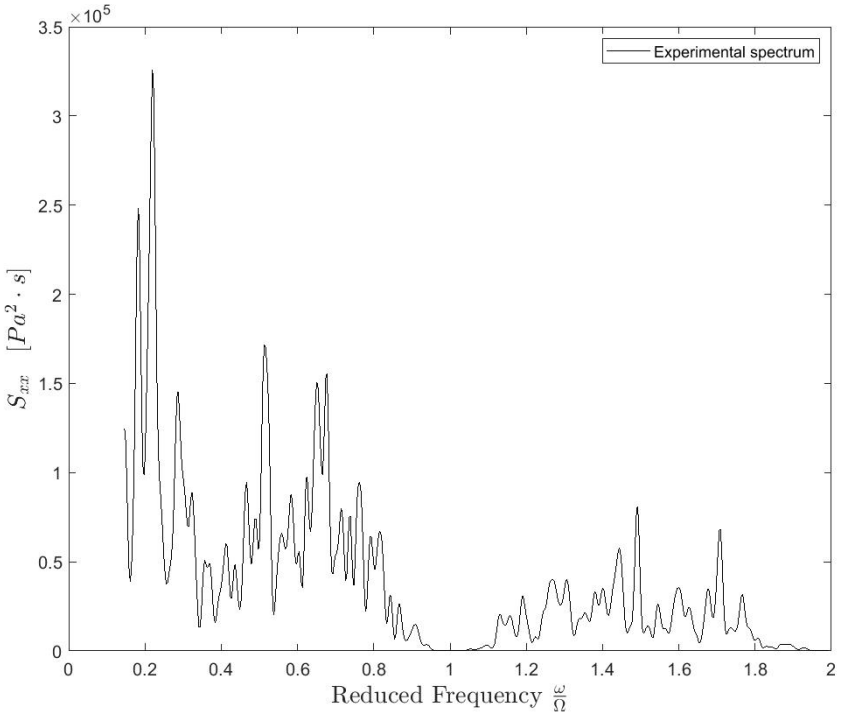

FIGURE 6.121: EXPERIMENTAL AUTO-CORRELATION PRESSURE SPECTRUM FOR RAPDUD WITH Φ = 0.8 Φ_D, EULER NUMBER = 0.1318.

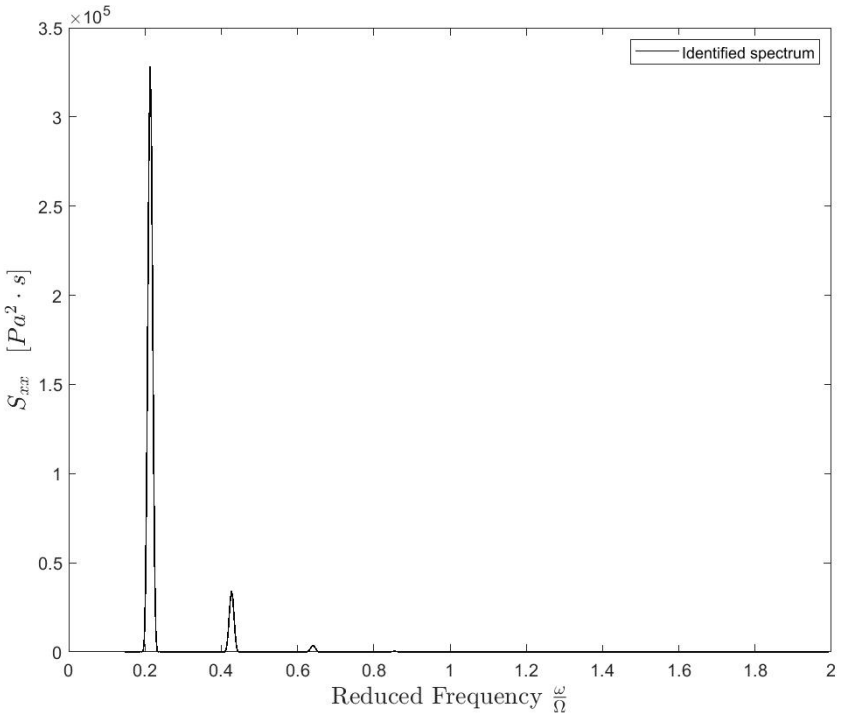

FIGURE 6.122: FULL-THEORETICAL AUTO-CORRELATION PRESSURE SPECTRUM FOR RAPDUD WITH Φ = 0.8 Φ_D, EULER NUMBER = 0.1318, N =5 VORTICES

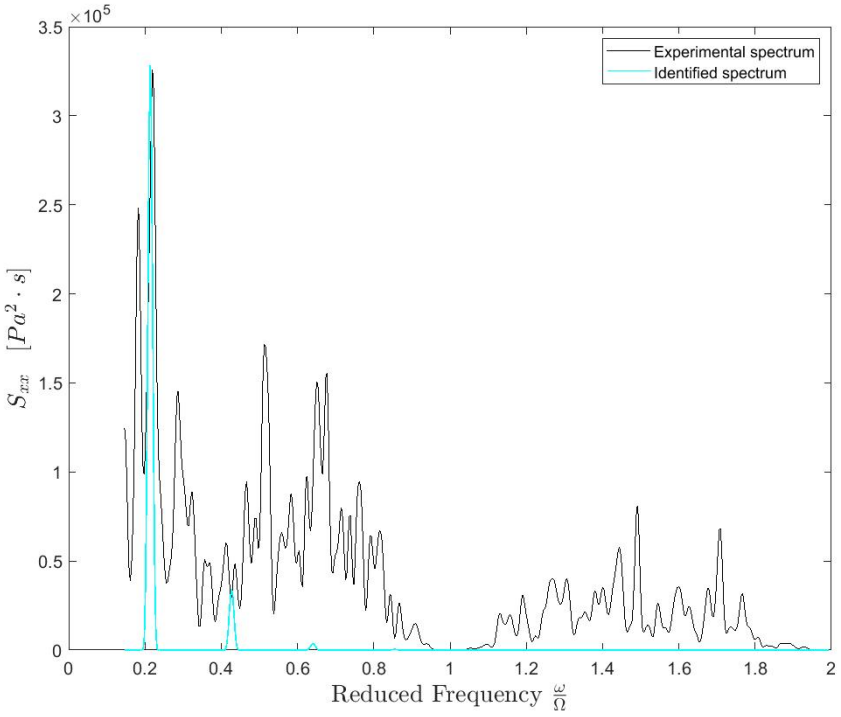

FIGURE 6.123: COMPARISON BETWEEN EXPERIMENTAL AUTO-CORRELATION SPECTRUM AND FULL-THEORETICAL SPECTRUM FOR RAPDUD WITH Φ =0.8 Φ_D, EULER NUMBER = 0.1318, N =5 VORTICES

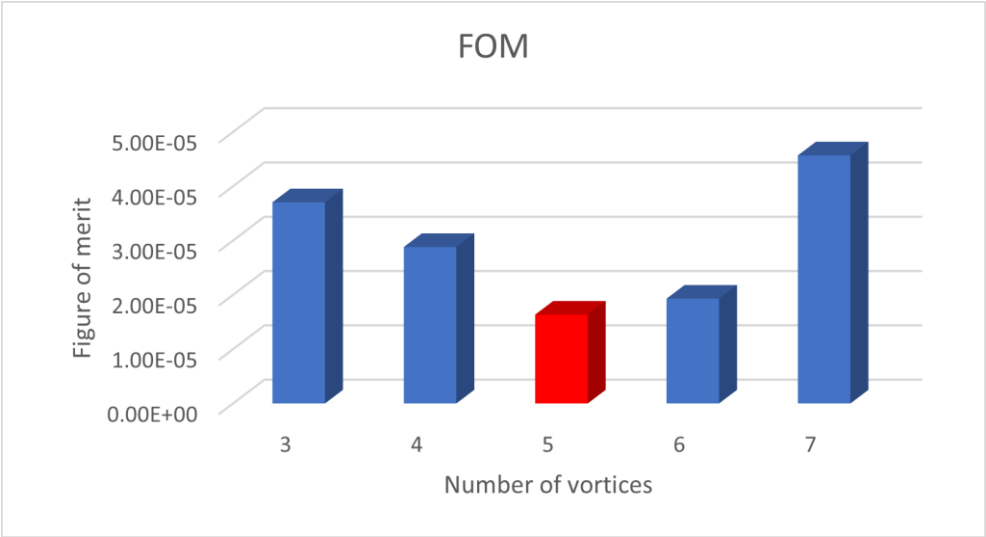

FIGURE 6.124: EVALUATION OF THE FIGURE OF MERIT WITH RESPECT TO THE NUMBER OF VORTICES FOR RAPDUD WITH Φ = 0.8 Φ_D, EULER NUMBER = 0.1318

N	ω/Ω	ε_{TOT}	Γ	ω_γ [rad/s]	a (%R)	σ_g
3	0.073	3.70E-05	0.03992	22.96	0.75549	0.19666
4	0.0549	2.88E-05	0.04365	17.27	0.791	0.19608
5	0.0427	1.64E-05	0.05064±32.64	13.43±1.64E-5	0.83968±0.0048	0.19606
6	0.036	1.93E-05	0.03673	11.32	0.89021	0.19717
7	0.03	4.57E-05	0.03818	9.44	0.88401	0.19715

TABLE 6.42: IDENTIFICATION ASSESSMENT ASSOCIATED WITH BACKFLOW INSTABILITIES ON RAPDUD INDUCER, 80% OF DESIGN FLOW COEFFICIENT, EULER NUMBER = 0.1318

- **σ = 0.2539**

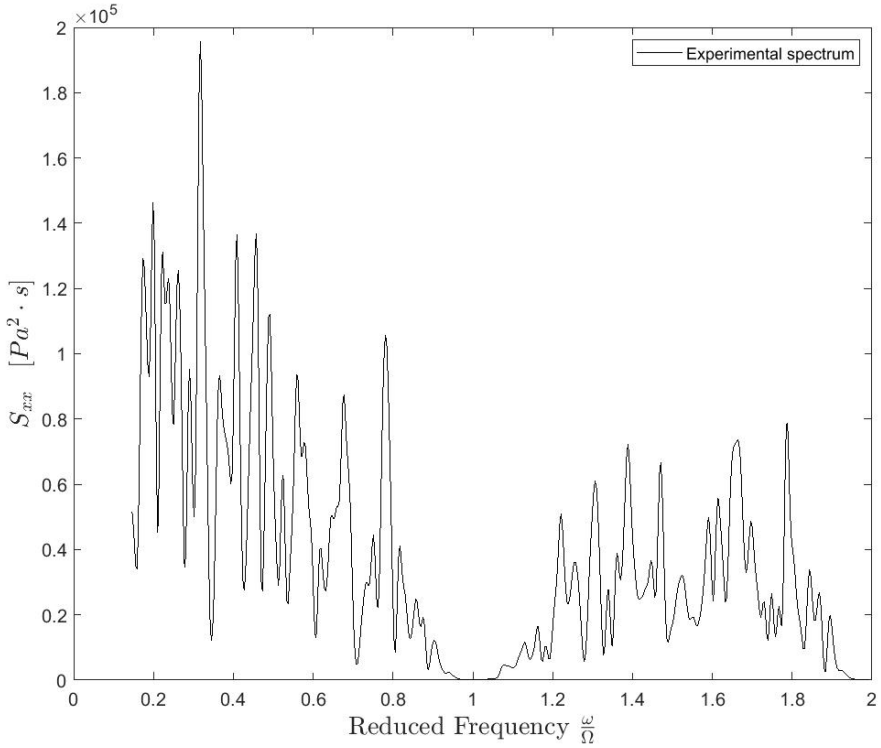

FIGURE 6.125: EXPERIMENTAL AUTO-CORRELATION PRESSURE SPECTRUM FOR RAPDUD WITH Φ = 0.8 Φ_D, EULER NUMBER = 0.2539.

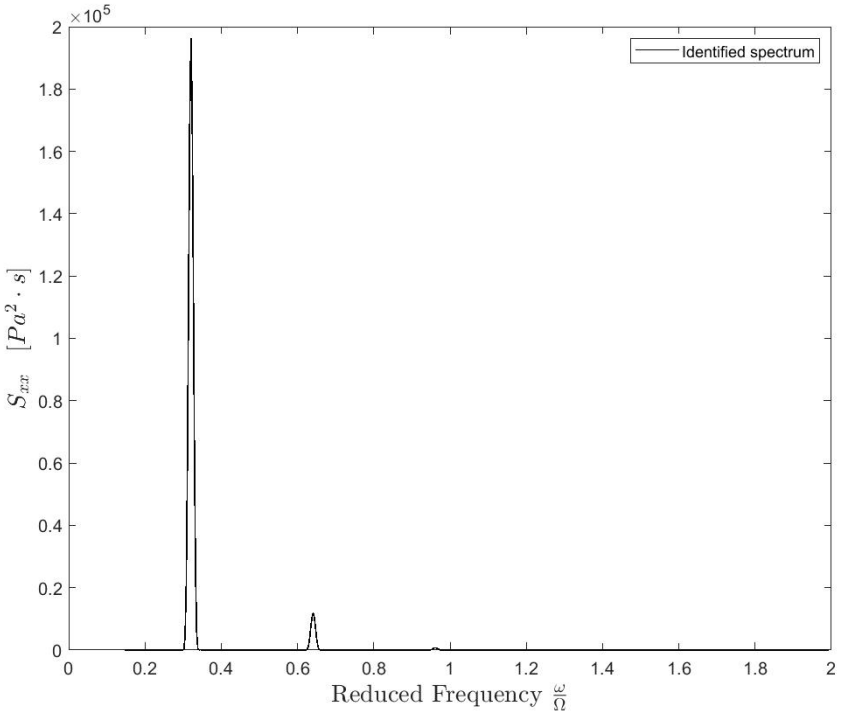

FIGURE 6.126: FULL-THEORETICAL AUTO-CORRELATION PRESSURE SPECTRUM FOR RAPDUD WITH Φ = 0.8 Φ_D, EULER NUMBER = 0.2539, N =5 VORTICES

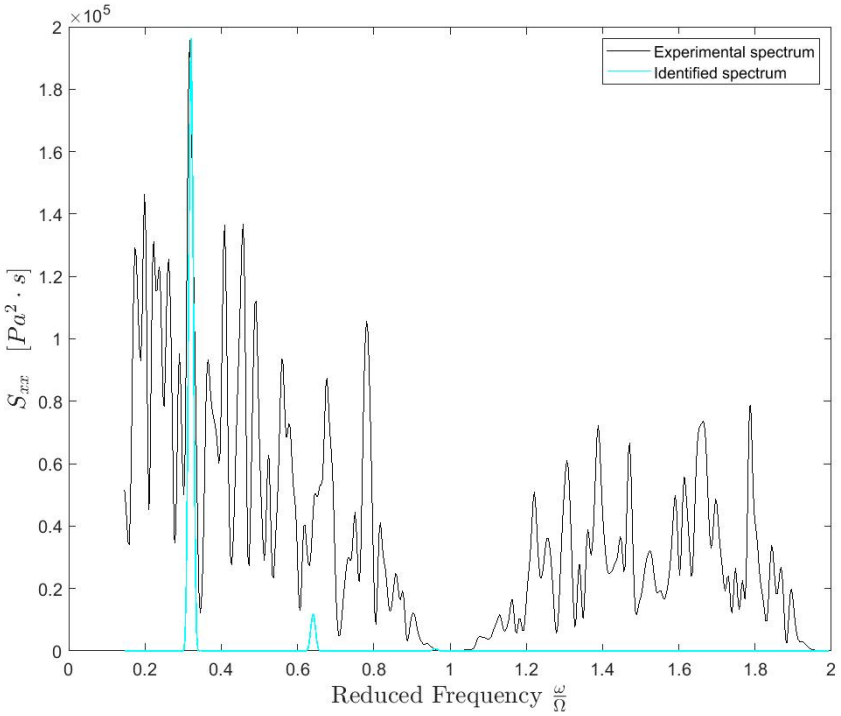

FIGURE 6.127: COMPARISON BETWEEN EXPERIMENTAL AUTO-CORRELATION SPECTRUM AND FULL-THEORETICAL SPECTRUM FOR RAPDUD WITH Φ =0.8 Φ_D, EULER NUMBER = 0.2539, N =5 VORTICES

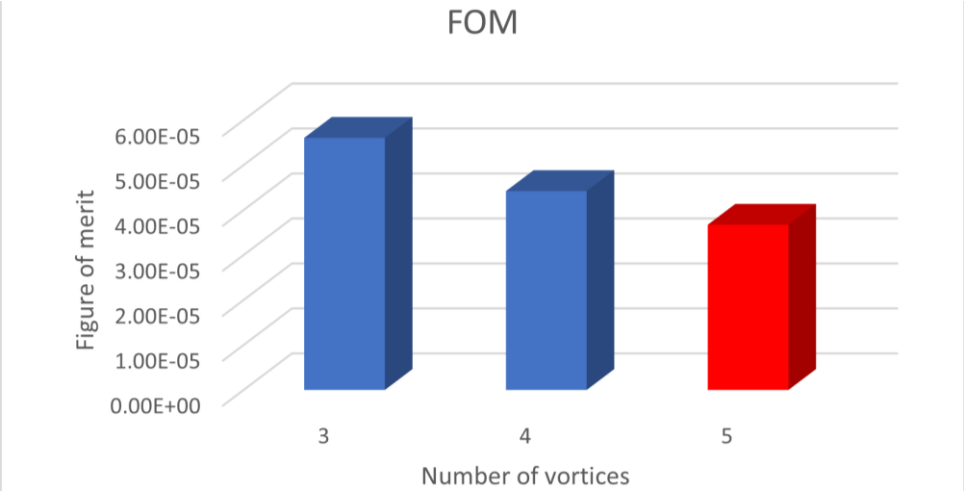

FIGURE 6.128: EVALUATION OF THE FIGURE OF MERIT WITH RESPECT TO THE NUMBER OF VORTICES FOR RAPDUD WITH $\Phi = 0.8\ \Phi_D$, EULER NUMBER = 0.2539

N	ω/Ω	ε_{TOT}	Γ	ω_γ [rad/s]	a (%R)	σ_g
3	0.106812	5.60E-05	0.02891	33.59	0.67901	0.19849
4	0.0793457	4.42E-05	0.0378	24.95	0.70096	0.19745
5	0.0640869	3.67E-05	0.03402±39.71	20.16±3.68E-5	0.76655±0.024	0.19765

TABLE 6.43: IDENTIFICATION ASSESSMENT ASSOCIATED WITH BACKFLOW INSTABILITIES ON RAPDUD INDUCER, 80% OF DESIGN FLOW COEFFICIENT, EULER NUMBER = 0.2539

- **σ = 0.2971**

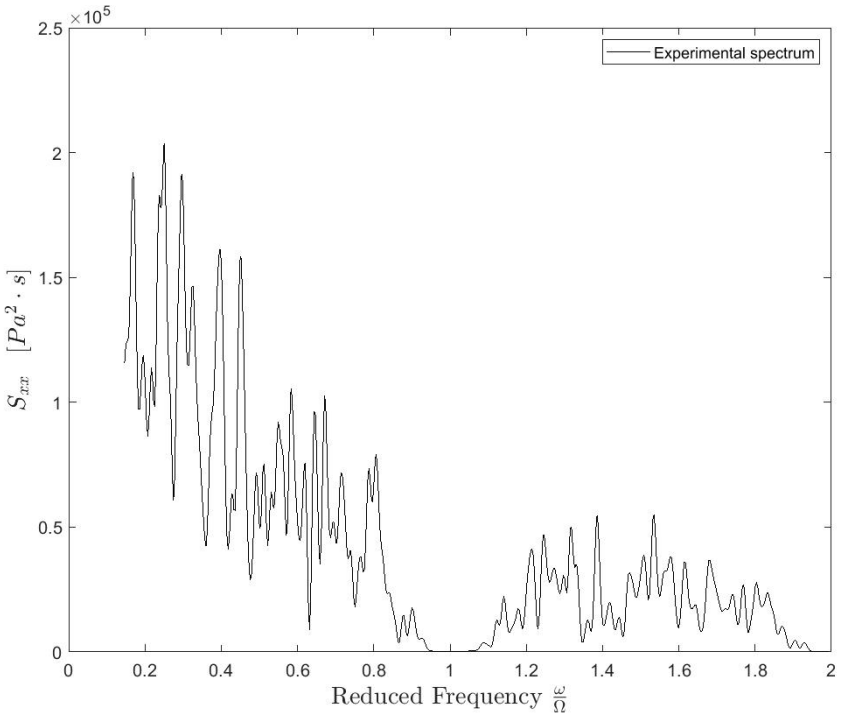

FIGURE 6.129: EXPERIMENTAL AUTO-CORRELATION PRESSURE SPECTRUM FOR RAPDUD WITH $\Phi = 0.8\ \Phi_D$, EULER NUMBER = 0.2971.

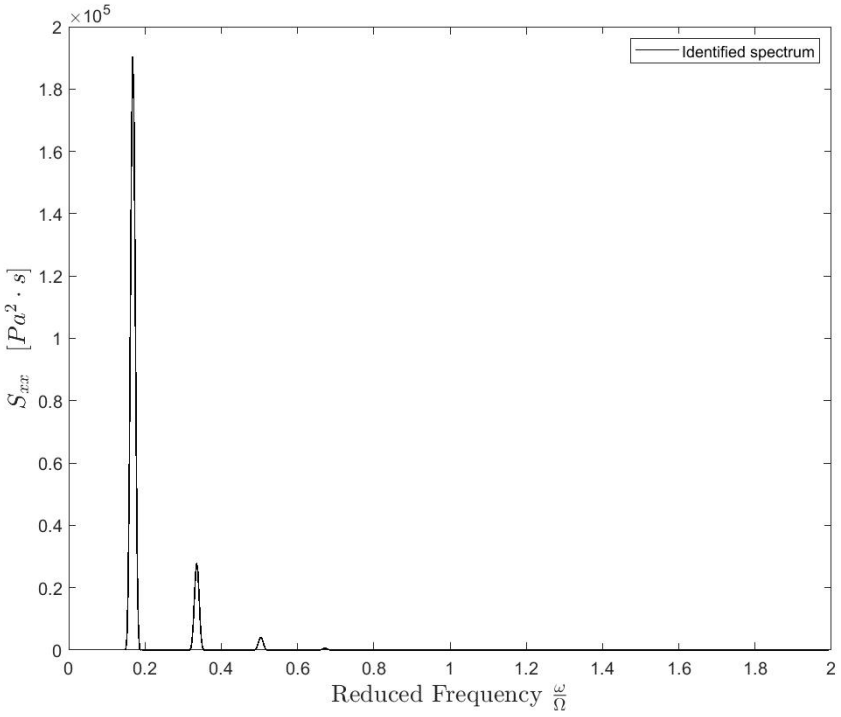

FIGURE 6.130: FULL-THEORETICAL AUTO-CORRELATION PRESSURE SPECTRUM FOR RAPDUD WITH Φ = 0.8 Φ_D, EULER NUMBER = 0.2971, N =5 VORTICES

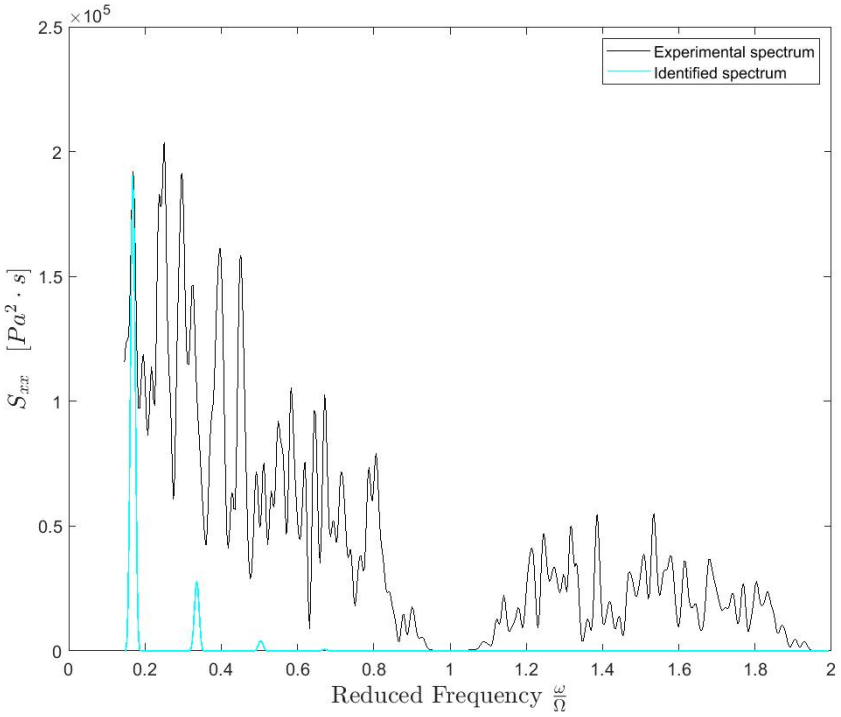

FIGURE 6.131: COMPARISON BETWEEN EXPERIMENTAL AUTO-CORRELATION SPECTRUM AND FULL-THEORETICAL SPECTRUM FOR RAPDUD WITH Φ =0.8 Φ_D, EULER NUMBER = 0.2971, N =5 VORTICES

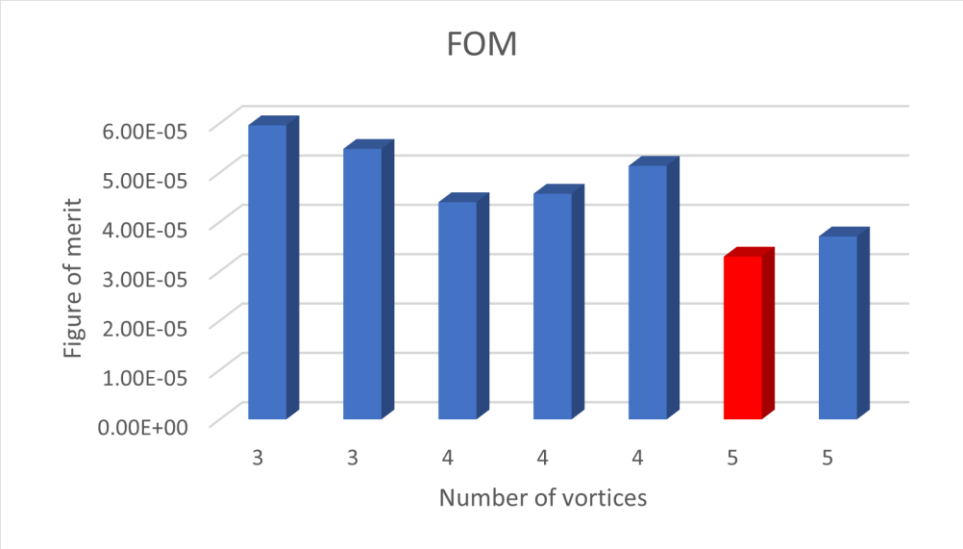

FIGURE 6.132: EVALUATION OF THE FIGURE OF MERIT WITH RESPECT TO THE NUMBER OF VORTICES FOR RAPDUD WITH $\Phi = 0.8\ \Phi_D$, EULER NUMBER = 0.2971

N	ω/Ω	ε_{TOT}	Γ	ω_γ [rad/s]	a (%R)	σ_g
3	0.0549316	5.75E-05	0.04449	17.28	0.74884	0.19625
3	0.0823975	5.96E-05	0.04298	25.91	0.66332	0.19659
3	0.0976562	5.48E-05	0.01964	30.71	0.8095	0.19971
4	0.0427246	4.40E-05	0.03658	13.44	0.834	0.19731
4	0.0610352	4.57E-05	0.04093	19.20	0.746	0.19659
4	0.0732422	5.14E-05	0.0388	23.03	0.71417	0.19709
5	0.0335693	3.30E-05	0.04092±51.41	10.56±3.31E-5	0.85493±0.0082	0.19652
5	0.0488281	3.71E-05	0.04757	15.36	0.76699	0.1966

TABLE 6.44: IDENTIFICATION ASSESSMENT ASSOCIATED WITH BACKFLOW INSTABILITIES ON RAPDUD INDUCER, 80% OF DESIGN FLOW COEFFICIENT, EULER NUMBER = 0.2971

7. Validation models

Since the identified instabilities are not directly detected experimentally, two analytical closed-form models based on the fundamental physics of flow have been developed to support the identifications.

Identifications are presented below, bringing together the frequency-processed experimental data, the Bayesian estimator and the designed theoretical model. The experiments carried out in the CPRTF generally indicate, as in Cervone et al. (2009), Torre et al. (2011) and Pace et al. (2019), that the main forms of flow instabilities in all the inducers are:

1) rotating cavitation modes with one or more co-rotating and/or counter-rotating lobes;

2) low frequency (sub-synchronous) cavitation auto-oscillation surge modes;

3) higher-order cavitation surge modes, occurring at super synchronous frequencies over a wider range of cavitation.

All the previous instabilities were detected and characterized using classical cross-correlations methods between multiple signals coming from different transducers, introducing limitations in the ability to highlight rotating phenomena and do not allow the actual number of lobes constituting the phenomenon to be identified with certainty, but only allow the minimum number of these to be highlighted.

However, noted that with the angular arrangement of the transducers (the angular separation is consistently 45°) it is not possible to discern whether phenomena with more than four lobes. To overcome this, a solution with spaced PCBs with an angular separation not constantly equal to 45° should be implemented. In this work, results are presented directly using a physics- based approach, since the simplicity of the developed 2D theoretical model, also compared to the stochastic and 3D nature of the selected phenomenon.

Two different verification theories are differentiated: **a priori N prediction** and **a priori $\boldsymbol{\omega_\gamma}$ prediction**.

7.1. A priori N prediction

The flow is modelled as an ideal complex flow, as depicted in Figure 4.4.

The flow is assumed to have a radially stratified velocity, where in the inner region (V_1) the flow does not have any radial component, while the behaviour in the external region (V_2) the flow is characterized by purely radial velocity.

$$V = \begin{cases} V_1(r) = 0 & 0 \le r \le r_\gamma \\ V_2(r) \neq 0 & r_\gamma \le r \le r_T \end{cases} \qquad 7.1$$

The interface, which is free interface, in the mixing zone is described by:

$$f\left(\mathbf{x},t\right) = r - r_g - e\left(J,t\right) = 0 \qquad 7.2$$

where the perturbations are assumed N-lobed and harmonical with angular frequency ω, such that:

$$\varepsilon\left(\vartheta,t\right) = \tilde{\varepsilon}e^{iN\left(\vartheta-\omega t\right)} \qquad 7.3$$

Moreover, as in the data-driven model, the vortices are assumed to have the same intensity such that:

$$\gamma_k = \gamma \qquad \Gamma = N\gamma = \sum_{k=1}^{N}\gamma_k \qquad 7.4$$

Building upon the continuity, irrotationality and Bernoulli's equation the field equations can be obtained as:

$$\begin{cases} \nabla^2 f_{1,2} = 0 & \text{(Laplace's equation)} \\ \dfrac{\P f_{1,2}}{\P t} + \dfrac{p_{1,2}}{r} + \dfrac{1}{2}\nabla f_{1,2}\cdot\nabla f_{1,2} = B_{1,2}\left(t\right) & \text{(Bernoulli's equation)} \end{cases} \qquad 7.5$$

where good boundary conditions are:

$$\begin{cases} \dfrac{Df}{Dt} = \dfrac{\P f}{\P t} + \nabla f_{1,2}\cdot\nabla f = 0 & \text{(free surface points remain on interface)} \\ p_1 = p_2 & \text{(negligible surface tension)} \end{cases}$$

$$f_1 \text{ regular at } r = 0 \qquad \text{(no singularity on the centreline)} \qquad 7.6$$

$$v = \frac{\partial\phi_2}{\partial r} = 0 \; at \; r = r_T \qquad \text{(impermeability condition on the duct wall)}$$

Using the classical expansion in steady and perturbation flow components, it is possible to obtain the equation for the complex velocity potential, that for N-lobed harmonic azimuthal perturbations become:

$$\nabla^2\phi'_{1,2} = \frac{1}{r}\frac{\partial}{\partial r}\left(r\frac{\partial\phi'_{1,2}}{\partial r}\right) + \frac{1}{r^2}\frac{\partial^2\phi'_{1,2}}{\partial\vartheta^2} = 0 \qquad \rightarrow \qquad \frac{\partial^2 R_{1,2}}{\partial r^2} + \frac{1}{r}\frac{\partial R_{1,2}}{\partial r} - N^2\frac{R_{1,2}}{r^2} = 0 \qquad 7.7$$

Applying the regularity and the impermeability conditions, the potentials in the two regions appear in the form:

$$\begin{cases} \hat{f}_1\left(r,J,t\right) = A_1 r^N e^{iN\left(J-\omega t\right)} \\ \hat{f}_2\left(r,J,t\right) = A_2\left(r^N + r_T^{2N} r^{-N}\right)e^{iN\left(J-\omega t\right)} \end{cases} \qquad 7.8$$

Exploiting the use of the Bernoulli's equation coupled with the negligible surface tension at the interface (dynamic condition at the interface), the following relationship is obtained:

$$A_1\left(w - \frac{\bar{V}_1}{r_g}\right) - A_2\left(w - \frac{\bar{V}_2}{r_g}\right)\left(1 + \frac{r_T^{2N}}{r_g^{2N}}\right) = 0 \qquad 7.9$$

being $\bar{V}_1$ and $\bar{V}_2$ are the average unperturbed azimuthal flow velocities in the core and backflow regions 1 and 2, respectively.

From the kinematic BC at the slip interface:

$$\begin{gathered} i\left(\omega - \frac{\bar{V}_1}{r_\gamma}\right)\tilde{\varepsilon} + A_1 r_\gamma^{N-1} = 0 \\ i\left(\omega - \frac{\bar{V}_2}{r_\gamma}\right)\tilde{\varepsilon} + A_2\left(1 - \frac{r_T^{2N}}{r_\gamma^{2N}}\right) r_\gamma^{N-1} = 0 \end{gathered} \qquad 7.10$$

that coupled with the Equation 7.9 forms a system of three equations in three unknowns. The characteristic equation for the natural frequencies of the slipline turns out to be the solution of the system.

$$\omega^2\left(\frac{r_T^{2N}}{r_\gamma^{2N}} - 1\right) + \left(\omega - \frac{\bar{V}_2}{r_\gamma}\right)^2\left(\frac{r_T^{2N}}{r_\gamma^{2N}} + 1\right) = 0 \qquad 7.11$$

It can be noticed that the natural frequencies of the slipline are complex conjugates, and it is temporally unstable with oscillation frequency (equal to the rotational speed of the vortices):

$$\begin{gathered} \omega_\gamma = Re\{\omega_{1,2}\} = \left(\frac{r_\gamma^{2N}}{r_T^{2N}} + 1\right)\frac{\bar{V}_2}{2\, r_\gamma} \\ N = \frac{ln\left(2\omega_\gamma r_\gamma/\bar{V}_2 - 1\right)}{2\, ln\left(r_\gamma/r_T\right)} \end{gathered} \qquad 7.12$$

Since the velocity discontinuity at the slipline $r = r_\gamma$ is $V_{2\gamma} = \Gamma/2\pi r_\gamma$ and the internal flow is not rotating, it is then reasonable to assume that the azimuthal velocity of the vortices g_k is:

$$\omega_\gamma r_\gamma \simeq \frac{1}{2} V_{2\gamma} \quad \Rightarrow \quad \omega_\gamma \simeq \frac{V_{2\gamma}}{2r_\gamma} \qquad 7.13$$

At this point one can assume for the backflow a Prandtl-type approximate turbulent velocity profile, allowing to solve explicitly for N:

$$\begin{gathered} \frac{V_2(r)}{V_{2\gamma}} = \left(\frac{r_T - r}{r_T - r_\gamma}\right)^{1/m} \\ N = \frac{ln(1/m)}{2\, ln\left(r_\gamma/r_T\right)} \end{gathered} \qquad 7.14$$

In Figure 7.1, the theoretical non-dimensional prediction of the forementioned model is depicted, using the prediction as a validation to sustain the carried-out identifications.

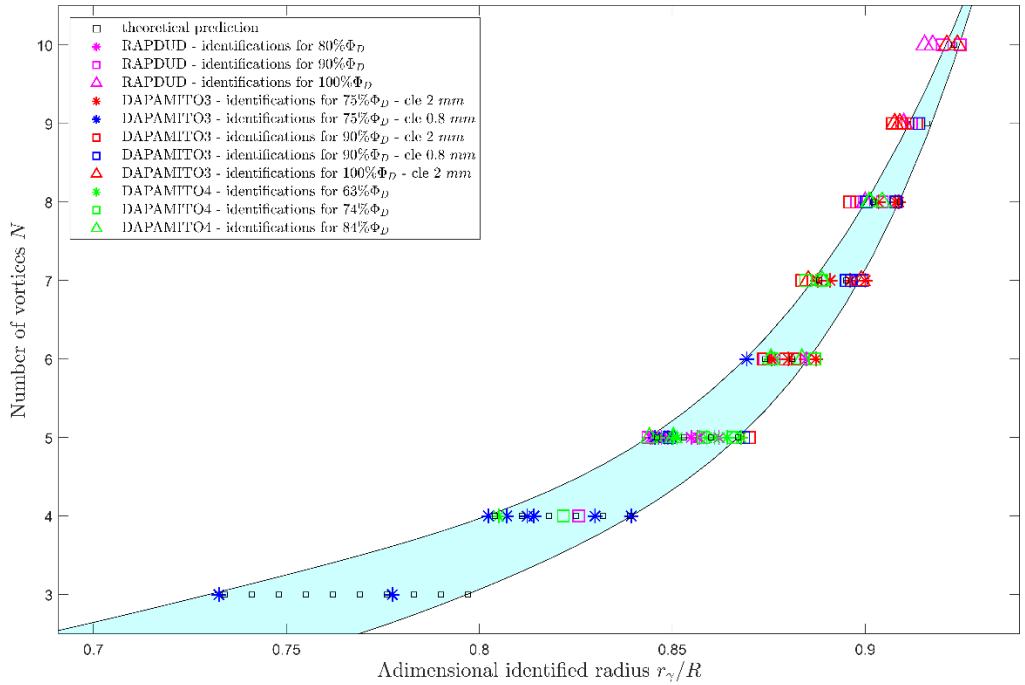

FIGURE 7.1: THEORETICAL PREDICTION OF THE NUMBER OF VORTICES COMPARED WITH THE IDENTIFICATIONS.

7.2. A priori ω_γ prediction

Using classical cascade theory, it is possible to obtain the total pressure jump as a function of the outlet blade tip angle (β_T) and the flow coefficient Φ :

$$\Delta p_T = \frac{1}{2}\rho\Omega^2 r_T^2\left(1-\Phi_1^2\tan^2\beta_T\right) \qquad 7.15$$

Taking into account Figure 7.2, and assuming a loss factor ξ = 1.5 (being 0.5 for entrance losses and 1 for no downstream pressure recovery), the inviscid tip leakage flow velocity u'_{TL} in the relative (rotating) frame is estimated as:

$$\Delta p_T = \xi \cdot 0.5 \cdot \rho \cdot u'_{TL} \cdot u'_{TL}$$
$$|u'_{TL}| = \sqrt{\frac{2\,\Delta p_T}{\xi\,\rho}} \qquad 7.16$$

Normal to the blade, and therefore, it can be written that:

$$u'_{TL} = \left|\overrightarrow{u'_{TL}}\right| \cdot (-e_\theta \cos\beta_T + e_z \sin\beta_T) \qquad 7.17$$

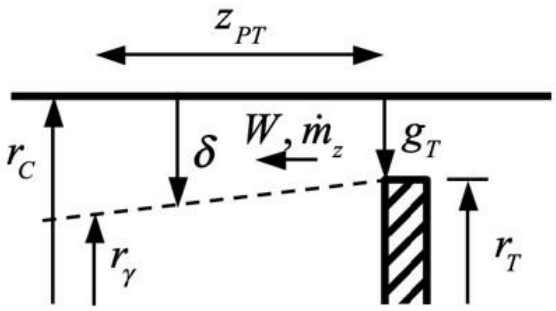

FIGURE 7.2: SCHEME OF BACKFLOW SWIRL.

In the relative frame, the volumetric tip leakage flow rate that is not intercepted by the next blade is:

$$V'_{TL} = C_c N s_T \sin\beta_T |u'_{TL}| g_T \qquad 7.18$$

Being C_c the contraction coefficient. It is around 0.611 for inviscid 2D flows but the actual contraction coefficient is even smaller in the case that the tip leakage flow is dominated by viscous effects, as in the case of small tip gaps. Then, the values between 0.4 and 0.6 are justified.

The corresponding tip leakage flow velocity in the absolute frame is:

$$u_{TL} = \left[e_\theta \left(\Omega r_T - \left| \overrightarrow{u'_{TL}} \right| cos\beta_T \right) + e_z \left(\left| \overrightarrow{u'_{TL}} \right| sin\beta_T \right) \right] \qquad 7.19$$

While the volumetric tip leakage in the axial direction is:

$$\dot{V_{TLz}} \simeq \dot{V'_{TL}} \sin\beta_T \simeq C_c N s_T \sin^2\beta_T |u'_{TL}| g_T \qquad 7.20$$

The axial flow rate is in fact constant in the assumption of axisymmetric flow ($r = r_\gamma$ is a streamline):

$$\dot{m}_z = \rho \dot{V_{TLz}} = constant \qquad 7.21$$

Integrating the axial momentum balance of an axial slice of the backflow region between z and z + dz:

$$\frac{d}{dz}(\dot{m}_z r_T \bar{V}) dz \simeq -r_T 2\pi r_T dz C_f \frac{1}{2} \rho \overline{V^2} \qquad 7.22$$

Being $\bar{V}$ the mean azimuthal flow velocity and C_f the wall friction coefficient.

It can be solved for $\overline{V_2}$ and recalling:

$$\frac{2\,\omega_\gamma r_\gamma}{\overline{V_2}} \simeq 1 + \frac{1}{m} \qquad 7.23$$

Finally, it is obtained the prediction of the angular velocity of the vortices as:

$$\frac{\omega_\gamma}{\Omega} \simeq \frac{\overline{V_2}}{2\Omega r_\gamma}\left(1+\frac{1}{m}\right) \qquad 7.24$$

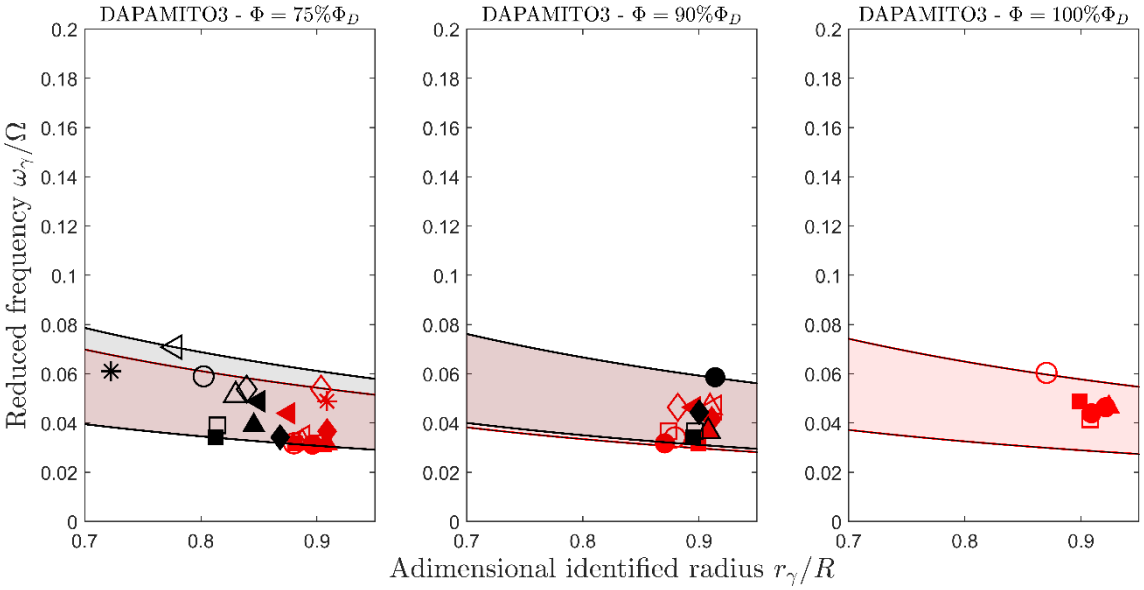

FIGURE 7.3: THEORETICAL PREDICTION OF THE ANGULAR VELOCITY COMPARED WITH THE IDENTIFICATIONS FOR DAPAMITO 3 AND STUDIED FLOW COEFFICIENTS.

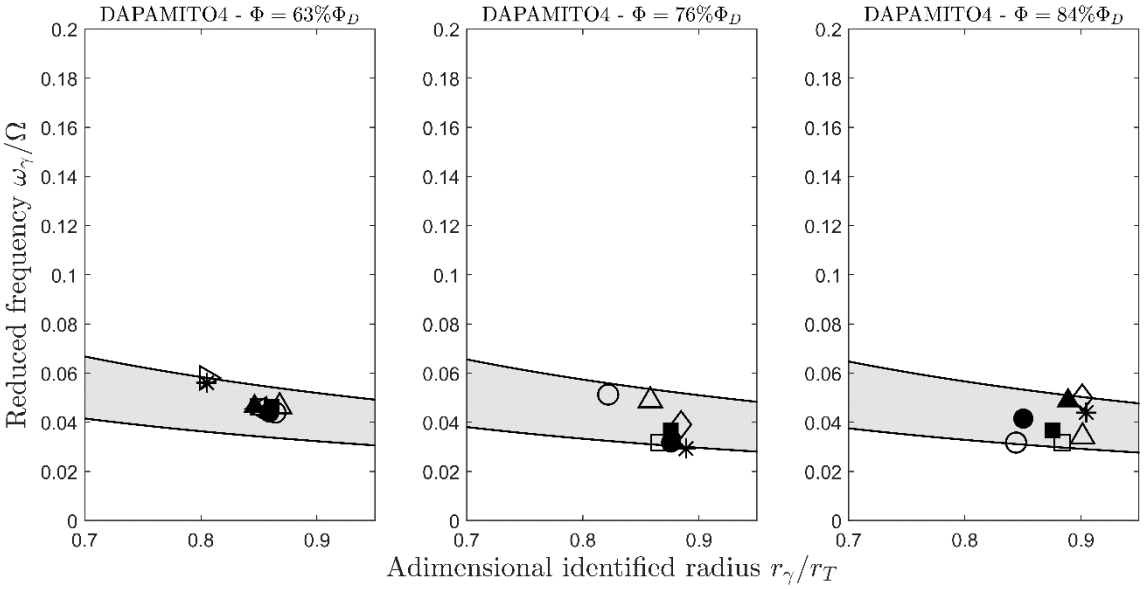

FIGURE 7.4: THEORETICAL PREDICTION OF THE ANGULAR VELOCITY COMPARED WITH THE IDENTIFICATIONS FOR DAPAMITO 4 AND STUDIED FLOW COEFFICIENTS.

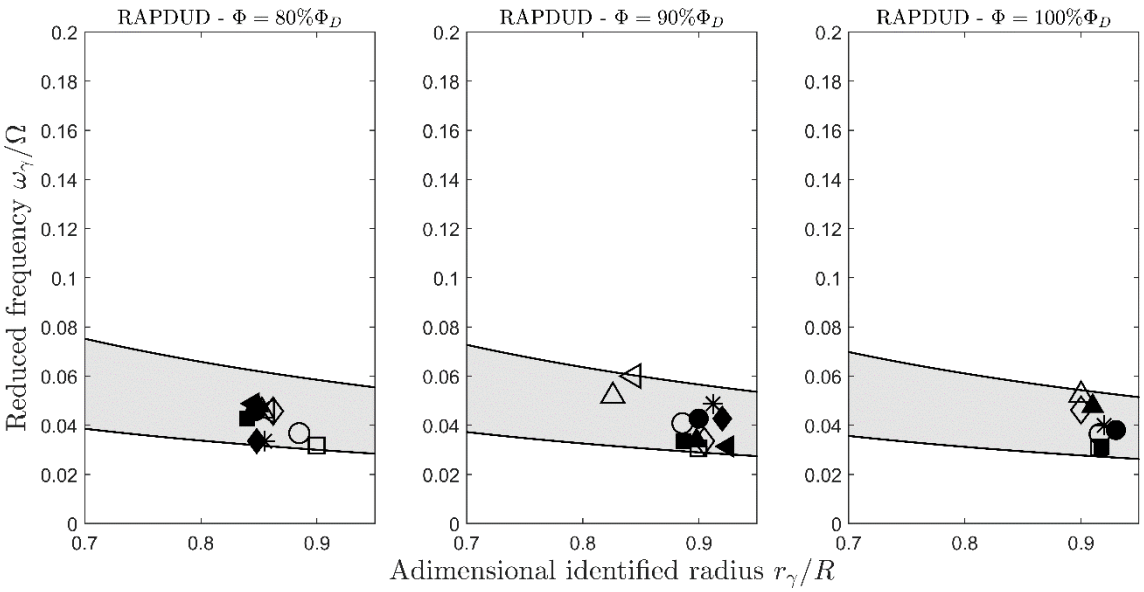

FIGURE 7.5: THEORETICAL PREDICTION OF THE ANGULAR VELOCITY COMPARED WITH THE IDENTIFICATIONS FOR RAPDUD AND STUDIED FLOW COEFFICIENTS.

Figure 7.3, 7.4 and 7.5 show the trend of the rotational speed of the vortices, normalized with the rotational frequency of the inducer, as a function of the normalized radial position.

The area is plotted as a function of two extreme values of typical drag coefficients characterizing these flows. The curves, in all the three cases, therefore, differ only for the dimensionless load value and tip clearance (as has been mentioned, only in DAPAMITO 3 case, which was tested with different tip clearance as can be seen on the red area of the Figure 7.3).

It can be noticed how the identifications fall exactly within the theoretical area. It can be seen that as the load increases, the points tend to move to the right: from a physical point of view, this means that they tend to move closer to the duct wall rotating slower. This is also in line with the previous model, where more vortices, which rotate more slowly, must be close to the inner walls of the duct.

8. Limitations, conclusions and future lines of research

In this thesis, different types of inducers with different configurations have been studied by an analytical model for identifying backflow vortex instability.

For DAPAMITO 3, DAPAMITO 4 and RAPDUD inducers, the cavitating and non-cavitating performance have been evaluated, determining the cavitation-induced instabilities in different configurations. To focus on backflow vortex phenomena, some filters were applied as a notch filter to avoid the effect of the blade passage.

Developing several evaluations, it can be concluded that the method detects and characterizes the backflow vortex instability phenomena in an effective way, for different kinds of inducer and for operations both on design and off-design. Besides, the identifications are robust since the values of the figures of merit that have been found are low and the identified and experimental spectra are practically coincident in most of the analysed cases. Another advantage of the model used is the use as input of the information of one unsteady pressure transducer, without needs of complicated experimental instrumentation to collect data.

Nevertheless, it has been seen that the physical expected results, as in the case of low clearance that a higher value of number of vortices was predicted, was satisfied only in some cases. The assumptions and hypothesis of the model result in very robust results but must be analysed with good engineering judgement and treated carefully, using them as an orientation to the backflow vortex phenomena about which there is a lot of work left to do. Also, the confidence intervals obtained as verification of the process were too high in the case of vortex intensity, research is necessary about the initial parameters that are used to estimate the results in the studies carried out. However, there were very small for the rotational speed of the vortices, due to the Bayesian estimator used to get the initial parametric vector.

As future lines of research based on the work done in this thesis and the references used, there are some projects that could start from the information already known:

- Analyse the thermal effect on the results, by applying the developed method to cases with high temperature, affecting the expansion of the materials and the characteristics of the results.
- Application of the aforementioned method to other inducers which experimental data is known in order to check its validity with a higher set of inducers.
- Develop an automatic model in which the different Euler numbers used for the identification could be analysed simultaneously. It could be developed a method to get the values from the cross-correlation and use them automatically on the identificatory for each flow coefficient analysed.

To sum up, in this Master's Project Thesis, the generalities of cavitation-induced instabilities and the backflow vortex cavitation in particular have been embodied and an analytical model for the identification of backflow vortex cavitation has been used with the aim of analyse the mostly unknown world of cavitation.

PART II: STATEMENT OF CONDITIONS

A. Statement of conditions

This Part defines the statement of conditions that specifies the situation and conditions that must be met by the contract between the contractor and owner for the execution of this work. To do this, various Subsections are presented defining the status of the materials used to carry out the project as well as the conditions present in its elaboration.

A.1. State of materials

In this Subsection, it is detailed the condition of materials used for the achievement of the Final Master Project.
The project consists in a comparative study by means of computing, so the basis of the materials used is the computer used, whose specifications are shown in Table A.1.

Used hardware conditions	
Maker	ASUSTeK Computer Inc.
Model	ASUS ROG STRIX G15
Processor	Intel(R) Core(TM) i7-10870H CPU @ 2.20GHz
Installed RAM	16 GB
Keyboard	Standard
Mouse	LOGITECH M171
Operating system	Windows 11 Pro

TABLE A.0.1: CONDITIOS OF THE COMPUTER SYSTEM USED

With respect to the software used, diverse informatic programs have been used with different functions in developing the project.
Mainly, MATLAB has been the software in which the code behind the project has been analysed and the comparative study between different cases has been developed.
For the treatment of numerical data and the organization of the cases of different inducers, the Excel tool has been used.
Finally, with the objective of text editing, the computer program Word has been the tool chosen for the drafting of this document.

A.2. Implementation conditions

By the nature of the project, safety and health provisions for workers on equipment with display screens can be found in Royal Decree 488/1997, of April 14. The mentioned Royal Decree is created as a transposition into Spanish Law of Directive 90/270/CEE of the Council of the European Union. Also, the article 6 of Law 31/1995 on the Prevention of Occupational Risks must be accordant to the Royal Decree 488/1997.
The minimum provisions that apply to this project are the following:

- Equipment

    - The use of the equipment must not be a source of risk for the user.
    - Possibility of varying the brightness of the screen without reflections that could disturb the user and the ability to tilt the screen to adapt to the user's needs.
    - The screen image should be stable and the characters well defined and clearly set with adequate spacing.
    - The keyboard surface should be matte to avoid reflections and the key symbols should be legible from a normal working position.
    - Tiltable keyboard independent of the screen to facilitate a comfortable posture, with a space in front of the keyboard so that the worker can rest their hands and arms.
    - The seat must be stable, with the ability to adjust height, recline the backrest and give the user freedom of movement.
    - The table should be large enough for the user to adopt a comfortable position and should not be very reflective.

- Environment

    - The workstation must be large enough and equipped with enough space to allow changes in posture and work movements.
    - Windows should be equipped with an adjustable cover to attenuate daylight in the work environment.
    - The noise of the work equipment must be considered as a determining factor in its design so that it cannot cause great inconvenience to the worker.
    - Adequate lighting levels and an adequate luminance ratio between the screen and the environment must be guaranteed. In addition, the layout of the workplace must be arranged in such a way that an artificial or natural light source does not generate annoying glare and reflections on the screen.
    - Work equipment must not emit additional heat that could harm the nature of the worker.
    - The humidity level in the work environment must be acceptable.
    - All radiation must be reduced to negligible effects to ensure the health and safety of the worker in charge of the equipment.

- Computer/Person interconnection

    - The working software must be adapted to the task to be performed.
    - The work software must be easy to use and capable of adapting to the user's level of knowledge and experience.
    - The systems will display the information in a format and rhythm adapted to the operators.
    - Systems must provide indications about their development.
    - The principles of ergonomics must be applied to the processing of information by the worker.

PART III: BUDGET

A. Budget

This Part defines the budget associated with the completion of the Final Master Project.
To do this, the expenses are divided into different Subsections, among which are the cost associated with the hardware, the cost associated with the software and the cost associated with the workers that have made the achievement of this project possible.
Finally, a summary of the breakdown of expenses is presented.

A.1. Hardware Budget

The hardware used, as mentioned above, is shown in Table A.1 of Part II. A breakdown of the costs associated with the hardware used in the work appears in Table A.1 of Part III.

Cost associated with hardware	
Computer ASUS ROG STRIX G15	975 €
Mouse LOGITECH M171	11.50 €
Total	**986.5 €**

TABLE A.0.1: COST ASSOCIATED WITH HARDWARE

In addition, we must add the price that implies the electricity consumed by the computer during working hours. Assuming an electricity price of 0.236 €/kWh in Italy and a computer consumption of 100 W/h, **the total electricity price 14.16 €.**

A.2. Software cost

The software used is based on MATLAB to carry out the project, however there are several programs that have been used for the realization of this project as it is detailed in Section A.1 of Part II.
The cost associated with software, however, is 0 € as the software has been used with student license, administered free of charge by the Polytechnic University of Valencia.

A.3. Workers cost

First of all, it should be noted that the teaching load of the Final Master Project is 24 ECTS. Dedicating a time of 25 hours per credit as recommended by the Treaty of Bologna signed by the UPV, the time dedicated to carrying out the work has been 600 hours. The working hours dedicated to the project can be divided into different well-differentiated tasks:

- **Writing report**: 120 hours.
- **Learning the use of the code and MATLAB**: 100 hours.
- **Carrying out the project**: 320 hours.
- **Search for information and bibliography**: 60 hours.

Assuming a salary of 30 €/hour for the author of the TFG and a salary of 60€/hour for the supervisors of this work, the cost of labour is presented in Table A.2. of Part III:

Cost associated with workers	
Author of the work	18000 €
Supervisor and counsellor of the work	6000 €
Total	**24000 €**

TABLE A.0.2: COST ASSOCIATED WITH WORKERS

A.4. Total cost

Summarizing the costs that have been presented throughout the Subsections A.1, A.2 and A.3, the Table A.3 presents a summary of the total cost associated with the Final Master Project.

Total cost of the project	
Hardware cost	986.50 €
Electricity cost	14.16 €
Software cost	0 €
Workers cost	24000 €
Total	**25000.66 €**

TABLE A.0.3: TOTAL COST OF THE PROJECT

Therefore, the total cost of carrying out the project is **Twenty-Five Thousand Euros and Sixty-Six Cents (25000.66 €)**

PART IV: BIBLIOGRAPHY

A. Bibliography

[1] **A. Pasini**. *Pumping Performance Similarity, Cavitation-Induced Instabilities and Fluid-Induced Rotordynamic Forces in Tapered Inducers*. PHD thesis, Università di Pisa, 2010.

[2] **S. Guidolotti**. *Backflow Vortex Instability Identification in Rocket Engine Inducers*. Master thesis, Università di Pisa, 2021.

[3] **K. Yamamoto, Y. Tsujimoto**. *Backflow Vortex Cavitation and Its Effects on Cavitation Instabilities*. Review paper, International Journal of Fluid Machinery and Systems, 2009.

[4] **A. Ishimaru, S. Fukao, C. Kato, Y. Tsujimoto**. *Numerical Study of Vortex Structure in the Shear Layer between Swirling Backflow and Axial Main Flow*. Journal of Fluid Science and Technology, 2007.

[5] **A. Costanzo, D. Valentini, G. Pace, R. Hadavandi, L. Torre, A. Pasini, L. d'Agostino**. *Parametric Identification of Rotating Cavitation in a Three-Bladed Axial Inducer*. Fluids Engineering Division Summer Meeting, 2021.

[6] **C. E. Brennen**. *Hydrodynamics of Pumps*. California Institute of Technology. 1994.

[7] **L. Torre, A. Pasini, A. Cervone, L. d'Agostino**. *Continuous Spectrum of the Rotordynamic Forces on a Four-Bladed Inducer*. Joint Fluids Engineering Conference. 2011.

[8] **G. Pace, D. Valentini, A. Pasini, R. Hadavandi, L. d'Agostino**. *Analysis of Flow Instabilities on a Three-Bladed Axial Inducer in Fixed and Rotating Frames*. Symposium on Transport Phenomena and Dynamics of Rotating Machinery. 2017.

[9] **L. Torre**. *Studio Sperimentale delle Prestazioni e delle Instabilità Fluidodinamiche di Cavitazione su un Prototipo dell'Induttore della Turbopompa LOX del Motore VINCI*. Tesi di laurea vecchio ordinamento. 2005.

[10] **A. Pasini, R. Hadavandi, D. Valentini, G. Pace, L. d'Agostino**. *Dynamics of the Blade Channel of an Inducer under Cavitation-Induced Instabilities*. International Symposium on Transport Phenomena and Dynamics of Rotating Machinery. 2017.

[11] **G. K. Batchelor**. *An Introduction to Fluid Dynamics*. Cambridge University Press. 2000.

[12] **J. G. Lucas**. *Apuntes de la Asignatura "Ampliación de Turbomáquinas"*. Universidad Politécnica de Valencia. 2020.

[13] **K. Yokota, K. Kurahara, D. Kataoka, Y. Tsujimoto, A. J. Acosta**. *A Study of Swirling Backflow and Vortex Structure at the Inlet of an Inducer*. Japan Society of Mechanical Engineers. 1999.

[14] **T. Kimura, Y. Yoshida, M. Shimagaki**. *Relation Between Geometries of Inducer Inlet and Backflow and Vortex Structures*. Joint Propulsion Conference and Exhibit. 2004.

[15] **T. Kimura, Y. Yoshida, T. Hashimoto, M. Shimagaki**. *Numerical Simulation for Vortex Structure in a Turbopump Inducer: Close Relationship with Appearance of Cavitation Instabilities*. Journal of Fluids Engineering. 2008.

[16] **N. Yamanishi, S. Fukao, X. Quiao, C. Kato, Y. Tsujimoto**. *LES Simulation of Backflow Vortex Structure at the Inlet of an Inducer*. American Society of Mechanical Engineers. 2007.

[17] **J. W. Cooley and J. W. Tukey**. *An Algorithm for the Machine Calculation of Complex Fourier Series*. Mathematics of Computation. 1965.
[18] **S. L. Brunton, J. N. Kutz**. *Data-Driven Science and Engineering: Machine Learning Dynamical Systems and Control*. Cambridge University Press. 2019.
[19] **L. Torre, A. Cervone, G. Pace, D. Valentini, A. Pasini, L. d'Agostino**. *Cavitation Instabilities and Rotordynamic Effects in Turbopumps and Hydroturbines: Turbopump and Inducer Cavitation, Experiments and Design*. Springer International Publishing. 2017.
[20] **S. C. Roy**. *Modeling and Analysis of Material Behaviour During Cavitation Erosion*. Université Grenoble Alpes, 2015.